

NASA Contractor Report 4637

Streamlined Design and Self Reliant Hardware for Active Control of Precision Space Structures

David C. Hyland, James A. King, and Douglas J. Phillips
Harris Corporation • Melbourne, Florida

National Aeronautics and Space Administration
Langley Research Center • Hampton, Virginia 23681-0001

Prepared for Langley Research Center
under Contract NAS1-19372

December 1994

This publication is available from the following sources:

NASA Center for AeroSpace Information
800 Elkridge Landing Road
Linthicum Heights, MD 21090-2934
(301) 621-0390

National Technical Information Service (NTIS)
5285 Port Royal Road
Springfield, VA 22161-2171
(703) 487-4650

Abstract

Precision space structures may require active vibration control to satisfy critical performance requirements relating to line-of-sight pointing accuracy and the maintenance of precise, internal alignments. In order for vibration control concepts to become operational, it is necessary that their benefits be practically demonstrated in large scale ground-based experiments. A unique opportunity to carry out such demonstrations on a wide variety of experimental testbeds was provided by the NASA Control-Structure Integration (CSI) Guest Investigator (GI) Program. This report surveys the experimental results achieved by the Harris Corporation GI team on both Phases I and II of the program and provides a detailed description of Phase II activities. The Phase I results illustrated the effectiveness of active vibration control for space structures and demonstrated a systematic methodology for control design, implementation and test. In Phase II, this methodology was significantly streamlined to yield an on-site, single session design/test capability. Moreover, the Phase II research on adaptive neural control techniques made significant progress toward fully automated, self-reliant space structure control systems. As a further thrust toward productized, self-contained vibration control systems, the Harris Phase II activity concluded with experimental demonstration of new vibration isolation hardware suitable for a wide range of space-flight and ground-based commercial applications. The CSI GI Program Phase I activity was conducted under contract NAS1-18872, and the Phase II activity was conducted under NAS1-19372.

TABLE OF CONTENTS

1. Introduction\Overview	1-1
2. Phase I Activities and Progress	2-1
2.1 Control Design Background	2-1
2.2 ACES Experiments: Facility Description and Control Design Test Results.....	2-3
2.3 Mini-MAST Experiments: Facility Description and Control Results.....	2-14
2.4 Phase I: Summary of Principal Findings.....	2-29
3. Phase II - Overview	3-1
4. Phase II — Robust, Fixed-Gain Control Design and Test Results.....	4-1
4.1 Control Design and Test Activities on the CASES Testbed at NASA/MSFC	4-1
4.2 Control Design and Test Activities on the CEM Testbed at NASA/LaRC.....	4-22
5. Phase II - Adaptive Neural Control for the CEM.....	5-1
5.1 Background and Motivation.....	5-1
5.2 ANC Technology Overview	5-1
5.3 Adaptive Neural Control Testing on the Phase 2 CEM Facility.....	5-9
5.4 Additional ANC Results and Further Directions	5-15
6. Phase II: Vibration Attenuation Module Test on the CEM	6-1
6.1 Introduction.....	6-1
6.2 AIF and VAM Overview	6-1
6.3 Phase 3 CEM Testbed Description.....	6-9
6.4 First VAM Test Session on the Phase 3 CEM.....	6-19
7. Concluding Remarks.....	7-1
8. References	8-1

LIST OF FIGURES

Figure 1-1 Major Thrusts of the Harris CSI GI Program Activities Range from Validation of the OPUS Control Design Theory to the Demonstration of Automated and Productized Vibration Control Hardware.....	1-2
Figure 2.1-1 Harris' Expertise in CSI Technology Ranges from Control Theory to Experimental Validation.....	2-2
Figure 2.2-1 The ACES Experiment.....	2-4
Figure 2.2-2 The ACES Test Article at Marshall Space Flight Center is Traceable to Future Space Systems and is Particularly Responsive to Line-of-Sight Control Issues	2-5
Figure 2.2-3 A Comparison of the FE Model (top), FRF (center) and ERA Model (bottom) for the AGS-Y to BGYRO-Y Loop	2-6
Figure 2.2-4 The Pattern of Strong and Weak Interactions in the System Dynamics Motivates a Decentralized Control Structure	2-8
Figure 2.2-5 The Integrated Controller Provided Greater Improvement in the DET-X Response to a BET-X Pulse than any of the Three Individual Controllers	2-11
Figure 2.2-6 Maximum Entropy Design Rendered the Compensators for the AGS to BGYRO Loops Positive Real in the Performance Region.....	2-12
Figure 2.2-7 For the AGS to BGYRO Loops Maximum Entropy Design Smoothed Out the Compensator Magnitudes in the Performance Region, thus Providing Performance Robustness and also Indicating that the Robust Controllers were Effectively Reduced-Order Control.....	2-13
Figure 2.2-8 For the AGS to BGYRO Loops Maximum Entropy Design Robustified the Notches for the High Frequency Modes by Increasing their Width and Depth.	2-15
Figure 2.3-1 The Mini-MAST Test Article	2-16
Figure 2.3-2 The Traceability of the Mini-MAST Structure to Future Space Missions.....	2-17
Figure 2.3-3 Design Configuration for the Precompensation Methodology	2-19
Figure 2.3-4 Implementation Configuration for the Precompensation Methodology.....	2-20
Figure 2.3-5 Torque-Y to Acceleration-1X: Model 2 Bode Plots vs. Experimental Frequency Response Function (Experimental = Solid, Model 2 = Dashed).....	2-21
Figure 2.3-6 Bode plots of Torque-Z to Rate Gyro-Z for Model 2	2-22
Figure 2.3-7 The Effectiveness of Constant Gain Rate Feedback in Eliminating the Influence of the Torsional Mode	2-24
(Without Feedback = Solid, with Feedback = Dashed)	2-24

Figure 2.3-8 Open-Loop vs. Closed-Loop Rate Gyro-Z Response for Constant Gain Feedback from Rate Gyro-Z to Torque-Z.....	2-25
Figure 2.3-9 Open-Loop vs. Closed-Loop Responses of Displacement A of Bay 18 for Controllers 1 through 4	2-26
Figure 2.3-10 Open-Loop vs. Closed-Loop Responses of Displacement A of Bay 18 for Controllers 4 through 7.....	2-27
Figure 2.3-11 Mini-MAST: Open-Loop vs. Closed-Loop Performance.....	2-28
Figure 2.4-1 Harris' Phase I CSI GI Efforts Proved OPUS Design Tools and Integrated them within a Practical Design and Test Methodology	2-31
Figure 2.4-2 The Gradualist Methodology Integrates Subsystems and Refines Control Algorithms Step-by-Step to Build Up to the Best Possible Performance.....	2-32
Figure 3-1 On-Site Design Methodology Drastically compresses the Design Development Process	3-2
Figure 3-2 Year 1: Cases (MSFC).....	3-3
Figure 3-3 These CSI Program Phase II Control Design Results for the MSFC CASES Testbed were Obtained by the Harris Team During the First Test Session with No Prior Modelling Information.....	3-5
Figure 3-4 Phase 2 CEM: A Multiple Payload Platform.....	3-7
Figure 3-5 Harris CSI Activity Demonstrated High Performance Structural Control on the CEM Testbed	3-9
Figure 3-6 Harris GI Phase II Research.....	3-10
Figure 3-7 In July 1993, NASA/LaRC Personnel Experimentally Demonstrated a Basic ANC System on the NASA/Langley Controls Evolutionary Model	3-12
Figure 3-8 VAM Photo	3-13
Figure 3-9 Harris' Vibration Attenuation Module (VAM) Successfully Demonstrated on EOS-AM 1 Laboratory Testbed.....	3-14
Figure 4.1-1 CASES Ground Test Facility at NASA/MSFC	4-3
Figure 4.1-2 Boom Tip: Side View	4-5
Figure 4.1-3 The Frequency Responses of the Full-Order (148 States) and Reduced- Order (60 States) ERA Models of the MHPE Obtained in One Afternoon Closely Resemble the Frequency Response Derived Directly from Test Data.....	4-7
Figure 4.1-4 For a Benchmark Problem State Space Popov Analysis Significantly out Performed Other Robustness Tests, Yielding Completely Non-Conservative Robust Stability Results and Vastly Improved Robust Performance Bounds.....	4-9
Figure 4.1-5 TIP Y Displacement Due to DSy Pulse (con5).....	4-11
Figure 4.1-6 Tip Y Displacement Due to DSy Pulse (con6)	4-12

Figure 4.1-7 Initial ID Results (Still in Huntsville)	4-14
Figure 4.1-8 As an Intermediate Step Toward the Ultimate Goal in Streamlining, We Accelerate the CASES Design Process so as to Demonstrate Advanced Design in Two Test Sessions (the First Session has been Completed)	4-15
Figure 4.1-9 Compensator Magnitude Plot for Refined Controller 1, BLTx-TGy Loop	4-17
Figure 4.1-10 Open-Loop Transfer Function Magnitude Plot for Refined Controller 1, BLTx-TGy Loop.....	4-18
Figure 4.1-11 Compensator Magnitude Plot for Refined Controller 2, BLTx-TGy Loop ..	4-19
Figure 4.1-12 Open-Loop Transfer Function Magnitude Plot for Refined Controller 2, BLTx-TGy Loop.....	4-20
Figure 4.1-13 Comparison of Controller 2 of the Second Test Session (a) with Controller 6 of the First Test Session (b). The Plots Show the Tip Displacements for Both Open-and Closed-Loop Cases	4-21
Figure 4.2-1 Phase 2 CEM: A Multiple Payload Platform.....	4-23
Figure 4.2-2 Comparison of Frequency Response Function Magnitudes (for Thruster 1 to Accelerometer 1) Derived from (a) FRF Experimental Data, (b) Finite Element Model and (c) ERA Generated State-Space Model	4-27
Figure 4.2-3a Typical Loop Transfer Function for Pre-Test Controller – Gain Plot	4-29
Figure 4.2-3b Typical Loop Transfer Function for Pre-Test Controller – Phase Plot.....	4-30
Figure 4.2-4a LOS Error Locus on the Sensor Target Plane at Gimbal C – Open-Loop	4-32
Figure 4.2-4b LOS Error Locus on the Sensor Target Plane at Gimbal C – Closed-Loop, Controller 1.....	4-33
Figure 4.2-4c LOS Error Locus on the Sensor Target Plane at Gimbal C – Closed-Loop, Controller 2.....	4-34
Figure 4.2-5a X-Axis LOS Error Time History – Open-Loop.....	4-35
Figure 4.2-5b X-Axis LOS Error Time History – Closed-Loop, Controller 1.....	4-36
Figure 4.2-5c X-Axis LOS Error Time History – Closed-Loop, Controller 2.....	4-37
Figure 5.2-1 ANC Executes Simultaneous System Identification and Adaptively Optimized Control	5-2
Figure 5.2-2 Hierarchy of Modular Neural Structures Progressing from Basic Constituents to Higher-Level Modules	5-4
Figure 5.2-3 Linear Replicators of Various Forms Correspond to Different Model Forms.....	5-5
Figure 5.2-4 Beam Experiment Shows Excellent Convergence Results After 100 Seconds.....	5-7

Figure 5.2-5 Neural Network Closed-Loop System Identification Experiment was Performed on the Dynamically Complex Multi-Hex Prototype Experiment (MHPE) Testbed	5-8
Figure 5.2-6 Simulation Results for the LaRC Mini-MAST Testbed Demonstrate Simultaneous System Identification and Control Optimization	5-10
Figure 5.3-1 Control Using Neural Networks - Simplified Version of ANC Using a Constrained - Deadbeat Controller Form	5-12
Figure 5.3-2 Two Basic Identification Schemes	5-13
Figure 5.3-3 CEM Testbed Configuration used for Adaptive Neural Control Testing	5-14
Figure 5.3-4 CEM Experimental Results (Disturbance Rejection - First Input-Output Pair)	5-16
Figure 5.3-5 CEM Experimental Results (Disturbance Rejection - Second Input-Output Pair)	5-17
Figure 5.3-6 CEM Experimental Results (On-Line Adaptive Parameter Identification)	5-18
Figure 5.3-7 CEM Experimental Results (OSS On-Line Prediction Error)	5-19
Figure 5.4-1 Adaptive Neural Control was Demonstrated using the MHPE Testbed	5-21
Figure 5.4-2 Multi-Tone Neural Algorithm Results	5-23
Figure 6.2-1 Both Resonant and Nonresonant Response is Suppressed Using Active Isolation	6-2
Figure 6.2-2 AIF Combines Off-The-Shelf Components to Provide Inexpensive, Highly Effective Isolation	6-4
Figure 6.2-3 Broadband Isolation Using the Harris AIF is Demonstrated by Experimentally Measured Results	6-6
Figure 6.2-4 Active Fitting Test Data for a Higher Bandwidth Design and Flexible Isolated Body	6-7
Figure 6.2-5 Active Fitting Test Results for a Two-Stage System (Two AIF's in Series)...	6-8
Figure 6.2-6 VAM Hexapod Concept	6-10
Figure 6.2-7 For the DMSP Applications, the VAM is Inserted Between the Astromast Deployment Cannister and the Spacecraft Bus	6-11
Figure 6.2-8 The VAM Isolator Greatly Attenuates the Impact of the Major Spacecraft Disturbances on the Magnetometer Attitude Errors	6-12
Figure 6.2-9 AIFs and VAMs Offer a Modular, Highly Adaptable Technology for Isolation and Precision Alignment.....	6-13
Figure 6.3-1 Phase 3 CEM Evolutionary Model.....	6-15

Figure 6.3-2 Phase 3 CEM Baseline Configuration (Orthogonal Views).....6-16

Figure 6.4-1 The VAM Replaced the Structural Mount of the MISR Simulator6-20

Figure 6.4-2 LOS Error in the OSS Target Plane for (a) Open-Loop, (b) Closed-Loop,
Control Configuration #16-21

Figure 6.4-3 LOS Error in the OSS Target Plane for (a) Open-Loop and (b) Closed-
Loop, Control Configuration #26-22

Figure 6.4-4 Z-axis Accelerometer Output Time Histories - Upper Plot Shows Open-
Loop Response. Lower Plot Shows Closed-Loop Response for Control
Configuration #16-24

Figure 6.4-5 Open Versus Closed-Loop Responses for Control Configuration #3. The
Top Pair of Plots Show LOS Error in the Target Plane. The Bottom Plots show
the Two LOS Component Time Histories.....6-25

Figure 6.4-6 Open Versus Closed-Loop Frequency Responses from Disturbance to
LOS Error6-26

LIST OF TABLES

Table 1-1 Harris CSI GI Program Accomplishments	1-3
Table 2.2-1 For a BET-X Pulse the DET-X Response Improved Each Time an Additional Feedback Path was Added to the Controller.....	2-10
Table 3-1 GIP Ø2 Schedule Year 2, CEM	3-6
Table 4.0 GI Phase II Schedule.....	4-2
Table 4-2 Phase 2 CEM Capabilities.....	4-25
Table 6.3-1 Simulated EOS AM-1 Payloads	6-17
Table 6.3-2 Phase 3 CEM Free-Free Modal Analysis.....	6-18

1. INTRODUCTION\OVERVIEW

A notable element of overall progress in the field of active vibration control for flexible space systems has been the emergence of "Guest Investigator" efforts which provide several investigative groups the opportunity to conduct multidisciplinary research on traceable testbeds that would otherwise be beyond the technical and financial means of individual researchers. The longest standing and, in our opinion, the most effective and productive effort of this kind is the NASA Controls-Structures Integration (CSI) Guest Investigator (GI) Program. In its first phase eight research groups, including Harris Corporation, were contracted to work on two NASA facilities (the Mini-MAST facility at NASA Langley Research Center (NASA/LaRC) and the ACES facility at NASA Marshall Space Flight Center (NASA/MSFC)) to research a variety of topics including modelling, system identification, line-of-sight pointing, vibration suppression, and fault detection (see Reference [1]). More recently, over the past two years, phase II of the CSI GI program engaged five investigative groups (again including Harris) for continued efforts in system modelling and control design on an additional suite of test facilities (the ASTREX facility of the Air Force Phillips Lab, the CASES facility at NASA/MSFC and the CEM facility at NASA/LaRC). This Final Report reviews the entire Harris activity and results on both phases of the program with particular emphasis on Phase II.

Besides the implementation and exploitation of advanced test facilities and the acquisition of real experimental results that illustrate the power of advanced vibration control technology, the research findings of the CSI GI program have significantly advanced the field toward one of professional competence backed by effective, reliable tools. In particular, thanks to the multiplicity of testbeds offered, Harris' structural control technology has been significantly advanced. Figure 1-1 illustrates the major thrusts of the Harris effort and Table 1-1 lists the principal accomplishments. Important progress was achieved not only in control algorithm design but in many other areas involved in practical implementation, including: (1) overall implementation and test methodology, (2) global control system architecture (actuation, information patterns, etc.) which have the greatest leverage on final achievable performance and (3) basic control strategies and new controls hardware approaches. Moreover, we have gained an understanding of how to orchestrate the above elements to achieve the *reliable, high performance yet rapid and inexpensive* design/implementation/test capability that is needed to make the active structural control field economically viable.

The story of the progress mentioned above spans both phases I and II of the program. Therefore, although our primary responsibility is to report results for Phase II, this report summarizes progress over the entire program.

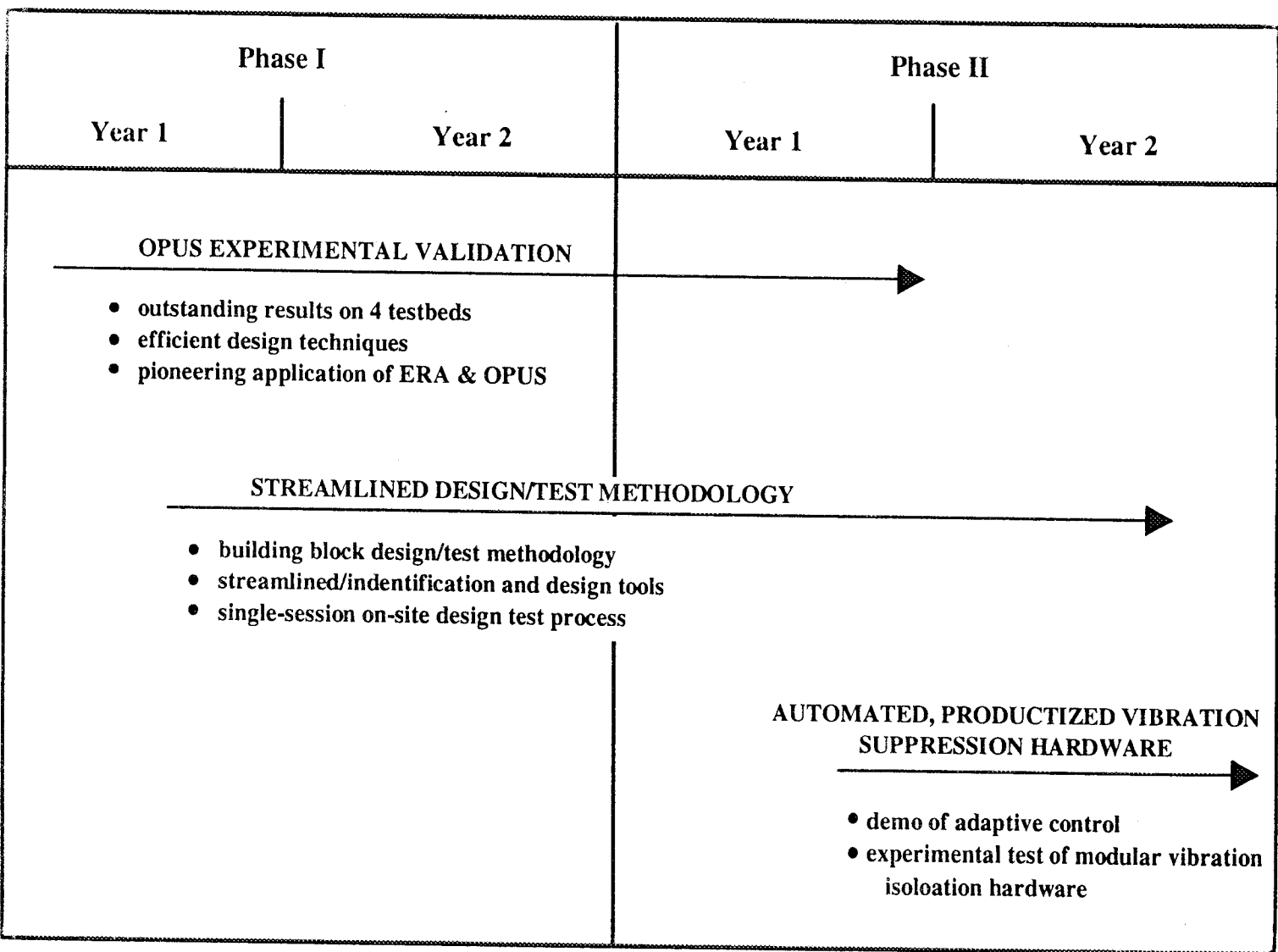
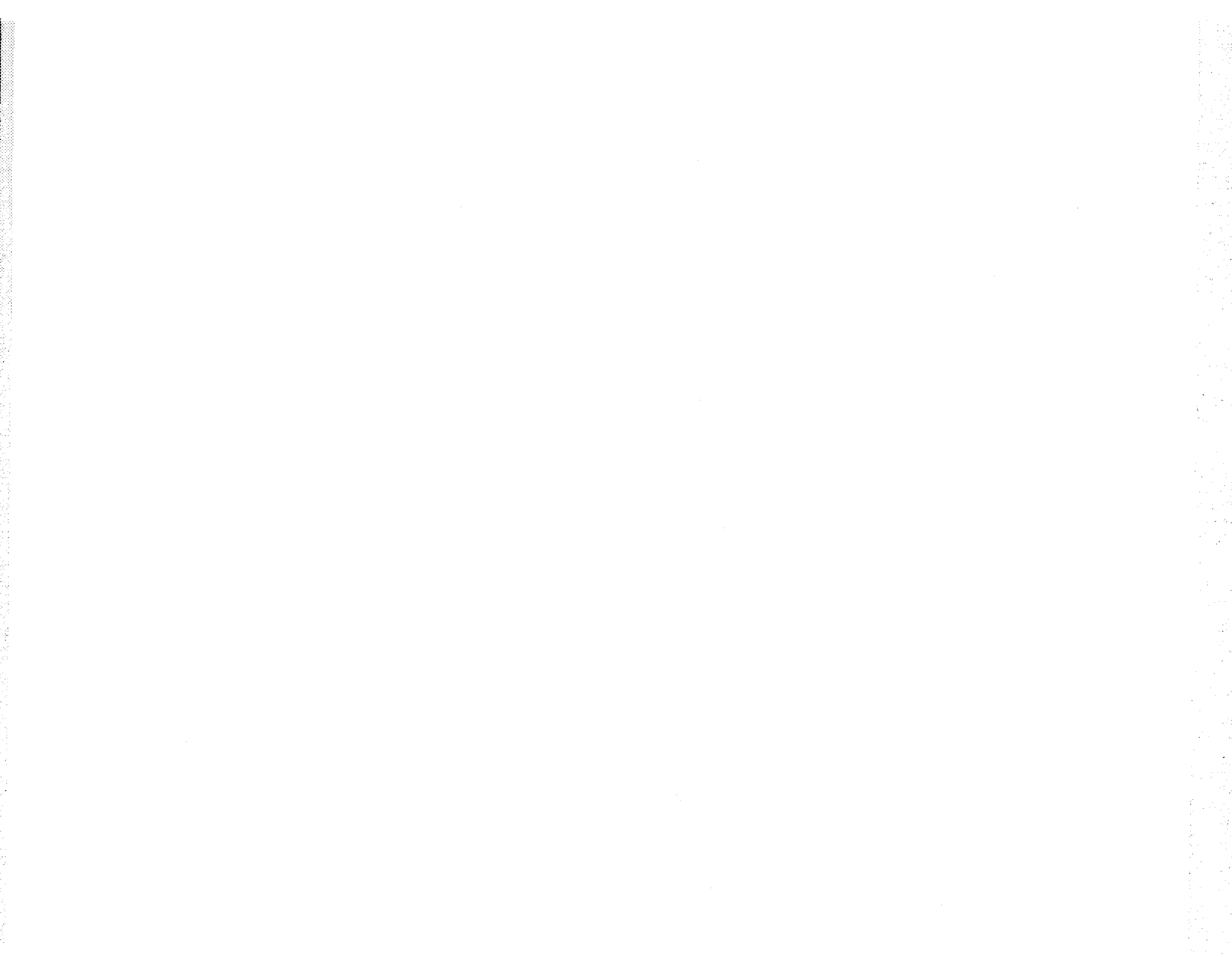


Figure 1-1 Major Thrusts of the Harris CSI GI Program Activities Range from Validation of the OPUS Control Design Theory to the Demonstration of Automated and Productized Vibration Control Hardware

Table 1-1 Harris CSI GI Program Accomplishments

<ul style="list-style-type: none"> • Experimentally demonstrated OPUS control design technology on four independently referred testbeds. <ul style="list-style-type: none"> - Control system performance uniformly outstanding and consistently matched predictions.
<ul style="list-style-type: none"> • Identified and demonstrated the robustifying features of OPUS design — i.e. established the phenomenology of how OPUS achieves robust design in the face of various types of parameter uncertainty.
<ul style="list-style-type: none"> • On Mini-MAST: Performed detailed assessment of cost and complexity versus performance tradeoffs by testing a sequence of distinct designs ranging from simple rate feedback to advanced centralized OPUS. This data helps characterize the utility of modern design methods versus classical methods.
<ul style="list-style-type: none"> • On ACES: Pioneered the application of ERA tools (developed at NASA/LaRC) for extracting system models directly from test data—this is a key component to a streamlined implementation methodology.
<ul style="list-style-type: none"> • On ACES and Mini-MAST: Evolved the "Gradualist" design/test methodology—a systematic methodology for using ERA and OPUS tools to achieve fast, economical control design and test. This methodology further streamlined in Phase II.
<ul style="list-style-type: none"> • Phase II: Compressed and speeded up the Gradualist methodology into a single session on-site control design and test process—executed this process on CASES and CEM testbeds. • Phase II: Using adaptive neural control technology, took major steps toward the complete automation of the structural control design/test process. Previous Harris work established a new neural architecture for system ID and adaptive control. Our collaboration with NASA/LaRC facilitated a demonstration of Adaptive Neural Control on the CEM testbed.
<ul style="list-style-type: none"> • On CEM Phase II: Provided hardware demonstration of the Vibration Attenuation Module (VAM) a new approach to active isolation of spaceborne sensors from spacecraft generated disturbances. VAMs actively cancel vibration transmission without reducing passive stiffness.



2. PHASE I ACTIVITIES AND PROGRESS

2.1 Control Design Background

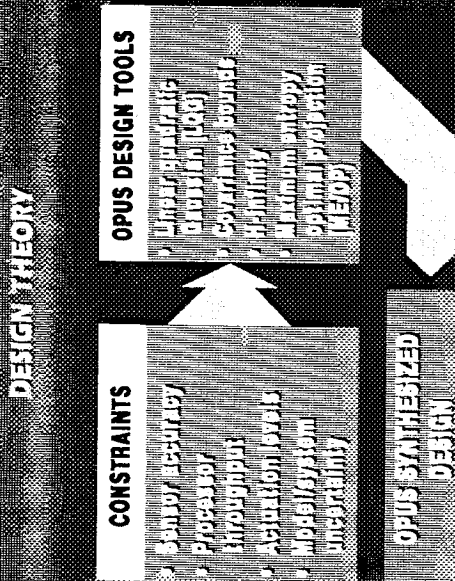
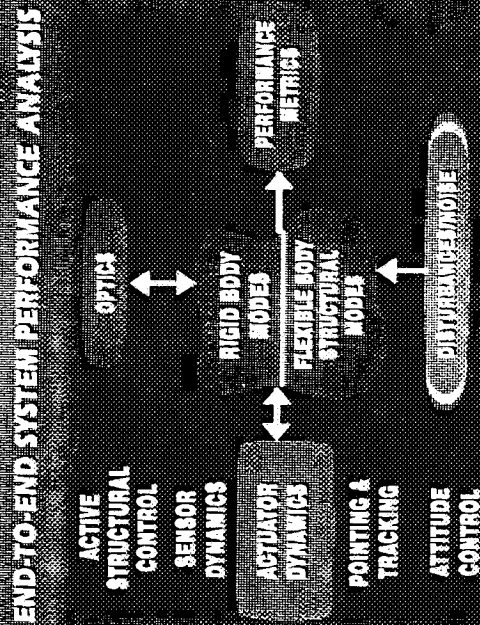
As illustrated in Figure 2.1-1, Harris has comprehensive experience and expertise in CSI technology, ranging from basic control theory to actual experimental verification, giving Harris a unique ability to integrate control technologies and apply them to structural systems.

The contributions of the Controls Technology Group at Harris to basic control theory have been diverse and have had a major impact on progress in controls research. Our overall OPUS (Optimal Projection for Uncertain Systems) approach [2] contains several key ingredients. Maximum entropy robustness design [3–5] was developed to allow robust control synthesis for flexible structures and has been shown in several studies and experiments to allow the development of practical robust controllers. The optimal projection characterization of optimal reduced-order controllers and models [6–10] was pioneered by Harris researchers and has led to the development of novel numerical algorithms and rigorous comparisons between optimal reduced-order controllers and reduced-order controllers obtained by sub optimal methods [11, 12]. Majorant analysis [13–16] has made major strides in the development of various types of robust performance bounds. The development of H_2/H_∞ synthesis [17, 18] was a major result that allows control design for the simultaneous rejection of both broadband and narrowband disturbances. Recent results on Popov analysis [19–21] enable robustness analysis for parametric uncertainty that is much less conservative than small-gain type tests such as H_∞ or complex structured singular value analysis. The combination of these elements gives a capability which accommodates numerous real-world constraints to design simple, reliable controllers.

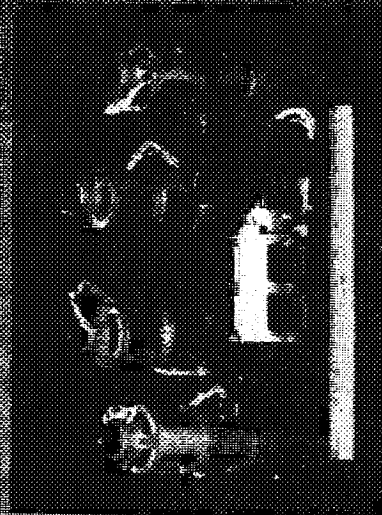
To compliment the basic theory discussed above Harris has developed reliable numerical algorithms based on homotopy approaches [22, 23]. These algorithms have global convergence properties and have been shown to be effective in the design of robust and reduced-order controllers. The implementation of these algorithms in a MATLAB environment has led to an efficient design environment for the control engineer.

The main thrust of the Phase I effort was to experimentally validate OPUS on independently refereed testbeds. The design work relied particularly on the maximum entropy and optimal projection components of OPUS. In addition, alternative design theories were also investigated (by appropriately specializing OPUS) in an effort to study the cost and complexity tradeoffs of various approaches. Phase I activities were directed at OPUS design and test on two experimental facilities: The ACES facility at NASA/MSFC and the Mini-MAST facility at NASA/LaRC. These efforts and corresponding results are described in the next two sections.

HARRIS CONTROLS RESEARCH SPANS THEORY TO HARDWARE VALIDATION

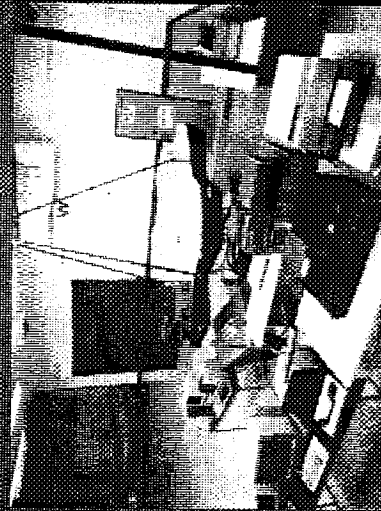


SENSOR AND ACTUATOR HARDWARE



Linear Precision Actuators (LPACT'S)

EXPERIMENTAL VALIDATION



Multihez Prototype Experiment

193-01(G)

Figure 2.1-1 Harris' Expertise in CSI Technology Ranges from Control Theory to Experimental Validation

2.2 ACES Experiments: Facility Description and Control Design Test Results

The Advanced Control Evaluation for Systems (ACES) facility (see [24]) was addressed by the Harris team in the first year of Phase I of the GI program. Full details of this Phase I activity are given in [25, 26].

The ACES experimental testbed [24] is located at NASA Marshall Space Flight Center (MSFC). The basic test article, a spare Voyager Astromast, is a deployable, lightweight (about 5 pounds), lightly damped beam, which is approximately 45 feet in length. The ACES configuration, shown in Figure 2.2-1 consists of an antenna and counterweight legs appended to the Astromast tip and the pointing gimbal arms at the Astromast base. Overall, the structure is very flexible and lightly damped. It contains many closely spaced, low frequency modes (more than 40 modes under 10 Hz). As illustrated by Figure 2.2-2 the ACES configuration is dynamically traceable to future space systems and is particularly responsive to the study of line-of-sight issues.

The goal of the control design is to position the laser beam in the center of the detector. The detector and pointing gimbals are each positioned on the end of a flexible appendage to increase the difficulty of the control problem. The lack of information about the appendage motion also adds complexity to the controller design (i.e., there is no accelerometer or gyro at the location of the gimbals or the detector).

The actuators and sensors available for controller implementation are listed in Figure 2.2-1. In our control design and implementation we used 8 control inputs and 8 measurement outputs. The inputs were the X and Y torques of the Image Motion Compensation (IMC) gimbals, the X and Y torques of the Advanced Gimbal System (AGS) and the X and Y forces of the two Linear Momentum Exchange Device (LMED) packages. The measurements consisted of the X and Y detector (DET) position outputs, the X and Y base gyro (BGYRO) rate outputs and the X and Y outputs of the LMED accelerometers. The disturbances were chosen to be position commands to the Base Excitation Table (BET). The BET motion is regulated by an analog controller which allows any type of BET movement within the frequency limitation of the hydraulic system.

Perhaps the most severe challenge on the ACES testbed was to secure a system model of adequate fidelity to support control design. In this experiment, a finite element model (FEM) was initially supplied by MSFC. Figure 2.2-3 shows a typical comparison between one of the FEM-generated frequency responses (top of the figure) and the corresponding frequency response function (FRF) generated from open-loop test data. Clearly the FEM had very serious discrepancies and could not be used reliably for control design.

At this point the traditional approach would have been to refine the finite element model to more closely match open-loop test data. However, this is a laborious, generally iterative and time consuming process. Since control design and test results were required within less than a

1. Base Excitation Table
2. 3 Axis Base Accelerometers
3. 3 Axis Gimbal System
4. 3 Axis Base Rate Gyros and Counterweight
5. 3 Axis Tip Accelerometers
6. 3 Axis Tip Rate Gyros
7. Optical Detector
8. Mirrors
9. Laser
10. 2 Axis Pointing Gimbal System
11. LMED System

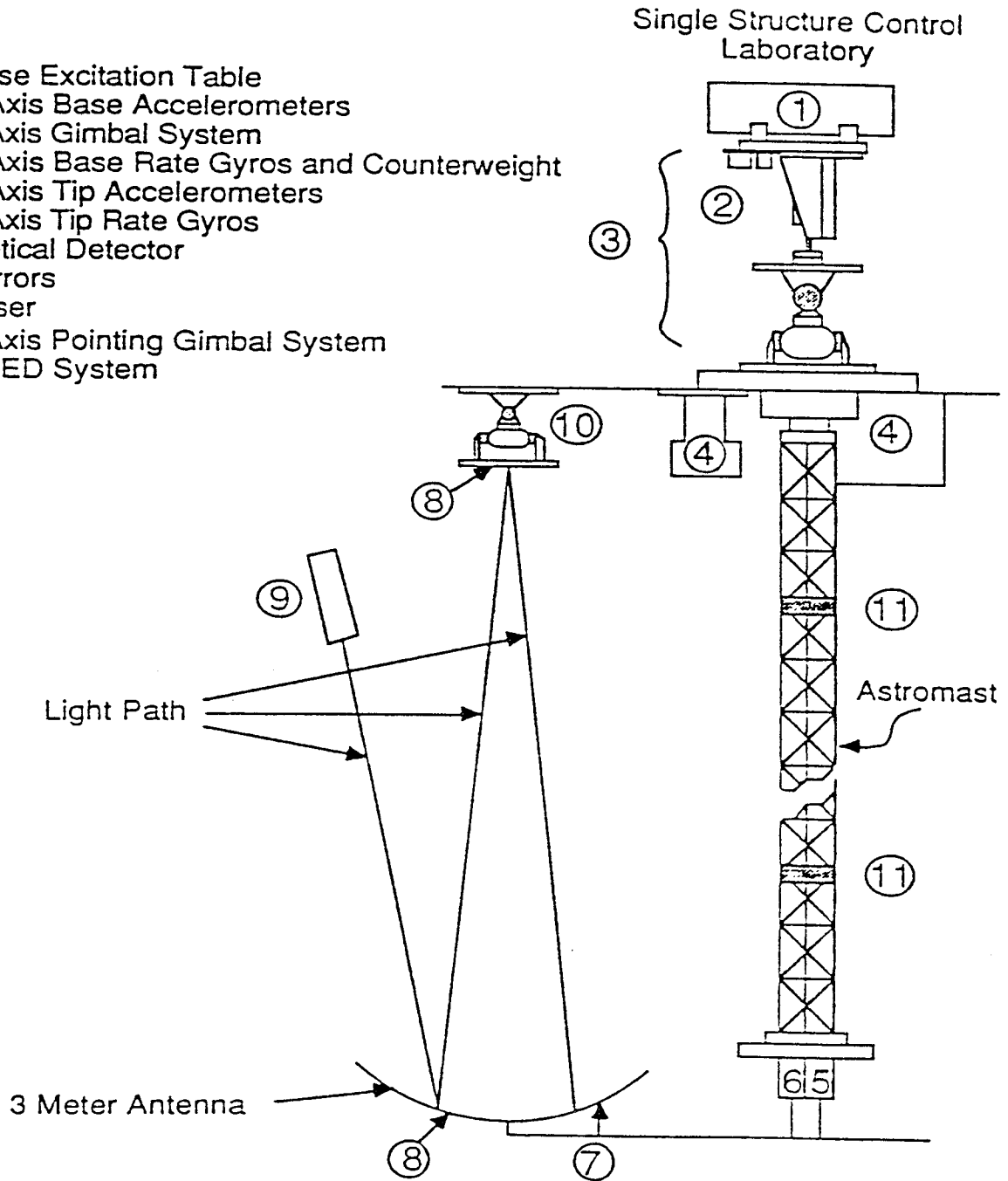
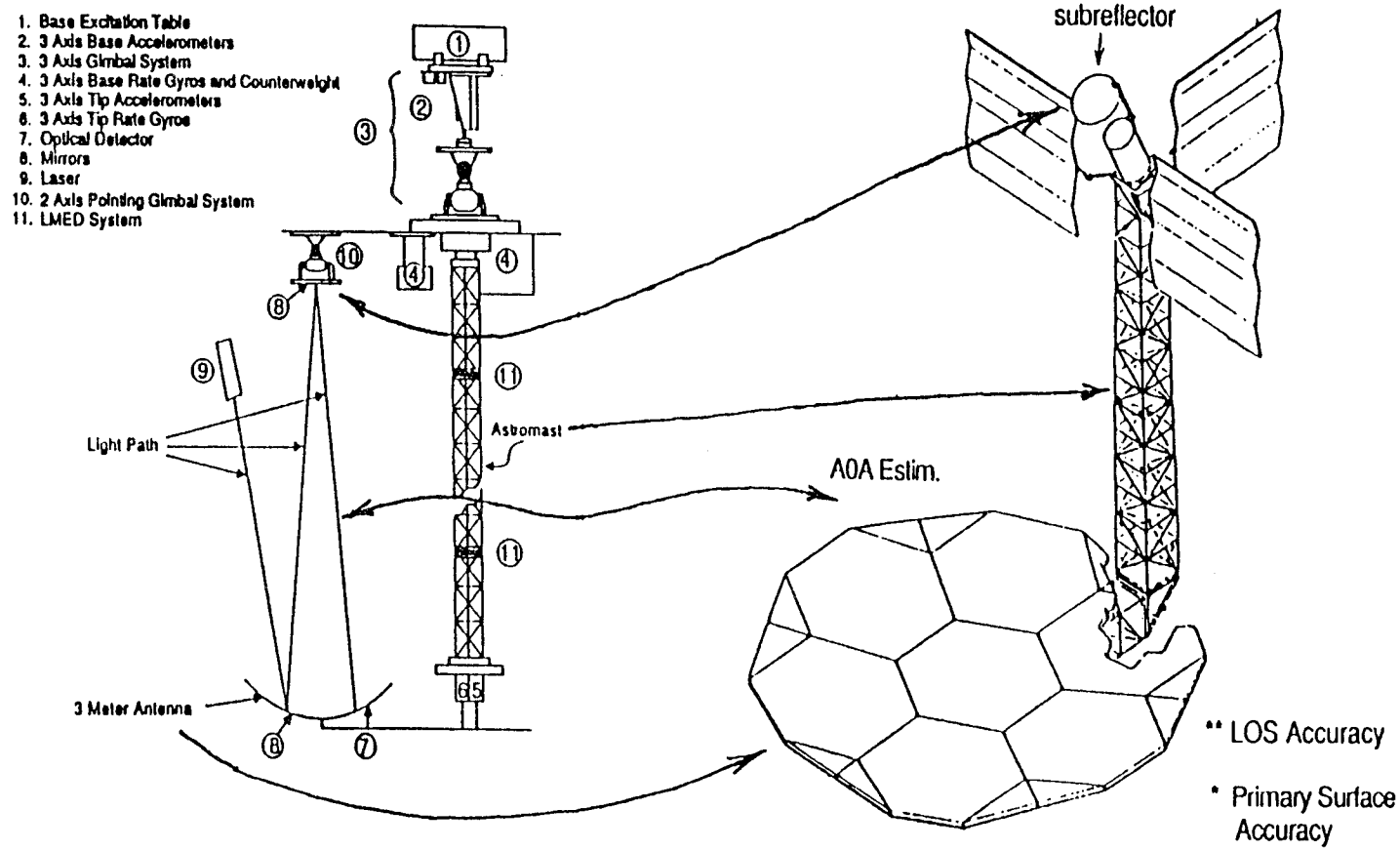


Figure 2.2-1 The ACES Experiment

Figure 2.2-2 The ACES Test Article at Marshall Space Flight Center is Traceable to Future Space Systems and is Particularly Responsive to Line-of-Sight Control Issues



- * ACES is particularly responsive to Line-Of-Sight (LOS) control issues in future LSS
- * Accordingly, our CSI GIP goal is reduction of LOS errors. Vibration suppression is sought only to the extent that it aids LOS control.

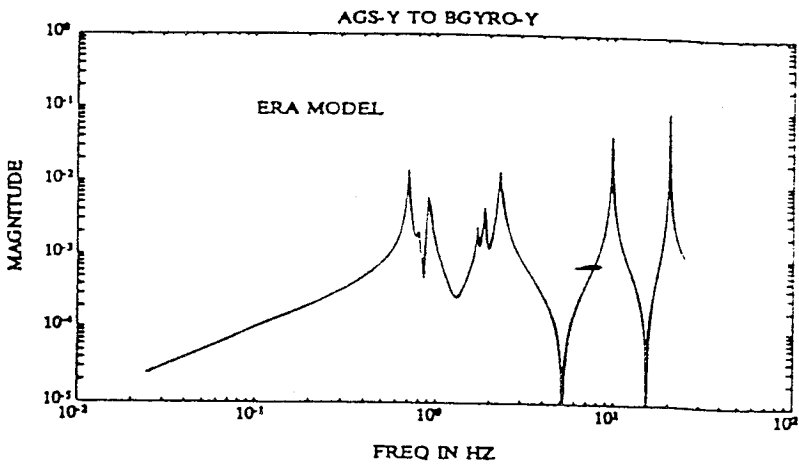
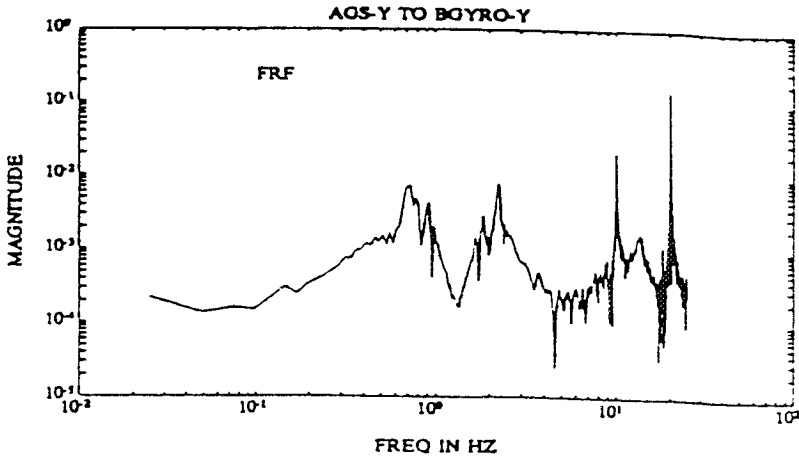
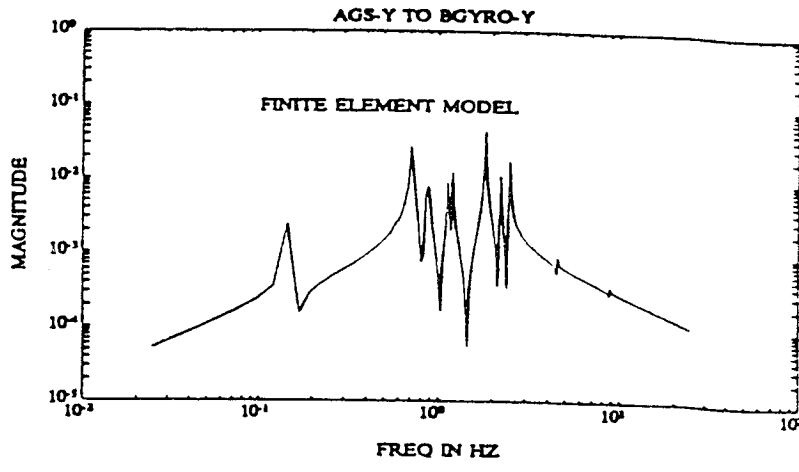


Figure 2.2-3 A Comparison of the FE Model (top), FRF (center) and ERA Model (bottom) for the AGS-Y to BGYRO-Y Loop

year with less than one man-year of effort, we elected to develop state space models directly from open-loop test data using the Eigensystem Realization Algorithm (ERA) developed by Juang and Pappa at NASA/LaRC [27, 28]. ERA permitted the rapid development of excellent system models with which to support control design in a timely manner. Figure 2.2-3 illustrates the very good agreement obtained between the ERA model and open-loop experimental data.

Our ERA-generated model was the first up-to-date and accurate model produced for the ACES testbed and we immediately provided this model data to the CSI Program Office for use by later GI's. Our use of ERA was also the first of several excellent technology transfers that enabled rapid progress on the program.

Inspection of both ERA and test-generated FRFs revealed insights that further streamlined the design process. The FRFs of the IMC-Y to DET-X and IMC-X to DET-Y loops revealed that those loops are influenced very little by the flexible modes of the structure. It follows that the IMC gimbals are not capable of controlling flexible modes to improve LOS performance. Thus, if one considers the four actuator inputs (IMC-X, IMC-Y, AGS-X and AGS-Y) and the four sensor outputs (DET-X, DET-Y, BGYRO-X, BGYRO-Y), it is not necessary to feed back the BGYRO outputs to the IMC gimbals since the BGYROs primarily contain information about the behavior of the flexible modes which the IMC's cannot control. In addition, the DET outputs do not contain much (if any) useful information for the AGS gimbals that is not already provided by the BGYRO's. Thus, the achievable performance cannot be improved by feeding back the DET outputs to the IMC gimbals or the BGYRO outputs to the AGS gimbals. As illustrated by Figure 2.2-4, analysis of test data also revealed that within the decentralized structure described above there were four dominant loops: AGS-X to BGYRO-X, AGS-Y to BGYRO-Y, IMC-X TO DET-Y, and IMC-Y TO DET-X.

This decentralized structure of the problem allowed us to take a building block approach, addressing each control subsystem (comprising separate groups of actuator and sensor hardware elements) one at a time, progressively integrating the subsystems and acquiring more and more modelling information to support further design. This building block approach was the genesis of the more formalized gradualist methodology to be described further below. Specifically, our overall procedure comprised an initial open-loop test session, to collect the data needed for ERA modelling, followed by a sequence of three closed-loop test sessions. Using the initial ERA models from the open-loop session, OPUS was used to design a controller for the IMC/DET subsystem, and this controller was tested in the first closed-loop session. Data from this first closed-loop test session was then used to obtain refined ERA models for the higher frequency

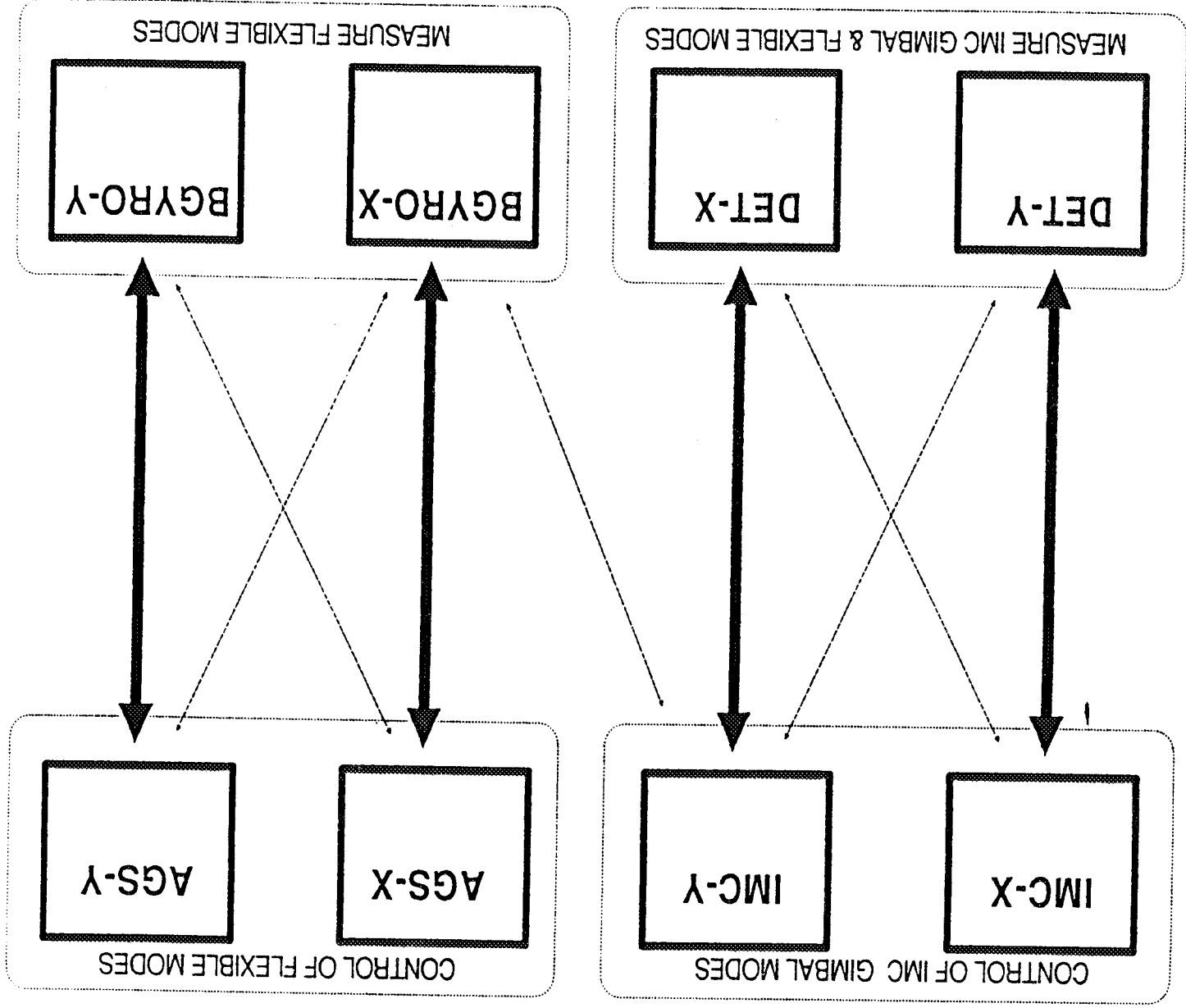


Figure 2.2-4 The Pattern of Strong and Weak Interactions in the System Dynamics Motivates a Decentralized Control Structure

modal dynamics associated with the Astromast in order to support the OPUS design of the AGS/BGYRO control subsystem. The combined IMC and AGS controllers were then tested in the second closed-loop session, during which refined modelling data on the LMEDs was also obtained. After designing the LMED controllers, the integrated controller comprising all three subsystems was tested in the final closed-loop session. Table 2.2-1 summarizes the performance results for each of the test sessions. In each session, test results were in close agreement with predictions, and as the right column of Table 2.2-1 illustrates, performance systematically improved as additional control subsystems were integrated. The outstanding performance achieved (an order of magnitude reduction in LOS jitter and three orders of magnitude in bias error) by the fully integrated controller is illustrated in Figure 2.2-5 which shows open versus closed-loop response of the x-axis of the detector to an impulsive BET disturbance.

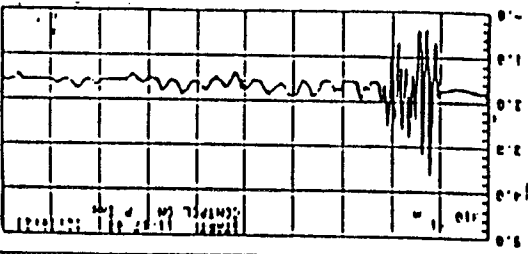
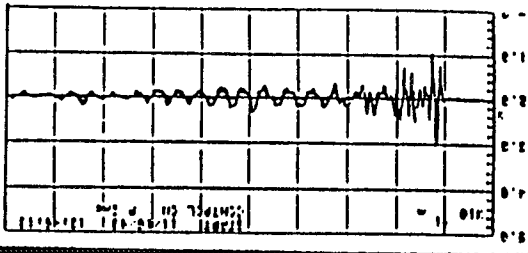
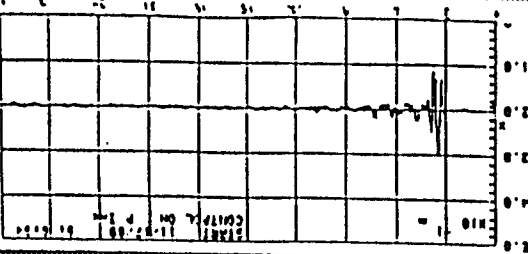
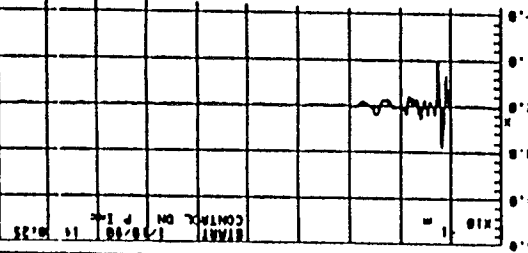
The results of this experiment illustrate that "simple" controllers, i.e. reduced-order and decentralized controllers, can provide very significant performance improvement. The total design model contained 45 states. However, the integrated controller contained only 28 states and had a decentralized architecture. This reduction in controller complexity is very important for the development of practical controllers due to the substantial limits on throughput capability of space-qualified processors.

In the process of obtaining the above performance results, we also obtained much insight into the practical features of Maximum Entropy (ME) design that are responsible for its robustness capabilities. These features are illustrated, for the case of the AGS/BGYRO controllers, in Figure 2.2-6 through 2.2-8.

Figure 2.2-6 describes the influence of ME uncertainty design on the phase of a full-order compensator in the performance region (i.e., less than 3 Hz). The phase of the LQG compensator varies widely over this frequency interval, implying that the Nyquist plot of the corresponding loop transfer function encircles the origin several times. As one would expect, these designs were nonrobust and were unstable when implemented. However, the ME designs became positive real in the performance region tending toward rate feedback. Thus the ME designs provided the needed stability robustness in the performance region.

Figure 2.2-7 describes the influence of ME uncertainty design on the magnitude shape of a full-order compensator in the performance region. Notice that the ME compensator magnitudes are smoother than those of the LQG compensators, thus providing performance robustness. Another implication is that the ME designs yield robust controllers that are effectively reduced order controllers. In practice, the full-order ME design actually provides insight into the choice of the order of the compensator and is a numerical aid in synthesizing reduced order controllers.

Table 2.2-1 For a BET-X Pulse the DET-X Response Improved Each Time an Additional Feedback Path was Added to the Controller

Controller (order)	Mean Error & Standard Deviation	dB Improvement	Test Result Time Histories for X LOS
Open Loop	mean = 0.0329 S.D. = 0.0256	—	
IMC (6 states)	mean = 8.5×10^{-5} S.D. = 0.01742	51.8 3.34	
IMC + AGS (16 states total)	mean = 8.4×10^{-5} S.D. = 0.0107	51.9 7.58	
IMC + AGS + LMED (28 states total)	mean = 4.2×10^{-5} S.D. = 9.0×10^{-3}	57.9 9.0	

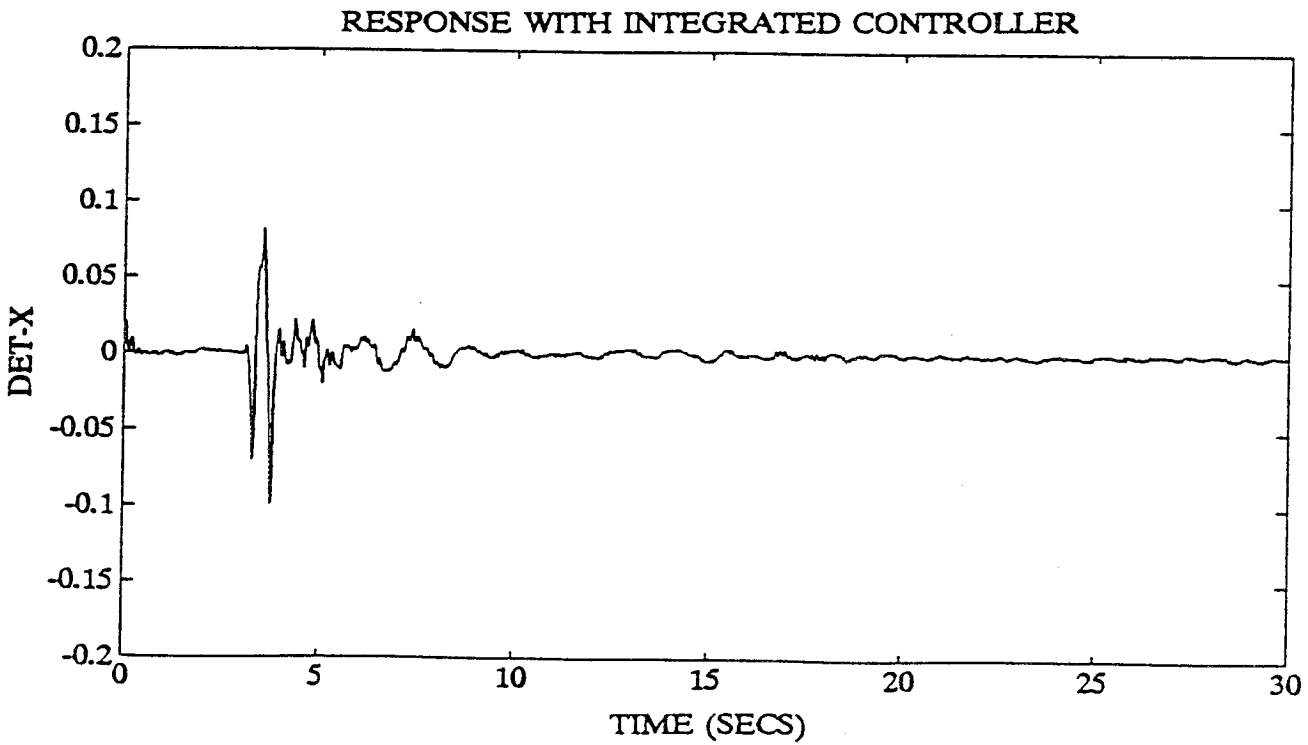
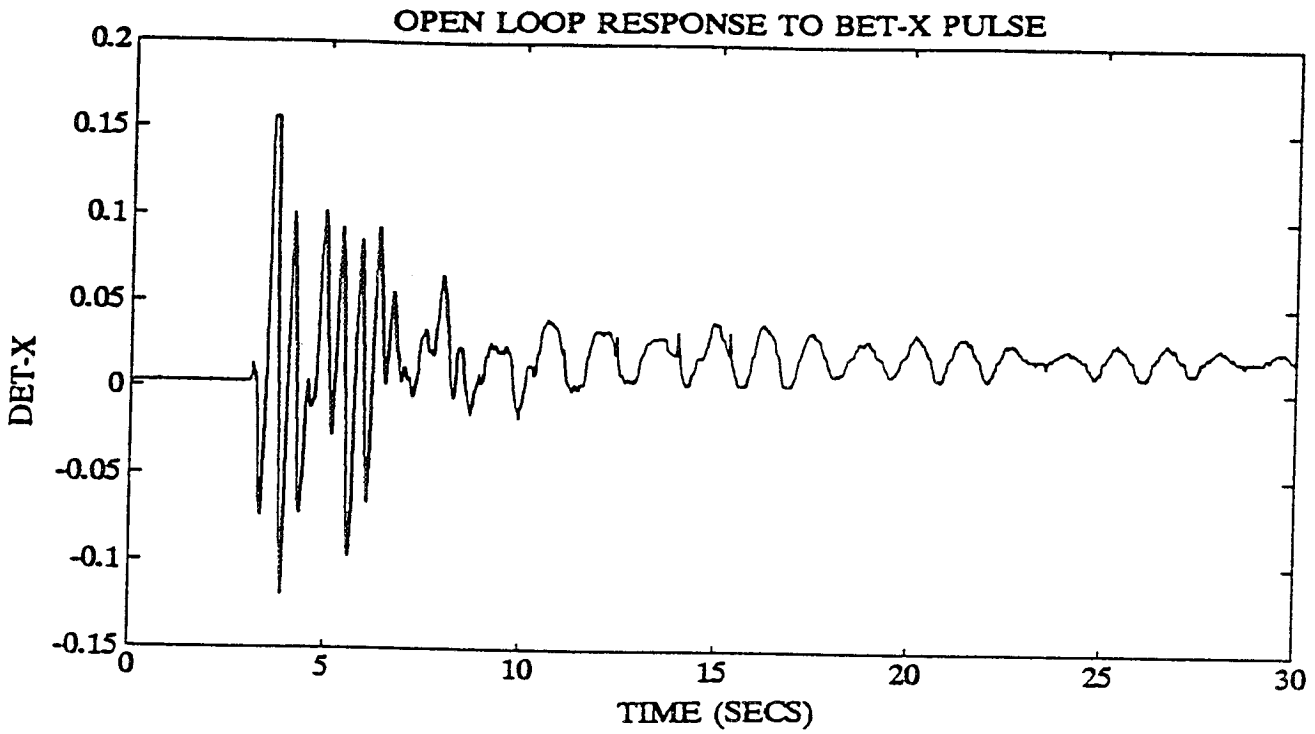


Figure 2.2-5 The Integrated Controller Provided Greater Improvement in the DET-X Response to a BET-X Pulse than any of the Three Individual Controllers

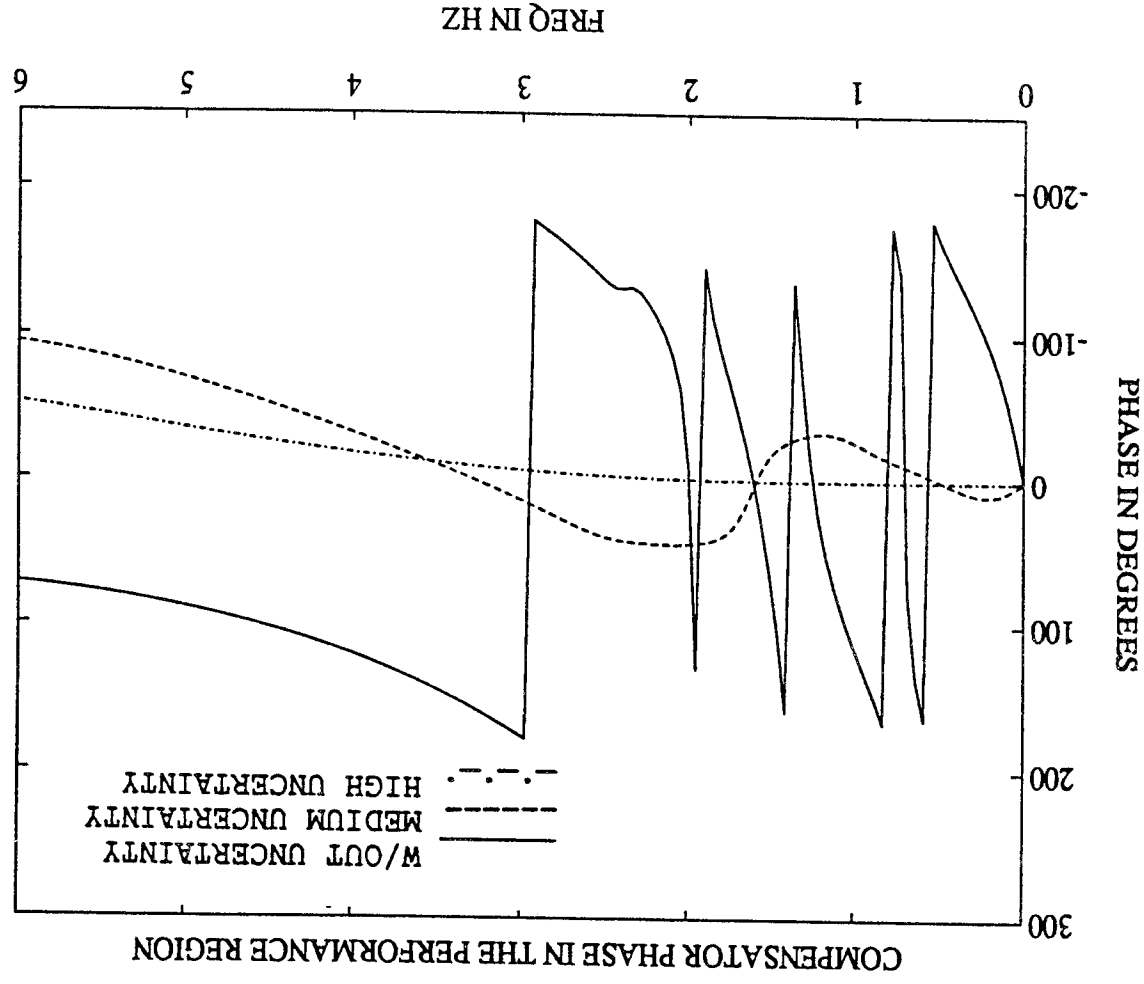


Figure 2.2-6 Maximum Entropy Design Rendered the Compensators for the AGS to BGYRO Loops Positive Real in the Performance Region

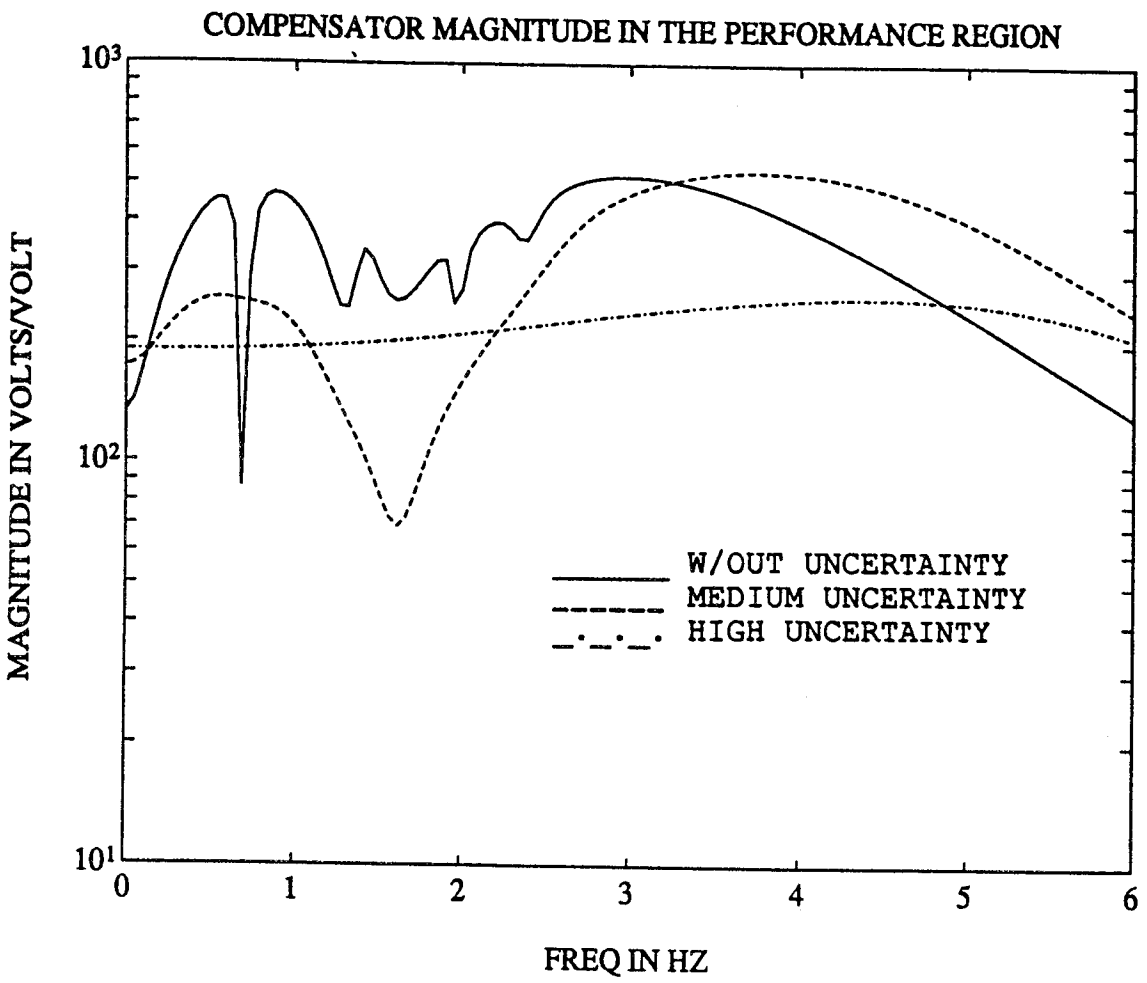


Figure 2.2-7 For the AGS to BGYRO Loops Maximum Entropy Design Smoothed Out the Compensator Magnitudes in the Performance Region, thus Providing Performance Robustness and also Indicating that the Robust Controllers were Effectively Reduced-Order Controllers

The higher authority controllers notched the high frequency modes that had high gain. As illustrated by Figure 2.2-8, ME design was able to robustify the controller notches. That is, the controller notches were increased in both width and depth.

The above features of the Maximum Entropy robustness design method proved to be crucial in developing stable controllers which yielded significant performance improvement when implemented.

2.3 Mini-MAST Experiments: Facility Description and Control Results

For the second year of Phase I of the CSI GI Program, the Harris team was assigned to the Mini-MAST facility at NASA/LaRC (see [29]). Details on the Harris GI effort on the Mini-MAST facility are given in [30, 31].

The basic Mini-MAST test article is a generic space truss designed and manufactured by Astro Aerospace Corporation. The tubing members of the truss are made of graphite/epoxy. The truss beam is deployable and retractable and has a triangular cross section. The total height of the truss is 20.16 meters and the truss consists of 18 bays, each of which is 1.12 meters in height.

The actuators and sensors available for control design implementation, disturbance generation, and performance evaluation are shown in Figure 2.3-1. The only actuators available for control are three torque wheel actuators that are mounted on the tip plate (top of Bay 18) parallel to the global x, y and z reference axes. The torque wheels provide both torsional and bending torque loads to the Mini-MAST.

The available control sensors are six Sundstrad QA-1400 servo accelerometers and three Watson angular rate gyros. Four accelerometers are located at the beam tip (Bay 18) and two are located on the mid platform (Bay 10). These sensors measure linear acceleration in the global x and y directions. The three rate sensors are located at the beam tip (Bay 18) and measure pitch (about the x-axis), roll (about the y-axis), and yaw (about the z-axis).

Fifty-one Kaman KD-2300 proximity probes (i.e, displacement sensors) are installed on the support structure along the Mini-MAST. These devices can be used for control but were primarily intended for structural dynamic testing and performance evaluation. In our experimentation, we used the three Kaman sensors at Bay 18 for performance evaluation.

Three Unholtz-Dickie 50-lb. shakers are attached at Bay 9 for disturbance generation. These shakers are oriented normal to the faces of the truss at each of the three vertices.

As illustrated in Figure 2.3-2, the Mini-MAST structure can be viewed as the secondary support tower of a precision reflector structure. To achieve high accuracy line-of-sight pointing in the structure of Figure 2.3-2 it is important to minimize the relative displacement of the tip of the beam with respect to the base. Hence, the primary objective of this experiment was to design controllers that provide substantial reduction of the displacement of the tip of the

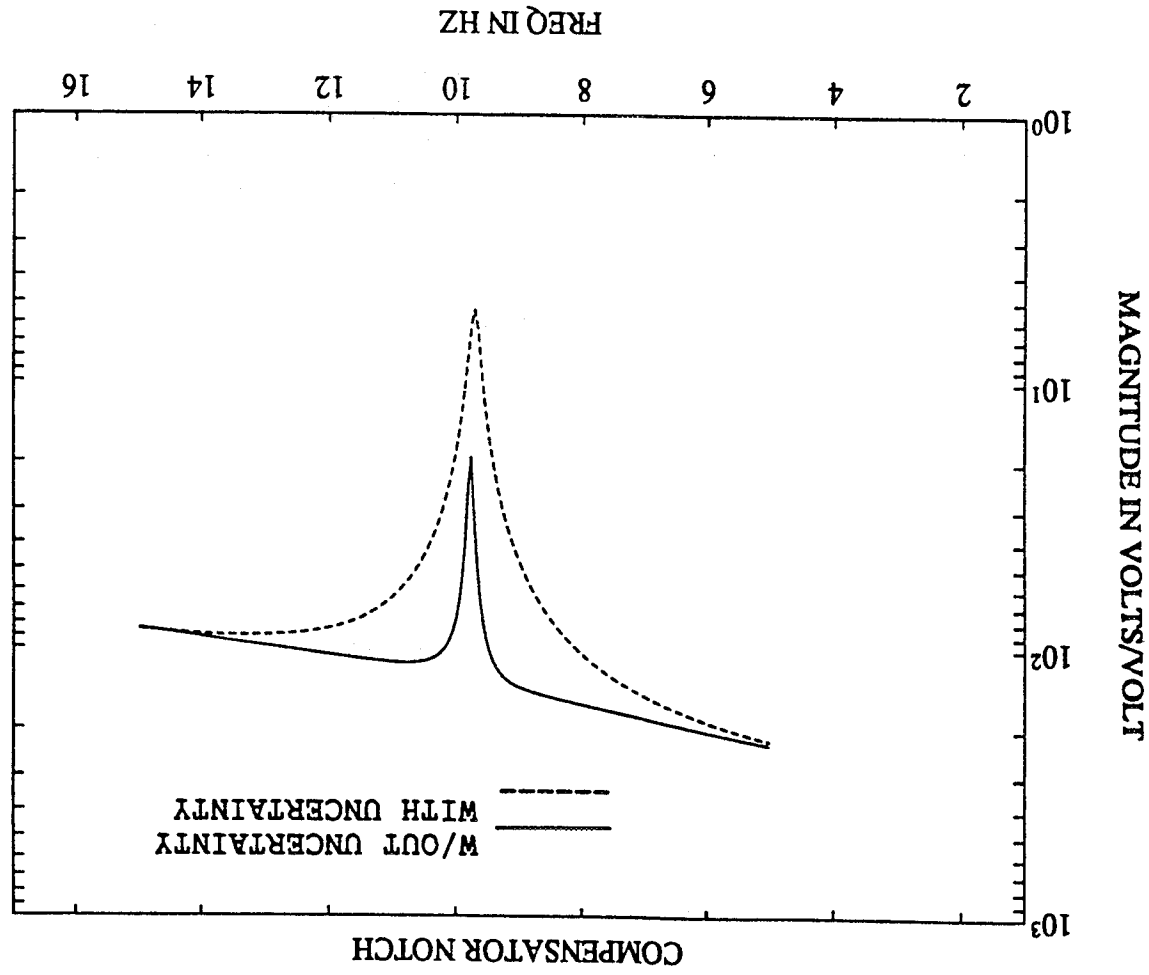
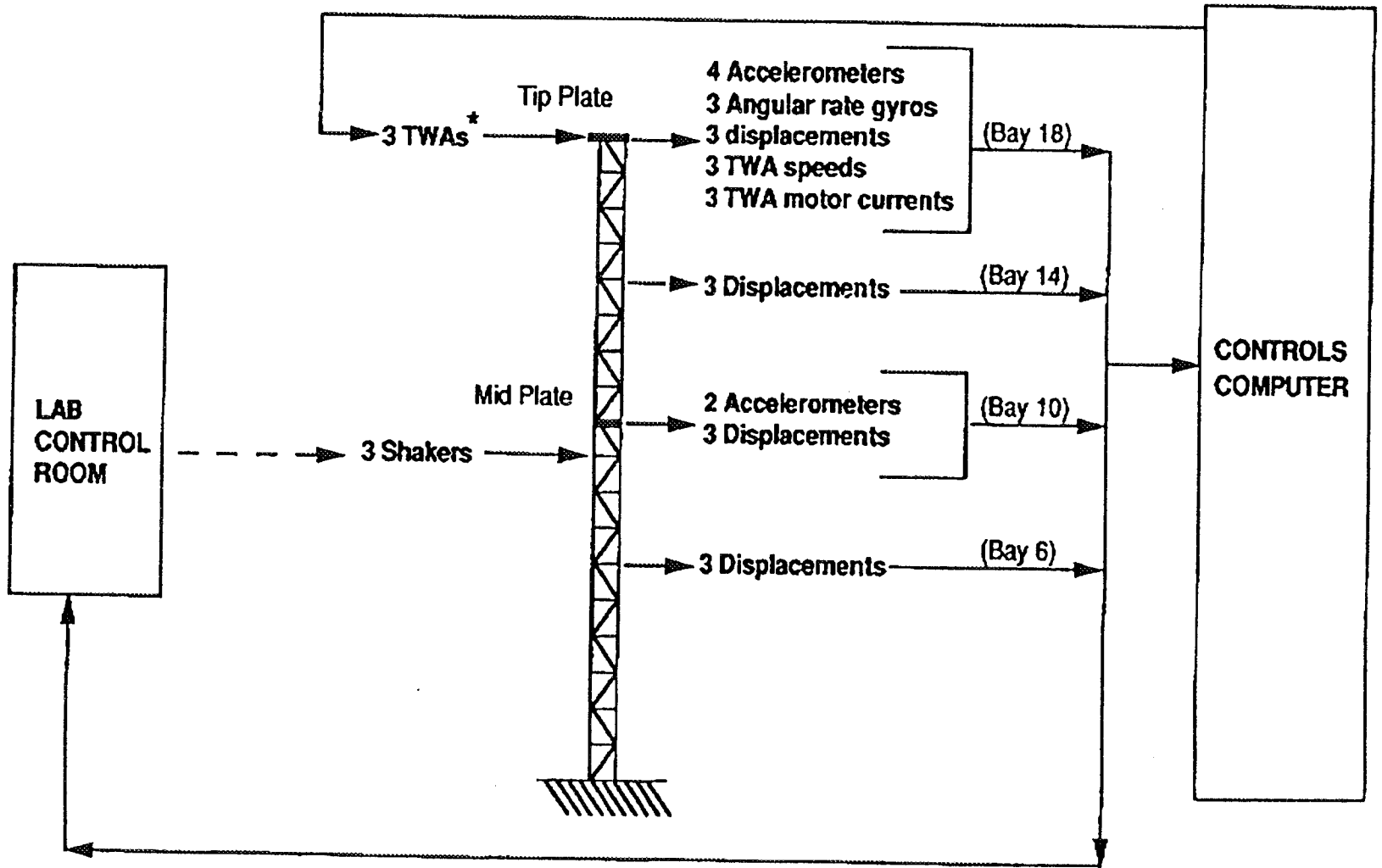
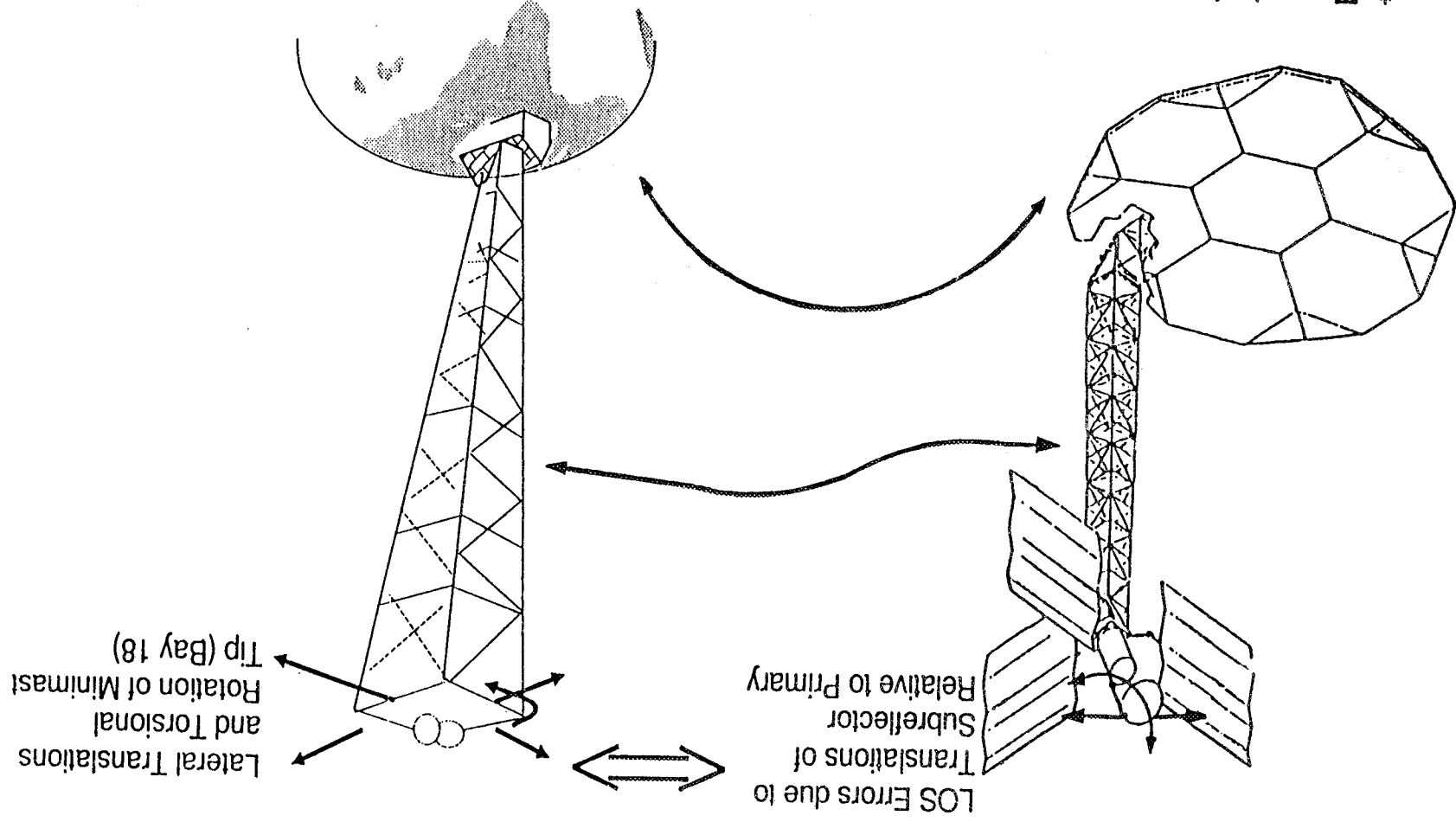


Figure 2.2-8 For the AGS to BGYRO Loops Maximum Entropy Design Robustified the Notches for the High Frequency Modes by Increasing their Width and Depth.



* TORQUE WHEEL ACTUATORS

Figure 2.3-1 The Mini-MAST Test Article



- * Translations and Rotation of Minimast tip corresponds to LOS errors due to decenter of subreflector
- * Accordingly, our goal is suppression of Minimast tip (Bay 18) lateral displacement and torsional rotation.

Figure 2.3-2 The Traccability of the Mini-MAST Structure to Future Space Missions

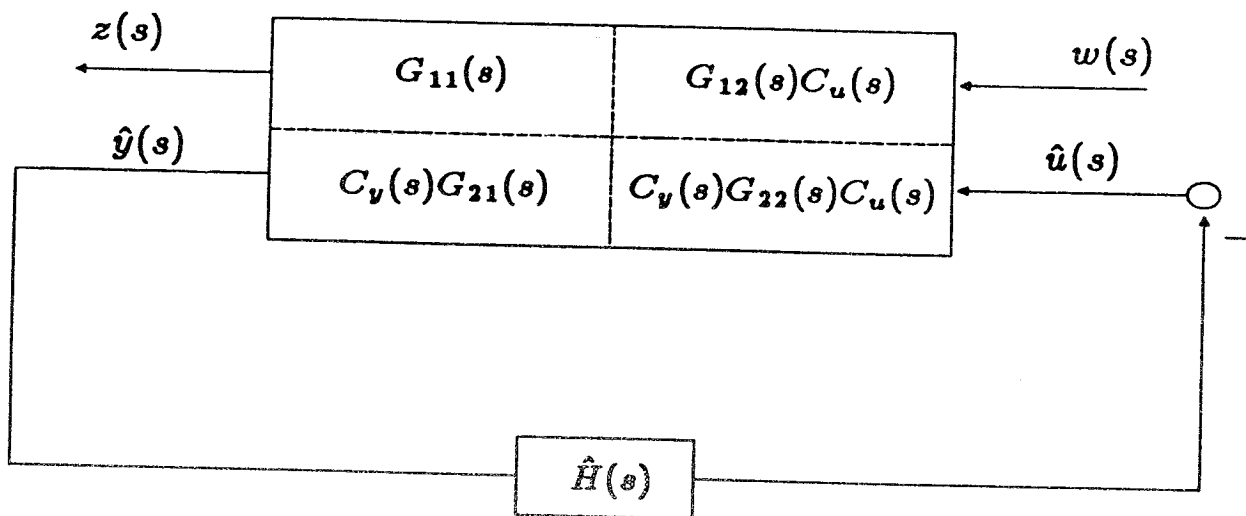
Mini-MAST structure. Particular emphasis was also placed on controller simplicity (i.e., reduced-order and decentralized controller architectures). Complexity reduction in control law implementation is of paramount interest due to stringent limitations on throughput of even state-of-the-art space qualified processors.

To maximize traceability to real flight systems, only the (acceleration and rate) sensors that are mounted on the Mini-MAST structure were used. Five sensors were used: four accelerometers and one rate gyro. Because of the two differentiators in the transfer functions from the control actuators to the accelerometers, the high frequency modes were much more observable in the accelerometers than in the displacement sensors. Because the performance objective required control of the low frequency modes without destabilizing the higher frequency modes (a standard structural control problem), the use of accelerometers for control design significantly increased the spillover problem. Thus, in this case, it was much more challenging to achieve high performance design using accelerometers rather than displacement sensors.

Because of the use of accelerometers, it was very important to ensure that the control laws rolled off sufficiently to avoid destabilizing the high frequency modes. In this experiment the roll-off was enforced by using a precompensation strategy. That is, practical roll-off filters ($C_u(s)$ and $C_y(s)$) were first designed and included as part of the plant as shown in Figure 2.3-3. Reduced-order LQG and Maximum Entropy control laws were designed using the modified plant. Then, as illustrated in Figure 2.3-4, the roll-off filters were appended to the reduced-order LQG and Maximum Entropy control laws to obtain the control laws which were actually implemented. As will be seen in the subsequent results, this methodology proved to be very effective for achieving the control design objectives for the Mini-MAST.

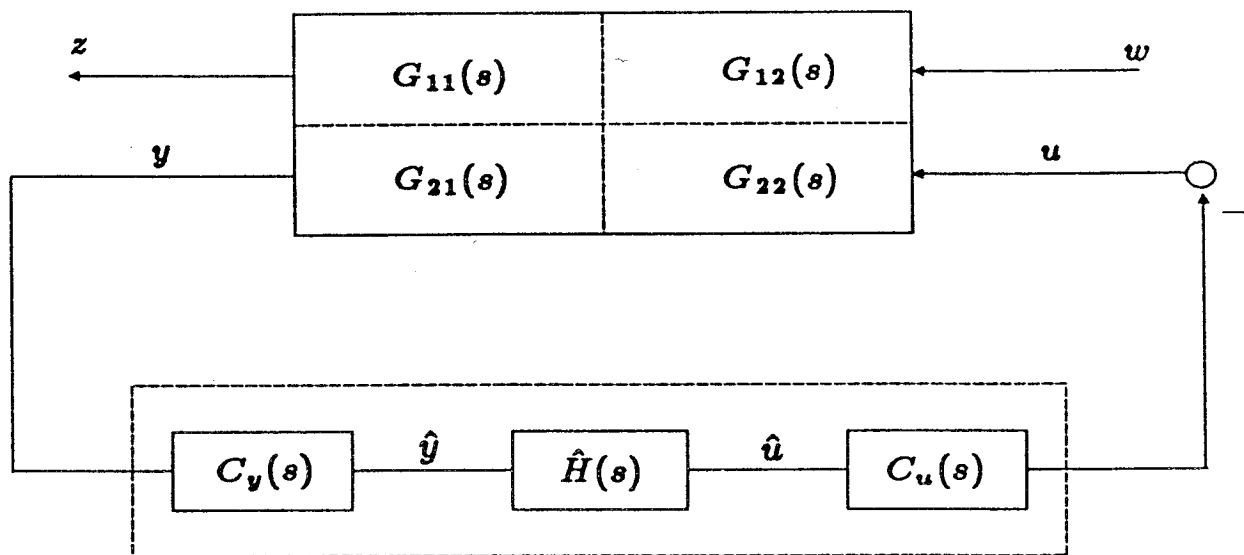
Two models of the Mini-MAST were provided by NASA Langley Research Center. The first model, Model 1, was used to generate the reduced order models that were used to design the decentralized controllers and had good correspondence to experimental data below 10 Hz. A second model, Model 2, that had even better correspondence to experimental data under 10 Hz was provided later in the program. This close correspondence is illustrated by Figure 2.3-5. Model 2 was used to generate the reduced order model that was used to design the centralized controllers. The final evaluation model for each of the control designs was the full-order representation of Model 2, discretized at 80 Hz, the sample frequency chosen for control law implementation.

At the very outset of the control design activity, we determined a very simple and effective way to suppress the torsional mode response, thereby saving our design resources for control of the bending motion. As Figure 2.3-6 shows, the transfer function from Torque-Z to Rate Gyro-Z was dominated by the first torsional mode at 4.4 Hz. Hence, it appeared feasible to use simple decentralized constant gain feedback from Rate Gyro-Z to Torque-Z to achieve high attenuation



$$\hat{y}(s) = C_v(s)y(s) \quad u(s) = C_u(s)\hat{u}(s)$$

Figure 2.3-3 Design Configuration for the Precompensation Methodology



$$H(s) = C_u(s)\hat{H}(s)C_v(s)$$

Figure 2.3-4 Implementation Configuration for the Precompensation Methodology

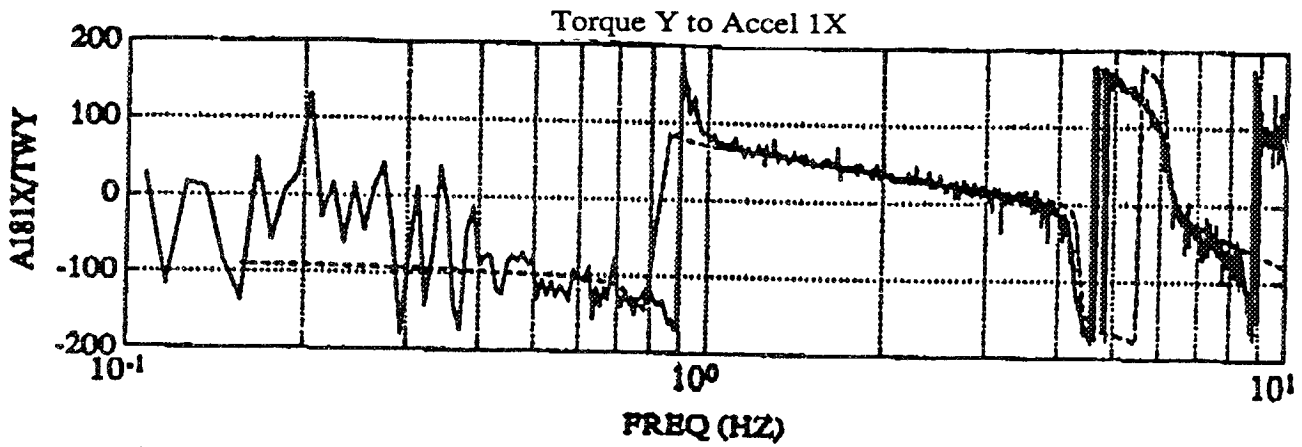
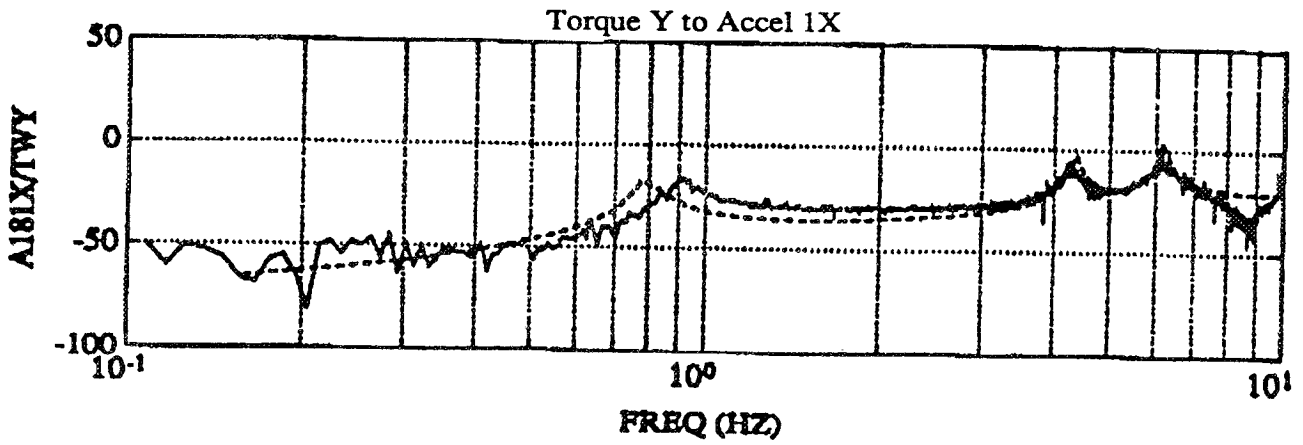


Figure 2.3-5 Torque-Y to Acceleration-1X: Model 2 Bode Plots vs. Experimental Frequency Response Function (Experimental = Solid, Model 2 = Dashed)

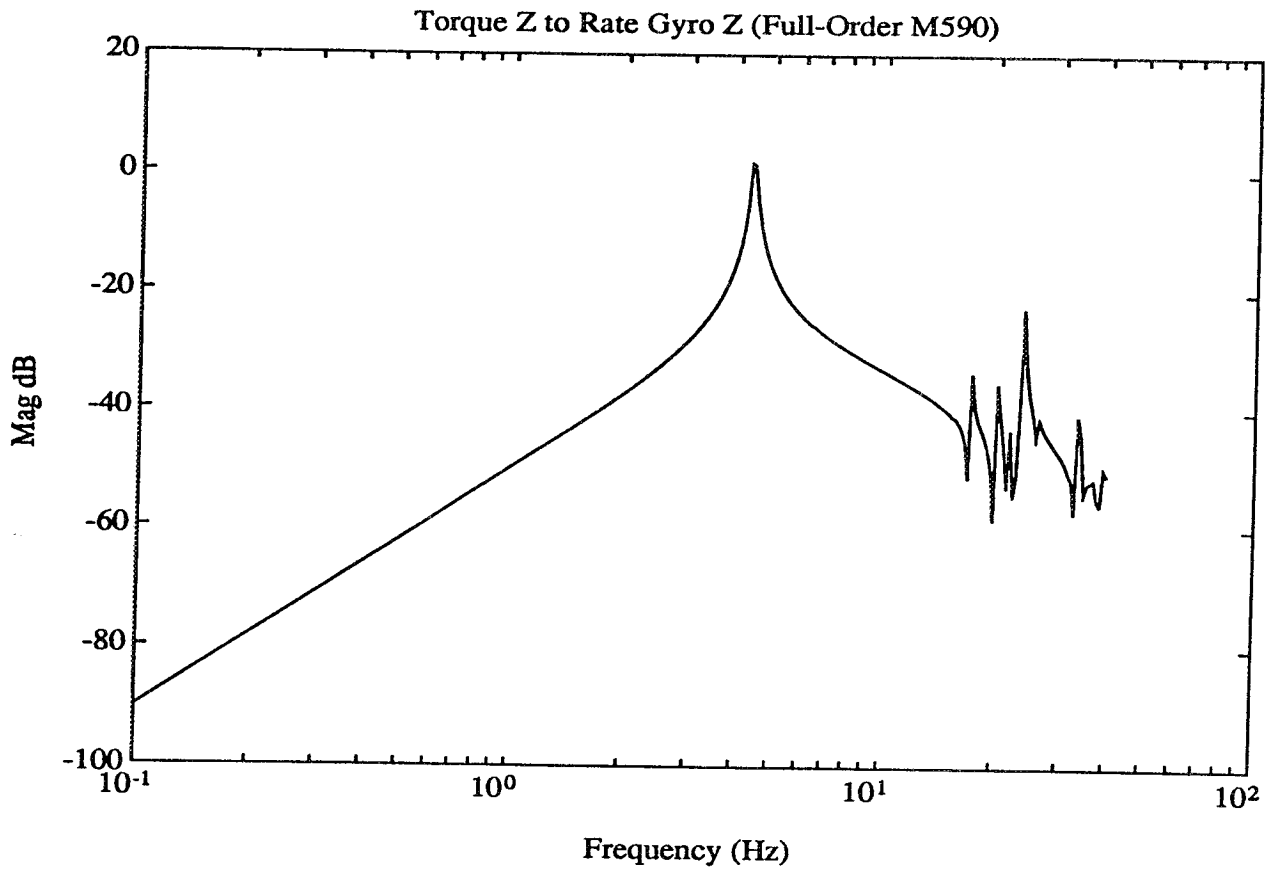


Figure 2.3-6 Bode plots of Torque-Z to Rate Gyro-Z for Model 2

of the torsional mode. A full-order discrete-time model of the system was developed using Model 1 to represent the system at the 80 Hz sampling frequency. This model was employed to determine that the optimal constant gain is $K=10$. All of the implemented controllers were designed assuming that this feedback loop was closed. These designs added feedback loops that used only the accelerometers and the X and Y torques. The use of the Rate Gyro-Z to Torque-Z feedback essentially eliminated the influence of the torsional mode on the remaining loops as illustrated by the dotted line in Figure 2.3-7. The resultant performance improvement in the torsional motion is shown in Figure 2.3-8.

Being in possession of high fidelity models and having disposed of the torsional mode, we then concentrated on the bending motion response and used our resources to explore design complexity versus performance tradeoffs. This was done by testing a sequence of distinct designs, ranging from simple "rate feedback" to advanced centralized OPUS design. First, controllers with simple architectures (decentralized, reduced-order, using few sensors) were developed and tested. Subsequently, centralized control laws were developed in order to improve the performance. The centralized design with the best performance did significantly improve the performance of the "best" decentralized design. This sequence of designs also represents a step-by-step, progressive improvement approach similar to that employed in the ACES testbed.

In all, seven distinct bending motion controllers were designed and tested over two test sessions. Figure 2.3-9 shows tip displacement response to a shaker impulse disturbance for the open-loop and for the four decentralized designs. Figure 2.3-10 shows tip responses for open-loop, the best decentralized design (controller 4) and the three centralized designs. These designs are numbered in the chronological order of their testing. All designs worked stably on the first try and each design in the sequence shows progressive improvement over its predecessor. Moreover, experimental results were in close agreement with analytical predictions so we show only the experimental data here.

With these results we can observe the relative performance benefits of the more complex modern multivariable designs over the simpler decentralized (SISO) designs. Try as we might, the simpler SISO designs could not be made to damp the tip deflection in less than several cycles of the primary pair of bending modes. This is evident from the bottom plot of Figure 2.3-9 for controller 4. Suppression of bending motion within one cycle was only possible with the centralized OPUS design as shown at the bottom in Figure 2.3-10. To our knowledge, comparable results were obtained only by the Cal. Tech. GI team using μ -synthesis—another modern multivariable method. In summary, Figure 2.3-11 shows a comparison of tip displacement response for the open-loop and for the advanced OPUS design under identical impulse disturbance. While the open-loop vibration persists for a dozen periods of primary bending motion, the closed-loop system is damped within approximately one cycle.

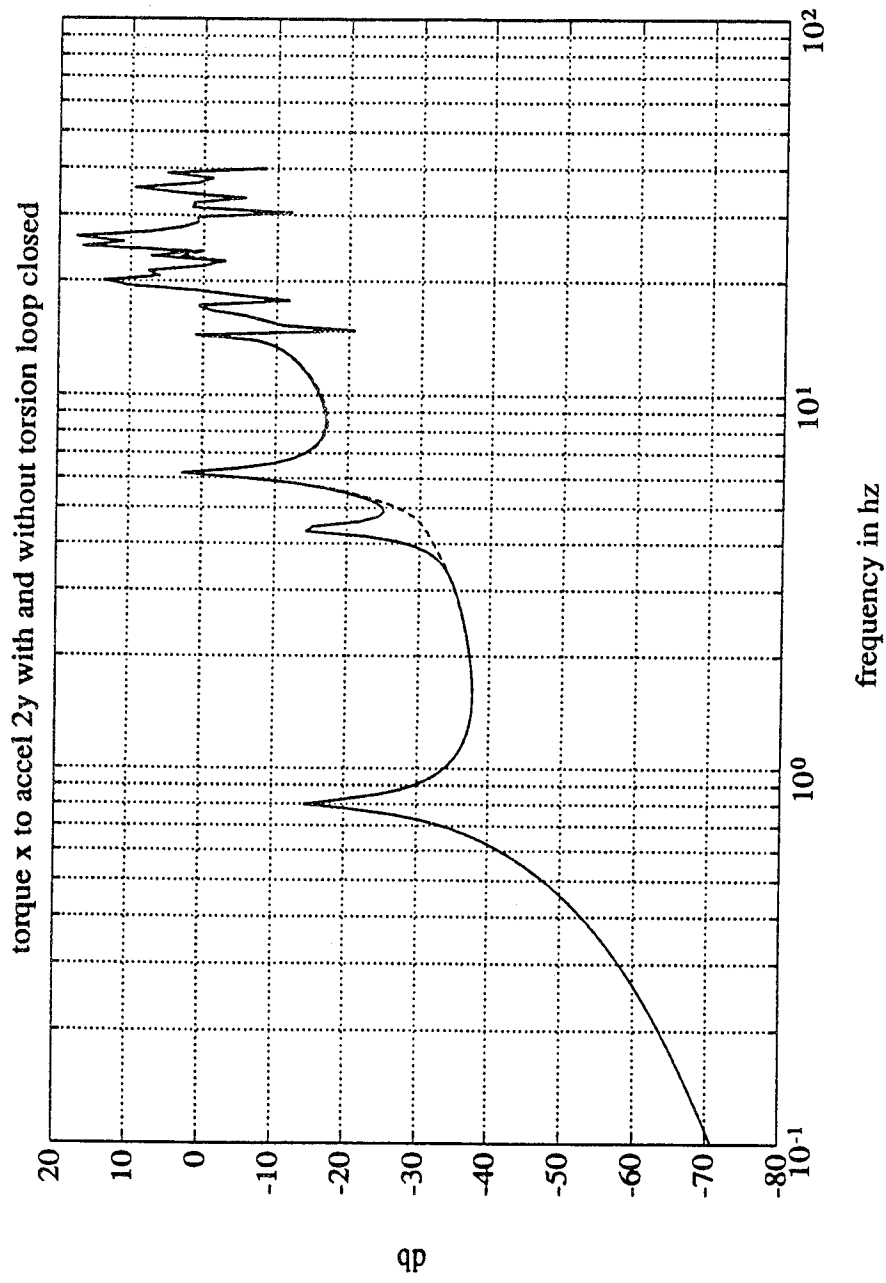
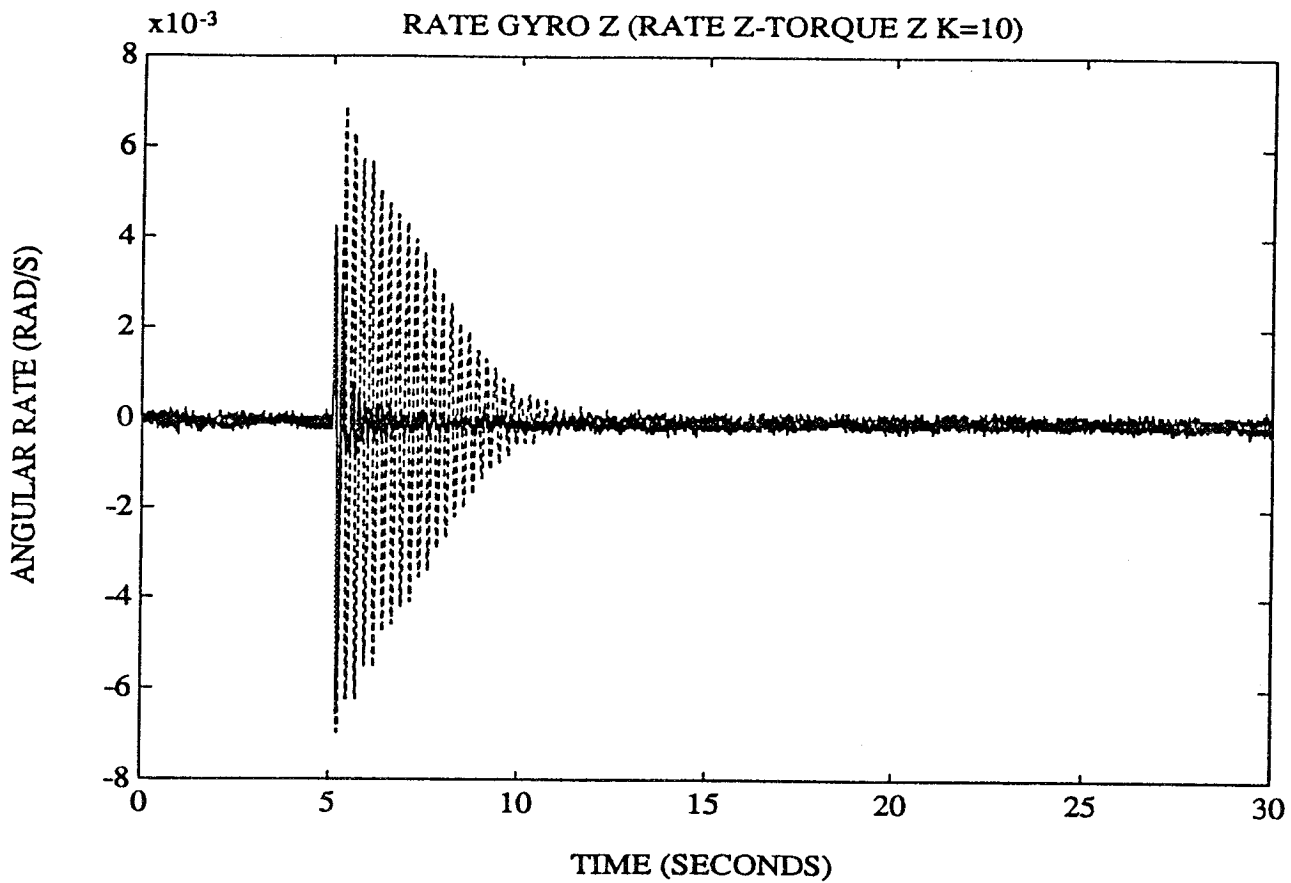


**Figure 2.3-7 The Effectiveness of Constant Gain Rate Feedback in Eliminating the Influence of the Torsional Mode
(Without Feedback = Solid, with Feedback = Dashed)**



(CLOSED LOOP = SOLID, OPEN LOOP = DASHED)

Figure 2.3-8 Open-Loop vs. Closed-Loop Rate Gyro-Z Response for Constant Gain Feedback from Rate Gyro-Z to Torque-Z

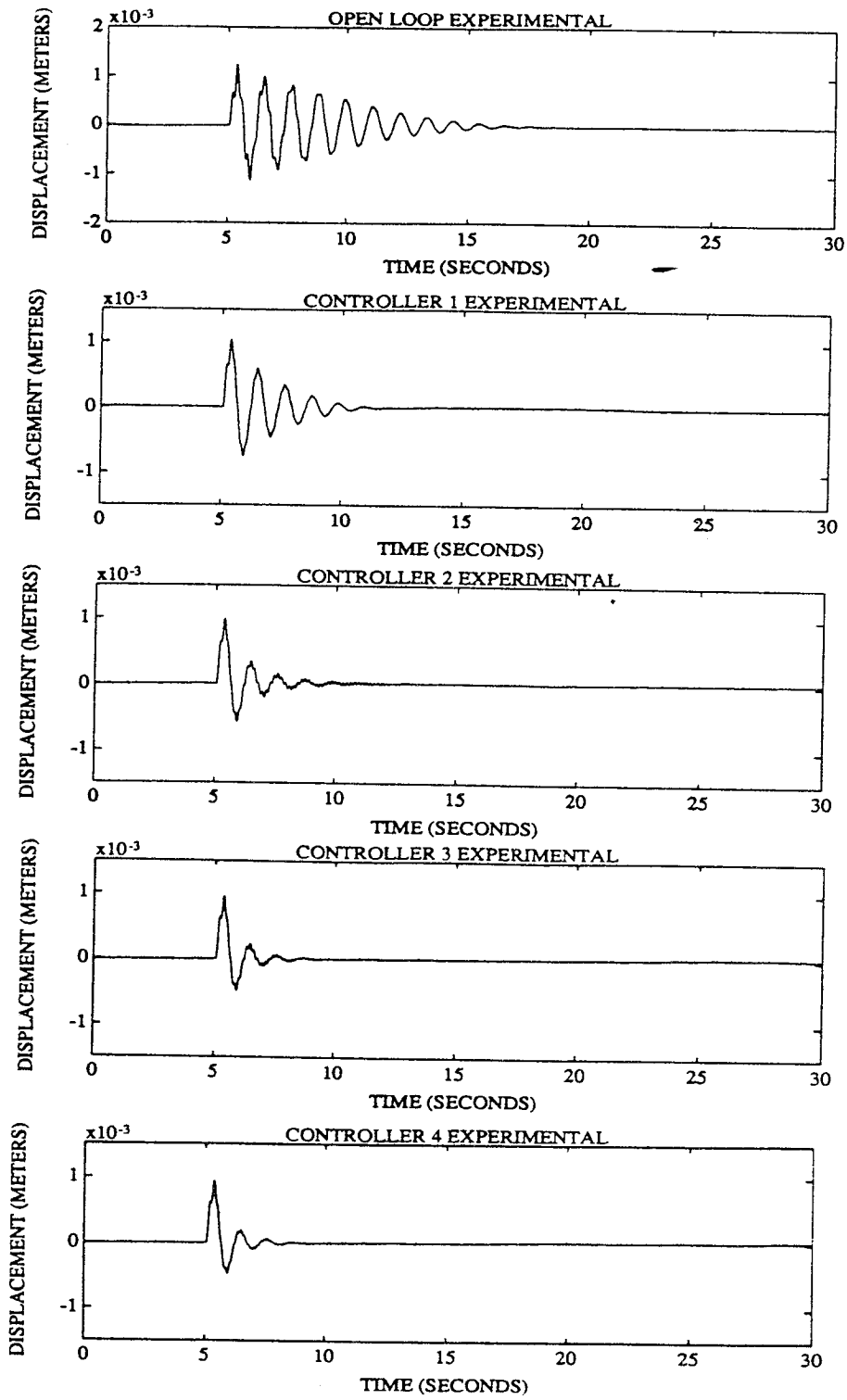


Figure 2.3-9 Open-Loop vs. Closed-Loop Responses of Displacement A of Bay 18 for Controllers 1 through 4

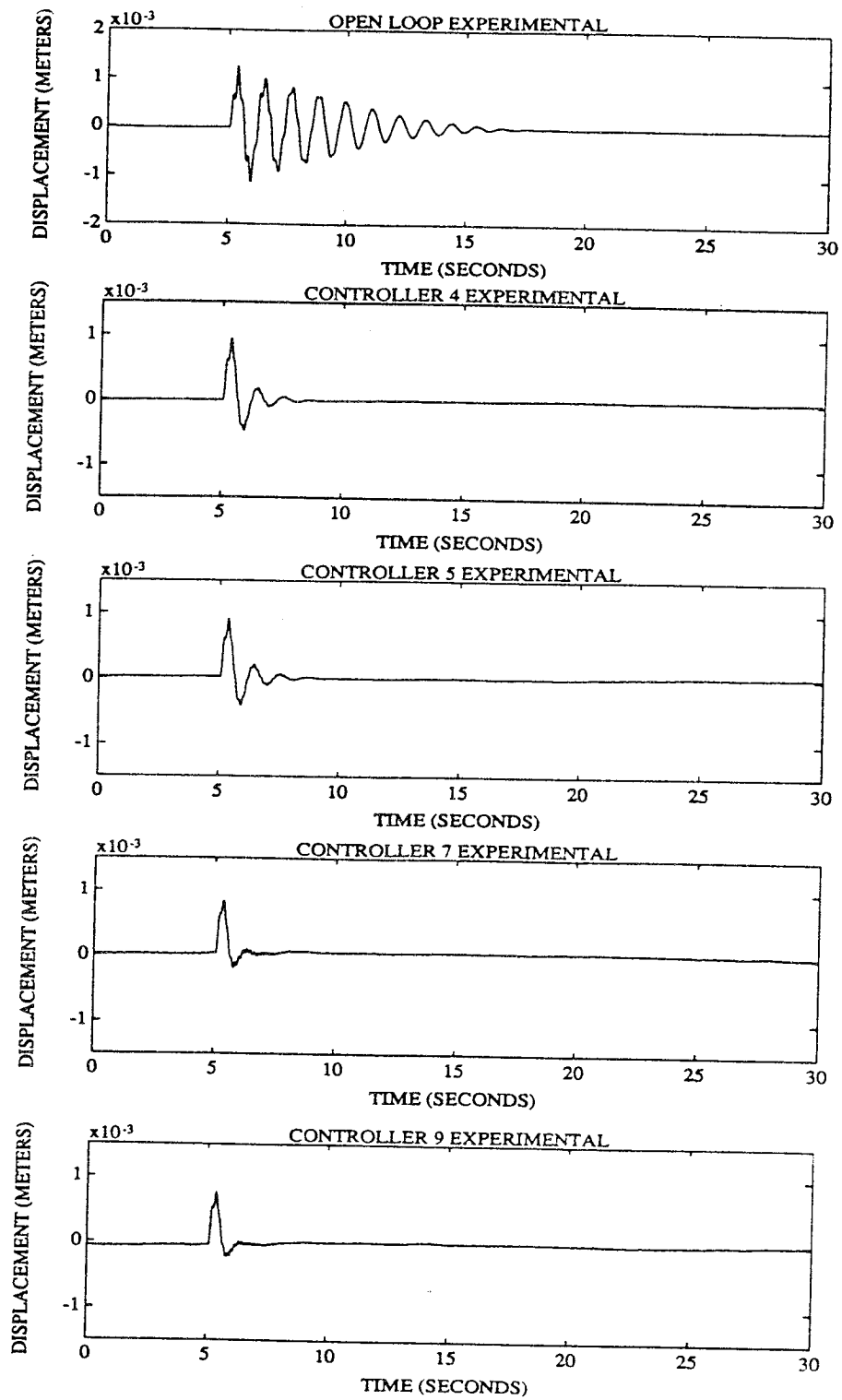


Figure 2.3-10 Open-Loop vs. Closed-Loop Responses of Displacement A of Bay 18 for Controllers 4 through 7

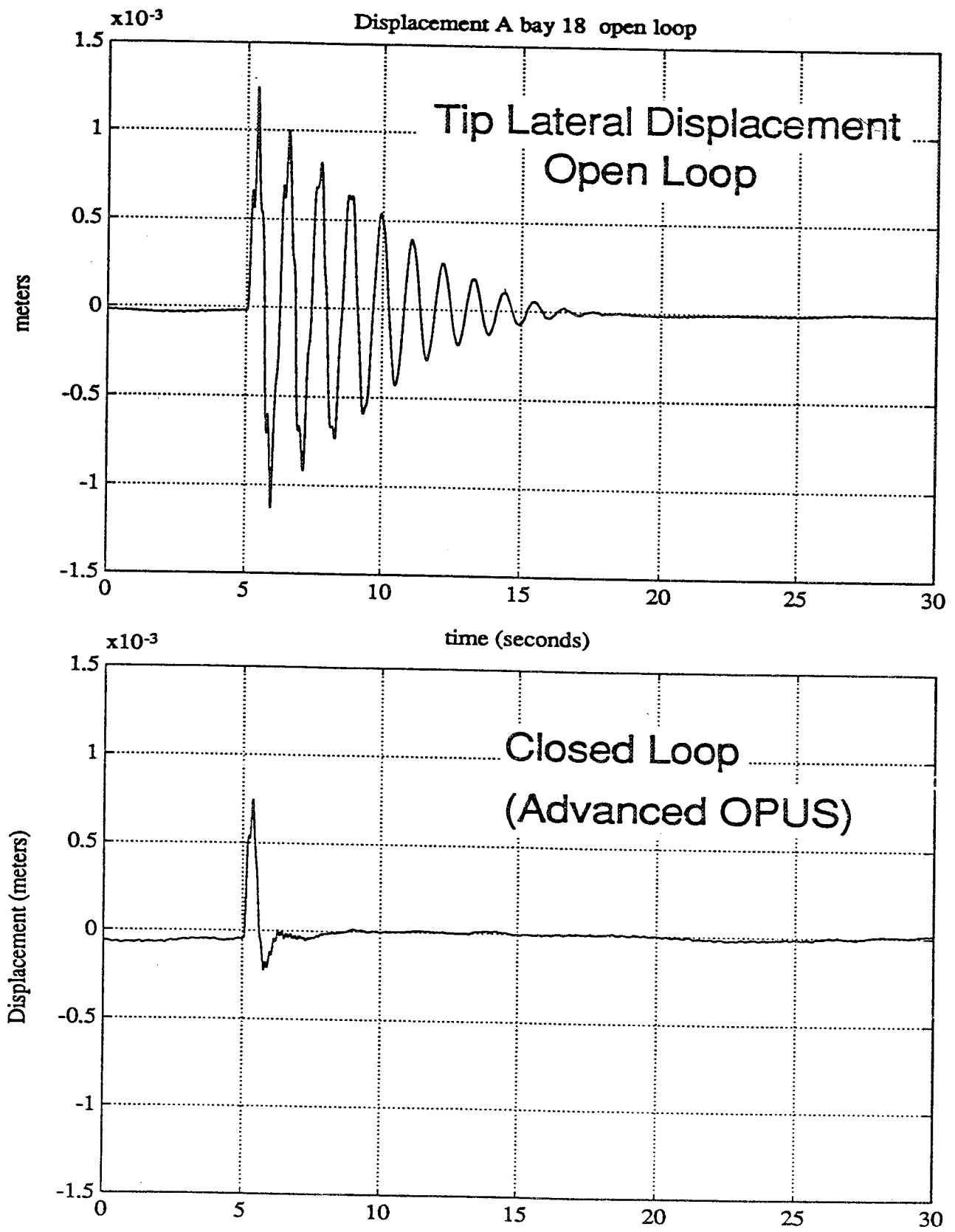


Figure 2.3-11 Mini-MAST: Open-Loop vs. Closed-Loop Performance

2.4 Phase I: Summary of Principal Findings

Phase I activities were invaluable in helping transition the Harris structural controls technology into practice. There were many areas of significant progress and several particular conclusions concerning more effective methodology that arose from the Phase I GI experiences. These are discussed under separate headings below.

Validation of OPUS Design and Investigation of OPUS Robustness Phenomenology

One accomplishment of the Phase I program was the experimental verification of the OPUS design technology, particularly the Maximum Entropy design feature. Experiences on both Phase I and Phase II, involving four independently refereed testbeds in all, have shown OPUS to be a reliable, effective tool for robust design. In all experiments, including those in Phase II, OPUS controllers displayed stable operation with performance close to predicted values from the very first try. Performance actually demonstrated on all testbeds was outstanding. In addition, practical implementation experience has built our understanding of the particular features of Maximum Entropy design that enable it to achieve robust performance e.g., the smoothing of compensator gain and phase, the widening of narrowband compensators, the widening and deepening of controller notches, etc. This improves our efficiency in the subsequent application of the design tools.

Importance of Automated System ID

One of the most important overall lessons learned on Phase I was that it is fundamentally the control designer's responsibility to secure system models with sufficient fidelity to support high performance control system design. Moreover, the ERA and its variants proved to be efficient, accurate and low cost tools for the acquisition of system models directly from test data. Our use of ERA on the program fits in with the space structure control scenario in which the system is initially (pre-launch) equipped with a simple, highly robust controller which is then refined on-orbit using in-mission identification testing. The use of ERA and similar automated identification tools marks significant progress toward an efficient low cost control design/verification methodology for precision space structures.

Utility of Low Order Models and "Simple" Controllers

The results of both the ACES and Mini-MAST experiments illustrated that simple controllers (reduced order and decentralized) based on reduced order models can provide very significant performance improvement. This reduction in controller complexity reduces the throughput requirements on space-qualified processors and reduces time and cost needed for design and implementation. From the GI experiences and similar exercises, we believe that a

practical control design and implementation approach has to start with "simple" controllers and then increase controller complexity as needed to attain performance goals.

Evaluation of a Fast, Low Cost Design and Test Methodology

As depicted in Figure 2.4-1, one of the most beneficial outcomes of the Phase I effort was our integration of OPUS and ERA tools into a practical, fast, and economical control design and test methodology. This "Gradualist" design and test methodology is a step-by-step building up process with alternating model-data acquisition and control design refinement steps. This is a design development process that leads rapidly to the final, advanced design while revealing the significant complexity versus performances tradeoffs.

The power of a multivariable design tool (such as OPUS) can sometimes beguile its users to expect a practically implementable and satisfactorily working control algorithm after a one-step application of the design software to system dynamic models and performance specifications. Such a "big-bang" approach seldom works in practice because of unforeseen complexities and modelling errors that attend real hardware. Thus, development of advanced design tools is not enough for successful implementation of working control systems. What is needed, in addition, is a practical *methodology* for using advanced design tools that meshes algorithm design, system modelling, and subsystem and component tests into a realistic strategy for implementation. The OPUS application methodology we have evolved is *gradualist* in that it progresses step-by-step from simpler control architectures (e.g., low-order, decentralized) to the more complex coordinated control algorithm, and from a small set of subsystem hardware elements (i.e., sensors and actuators) toward integration of all hardware elements. A key element of this methodology is its emphasis on dynamic models extracted directly from test data. We rely primarily on the Eigensystem Realization Algorithm developed by Juang and Pappa at NASA/LaRC and have acquired experience with its most recent refinements. While exploiting the capabilities of both the OPUS multivariable control design methods and the ERA system ID methods, the Gradualist methodology allows flexible response to unforeseen contingencies and to new modelling data, thereby recapturing some of the flexibility inherent in classical design procedures.

The Gradualist methodology is depicted in Figure 2.4-2. Two layers of gradualism are evident. The first of these involves hardware subsystems which are first treated separately (as in the ACES experiments) before being integrated as a single monolithic system. In addition to the reduced complexity of initially separate treatment, this stepwise methodology allows assessment of the real contributions made by each subsystem to overall performance improvement. Perhaps even more important to the success of the methodology is the second layer of gradualism, which determines how the control system for a given set of hardware is developed and demonstrated.

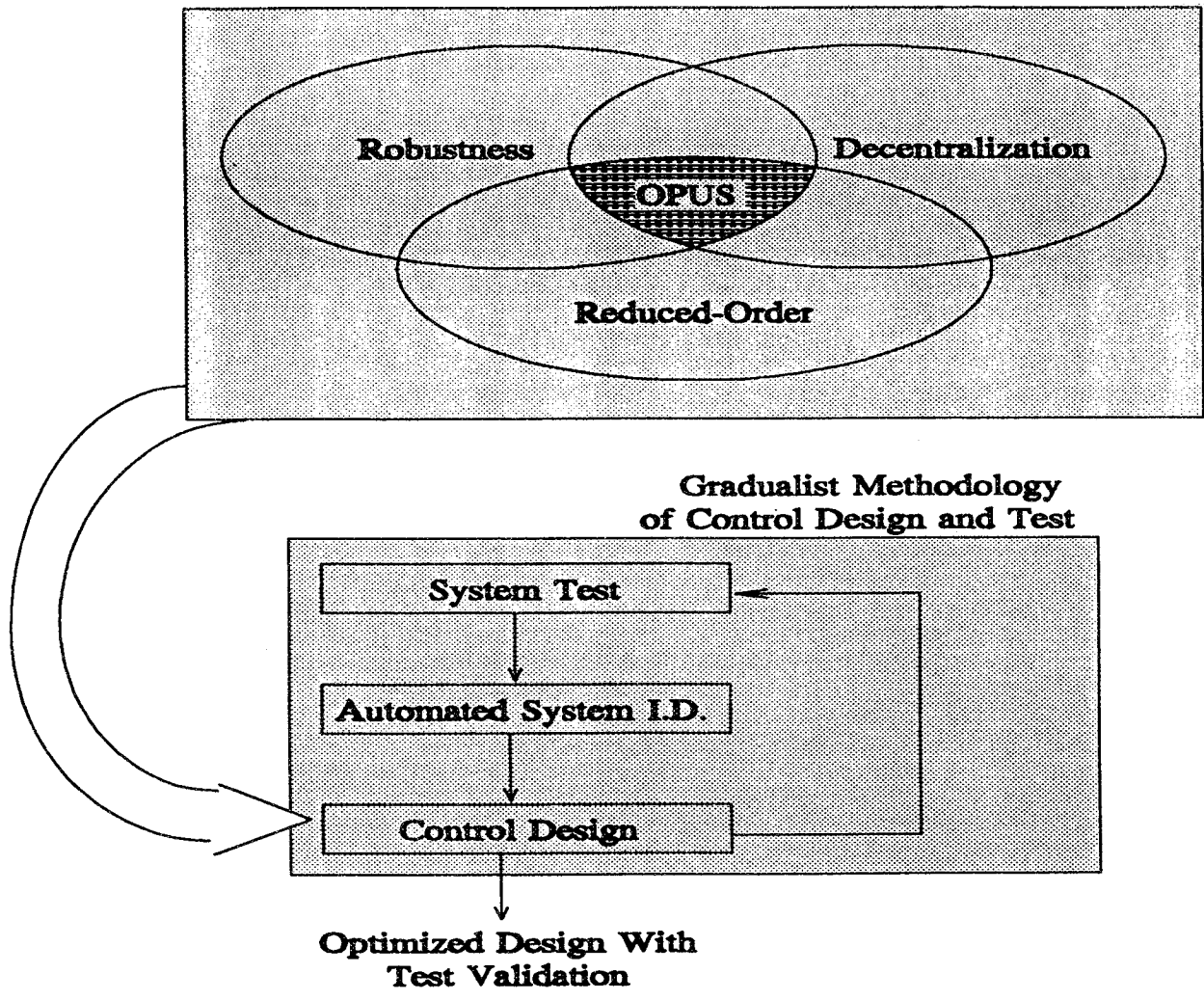
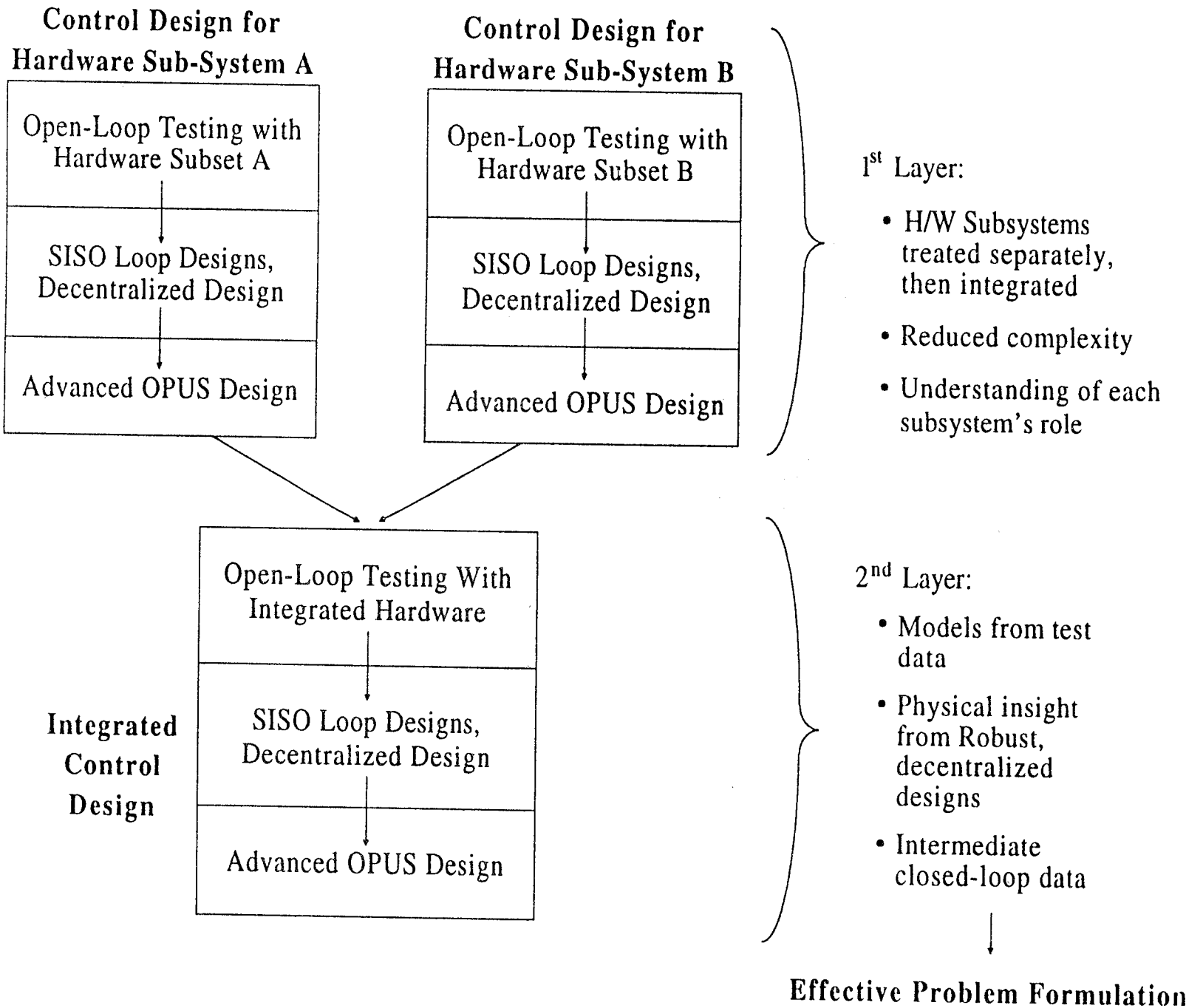


Figure 2.4-1 Harris' Phase I CSI GI Efforts Proved OPUS Design Tools and Integrated them within a Practical Design and Test Methodology

Figure 2.4-2 The Gradualist Methodology Integrates Subsystems and Refines Control Algorithms Step-by-Step to Build Up to the Best Possible Performance



The process for development can be roughly split into three stages:

- (i) open-loop testing and modelling,
- (ii) inherently robust decentralized design, and
- (iii) advanced centralized design.

When properly executed, this process yields a set of designs of incrementally increasing performance (and complexity) which can be traded to obtain an optimal compromise.

In the first step, open-loop testing, is performed on the integrated hardware and the test data utilized, via ERA or equivalent, to generate system dynamics models. This allows controls design to proceed not with idealized models but with actual test data including all the vagaries of hardware.

The second step, which can sometimes be performed during the same test period as the first, is to try out an inherently robust (rate feedback or positive real), decentralized design. Such a design yields valuable insight into the effectiveness of the control hardware and the performance improvements that are realistically possible. Typically this design is extremely simple and does not involve any connections among separate hardware units. The exercise of perfecting a decentralized design, however, does force the designer to understand the physics of the system and allows him to individually tailor each control subsystem according to insight and discretion.

Finally, the design and demonstration data developed in the first two steps are applied to an advanced multivariable design using OPUS. At this point, the designer has the benefit of closed-loop tests using the hardware in question, a system model that has evolved (via application of ERA) from several test iterations and good insight into the physics of the system behavior. All of these are prerequisites to *effective problem formulation*, which is the key step in application of modern tools like OPUS.

The Phase I results show that the basic design/test methodology and its underlying tools are well in hand and have seen successful demonstration on non-trivial test articles. Thus at this point, two questions naturally arise: "Can we *speed up* the design/test process?" and "Can we substantially *automate* the process?" One of the main thrusts of the phase II effort was to answer these questions.



3. PHASE II - OVERVIEW

As described in the previous section and illustrated in Figure 3-1, the practical design/test methodology we evolved on Phase I typically entails a sequence of three on-site test sessions interspersed with modelling and control design steps. At the start of Phase II, the progress of our work was somewhat beyond the stage of evaluating the relative benefits of different control algorithm design methods. Moreover, our overall methodology was found to work well. Therefore, to secure the greatest degree of progress, the Phase II CSI GI activity thrusts toward streamlining and automating our incremental design and implementation process and toward the experimental demonstration of new modular and productized vibration suppression hardware.

The first task was to compress or speed up the whole process shown at the top of Figure 3-1 into a *single-session, on-site* controls design and test methodology.

Speeding up the design/test process would not only reduce engineering development time, it would also benefit system operations on future NASA missions. In one sense, our incremental design/test methodology demonstrations for CSI testbeds to-date have been ground-based "dress rehearsals" of a corresponding on-orbit design/test methodology. In this scenario one designs an initial pre-flight control system that is low performance but very robust. Once the system is deployed on-orbit one conducts system ID tests by ground commands, and down-links test data via telemetry. On the ground, this data is used for system ID and design of a refined, improved performance controller. The refined controller gains are then up-linked to the on-line control processor. This process continues until all mission-driven performance specifications are met. The process is also repeated whenever the in-mission structural properties change and/or equipment failures cause performance to degrade. Now, the current design/test methodology typically involves on-site test sessions of a few days alternating with longer off-site analysis and design episodes. This translates into on-orbit controls refinement requiring significant access to the hi-reliability mission hardware spread over considerable calendar time. Drastic compression of the on-orbit design/test process would allow design refinement to occur in one brief bout, thereafter freeing on-orbit hardware to perform its intended missions.

In addition to the above long-term benefits, a streamlined design/test process turned out to be a necessity for successful results on Phase II because of unforeseen shifts in program resources.

Originally, the Harris team was assigned to the Controls, Astrophysics and Structures Experiment in Space (CASES) facility at NASA/MSFC for the full two year duration of the CSI GI Phase II Program. Figure 3-2 shows the planned schedule for the first year which called for test results six months into the program. Based on the actual start date, this first test session was planned for December 1991. However, because of test facility readiness delays, the first test session was held August 3-7, 1992. Moreover, although open-loop response data covering

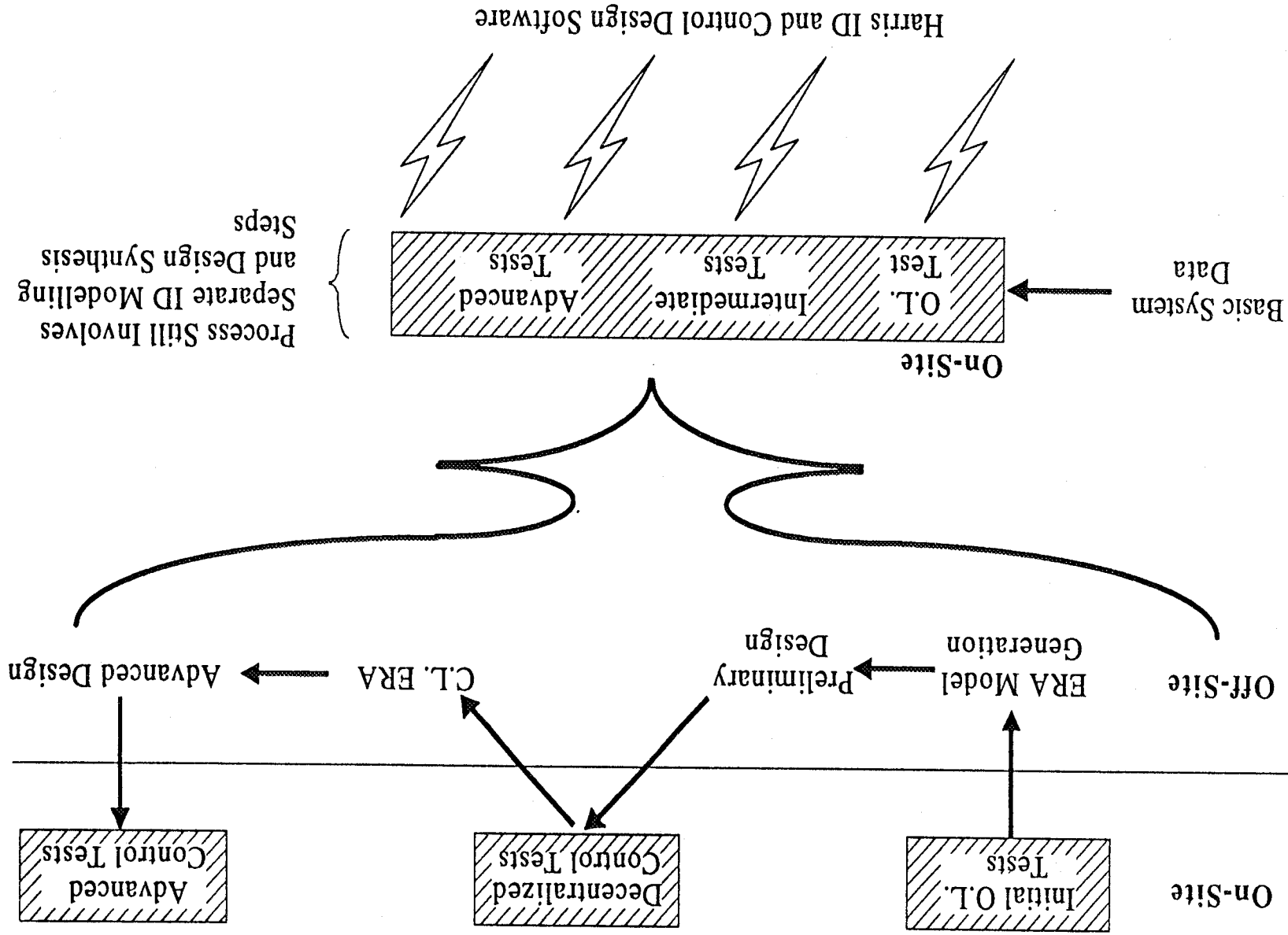
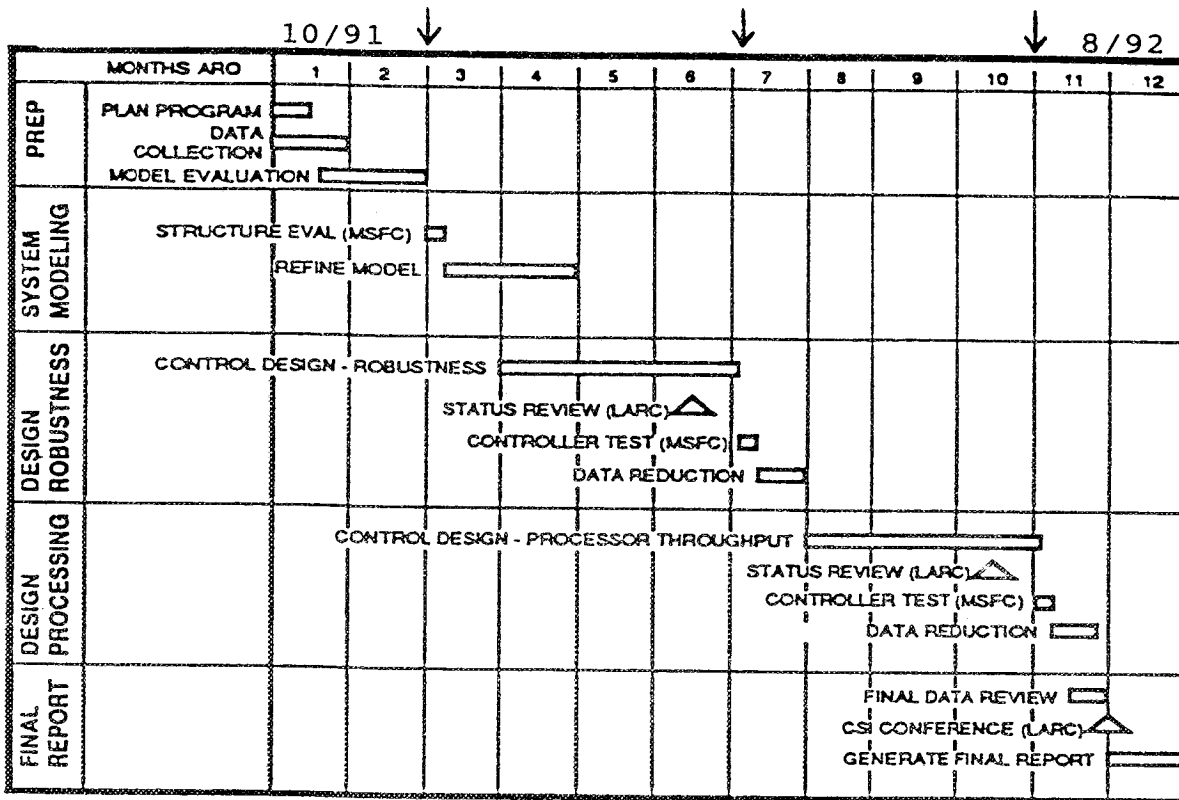


Figure 3-1 On-Site Design Methodology Drastically compresses the Design Development Process

YEAR #1: CASES (MSFC)



-HARRIS CORPORATION

Planned Start 6/91
Actual Start 9/91

- Based on actual start, 1st test session was planned for December '91.
- Because of test facility readiness delays, 1st test session was held August 3-7, '92.
- Data received before 1st test session:
Open-Loop response data, 1-20 Hz.

Figure 3-2 Year 1: Cases (MSFC)

the 1 to 20 Hz frequency band was provided prior to the August test, the dominant modes of the CASES structure are all below 1 Hz. Finally, shortly after the August test session, the CSI program activity at NASA/MSFC was terminated. Consequently, execution of a *single-session, on-site* design/test methodology was rendered a necessity.

To streamline our incremental design/test process we first implemented new, faster converging homotopy methods for solving the OPUS design equations. We also devised a practical, streamlined methodology for application of ERA to automated model acquisition from test data.

In a few days in August 1992, control design for the CASES testbed was addressed. As described in a subsequent section, the main structure of CASES is a 103.5 ft Astromast truss beam. As in Mini-MAST the control objective is to suppress tip displacements due to impulsive disturbances. With no prior relevant modelling information and in a single test session, the results shown in Figure 3-3 were obtained. This Figure compares the open-versus closed-loop tip displacement. Note that the open-loop response of the CASES structure "rings" far longer than the Mini-MAST. Moreover, there is a previously unidentified 1/50 Hz mode. But, as in the case of the Mini-MAST the closed-loop system response damps out in one (primary mode) cycle. However, unlike Mini-MAST, the CASES results shown in Figure 3-3 were obtained in a single test session not a sequence of three sessions.

For the second year of the Phase II program, the Harris team was re-assigned to the CSI Evolutionary Model (CEM), Phase II testbed at NASA/LaRC. Besides the by now customary, vibration control design and test activity on the CEM, our plan was extended to encompass validation of modular, productized technology components. These additional activities included simulation and test of an adaptive neural control (ANC) algorithm in order to progress toward autonomous spacecraft control and experimental demonstration of the Harris Vibration Attenuation Module (VAM), a new approach to active vibration isolation.

The originally planned schedule for the three CEM activities is shown in Table 3-1. This plan called for the test of the OPUS fixed-gain controller in late May 1993, test of the ANC in July, and two tests of a VAM unit (fabricated on a Harris IR&D program in June and July, 1993) on the CEM in late August and mid-September. In the following, we briefly describe the actual progress made and the necessary modifications to the above schedule.

First, the CEM testbed, shown in Figure 3-4 emulates the dynamics of a multi-sensor space platform and features several simulated sensor packages (SIS's) gimballed off the main structural framework. The basic method of exercising this testbed is to disturb the structure by commanding (broadband or in scan mode) the gimbal package of one SIS and then using the control instrumentation on the structure to maintain the pointing accuracy of the remaining SIS's.

**LOS Response - Open-Loop Versus Harris' Current GI
Phase 2 Control Design**

TDSdy Response to DSy Pulse (BLTx,MCS full;BLTy @2)

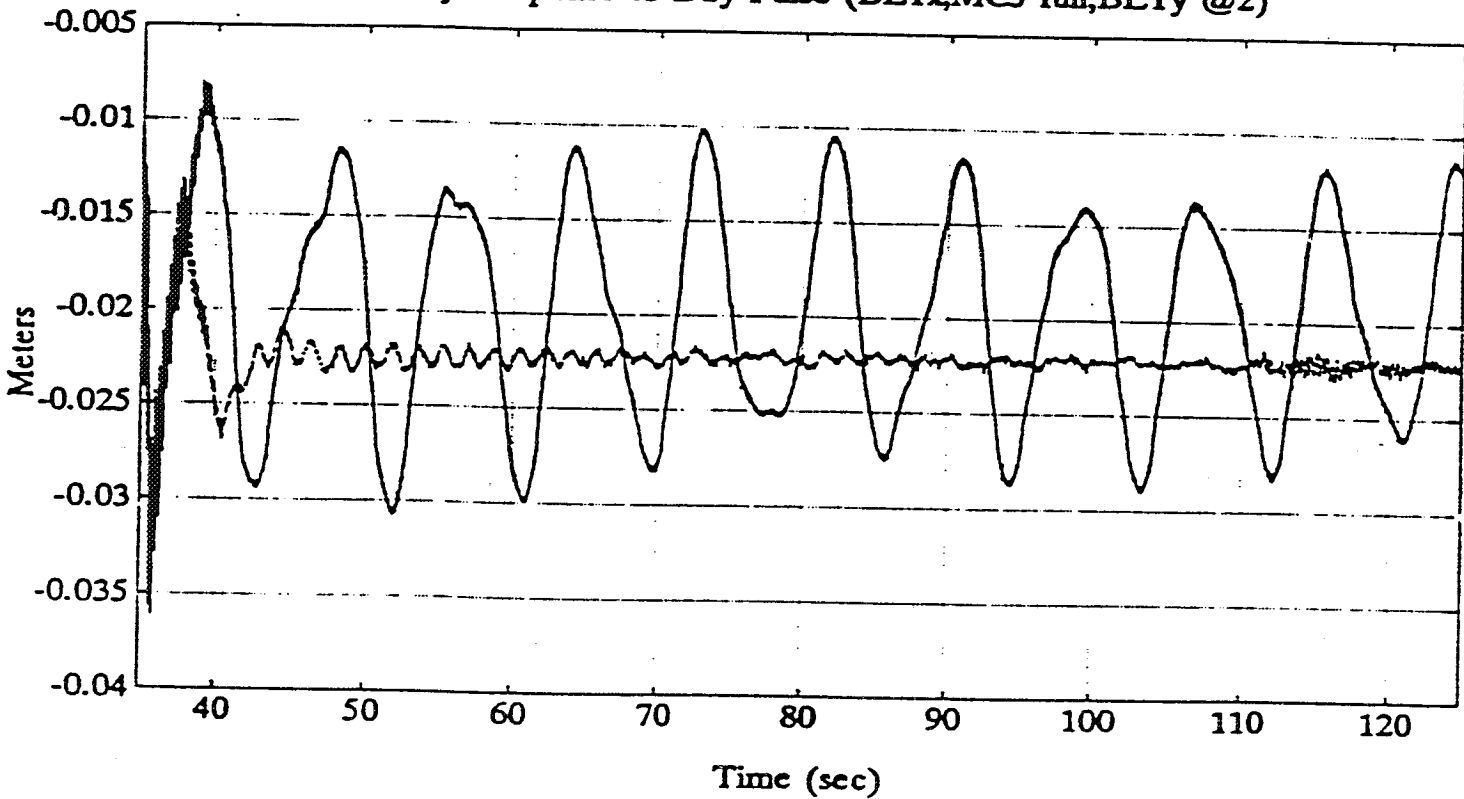


Figure 3-3 These CSI Program Phase II Control Design Results for the MSFC CASES Testbed were Obtained by the Harris Team During the First Test Session with No Prior Modelling Information

Table 3-1 GIP Ø2 Schedule Year 2, CEM

Task	Mar.	Apr.	May	June	July	Aug.	Sept.
Build Model	1 m - wk 						
Controller Design		2 m - mos 					
Test Trip #1							
Advanced Controller Design & Neural Controller				2 1/2 m - mos 			
Test Trip #2							
Active Isolation Preliminary Analysis		1 m - mo 					
Fabrication and Test						1 1/2 m - mos 	
Test Trip #3							
Test Trip #4							
Final Report							

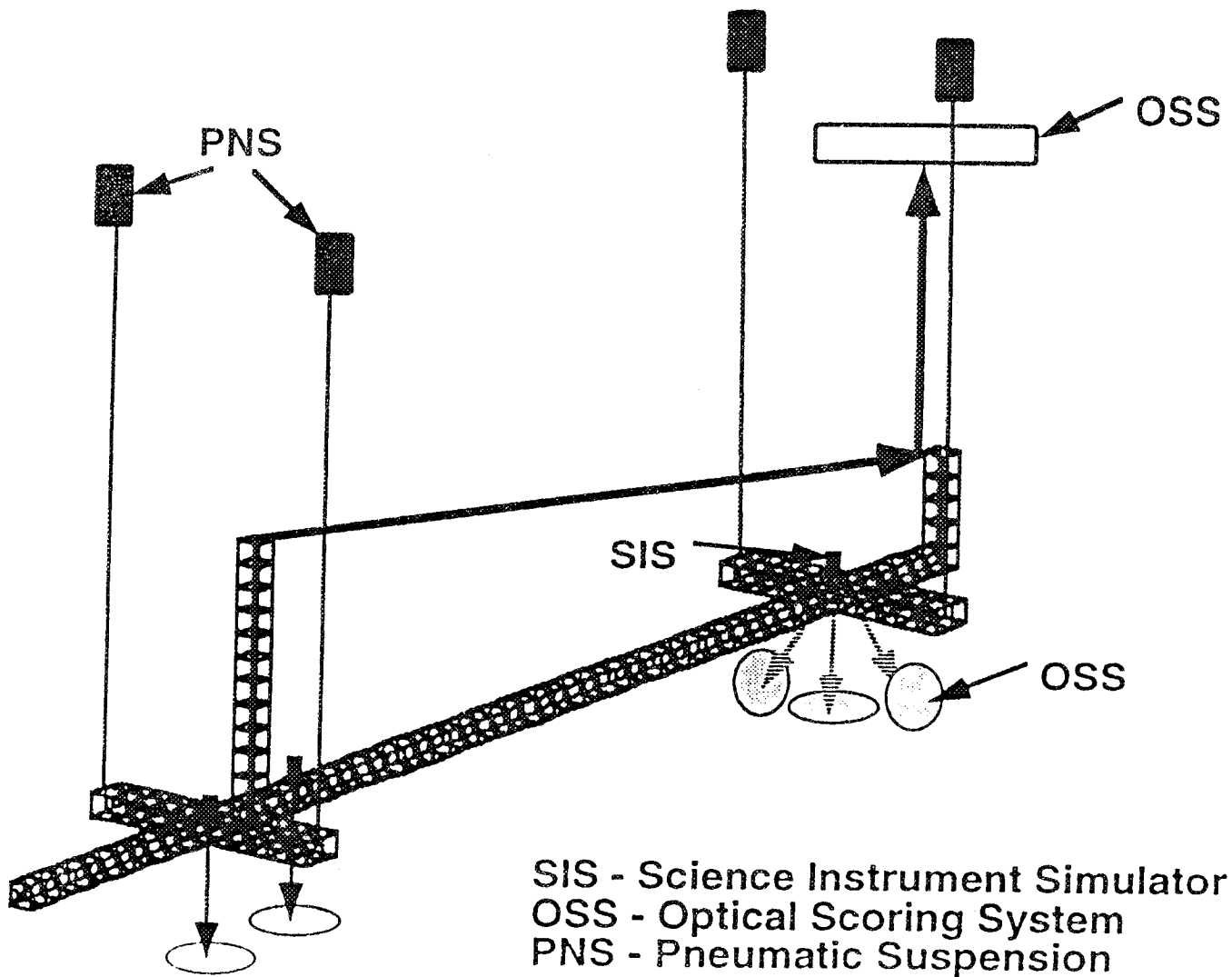


Figure 3-4 Phase 2 CEM: A Multiple Payload Platform

Using the eight accelerometers and eight thrusters distributed over the structure, the Harris team committed to the design and test of an OPUS control algorithm. The main thrust of this effort was to continue our progress in developing streamlined design/test methods, working toward the goal of a reliable single-session controls implementation methodology.

Here again, unforeseen changes in program and facility schedules rendered on-site single session design a necessity. Although excellent system models were finally provided by NASA/LaRC, there was an approximately three month delay in assembling the modelling data. Thus, the first CEM test session (see Table 3-1) was delayed until late August 1993. Moreover, NASA's plans called for the re-configuration of the CEM into the present EOS-like configuration (CEM, Phase III) in September 1993. Thus the August test session turned out to be the only experimental opportunity on the Phase 2 CEM.

Nevertheless, armed with accurate system models provided prior to the CEM test session and with our experience with the streamlined methodology acquired in CASES testing, we succeeded in designing and implementing a high performance controller, as indicated by the experimental data in Figure 3-5. This shows open-versus closed-loop target plane traces from one of the Optical Scoring Systems (of Gimbal C) when the structure is excited by a scanning disturbance by one of the other SIS's (Gimbal A). Clearly there is very significant LOS error reduction for this narrowband disturbance and a 50 to one reduction in RMS error was achieved for broadband disturbances.

Following the single session, fixed gain control system implementation exercise we embarked on qualitatively new efforts involving the CEM, as illustrated in Figure 3-6. First, we attempted a qualitative advance in control design and test automation and autonomy by testing the Adaptive Neural Control (ANC) technology under development for several years. Secondly, we sought to demonstrate a qualitative controls hardware advance (and facilitate a significant technology diversification) by testing a self-contained active isolation system—the Vibration Attenuation Module (VAM).

The motivation of the first effort above was the realization that if one could systematize and streamline a human-operated design/test process, one ought to be able to automate the entire process. This is the thrust of the new adaptive neural control (ANC) processing architecture developed at Harris over the past several years and significantly refined via collaboration with NASA/LaRC personnel—notably Drs. J.-N. Juang and M. Phan. Essentially, ANC is a logical extension of our efforts on CASES and CEM to streamline and reduce engineering development time for structural control implementation. ANC takes automation to the limit by executing on-site design with little or no human intervention. More specifically, the ANC algorithms builds,

ORIGINAL PAGE IS
OF POOR QUALITY

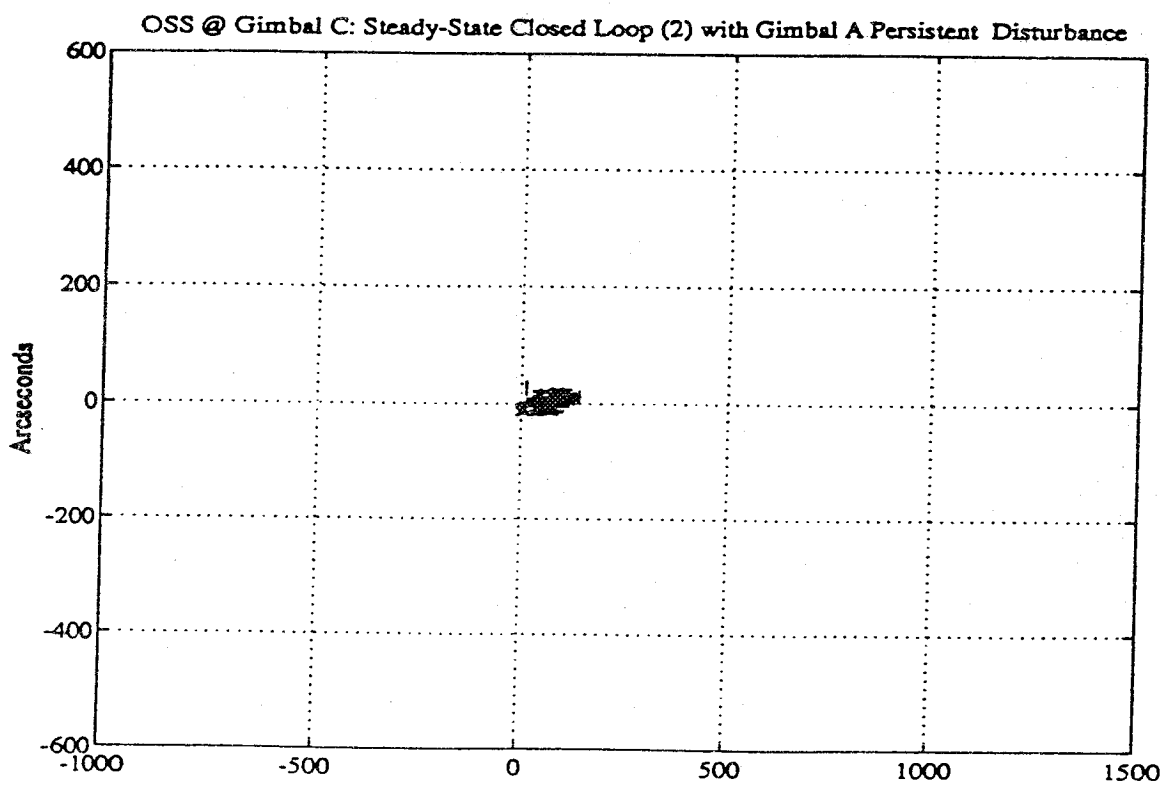
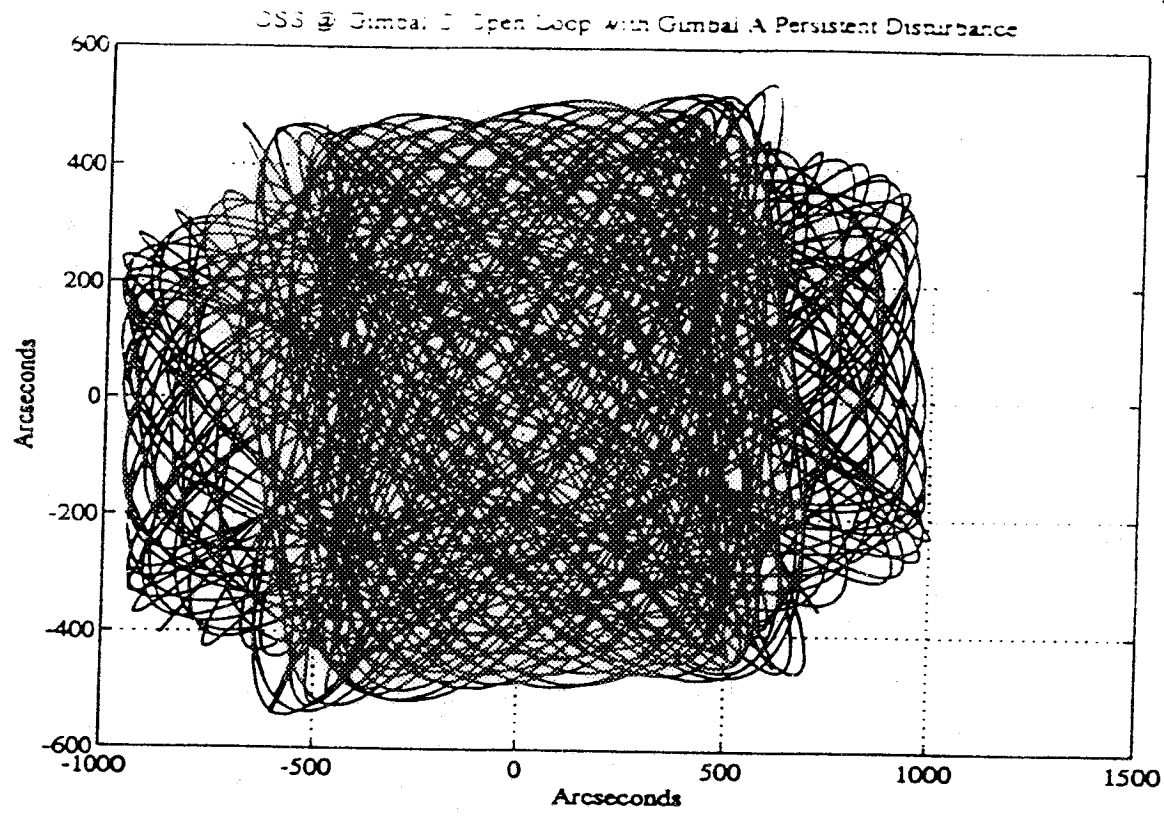


Figure 3-5 Harris CSI Activity Demonstrated High Performance Structural Control on the CEM Testbed

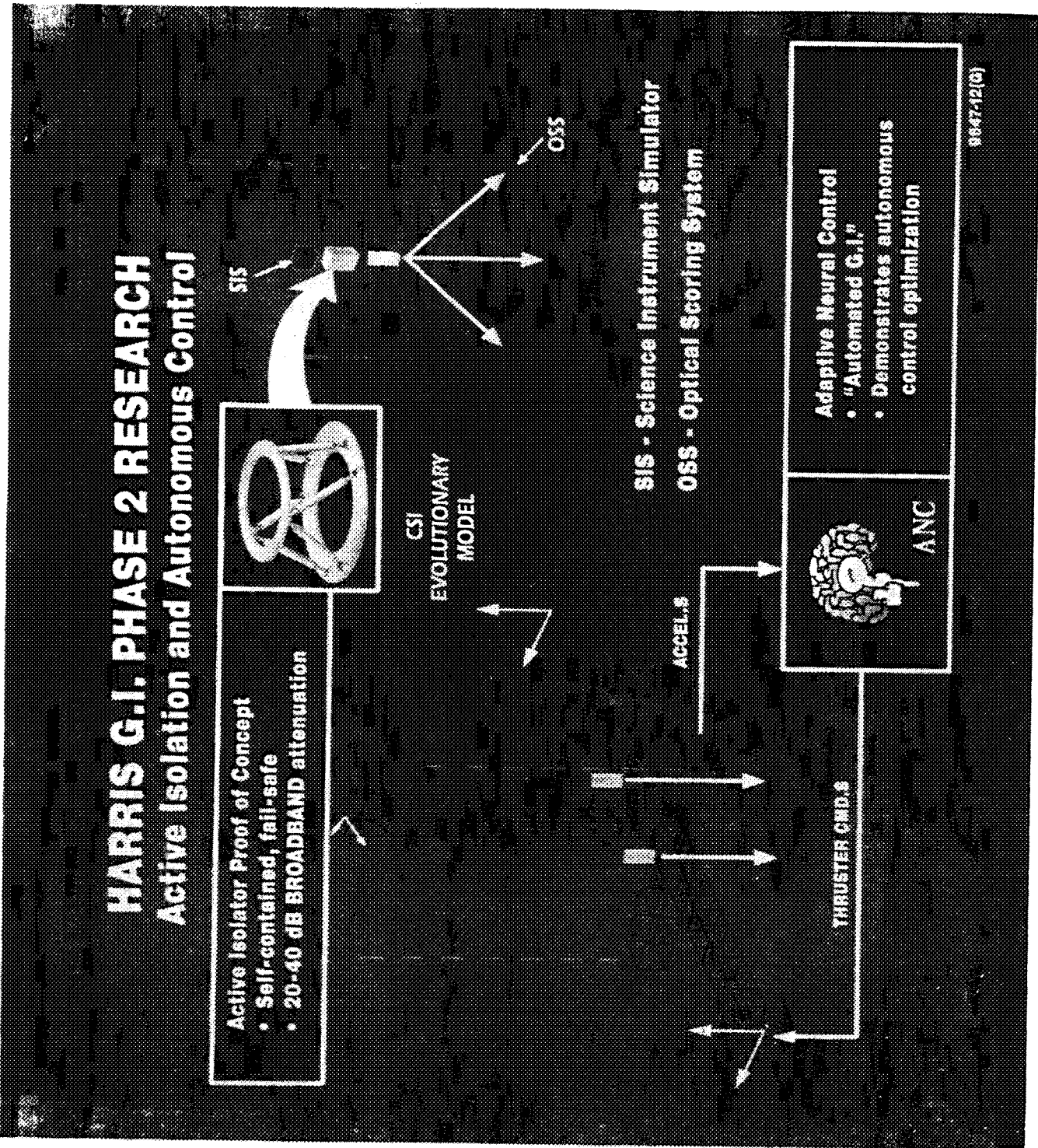


Figure 3-6 Harris GI Phase II Research

on-line, an internal model of the plant and, again on-line, determines and implements an optimal control within a model reference adaptive scheme.

The CEM facility reconfiguration and the scheduling difficulties described above in connection with the fixed-gain controller tests precluded an ANC test session by the Harris team. However, due to long-term collaboration in the ANC area and preparatory technology transfer activities, NASA/LaRC personnel were able to implement and test a basic version of ANC on the Phase 2 CEM, with the algorithms executed by the on-line computer. The excellent experimental results obtained are illustrated in Figure 3-7. After a ten second learning period, the ANC algorithm applies its controller to suppress LOS error of on SIS due to disturbances injected via command inputs to another gimbal package.

The above results show that ANC is practicable and fully achieve the technological objectives of our GI plan. Altogether these results are another excellent example of rapid technology development through NASA/Industry collaboration and technology transfer.

A second novel effort on Phase II of the GI program was to test the Vibration Attenuation Module (VAM). This is a hexapod mount employing a new approach to active vibration isolation. VAMs actively cancel vibration transmission from spacecraft generated disturbances into precision pointing sensors. This is done without reducing the passive stiffness of the equipment mount—thereby permitting both vibration isolation and precision pointing. In bench testing 20–30 dB of isolation over 10 to 200 Hz has been repeatedly demonstrated.

Basically, the VAM is an outgrowth of our entire CSI GI experience and similar experimental work on other testbeds. The totality of the work has shown that, perhaps the most critical element of a structural control design – even more fundamental than the one-line algorithm in establishing the level of achievable performance – is the overall architecture — i.e. the types of actuation and sensing, the basic information patterns, etc. These architectural considerations clearly point to the need for active vibration isolation serving as a key component in the overall vibration suppression strategy. Furthermore, our GI experience directly underscores the importance of simple modular control channels and modular, self-contained architectures. From these insights, a new highly effective isolation approach was developed and then embodied in the self-contained VAM package.

By November, 1993, a VAM unit was fabricated and bench tested within a Harris IR&D program. Figure 3-8 shows a photograph of this unit. In an on-site test session February 22–24, 1994 at NASA/LaRC, the VAM hardware was installed on the new CEM Phase III configuration. As shown in Figure 3-9, the VAM replaces the SIS support truss, connecting the gimballed sensor package with the main CEM structure. Test results illustrated in the right-hand portion of the Figure show excellent broadband isolation performance.

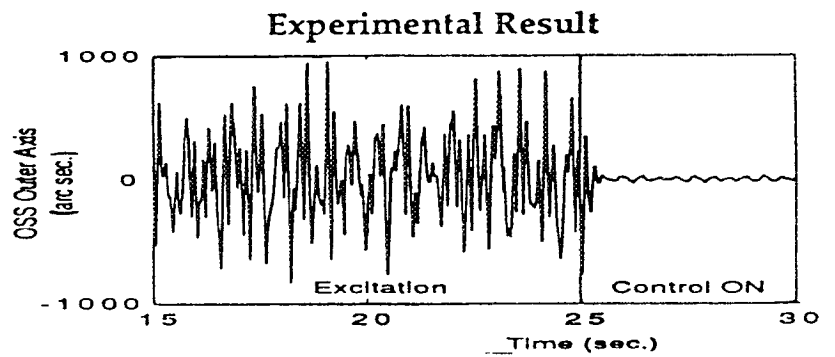
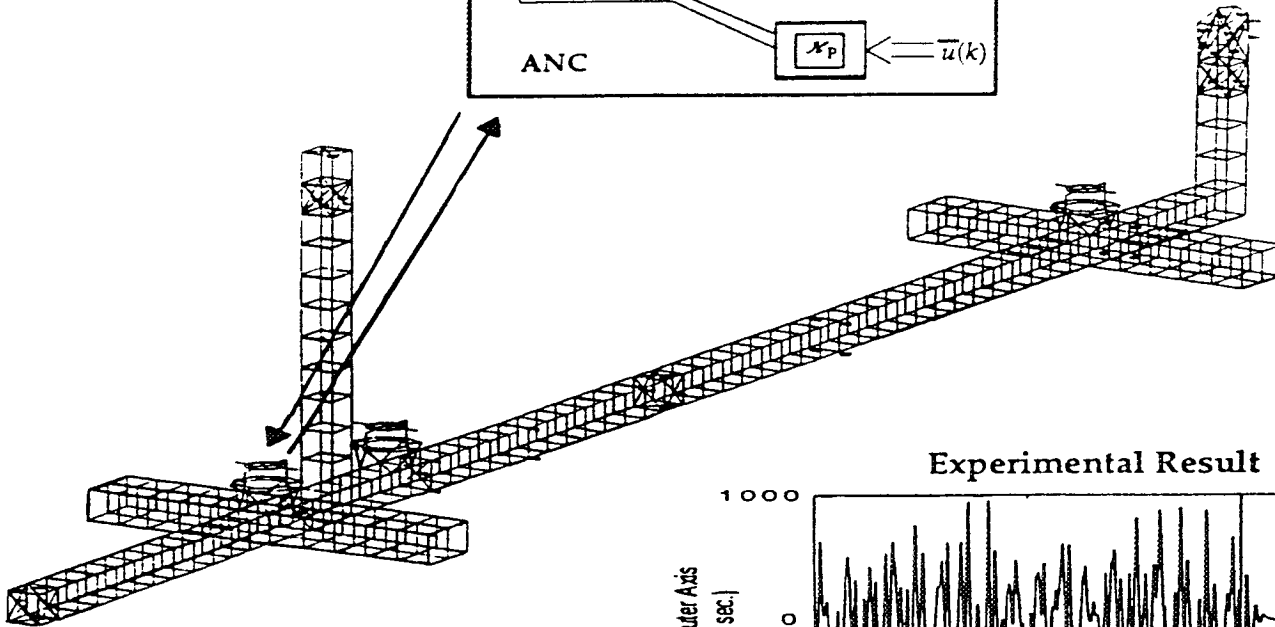
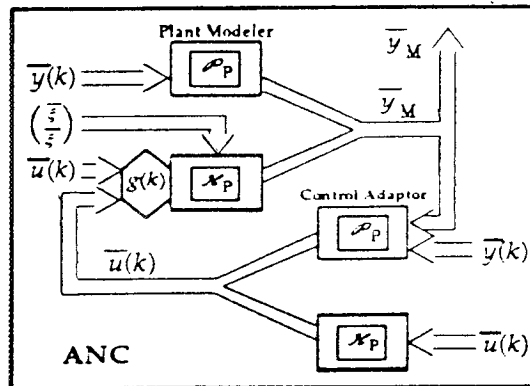


Figure 3-7 In July 1993, NASA/LaRC Personnel Experimentally Demonstrated a Basic ANC System on the NASA/Langley Controls Evolutionary Model

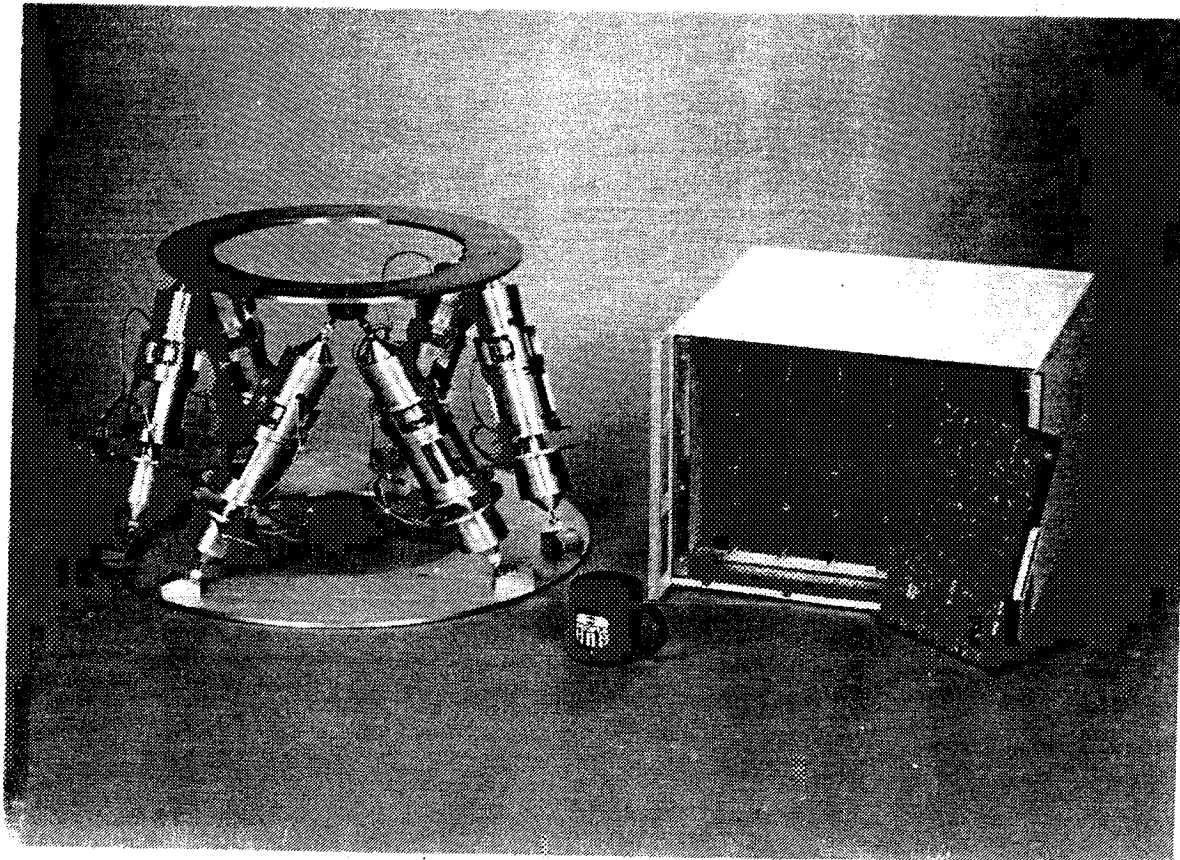
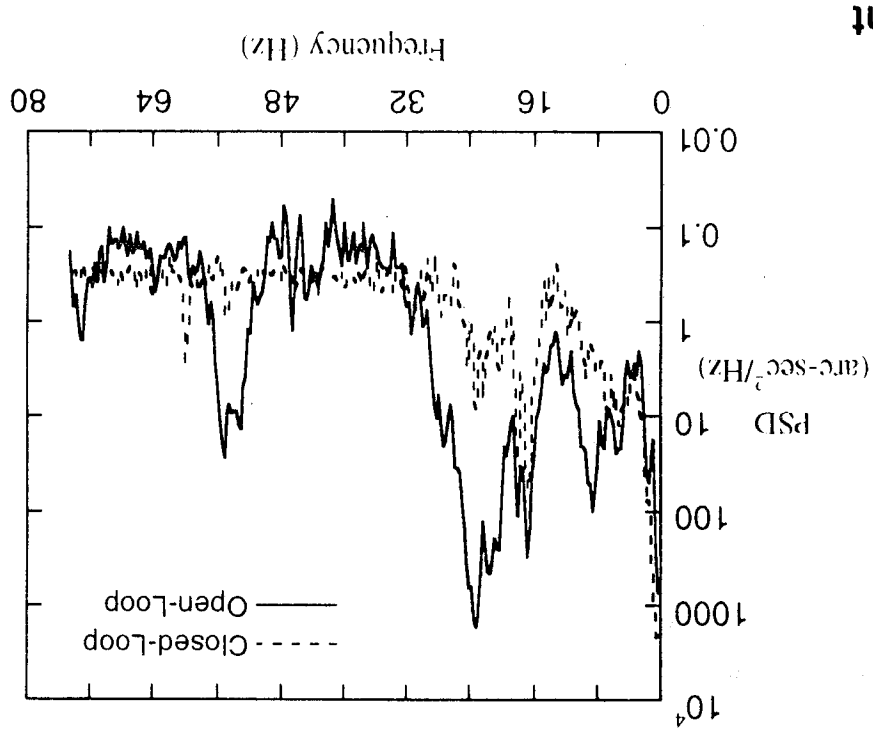
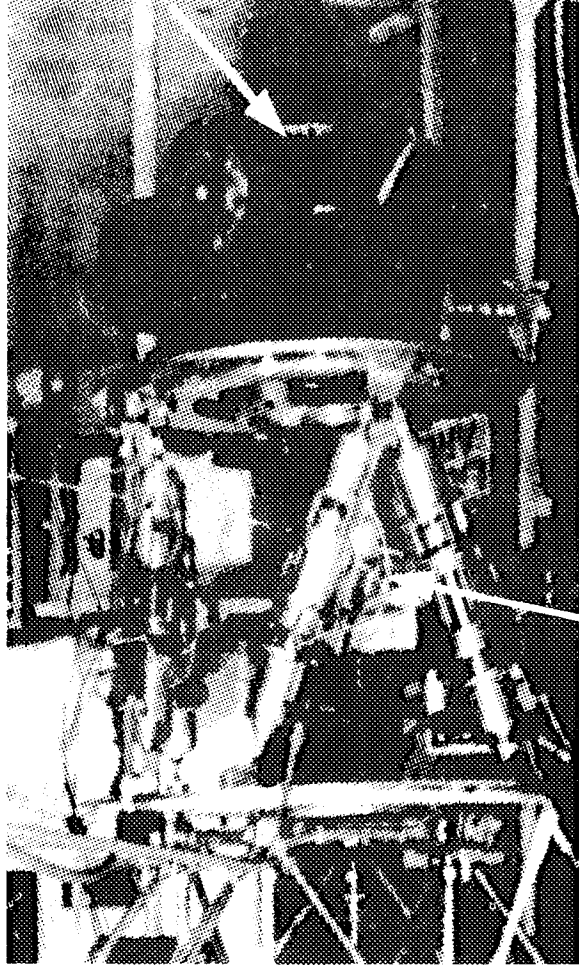


Figure 3-8 VAM Photo

- Random disturbances at SWIR and CERES
- Responses measured at MISR bore-sight



MISR Instrument



VAM

Figure 3-9 Harris' Vibration Attenuation Module (VAM) Successfully Demonstrated on EOS-AM 1 Laboratory Testbed

The VAM effort represents the use of NASA's CSI facilities to help validate self-contained, productized vibration suppression hardware. VAMs and their components have numerous commercial and non-space applications. The success of the VAM effort is a third excellent example of how Industry/Government program coordination and technology transfer result in accelerated development and important technology diversification.

The details of the Phase II activities briefly reviewed above are given in the remainder of the report. The robust fixed-gain control design and test efforts on the CASES and Phase 2 CEM testbeds are described in Section 4. Further details on the Adaptive Neural Control technology are given in Section 5. Finally, Section 6 discusses the Vibration Attenuation Module testing activities.



4. PHASE II — ROBUST, FIXED-GAIN CONTROL DESIGN AND TEST RESULTS

In this Section, we give detailed discussions of the robust fixed-gain control testing activities on both the CASES and CEM-Phase II facilities. The original schedule and the various scheduling changes that became necessary have been described in the preceding Section. The actual schedule of events on Phase II, is given in Table 4.0. As has been noted, a delay in the CASES hardware readiness resulted in the first test session being held in August 1992. A brief follow-up test session was executed in November 1992. Details of the CASES activity are given in Section 4.1.

Modelling and design activities for the CEM testbed began in March 1993 and the single CEM test session was executed in August 1993. The following month, the testbed was reconfigured into the CEM Phase III configuration. Details of the CEM design and test activities are given in Section 4.2.

4.1 Control Design and Test Activities on the CASES Testbed at NASA/MSFC

CASES Facility Description

The Controls and Structures Experiments in Space (CASES) facility, a schematic of which is shown in Figure 4.1-1, is located at MSFC in the high bay area of Building 4619 [32]. CASES emulates the dynamics and CSI issues for a pinhole occulter concept for space-borne astrophysics studies. The test article is vertically suspended from a platform at the 132 foot level. The disturbance system will provide two translation Degrees of Freedom (DOF). A simulated Mission Peculiar Experiment Support Structure (MPESS) interfaces the disturbance system with the test article to simulate a flight experiment interface between the Shuttle, MPESS, and the payload. The CASES test article consists of a 105 foot boom which supports a simulated occulting plate at the boom tip. The control objective is to maintain alignment of the tip plate with the simulated detector at the MPESS. In terms of a flight system, this would allow the occulting plate to point towards a star to perform an X-ray experiment. Control authority is provided by Angular Momentum Exchange Devices (AMEDs), thrusters and a motor.

Referring to Figure 4.1-1, the primary structural component is the 105 foot Solar Array Flight Experiment-I (SAFE-I) boom which has been modified for the CASES facility. The boom has 135 individual bays, weighs about 25 lbs, and retracts into a cannister 72 inches long. The boom has a triangular cross section with 10" sides. The longitudinal members (longerons) are continuous elements composed of a fiberglass composite.

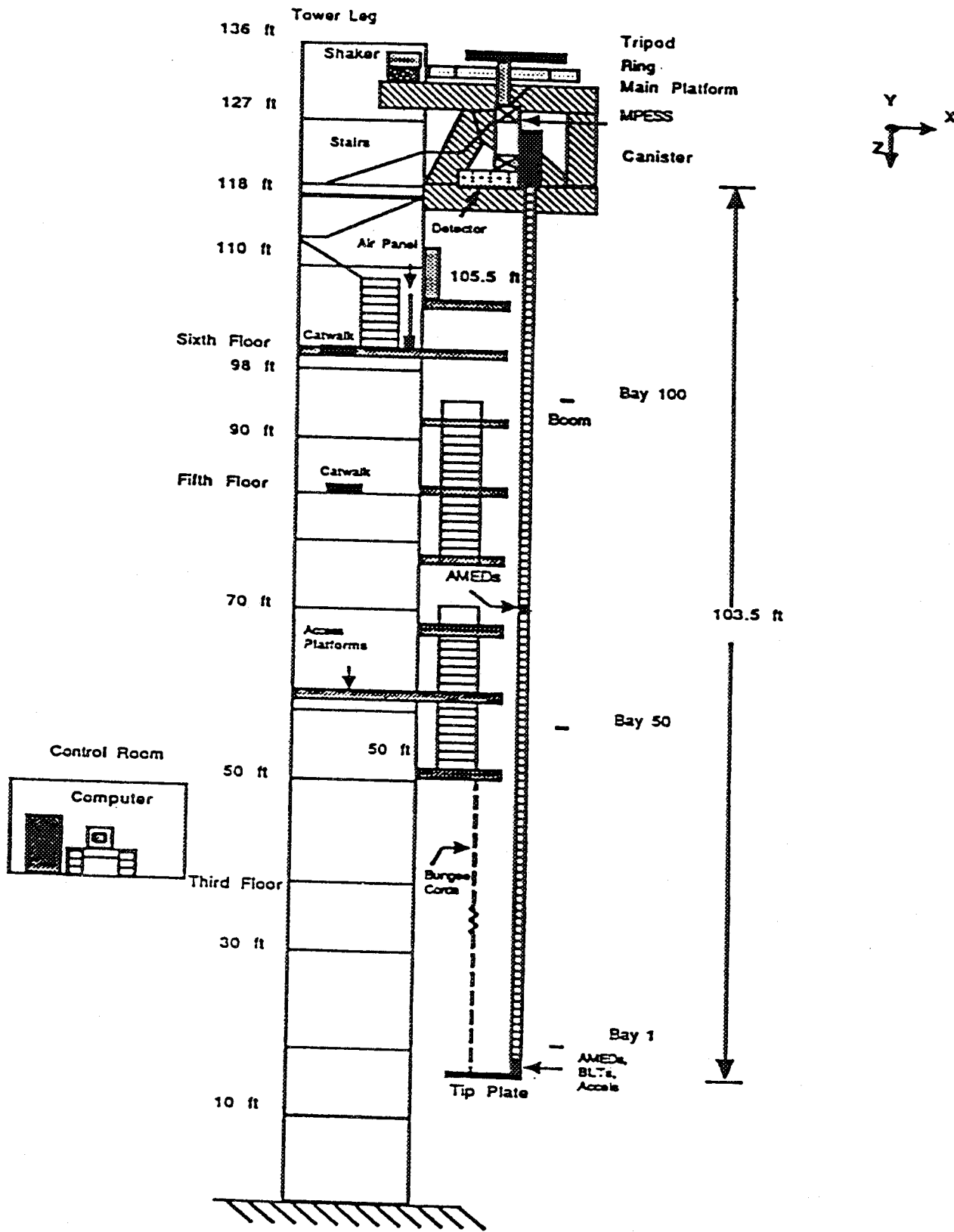


Figure 4.1-1 CASES Ground Test Facility at NASA/MSFC

The simulated MPESS, which emulates the Shuttle/experiment interface, has 4 horizontal bays where each bay is 28" x 28" x 23". The MPESS is connected to the tripod via a 5 ft pipe (16" diameter), a 1" thick aluminum interface plate, and several plates which act as bending and torsional stiffeners.

The tip plate, which simulates an occulting plate, was designed and fabricated by the University of Alabama Aerospace Engineering Department. The plate has four simulated masks, is about 80" x 80" excluding the boom/plate interface device, and weighs about 70 lbs. A simple bungee cord suspension system (bottom of Figure 4.1-1) was designed to off-load the tip plate.

The disturbance system provides two translational degrees of freedom at the base of the experiment (top of Figure 4.1-1). Disturbances are provided via two orthogonal shakers which translate an air-supported tripod to which the test article is attached. The tripod supports the experiment (boom) through the simulated MPESS. Each shaker (Unholtz-Dickie Model 6) provides 1000 lbs peak sine force with a ± 3 inch stroke and a 1000 Hz bandwidth. A Linear Motion System (LMS) interfaces each shaker with the tripod to allow for low-friction motion in two directions simultaneously.

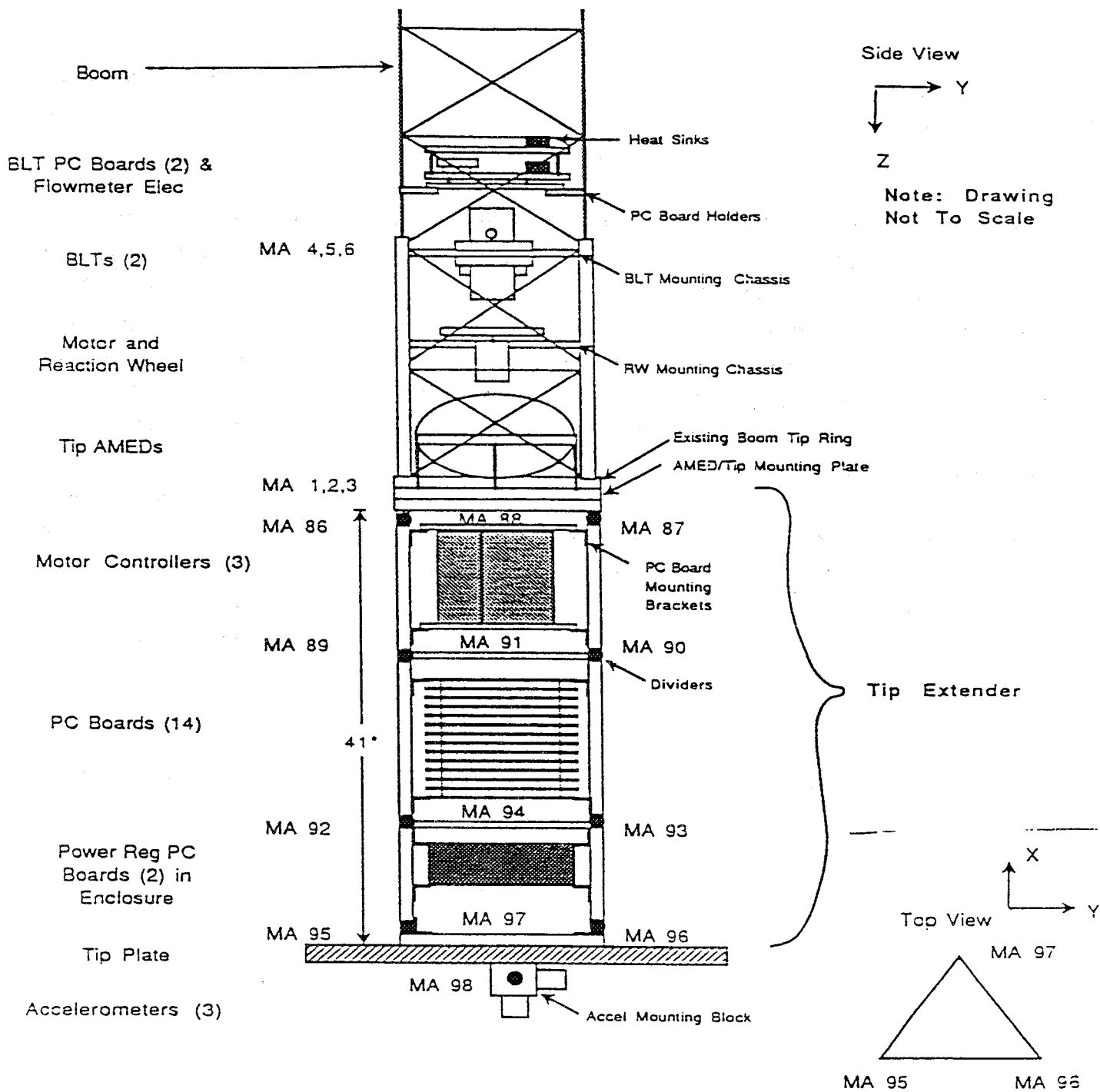
The control actuation system consists of two single-axis AMEDs at a mid-length position on the boom, two or three single-axis AMEDs at the boom tip and two single-axis thrusters at the boom tip. (See Figure 4.1-2).

The AMEDs are used for vibration suppression at a mid-point and at the tip of the boom. The midlength AMED package consists of two motors attached to reaction wheels and two 2-axis gyros. The tip AMED package has two motors with reaction wheels and two 2-axis gyros. Each housed motor weighs 14 oz. and has peak rated torque of 290 oz-in.

Two orthogonal thrusters are provided for vibration suppression. It should be noted that vibration suppression of the low frequency modes (0.15 Hz) is somewhat comparable to pointing control. The Boeing thrusters are bidirectional, linear, cold gas thrusters with a force capability of ± 2 lbs up to about 10 Hz. Each thruster weighs about 4 lbs. The linearity of the thruster forces makes the control design easier than in the case where on/off thrusters are used as control actuators.

The measurement system consists of angular velocity and acceleration sensors at the base, boom angular velocity sensors in the mid-length and tip AMED packages, tip acceleration sensors, and a Tip Displacement Sensor (TDS). Auxiliary measurements include reaction wheel speed, AMED motor current, and fault indicators.

The TDS is an optical sensor which provides two translational measurements at each of four target locations on the tip plate. The TDS is composed of two linear Charge Coupled Device (CCD) detectors, each having an optical lens system and signal processing to provide



Note: Five holes exist on the tip plate for boom tip mounting
 Two holes must be drilled to mount accels
 Holes may need to be drilled to mount tip extender

Figure 4.1-2 Boom Tip: Side View

subpixel accuracy. The two detectors are located on the MPSS and the four active laser diodes serve as targets on the tip. The TDS provides 2 translational degrees-of-freedom for 4 targets at a rate of up to 500 Hz with an accuracy of 0.01".

Preparatory Activities: Implementation of Streamlined Modelling and Design Tools

As noted above, the first CASES test session had to be postponed for approximately eight months owing to unforeseen test facility hardware integration delays. When the possibility of significant delay became apparent it was clear that a greatly compressed modelling, design and test schedule would have to be implemented. Consequently, some initial efforts were devoted to the development and integration of streamlined tools for system identification and OPUS control design in the hope these would permit faster design turnaround once the CASES hardware became ready for testing.

The first candidate for streamlined operations was the area of system modelling for control design. Due to the labor and time generally required for the development and refinement of finite element models (FEMs), we decided during Phase I to extract system models directly from test data using the Eigensystem Realization Algorithm (ERA). Because of the test facility readiness delay noted above, there remained virtually no time to develop system models via FEM's that could be corrected with test data. Thus use of ERA was the only tenable option.

To prepare for a very rapid modelling and design exercise we first obtained the MATLAB toolbox "System/Observer/Controller Identification Toolbox" [33] developed by LaRC researchers to implement more efficient versions of ERA. To ensure that our GI team could use this toolbox quickly and effectively, we exercised it on numerous test cases—both analytical examples and in-house testbeds. In the process, a practical methodology was worked out for rapid system ID, as reported in [34]. We provided crucial demonstration of the ERA application process on the Harris Multi-Hex Prototype Experiment (MHPE) [35]. Without prior preparation, a 60 state model of the MHPE with six inputs and six outputs was derived from test data in a single afternoon! As evidenced by Figure 4.1-3 the frequency responses of the ERA model closely matched those derived directly from the test data.

The above identification process uses the ERA/DC algorithm. However, we also incorporated the use of the Observer/Kalman Filter Identification (OKID) [33] algorithm that allows simultaneous system identification and Kalman filter design. The successful use of this algorithm further integrates the identification and control design process, leading to further streamlining of the overall design process.

Seeking similar improvement in the control design process, Harris implemented in a MATLAB environment a new class of homotopy algorithms [36, 37]. These algorithms allow the

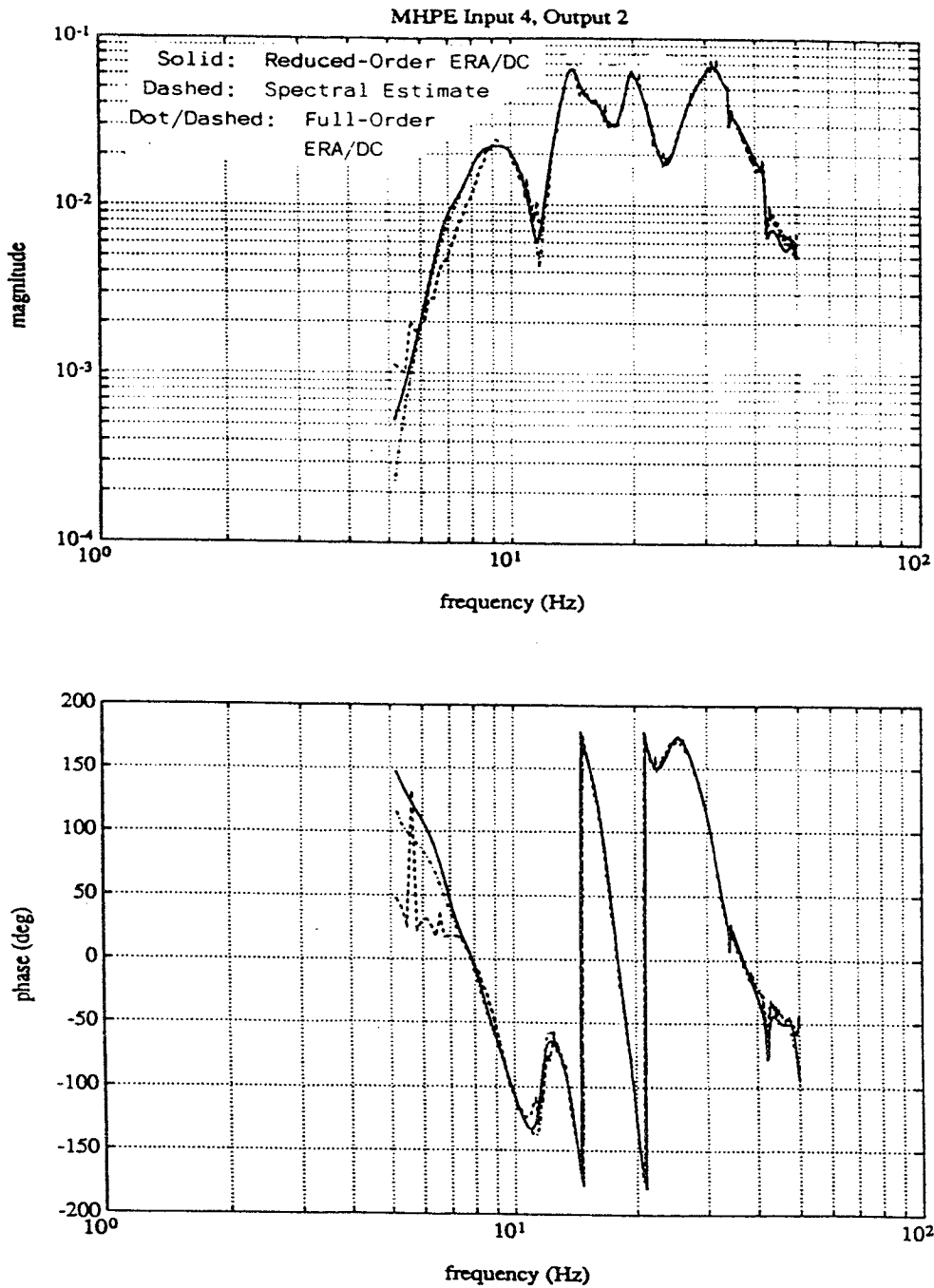


Figure 4.1-3 The Frequency Responses of the Full-Order (148 States) and Reduced-Order (60 States) ERA Models of the MHPE Obtained in One Afternoon Closely Resemble the Frequency Response Derived Directly from Test Data

design of robust and reduced-order controllers for both continuous-time and discrete-time systems. The speed of these algorithms are vastly superior to the speed of the previous homotopy algorithms. In addition, their convergence is not dependent on finding initial conditions that are close to the desired answer. This global convergence property allows the reliable design of robust, reduced-order controllers.

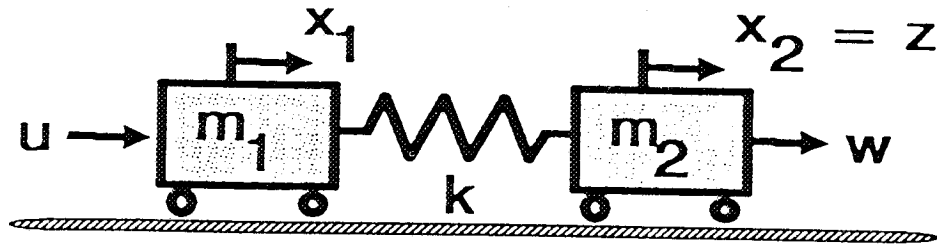
In addition, Harris has demonstrated novel algorithms for robustness analysis. State space, Popov analysis was applied to a benchmark problem [38] and, as illustrated by Figure 4.1-4 was shown to give much less conservative results than the small-gain and positivity test. In fact, for this example Popov analysis was completely nonconservative. In addition, a new majorant analysis technique [39] has been developed and implemented at Harris that allows the development of frequency domain performance bounds for positive real systems. These new bounds are less conservative than previous methods. User friendly MATLAB packages were developed to allow the implementation of Popov and majorant analyses.

With the above improvements in place, it was apparent that our incremental design\test methodology which normally entailed three test sessions alternating with in-house analysis and design efforts could be considerably compressed. For example, the new faster tools would allow one to perform open-loop testing, extract an accurate model, determine an initial robust control design and then test the design—all in the first test session. Thus one test session can achieve the results that previously required two sessions and an interim period of analysis.

CASES Test Session 1

The CASES facility was integrated and operational just prior to the Harris team's test session scheduled for August 3-7, 1992. At this point, the finite element model was not yet correlated with open-loop test data. Open-loop data was provided for the frequency band 1 to 20 Hz. However, the dominant modes of the structure are all below 1 Hz. In the absence of accurate modelling information for the bandwidth of interest, this was a good opportunity to try our compressed "on-site" design methodology using the streamlined tools and procedures described above.

Our initial control strategy, based on the overall testbed set up was to use the collocated AMED-GYRO loops to augment the beam damping then close the Thruster-LOS Detector loops to enable the laser to track the detector. In preparation, four "template" control designs were devised based on the extremely preliminary modelling information at hand. The initial test plan was to (a) perform open-loop tests to characterize performance and to execute system ID, (b) perform closed-loop tests with simple, robust controllers designed on site (so as to gain insight into strategies to be used for more advanced designs) and (c) perform closed-loop ID and generate and test more advanced designs for improved performance.



uncertain stiffness k
 $k = k_0 + \Delta k$

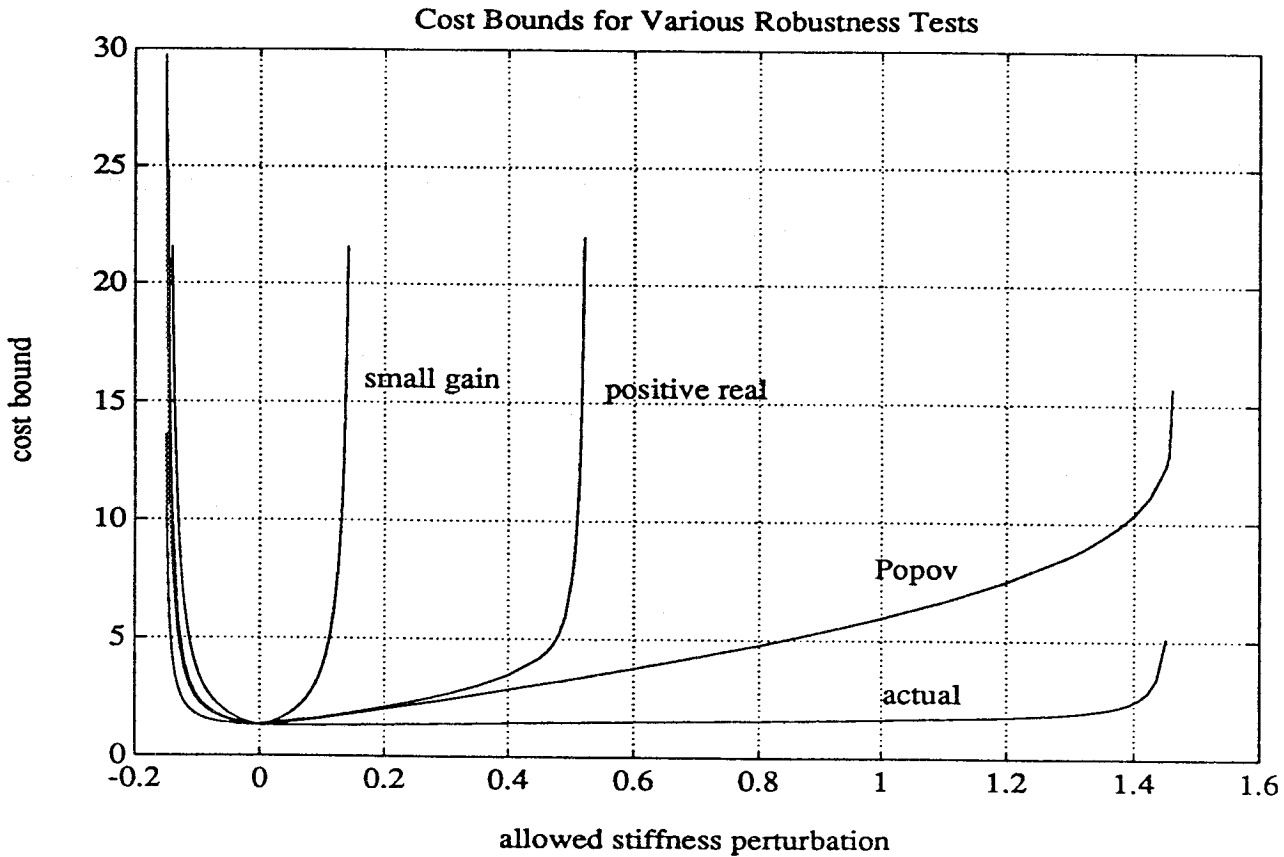


Figure 4.1-4 For a Benchmark Problem State Space Popov Analysis Significantly out Performed Other Robustness Tests, Yielding Completely Non-Conservative Robust Stability Results and Vastly Improved Robust Performance Bounds.

From the initial open-loop tests a good model of the dynamics below 1 Hz was obtained. Performance (LOS error as measured by the detector) due to pulse disturbances from the base disturbance system was seen to be dominated by the first bending modes near 0.1 Hz. In addition, previously unknown ultra-low frequency oscillation was observed near 0.01 Hz. This was apparently associated with the bungee-cord tip plate suspension system. Furthermore the first torsion mode was found to be highly coupled with the lowest bending modes. Finally, the open-loop behavior made it evident that the torque output of the AMEDs was insufficient for satisfactory control authority over the bending modes. Thruster-Detector loops were deemed more satisfactory for this purpose.

In response to the above observations the pre-test "template" controllers were not considered appropriate and were not tried. Instead, two new controllers (labelled controllers "5" and "6") were devised having the following architectures:

- Controller "5":**
- (1) Close MC5-TGZ* loops to attenuate the first torsion mode (as in Mini-MAST)
 - (2) Close Thruster-Detector loops to attenuate the first bending modes
- Controller "6":** To the setup of controller 5, add MC3-TGY, MC4-TGX loops to attenuate higher bending modes.

These controllers were designed on-site then tested. Figure 4.1-5 shows the y-axis tip displacement due to a base excitation pulse for the open-loop system and for the closed-loop system with controller 5. As indicated in this plot open-loop vibration of the dominant 0.1 Hz bending mode persists for a very long time. Also evident is the very low frequency "bungee-cord" mode. Controller 5 succeeds in suppressing the dominant modes in approximately one cycle. Although a higher frequency bending mode is apparent in the closed-loop response, this mode is observed because it is excited initially by the pulse disturbance, not because it is amplified by the controller. These 0.6 Hz modes are essentially outside the bandwidth of controller 5.

Controller 6 adds AMED-rate gyro loops in order to augment the damping of the 0.6 Hz modes. Figure 4.1-6 shows open-and closed-loop responses for the same excitation conditions as Figure 4.1-5. The results are very nearly the same as for controller 5 and little attenuation of the higher bending modes is observed.

* MC = Motor Controller (AMEDs)
BLT = Base Linear Thruster
TG = Tip Gyro

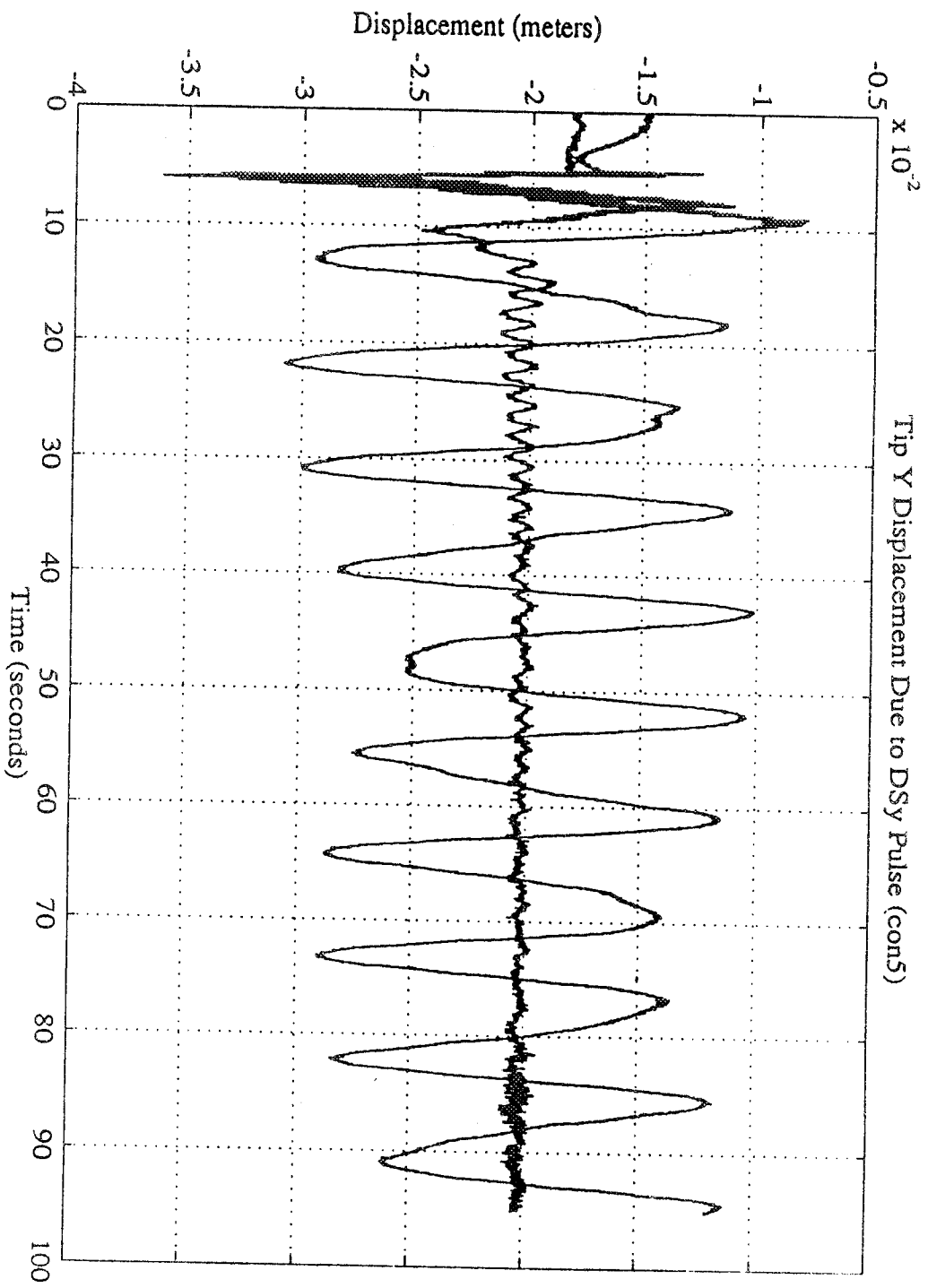


Figure 4.1-5 TIP Y Displacement Due to DSy Pulse (con5)

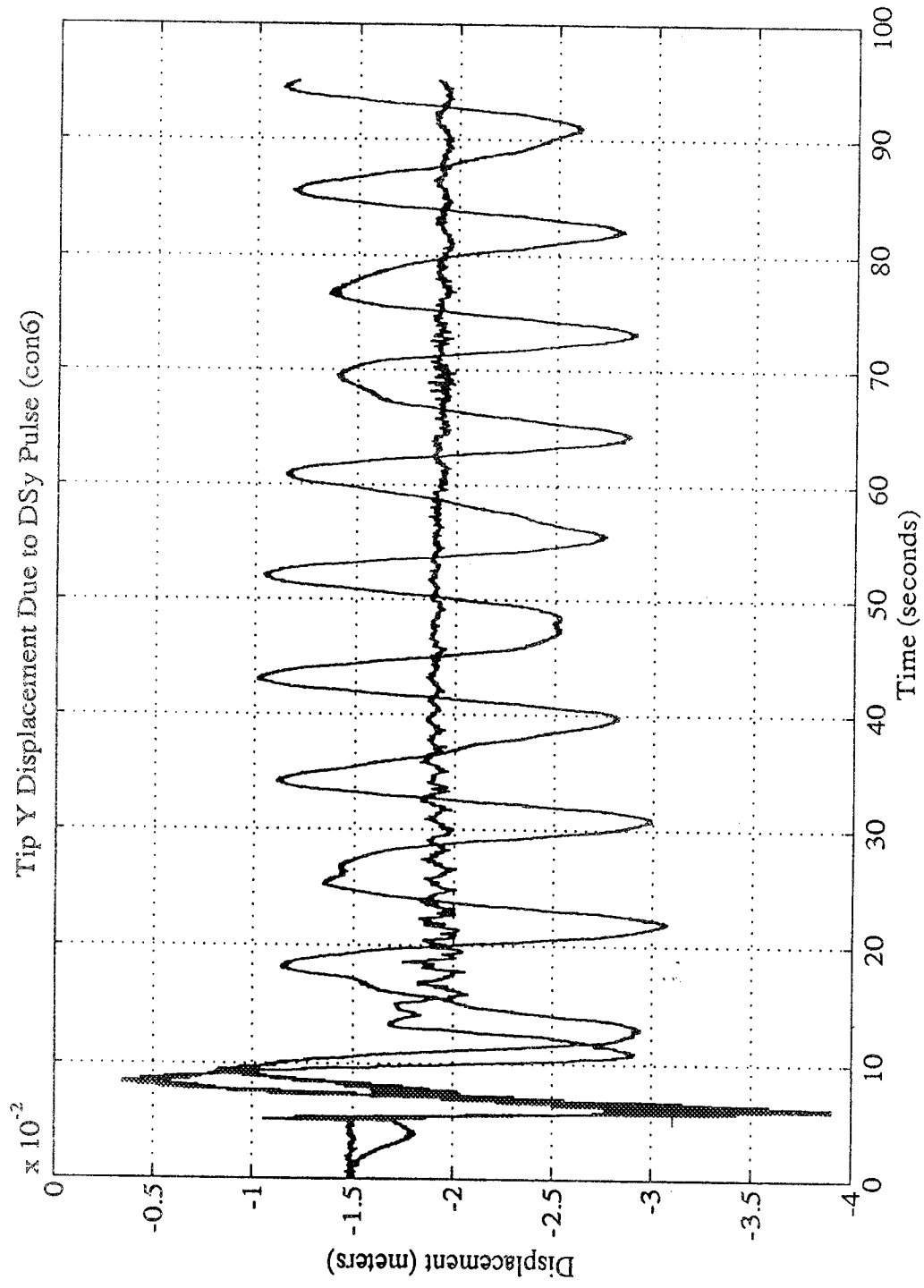


Figure 4.1-6 Tip Y Displacement Due to DSy Pulse (con6)

The lack of improvement in controller 6 for the 0.6 Hz modes was due to poor modelling information leading to insufficient control gain at 0.6 Hz. It was hoped that the needed information would be provided by the planned closed-loop system ID tests. However, it was noted from the results that the dynamic range of the Detector (~ 40dB) prevents tests using constant amplitude excitation of the thrusters from being effective for the identification of modes beyond the first bending modes. Figure 4.1-7 sketches the situation. Essentially the system response is below the "noise floor" at higher frequencies, so modal dynamics near 0.6 Hz could not be identified. At this point, it was too late to repeat the closed-loop ID tests and the GI team could not finalize the thruster-detector loop controllers during this test session.

The first CASES test session made significant progress toward the ultimate goal of a single-session design/test capability. As summarized in Figure 4.1-8, results normally requiring two test sessions in our incremental methodology were achieved in one session. Furthermore, as in the case of Mini-MAST, the controller succeeded in damping the dominant lowest bending modes within one cycle. However, although this was tried, we could not wrap up the design process in a single session and attain high gain control of the second order bending modes. Hence, we planned an off-site closed-loop identification (based on additional ID tests to be performed by NASA/MSFC personnel) followed by an advanced control design and a second test session.

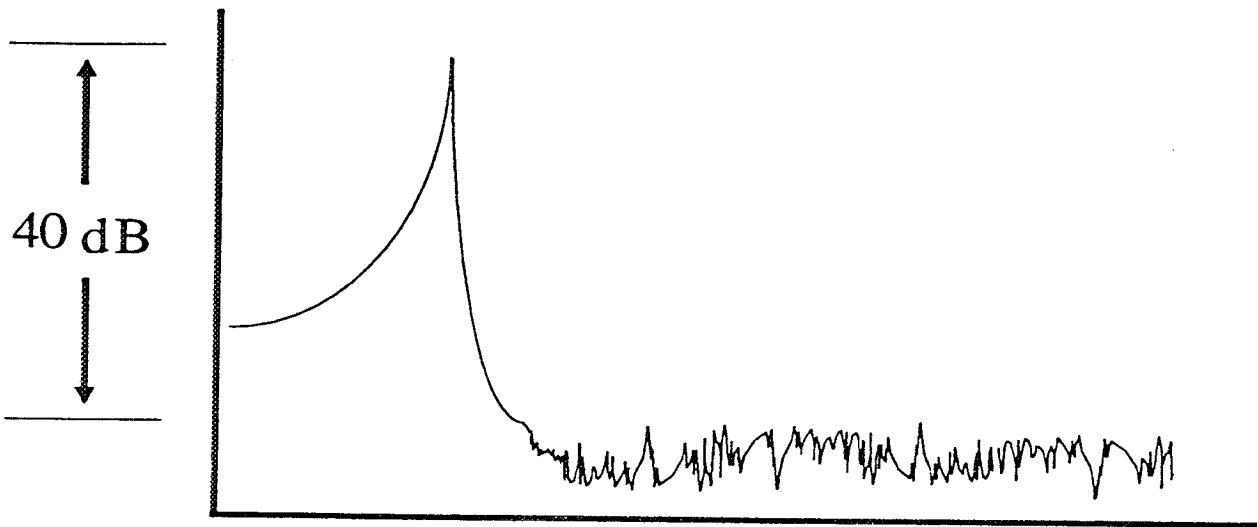
The above plan was carried out despite the fact that, shortly after the first test session, it was determined that MSFC's CSI activity and the testbed support would soon be terminated. The off-site modelling and design activity was accelerated and a second test session was held in late November 1992.

Refined Designs and Second Test Session

Subsequent to the first test session, analysis was performed to determine how the performance of the initially tested controllers could be improved. It became evident that the bending mode control requires higher bandwidth in order to attenuate the higher order bending modes and achieve greater attenuation of the lowest bending modes. This improvement can be accomplished by using the Thruster-Gyro loops to control bending modes since these modes are more strongly observable from the gyros. Also the thrusters are the only actuators with sufficient authority to significantly improve bending mode control.

Having formulated the above strategy, we first determined refined state-space models using the Harris methodology for applying ERA/DC to the first test session data. Using the refined model, we designed LQG controllers for precompensated Single Input, Single Output (SISO) plants (for the BLTx-TGy and BLTy-TGx loops) and then applied Maximum Entropy

Dynamic Range of Detector (~ 40 dB) prevents tests using constant amplitude excitation of thrusters from being effective for ID of modes past 1st bending



Too late to repeat tests, so unable to improve upon performance of simple controllers for Thruster-Detector loops

Figure 4.1-7 Initial ID Results (Still in Huntsville)

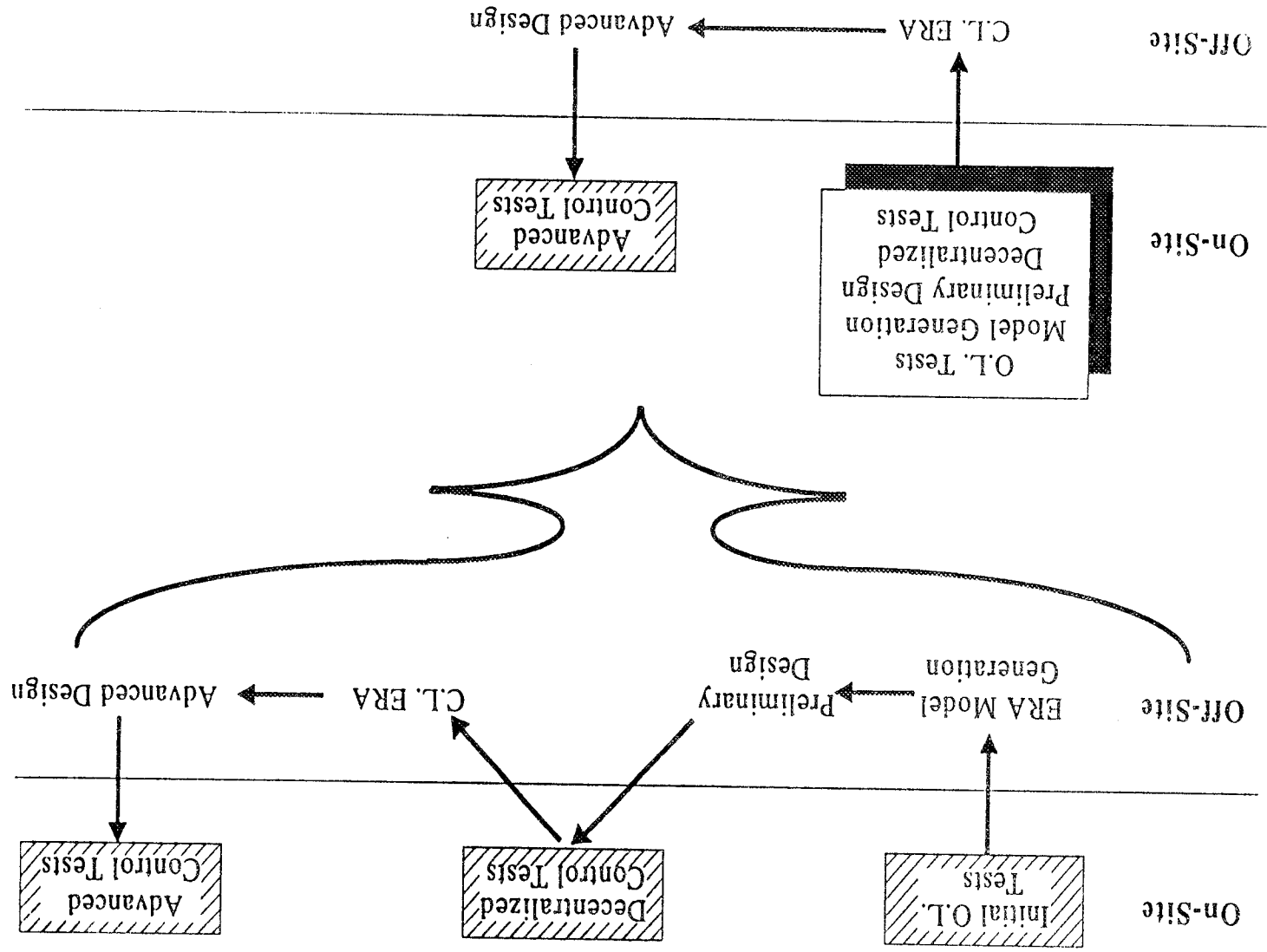


Figure 4.1-8 As an Intermediate Step Toward the Ultimate Goal in Streamlining, We Accelerate the CASES Design Process so as to Demonstrate Advanced Design in Two Test Sessions (the First Session has been Completed)

design to reduce model error sensitivity, where appropriate. Finally, the order of the full order dynamic compensators were reduced via balancing to arrive at low order, more conveniently implementable controllers.

Two candidate controllers were obtained through the above procedure:

Controller 1: Uses the same MC5-TGZ design (to control the torsional mode) tested on site, coupled with BLTx-TGy, BLTy-TGx compensators. The total number of states of this controller is 18.

Controller 2: Identical to controller 1 except that first order high pass filters (0.03 Hz corner frequency) are added to the thruster loops. This was done to provide added stability margin in the event that controller 1 somehow excites the ultra-low-frequency behavior that is not precisely characterized.

Figure 4.1-9 shows the compensator magnitude plot and Figure 4.1-10 shows the corresponding loop transfer function for the controller 1 BLTx-TGy loop. The compensator maintains high gain out to the higher order bending mode near 0.6 Hz then rolls off, beginning roughly at 1.5 Hz. Characteristics of the BLTy-TGx compensator are similar. Figures 4.1-11 and 4.1-12 show corresponding results for Controller 2. The impact of the high pass filter is evident at the low frequency region in Figure 4.1-11.

The above controllers were tested in late November, 1992. At the start of this test session, it was found that high pass filters were needed on the Z-axis gyro output because the gyro biases were not removed from the measurements. The required high pass filters were added to the MC5-TGZ loop on-site.

With the above modification, the new controllers were tested. Test results showed improved performance on the higher frequency modes but the new designs sacrificed some performance on the lowest bending modes, relative to controller 5 of the first test session. This is illustrated in Figure 4.1-13 which shows the X-axis tip displacement time histories for controller 2 of the second test session (part (a)) and for controller 6 of the first test session in response to an impulsive base disturbance input. In both plots, the open-loop response is superimposed. Whereas, the earlier controller (Figure 4.1-13.b) damped the primary bending modes in a single cycle but did not suppress the higher bending modes, the revised controller (Figure 4.1-13.a) added damping to the higher modes but damped the primary modes in approximately three cycles. The behavior of the revised controller can be attributed to reduced loop gain at the primary mode frequencies due to the use of gyros instead of detectors, and had time permitted this would have been easily rectified. On the whole the results show that the best type of controller would be a hybrid of the first and second session designs, involving the feedback of both gyros and detector measurements to both thrusters and AMED's at the tip. However, since the NASA/MSFC CSI activity had already been discontinued there was no opportunity to further refine the design.

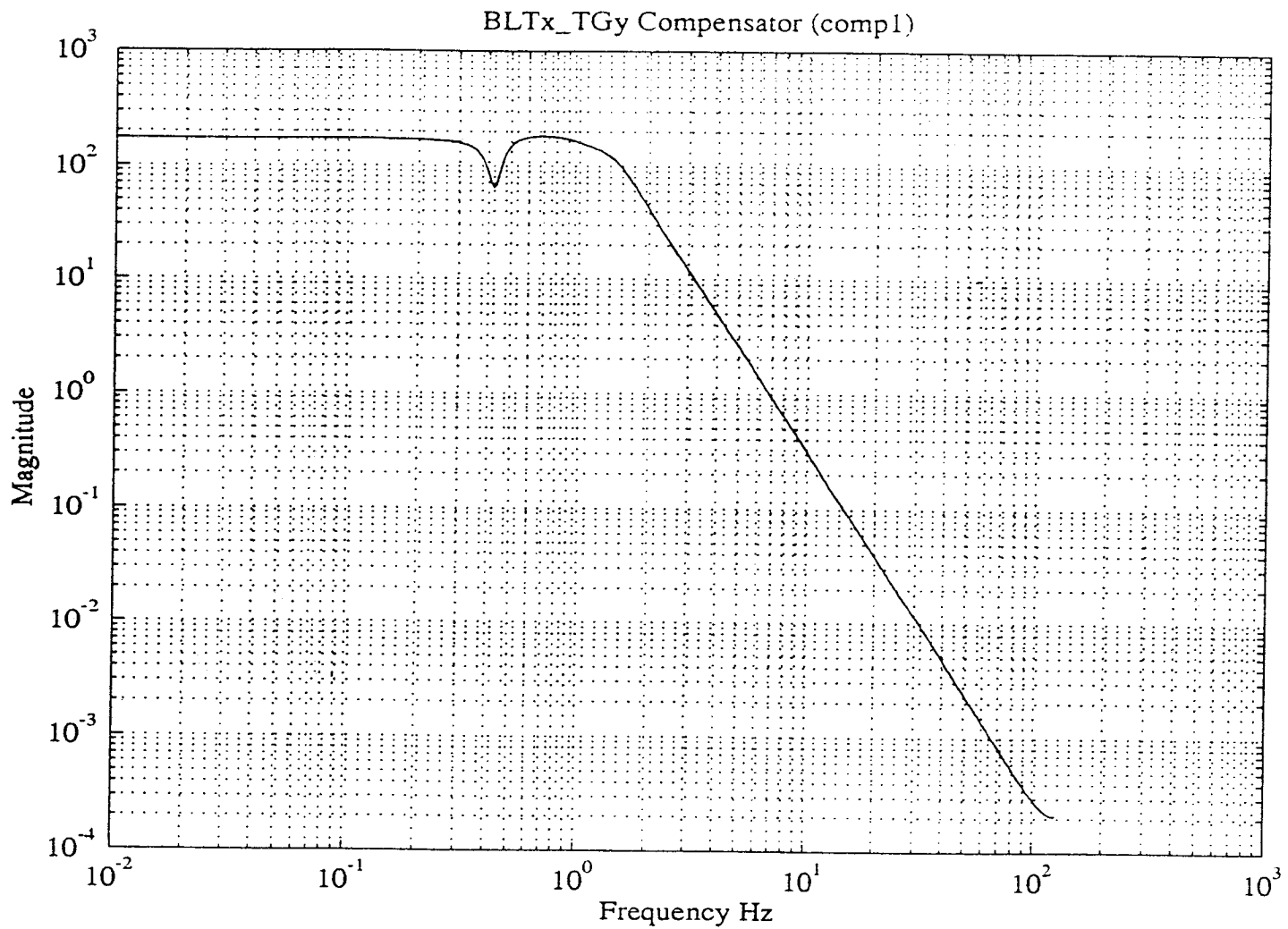


Figure 4.1-9 Compensator Magnitude Plot for Refined Controller 1, BLTx-TGy Loop

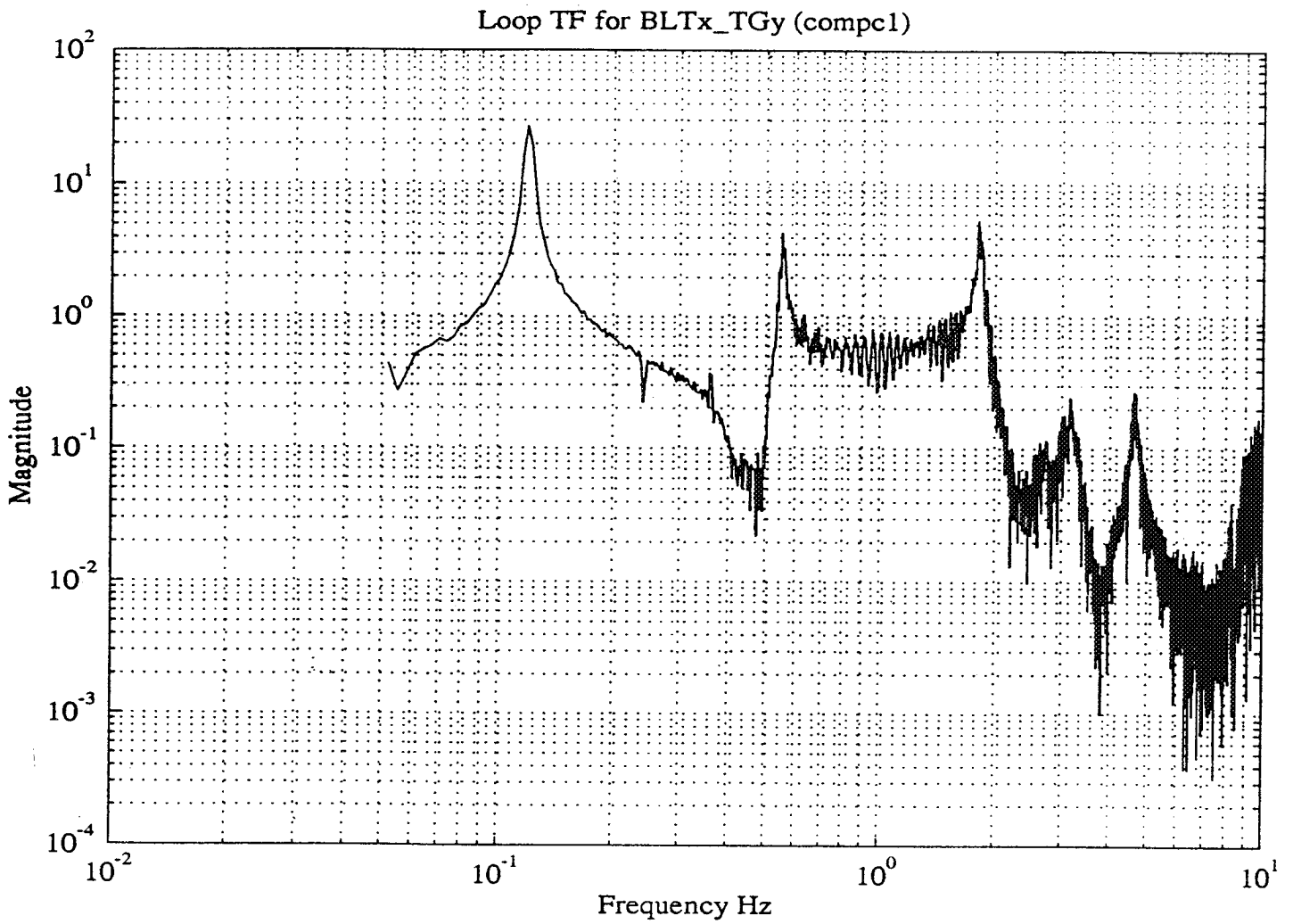


Figure 4.1-10 Open-Loop Transfer Function Magnitude Plot for Refined Controller 1, BLTx-TGy Loop

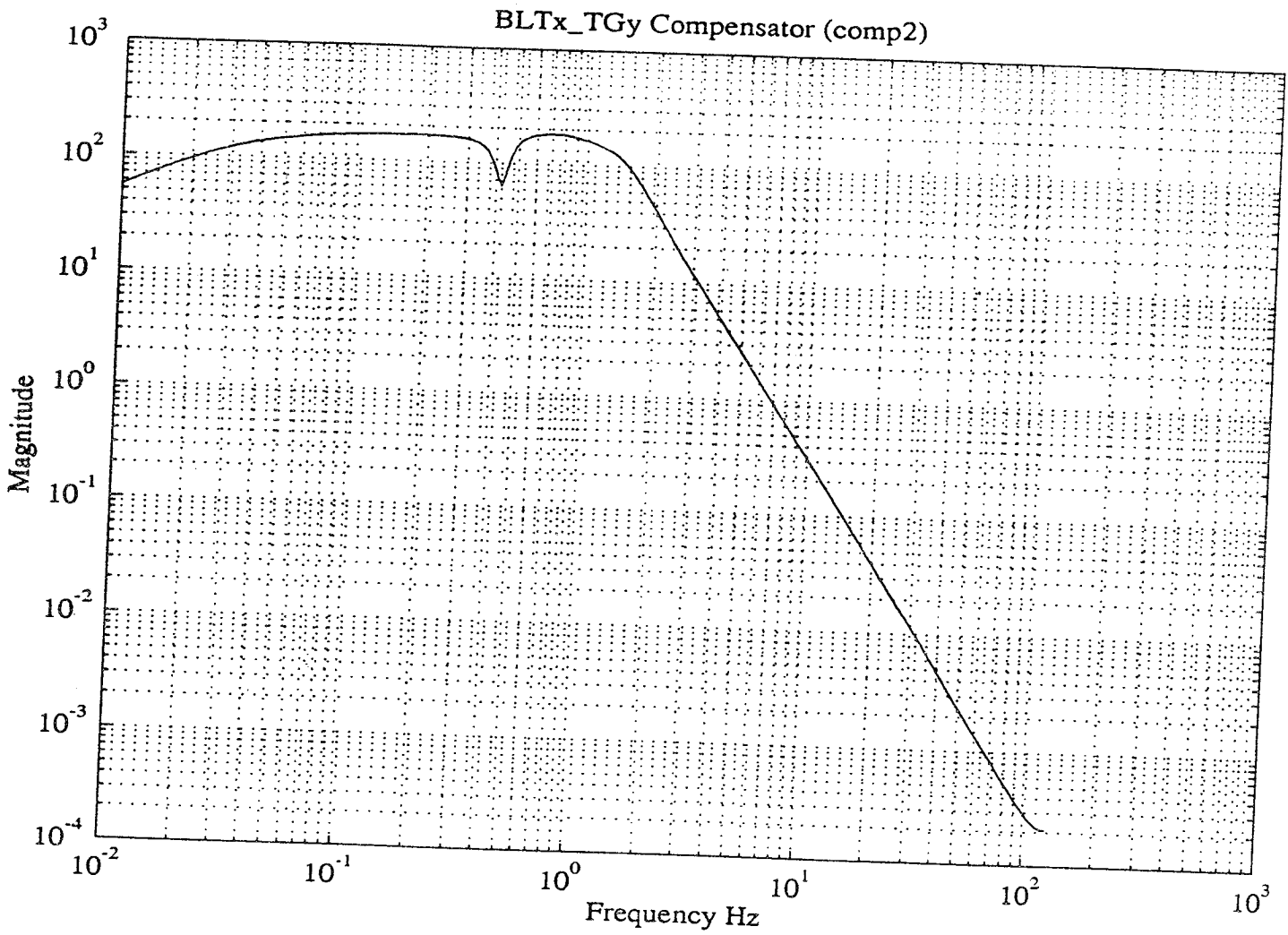


Figure 4.1-11 Compensator Magnitude Plot for Refined Controller 2, BLTx-TGy Loop

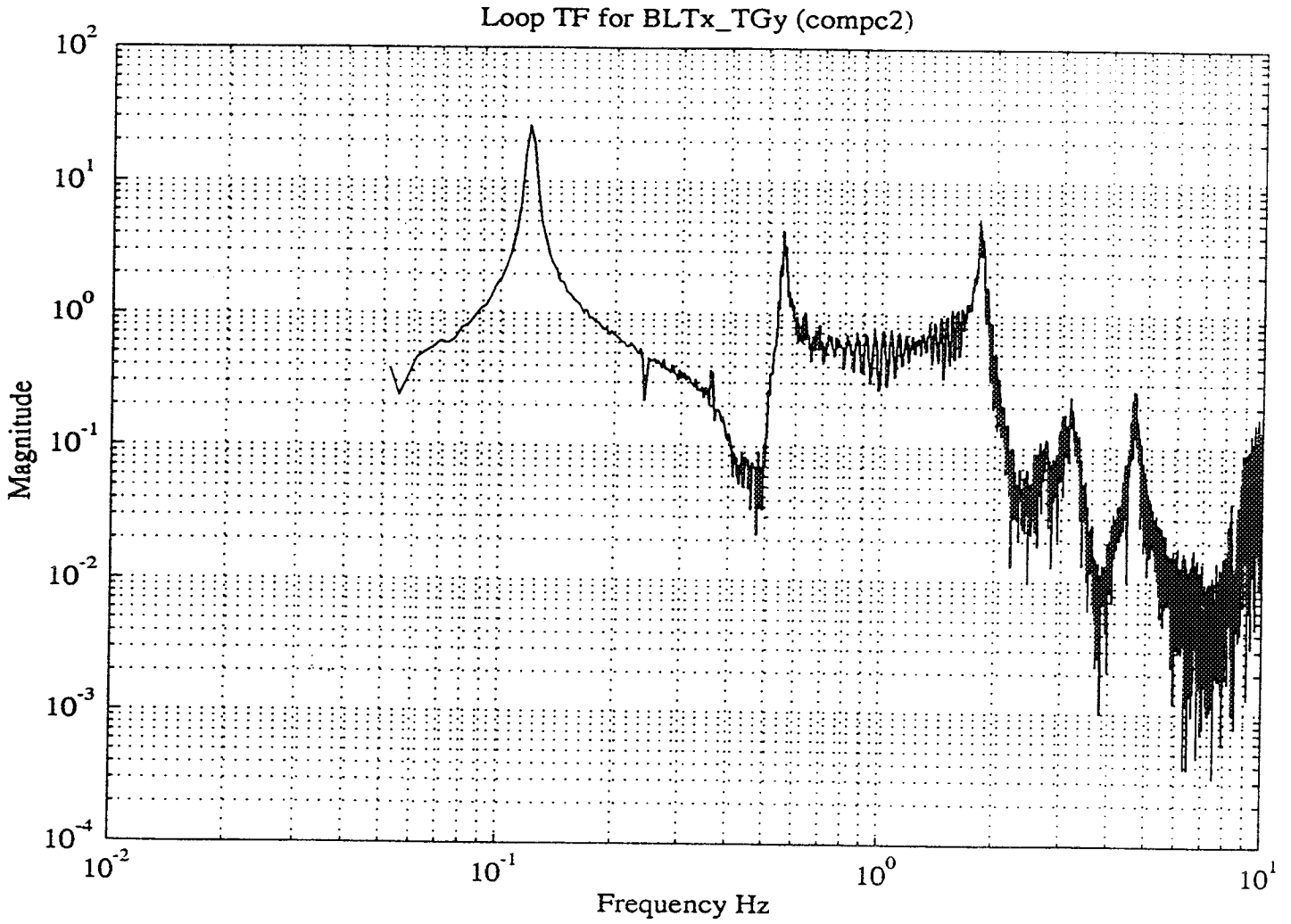


Figure 4.1-12 Open-Loop Transfer Function Magnitude Plot for Refined Controller 2, BLTx-TGy Loop

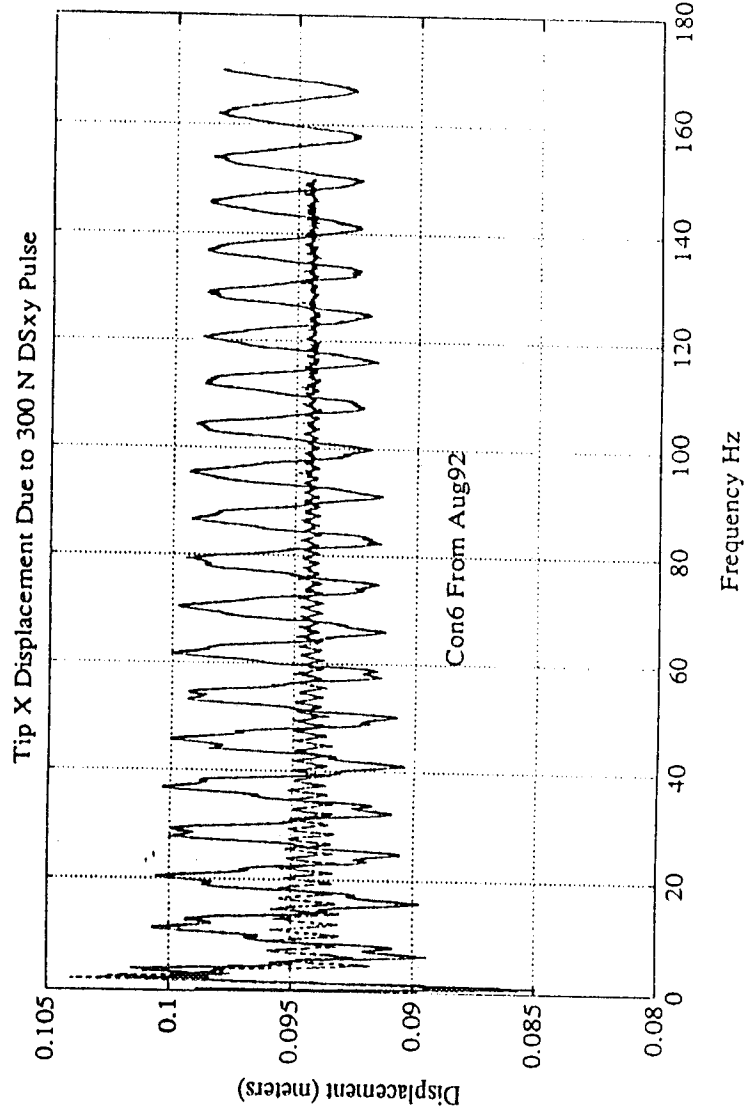
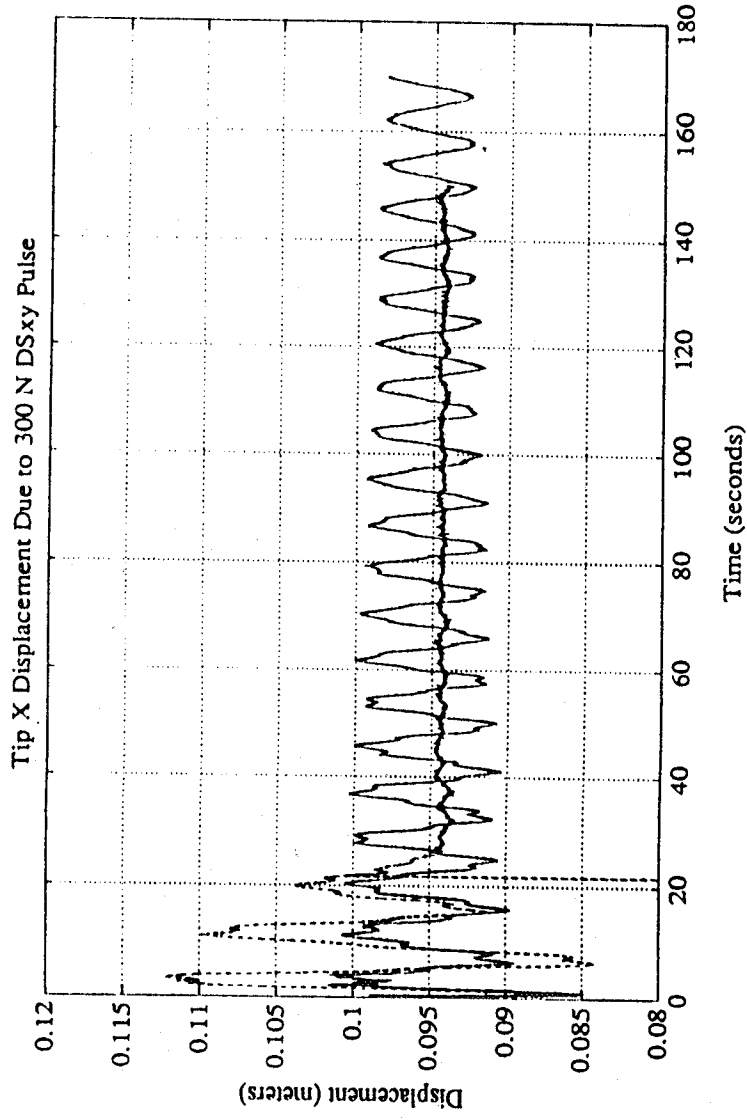


Figure 4.1-13 Comparison of Controller 2 of the Second Test Session (a) with Controller 6 of the First Test Session (b). The Plots Show the Tip Displacements for Both Open-and Closed-Loop Cases

In summary, several conclusions may be drawn from the CASES testing experience. First, the initial test session results indicate that on-site design of controllers can be quite effective. These results also show that careful thought needs to be given to the form of the excitation used for system identification tests. It is not always sufficient to vary the frequency content and test duration, but may also be necessary to vary excitation amplitude versus frequency. The advanced design techniques and revised architecture of the refined controllers allowed for increased bandwidth, but the use of gyros instead of detectors sacrificed some performance on the lowest bending modes. Finally, the results validated a streamlined "Gradualist" approach to control design implementation and test although practical and programmatic obstacles did not permit the final step in design refinement. On the whole, complete on-site design requires the supply of some identification data prior to the test session.

4.2 Control Design and Test Activities on the CEM Testbed at NASA/LaRC

For the second year of the Phase II program, the Harris team was assigned to the CSI Evolutionary Model (CEM), Phase 2 testbed at NASA/LaRC. As discussed, several diverse activities were accomplished on the CEM. This section describes only the fixed-gain control design and test activities that were carried out using the structure-mounted thrusters and accelerometers.

CEM Facility Description

As illustrated in Figure 4.2-1, the Phase 2 CEM testbed (see [40]) assumes the form of a multi-sensor space platform with several simulated sensor packages (SIS's) gimballed off the main structural framework. The structure is disturbed by commanding (broadband or in scan mode) the gimbal package of one SIS. We briefly describe the various components of the system as follows.

The overall structure consists of a three-dimensional aluminum truss 620 inches long constructed from 10-inch cubical bays. The truss has a 62 bay long main bus, four 2 X 5 bay horizontal suspension trusses, an 11 bay vertical laser tower, and a four bay vertical reflector tower. There are three two-axis gimbals mounted on the main bus. Also a 17-inch diameter reflector is mounted at the top of the vertical tower on the aft end of the structure. All main components are labeled in Figure 4.2-1. Four cables support the structure from the ceiling, each cable in series with a pneumatic suspension system. Active suspension allows all six suspension modes to have a frequency less than 0.2 Hz.

An important component of the global line-of-sight (LOS) pointing subsystem is the reflector which consists of a 17-inch diameter 0.375-inch thick aluminum plate with a 10-inch diameter, 0.25-inch thick mirror mounted on its surface. A steel circular plate 1.25 inches thick and 16.5 inches in diameter is mounted on the back of the aluminum plate to stiffen and add mass

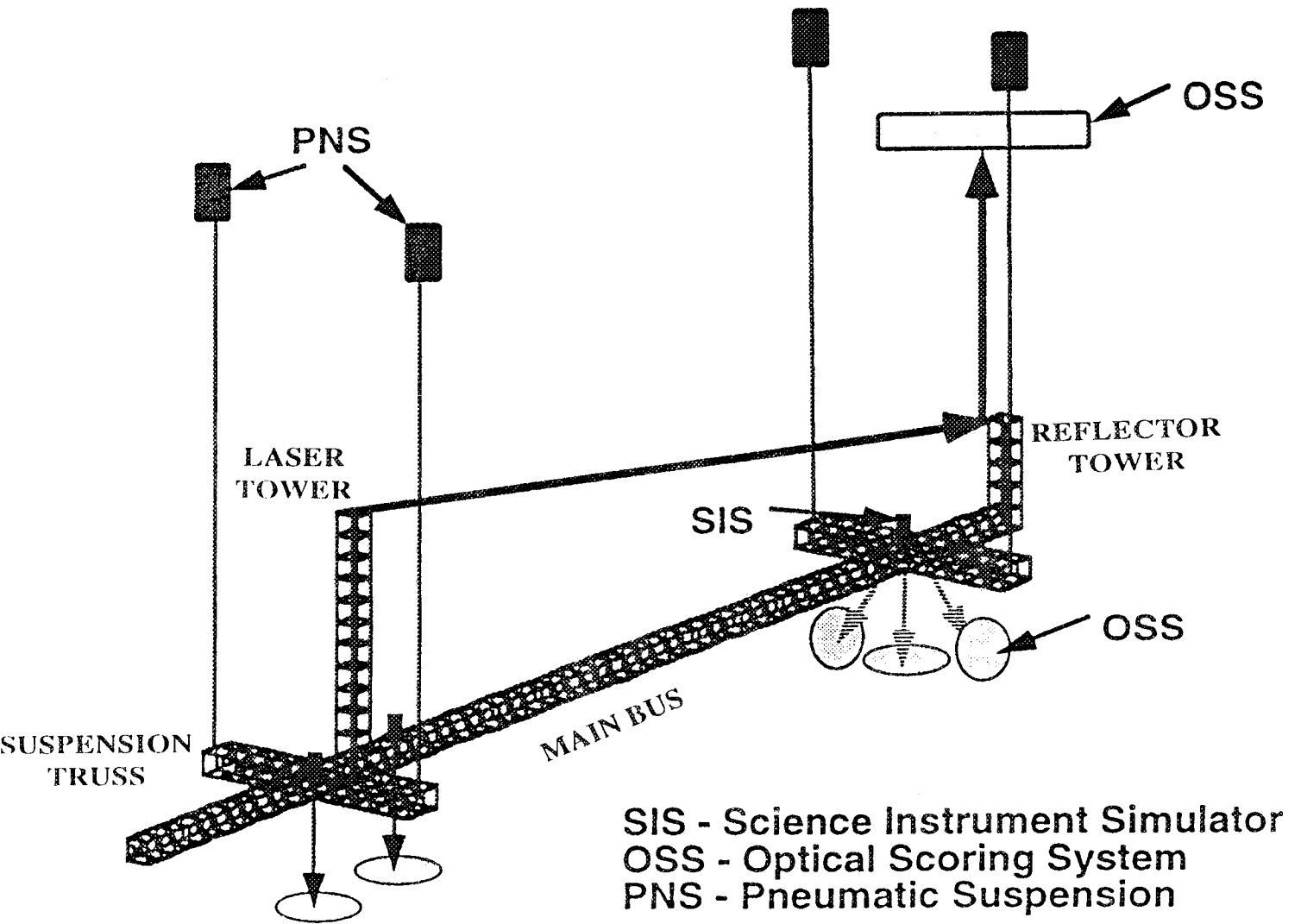


Figure 4.2-1 Phase 2 CEM: A Multiple Payload Platform

to the structural appendage. A tapered truss bay on the upper part of the aft truss tower supports the reflector at a 39.1 degree inclined position.

To monitor the LOS pointing accuracy, a laser mounted on the forward vertical truss tower is pointed towards the reflector and the laser beam reflection is measured by a photo-diode array over 600 inches above the reflector. This laser-reflector-detector system allows laser position measurements to within 0.3 inches. Laser position is sampled and forwarded to the main computer at a maximum rate of 50 Hz.

To simulate interaction of instruments mounted on a spacecraft and the spacecraft control system, three two-axis gimbal systems were fabricated and installed on the model. The locations of the gimbal systems, known as the Science Instrument Simulators (SIS), are shown in Figure 4.2-1. Each gimbal system is capable of slewing or pointing to a fixed point on earth with a pointing jitter of less than 2 arc-seconds. Angular measurements are obtained using an Optical Sensor System (OSS) mounted on the floor underneath the gimbals.

The gimbal structure consists of two pivoting aluminum rings that are coplanar and concentric when in the null position. Axes associated with the interior and exterior gimbal rings have been named the "inner" and "outer" axis, respectively. Each ring has a motor module on one end, and sensor module at the other end. Each motor module includes a torquer and cable wrap-up mechanism. The sensor module includes an optical encoder, interpolation electronics, electromagnetic brakes, and a cable wrap-up for the payload and inner gimbal sensor module.

The gimbals are controlled via a 386SX computer that reads encoder pulses, and commands the gimbal torque motors. During gimbal operation, this computer provides commands to control gimbal brakes, motor torque, and also provides status information to maintain communications with the main computer.

To test the gimbal with a realistic inertia and payload, a dummy payload is mounted in the two-axis gimbal. The dummy payload assembly, consists of two steel quarter sections, a top aluminum plate with a mirror and plate bracket, a bottom aluminum plate with a laser mounting clamp, a laser, and mounting ring. The payload is tailored to have a higher mass moment of inertia about the inner axis than the outer axis to counterweight the smaller outer axis inertia. A laser source is clamped at the payload bottom plate and is pointed towards the Optical Scoring System.

The Phase 2 CEM capabilities are summarized in Table 4-2. The experiments performed by the Harris GI team disturbed the structure using one SIS and monitored the pointing errors of the remaining SIS's with their associated OSS's. The controls actuation and sensing devices used in closed-loop testing consisted of the eight accelerometers and eight thrusters distributed over the structure. Using OPUS control design technology, we continued our progress in developing

Table 4-2 Phase 2 CEM Capabilities

Platform

Physical Properties

**620 inches long, 110 inches wide, 120 inches tall
~900 lbs in weight (50 % Truss)
 $I_{xx} \sim 8000 \text{ lb-in}^2\text{-s}^2$, $I_{yy} \sim I_{zz} \sim 100000 \text{ lb-in}^2\text{-s}^2$**

Dynamic Properties

**6 Rigid Body Modes < 0.2 Hz.
First Flexible Body Mode ~ 1.85 Hz.
~20 Dominant Structural Modes Below 20 Hz.**

Science Instrument Simulators

**Three two-axis gimbals
Up to 25 lb Payload, CG offset < 5 in.
15 degree range of motion
2.5 arc-sec pointing resolution**

streamlined design/test methods, working toward a reliable single-session controls implementation capability.

Pre-Test Modelling and Control Design Activities

During year 2 of the Phase II program, during which the Harris team was assigned to the CEM testbed, there was an initial three month delay in assembling the modelling data. Further scheduling conflicts forced a first test session in late August. Moreover, in September, the CEM was scheduled to be reassembled into an EOS-like configuration (the CEM Phase 3 configuration). Therefore, once again, a single-session, on-site design was required. The above scheduling difficulties were offset, however, by the provision of accurate models before the test session, thereby providing a good start toward initial control design.

The CEM modelling data supplied by NASA/LaRC consisted of several items: (1) a detailed finite element model (FEM), (2) Frequency Response Function (FRF) test data obtained by LaRC in June and (3) an ERA model. Inspection of this data showed that the off-diagonal (noncollocated sensor/actuator pairs) transfer functions were not of sufficient fidelity to support the design. Also the very low frequency (quasi-rigid-body) mode FRF data was also of insufficient fidelity due to inadequate data averaging periods. Consequently, we devised a hybrid model derived from the FRF (and ERA) data for the higher order modes and the FEM data for the quasi-rigid-body modes.

The above points are illustrated by a comparison of transfer functions obtained from FRF data, the FEM and the ERA model. Figure 4.2-2 shows such a comparison for a typical transfer function. It is seen that for modes above 1 Hz, the ERA model yields virtually exact agreement with the FRF data. Consequently, our control design model relied on ERA in this frequency regime. The quasi-rigid-body modes near 0.15 Hz are poorly estimated by ERA and the FRF measurements because of insufficient dwell time. In contrast the FEM model gives an accurate rendering of these modes, but relatively inaccurate results for the elastic modes above one Hertz. Our control design model truncates the states associated with the low frequency dynamics in the ERA model and substitutes modal data obtained from the FEM. The resulting model has excellent accuracy over the entire frequency range of interest.

The accurate model we were able to obtain permitted a good head-start in controller design prior to the test session. The control design activity considered only the use of the eight thrusters distributed over the CEM structure and the eight collocated accelerometers. The control objective was to stabilize the pointing performance of one SIS in the presence of disturbances generated in the structure by commanding one of the SIS's in either a scanning maneuver or a relatively broadband repointing maneuver. This is a meaningful control exercise because it shows the beneficial impact of structural vibration suppression in the multi-sensor

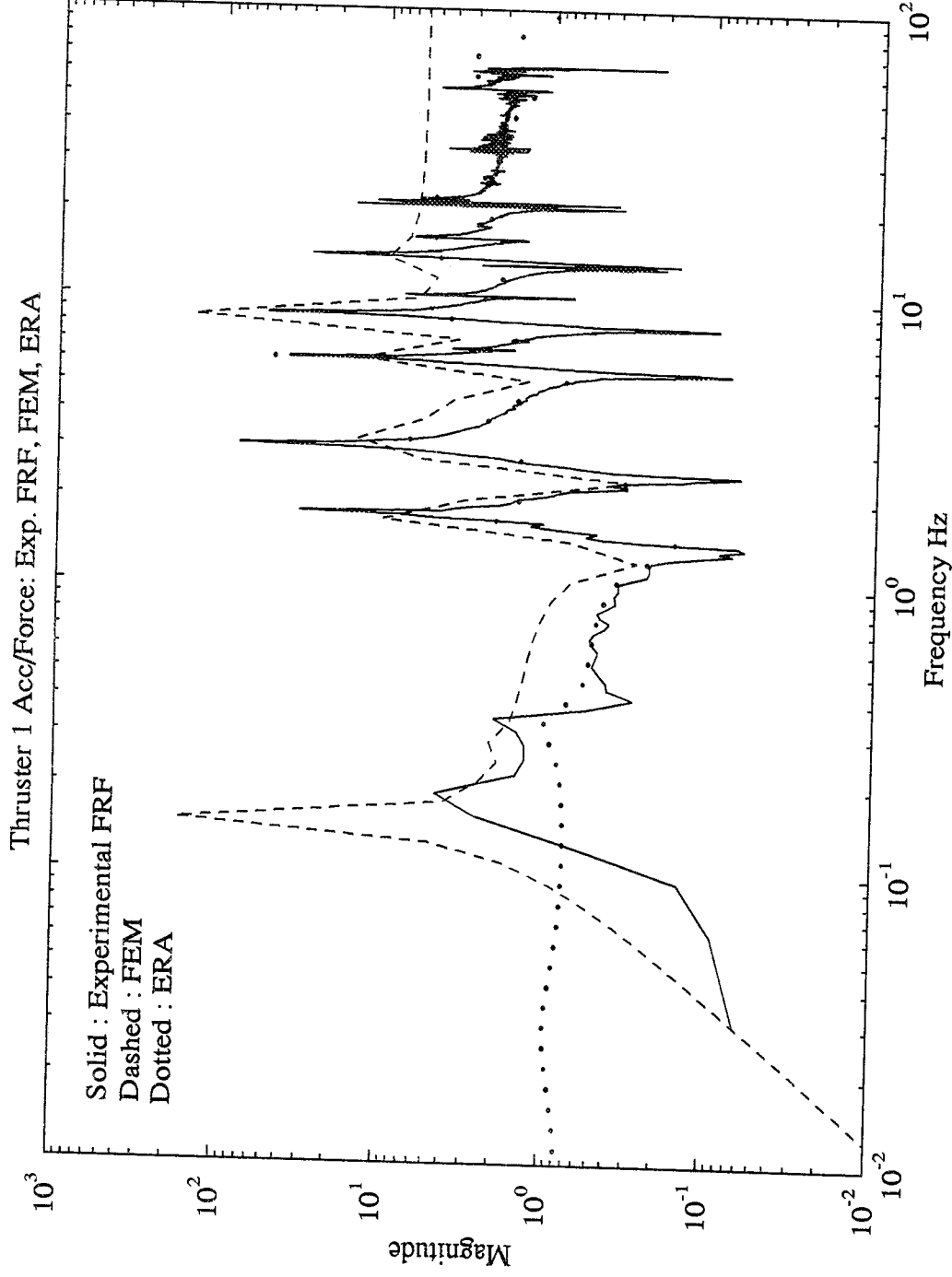


Figure 4.2-2 Comparison of Frequency Response Function Magnitudes (for Thruster 1 to Accelerometer 1) Derived from (a) FRF Experimental Data, (b) Finite Element Model and (c) ERA Generated State-Space Model

platform on the effectiveness and bandwidth of the Bendix 2-axis pointing gimbals of the SIS assemblies. Vibration control not only reduces the range of motion that must be handled by each gimbal, it stabilizes vibration modes that might otherwise be destabilized by the gimbal pointing servos. This permits greater bandwidth in the gimbal servos, further enhancing performance.

To reduce low frequency noise and drift, we filtered the accelerometer outputs with standard "roof top" integrators (so called because their Bode gain plots resemble a roof top – with +1 slope below the integrator corner frequency and -1 slope above this frequency). The roof top integrator poles were placed at 0.05 Hz in order to phase stabilize the quasi-rigid-body modes. With the roof top integrators incorporated into the design model, OPUS software was exercised to obtain a decentralized design with more than 20 to 30 dB loop gains on all significant modes. These features are illustrated in Figure 4.2-3a, b which shows the gain and phase for a typical loop transfer function. Including the sensor post-filters, the total controller order was 28 states.

On-Site Design and Test Activities and Results

For on-site testing August 23-24, 1993, disturbances were injected at gimbal A and line-of-sight (LOS) errors were monitored at gimbals B and C. Originally, a broadband random gimbal disturbance command was specified but open-loop tests quickly showed that the response magnitudes were too small relative to the LOS sensor resolution. Since the broadband disturbance provided inadequate signal-to-noise ratio, we elected to use a sine dwell disturbance on both gimbal axes independently. The following amplitudes and frequencies were used:

Outer gimbal (X-axis):	10,000 arc-sec amplitude
	1.7 Hz frequency
Inner gimbal (Y-axis):	15,000 arc-sec amplitude
	2.433 Hz frequency

The above frequencies are close to the resonance frequencies of several dominant modes. Consequently, response amplitudes were well above the LOS sensor resolution.

On the first trial of the pre-test control design, the low frequency drifts of the accelerometers were found to be excessive. To remedy this, we raised the roof top integrator pole frequencies to ~1 Hz. Recall that these frequencies were initially chosen at 0.05 Hz to phase stabilize the quasi-rigid-body modes. However, this was unnecessary because these modes are not significantly excited. With the high roof top pole frequencies, drift ceased to be a problem. The resulting design (having all other characteristics the same as the pretest design) is designated as "controller 1".

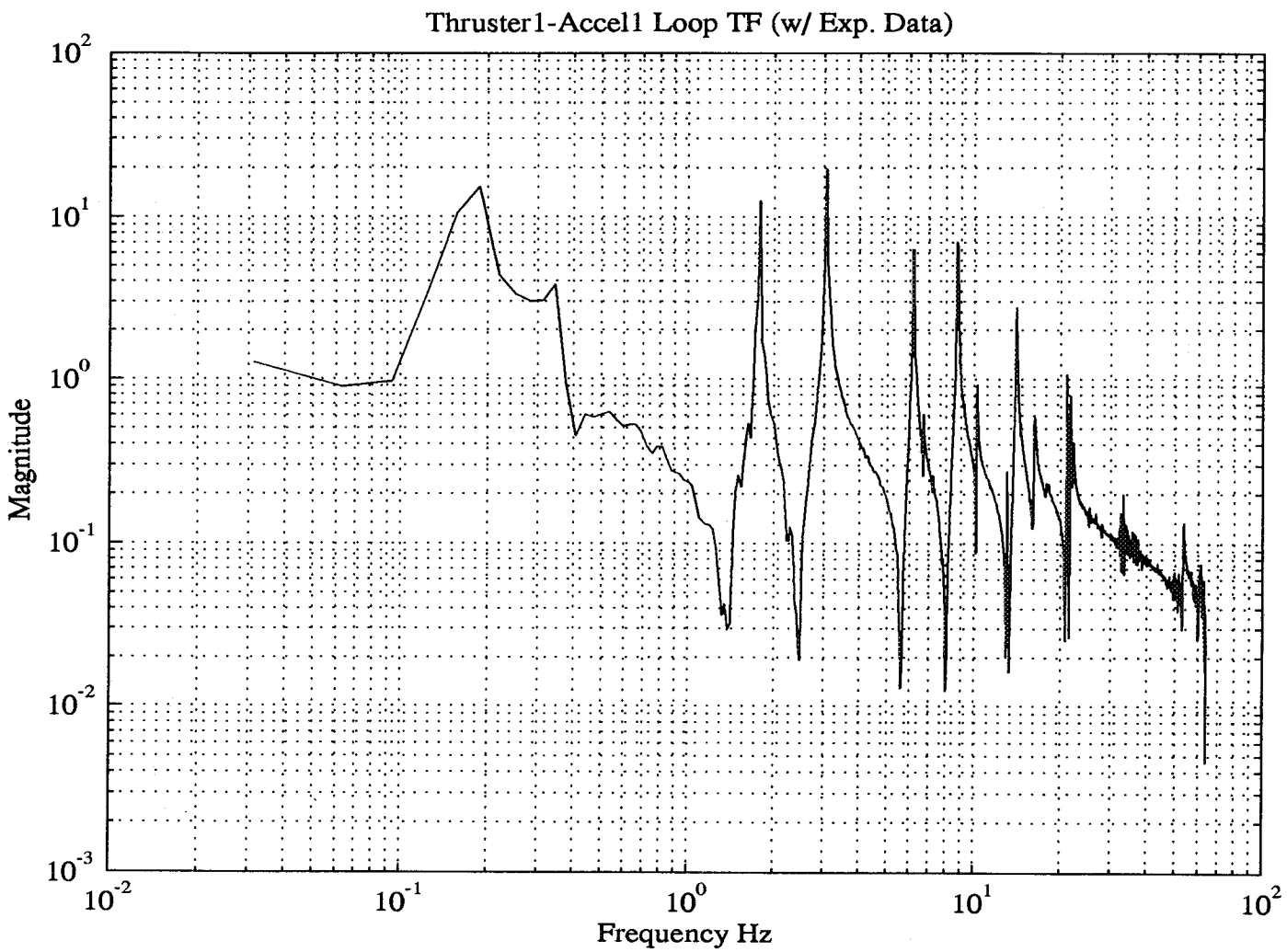


Figure 4.2-3a Typical Loop Transfer Function for Pre-Test Controller – Gain Plot

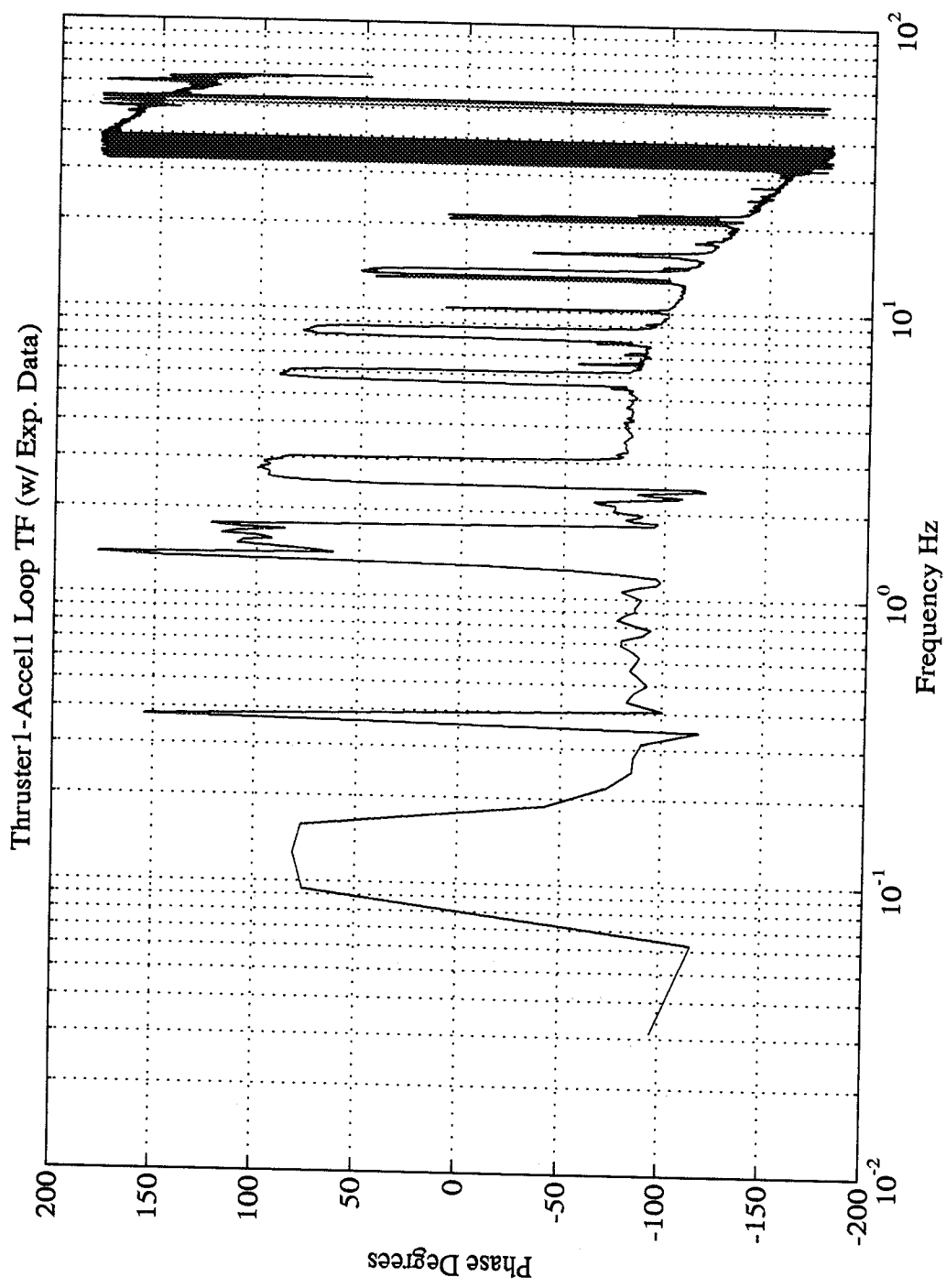


Figure 4.2-3b Typical Loop Transfer Function for Pre-Test Controller – Phase Plot

After testing controller 1, further attenuation of a rotational/rocking mode (along the X-axis) was sought. The control loop for one thruster on the laser tower was redesigned to achieve greater authority over one of the quasi-rigid-body modes. The resulting controller is designated "controller 2".

Closed-loop tests were documented in a video recording which shows the dramatic LOS pointing improvements of both controllers relative to the open-loop. The tests results also establish that controller 2 did achieve the desired improvements over controller 1.

To illustrate these points, Figure 4.2-4a shows the gimbal C LOS error trace on the target plane in the open-loop. Total excursions are seen to be approximately 2000 and 1000 arc-sec. on the two axes. The same plot for closed-loop operation using controller 1 is shown in Figure 4.2-4b. The total excursions are now approximately 400 and 50 arc-sec, respectively. The 400 arc-sec excursions along the X-axis are due to the torsional/rocking mode. In contrast, controller 2, as shown in Figure 4.2-4c, reduces the excursion to ~100 arc-sec. On the whole, controller 2 achieves from 20 to 40 fold reduction in LOS error relative to open-loop.

The same general conclusion may be drawn from LOS time histories on the two separate axes. For example, the time histories of the X-axis LOS error measurement are given in Figures 4.2-5a, b and c for the open-loop, closed-loop controller 1 and closed-loop controller 2, respectively. As the open-loop plot shows, the system response is allowed to ramp up from the time ($t=0$) at which the disturbance is initiated. In the closed-loop plots, the controller is turned on at $t=15$ seconds. Controller 1 (Figure 4.2-5b) shows some significant oscillation at approximately 0.4 Hz. As Figure 4.2-5c shows, this is suppressed by controller 2.

In summary, thanks to good pre-test modelling information and sufficient preparation of controller designs, the CEM test experience shows excellent controller performance as a result of a single design/test on-site session.

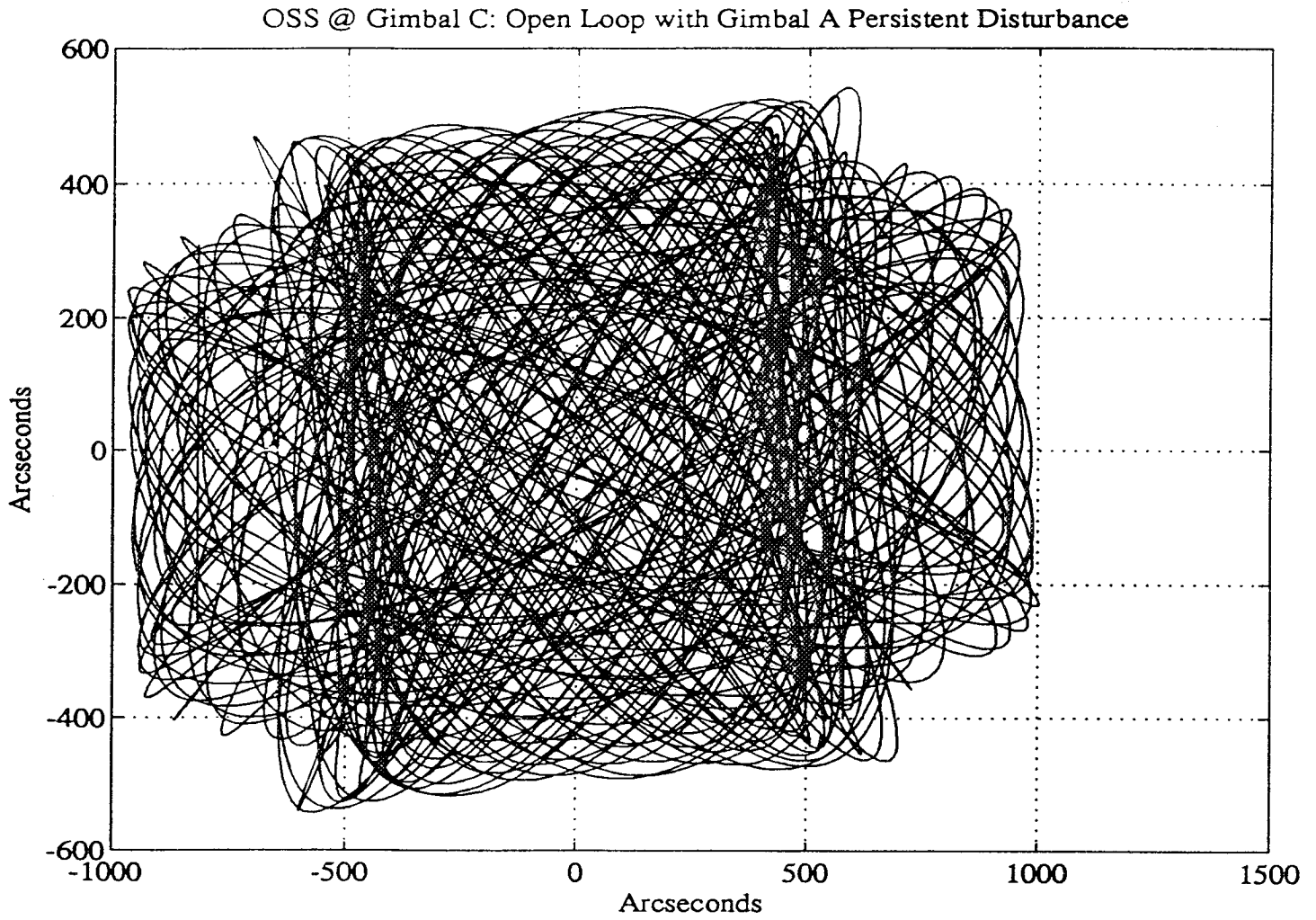


Figure 4.2-4a LOS Error Locus on the Sensor Target Plane at Gimbal C – Open-Loop

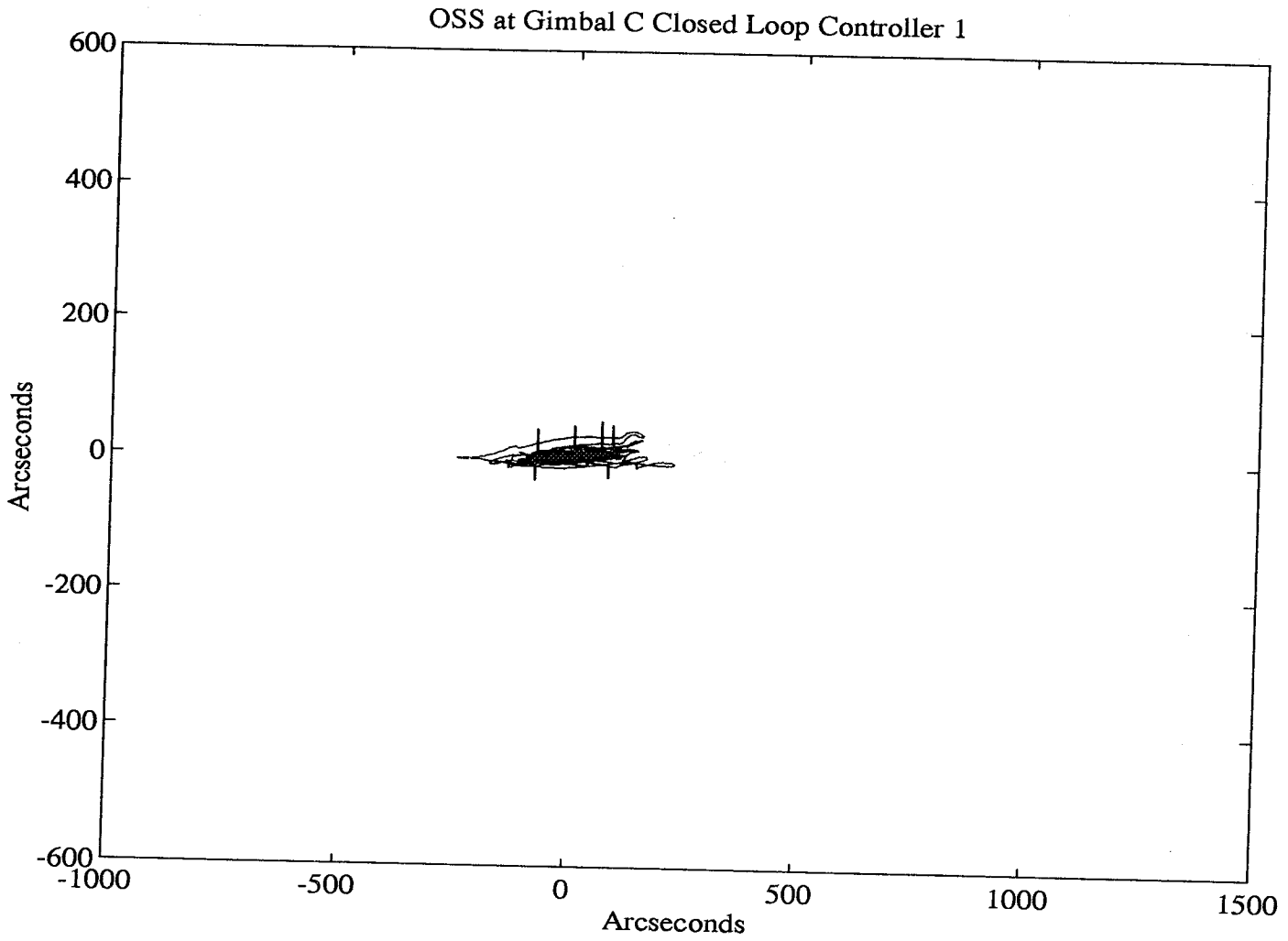


Figure 4.2-4b LOS Error Locus on the Sensor Target Plane at Gimbal C – Closed-Loop, Controller 1

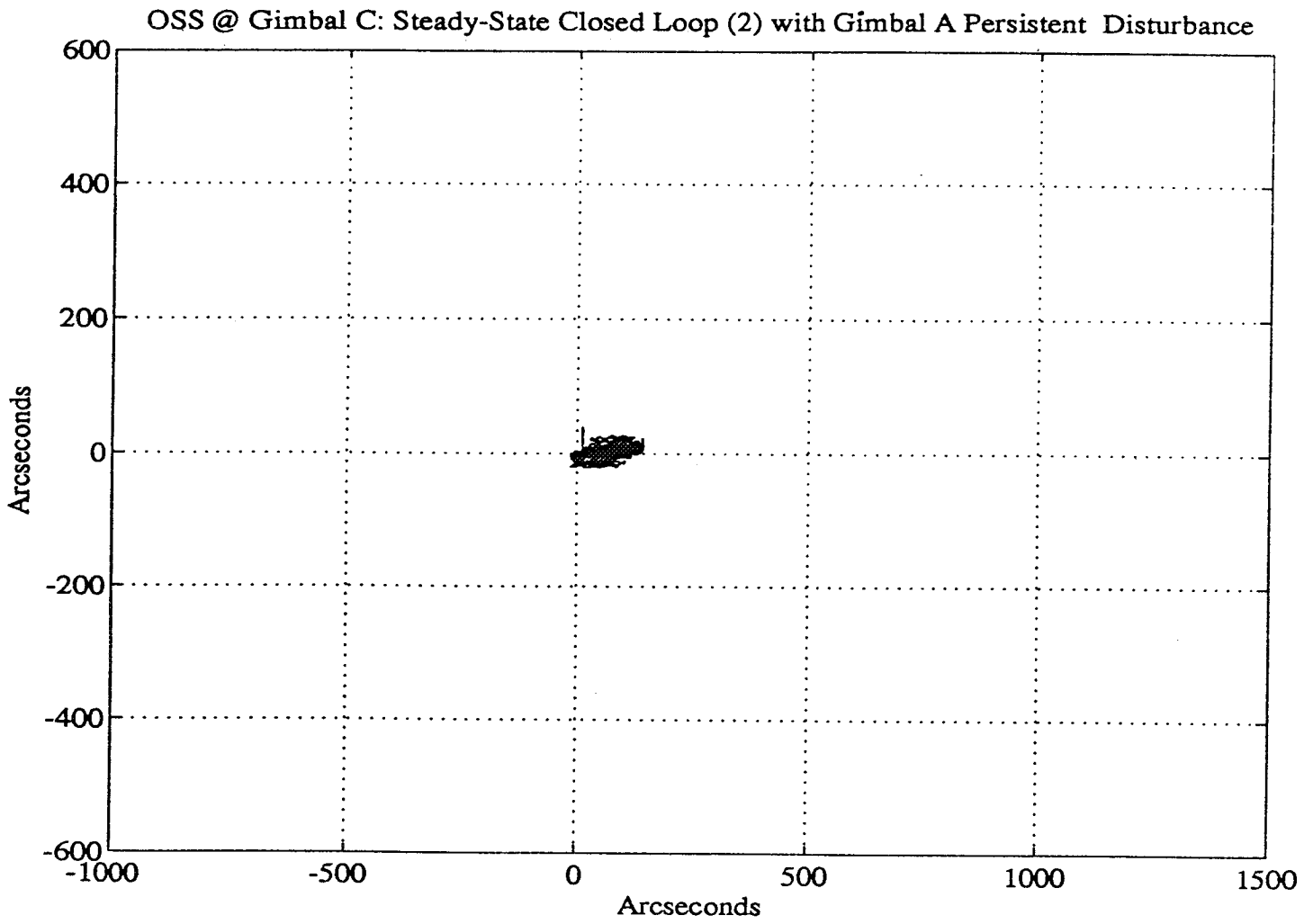


Figure 4.2-4c LOS Error Locus on the Sensor Target Plane at Gimbal C – Closed-Loop, Controller 2

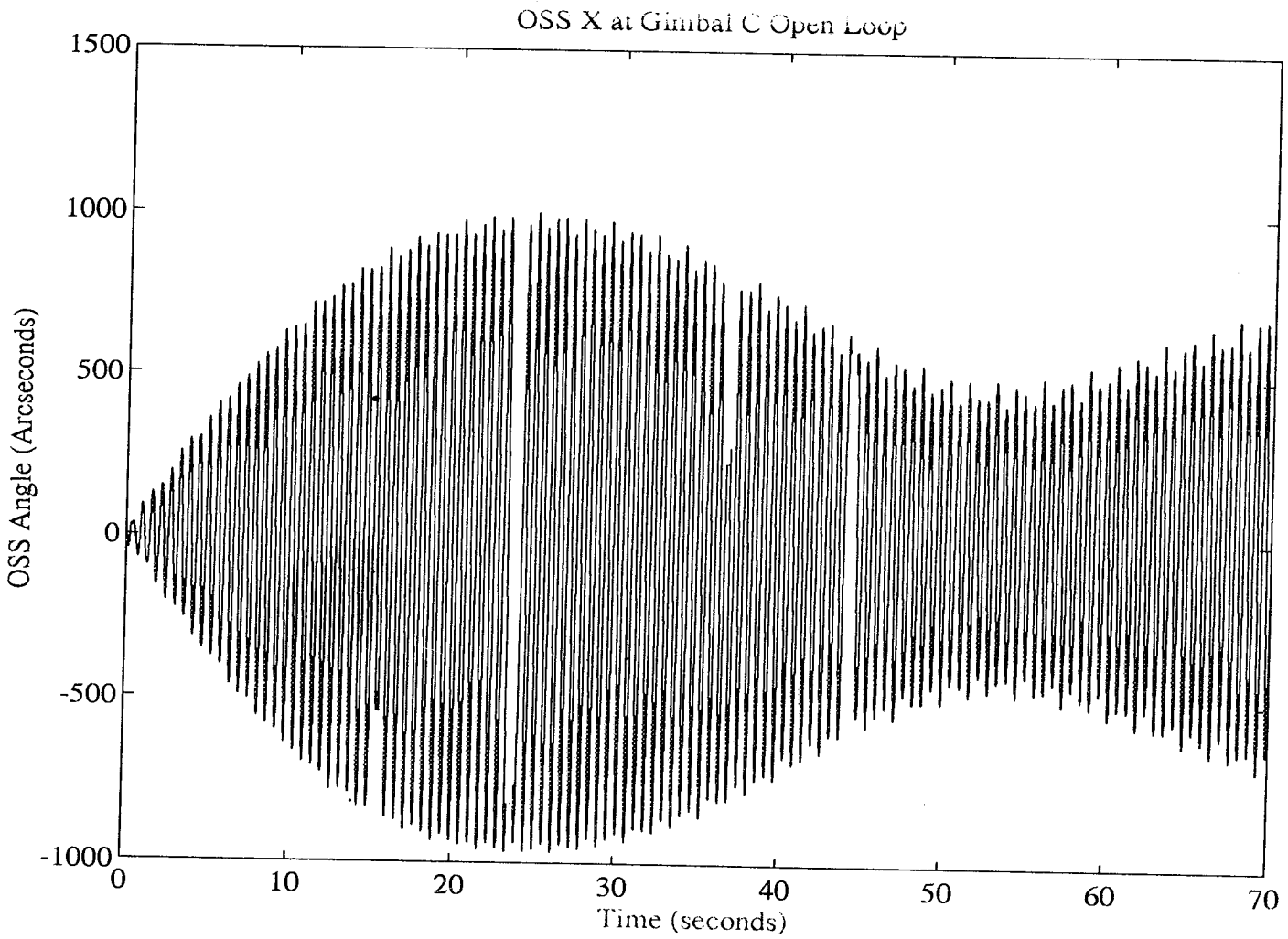


Figure 4.2-5a X-Axis LOS Error Time History – Open-Loop

C-2

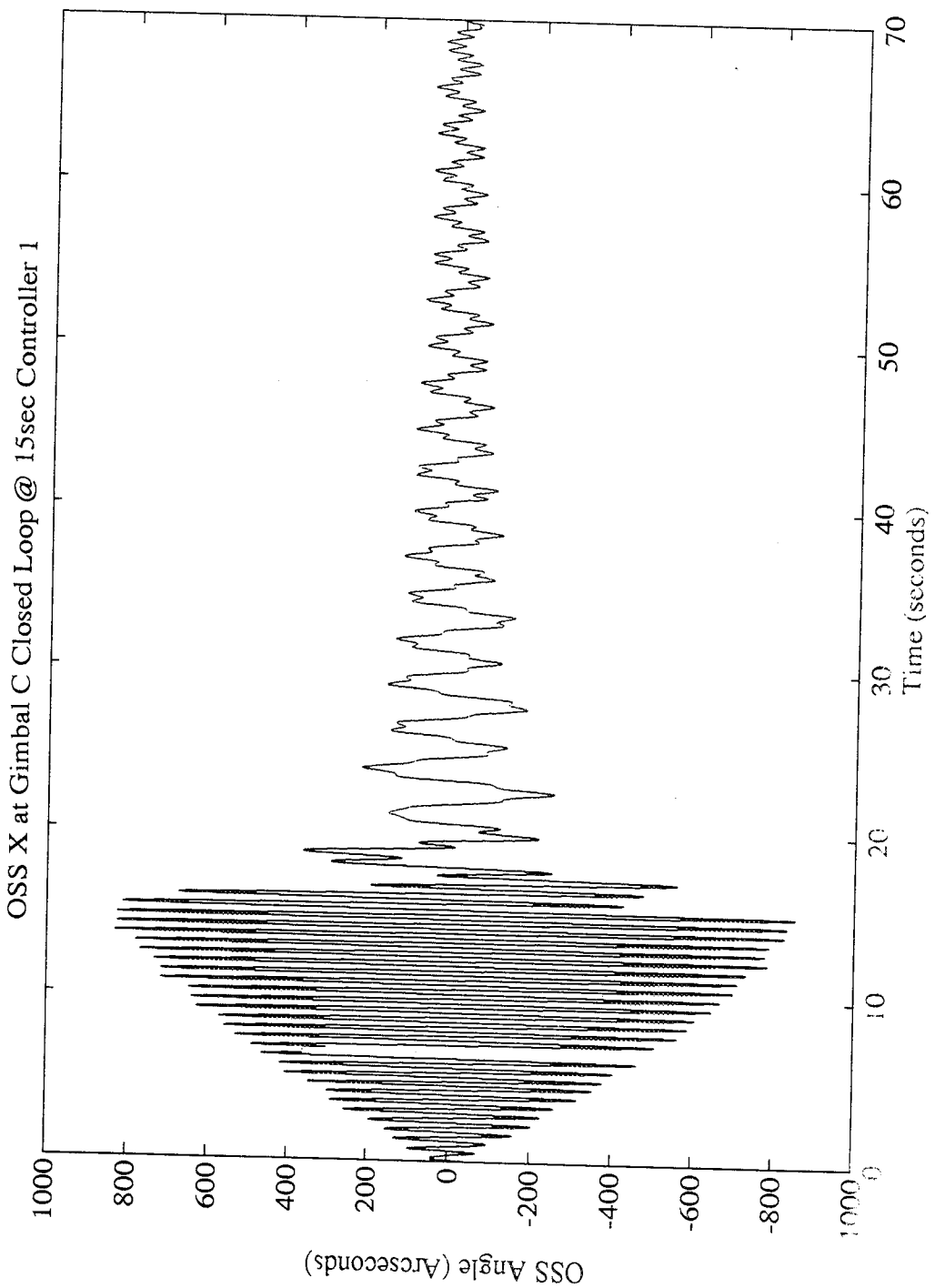


Figure 4.2-5b X-Axis LOS Error Time History – Closed-Loop, Controller 1

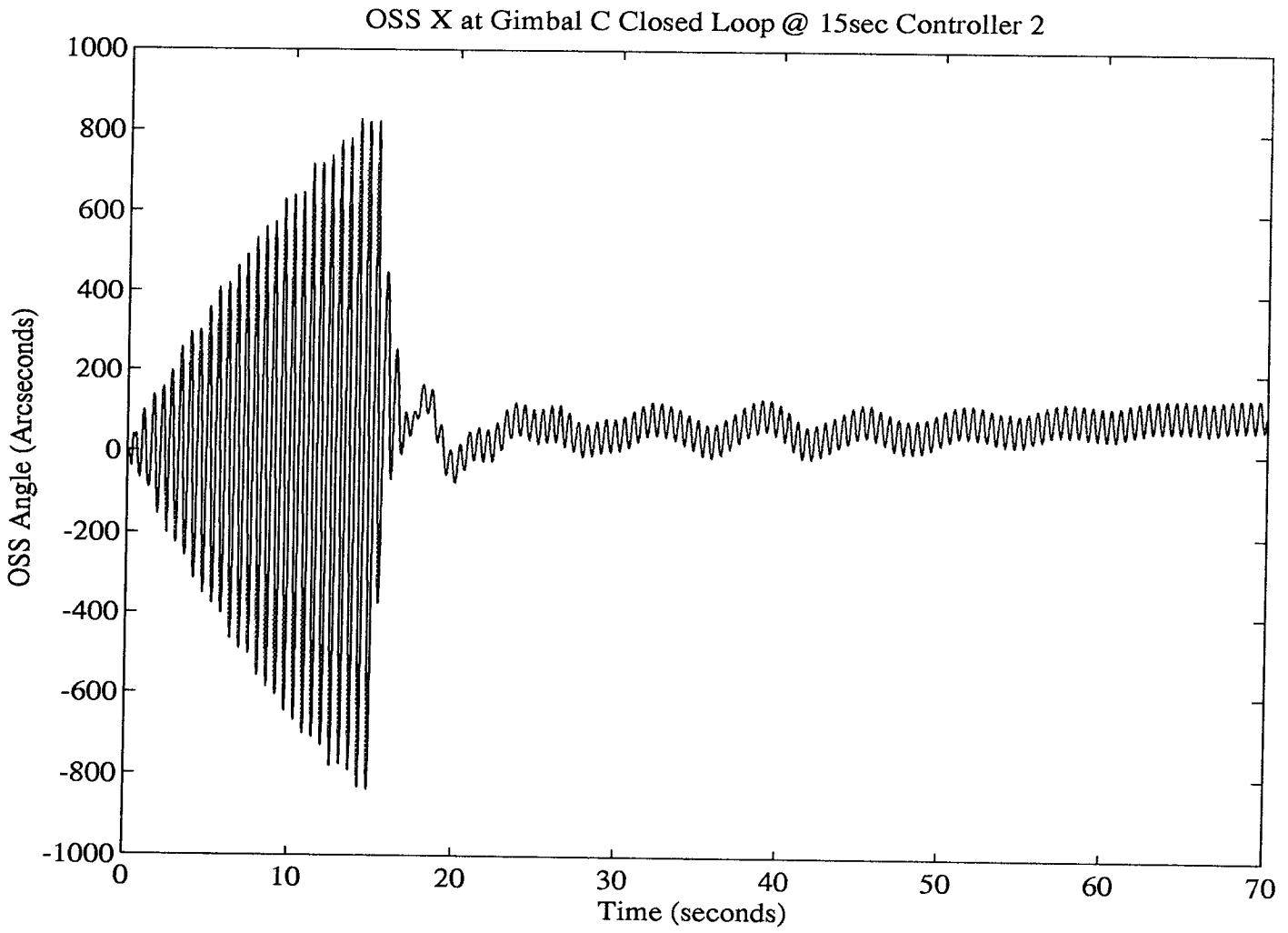


Figure 4.2-5c X-Axis LOS Error Time History – Closed-Loop, Controller 2



5. PHASE II - ADAPTIVE NEURAL CONTROL FOR THE CEM

5.1 Background and Motivation

To progress beyond the streamlined, single-test session control implementation capability demonstrated on the CASES and CEM test facilities, the activity described here attempts a qualitative advance in control system autonomy. For the past four years, Harris has been developing a new neural network architecture, called the Adaptive Neural Control (ANC) architecture, to implement on-line systems identification and adaptive control systems. Basically this thrust takes autonomy to the limit to execute on-site design without human intervention.

ANC developments began in 1989 with the discovery by Dr. D.C. Hyland of the new neural architecture for identification and control. This architecture was refined and fully extended to IIR (Infinite Impulse Response) systems thanks to informal technical collaboration with NASA/LaRC personnel, most notably Dr. J.-N. Juang and his colleagues. The ANC architecture has led to a sequence of successful demonstrations and new development efforts.

In particular, through collaboration with NASA/LaRC, an ANC-based algorithm was implemented on the host computer and demonstrated on the Phase 2 CEM test facility. These results constitute the first instance, within the CSI Program, of a totally automated design and test process and one of the first steps toward autonomous space structure control systems.

Automation of the design test process is needed because the current methodology still engages significant human resources. Since designs involving fixed-gain controllers must be updated periodically to reflect in-mission changes in system dynamics, this implies burdensome ground support activities. But, besides reducing engineering manpower requirements, such advances in automation support NASA's long-term space exploration objectives for which autonomous spacecraft involving self-reliant control systems are a necessity. Such robot explorers would have to independently update control laws, detect faults and reconfigure control systems.

5.2 ANC Technology Overview

Much of previous work in adaptive control via neural networks (see [41] for an excellent review) concentrated on highly nonlinear but low dimensional systems. In contrast, the ANC architecture concentrates on neural schemes particularly geared to problems involving high order systems exhibiting very broadband dynamics. As indicated in Figure 5.2-1 ANC combines tapped delay lines with "static" neurons (each neuron is a two-way device incorporating a back propagation path) to perform on-line system identification and adaptive control. The system adapts in the presence of unknown persistent plant disturbances and instrumentation noise and requires no detailed prior modelling information.

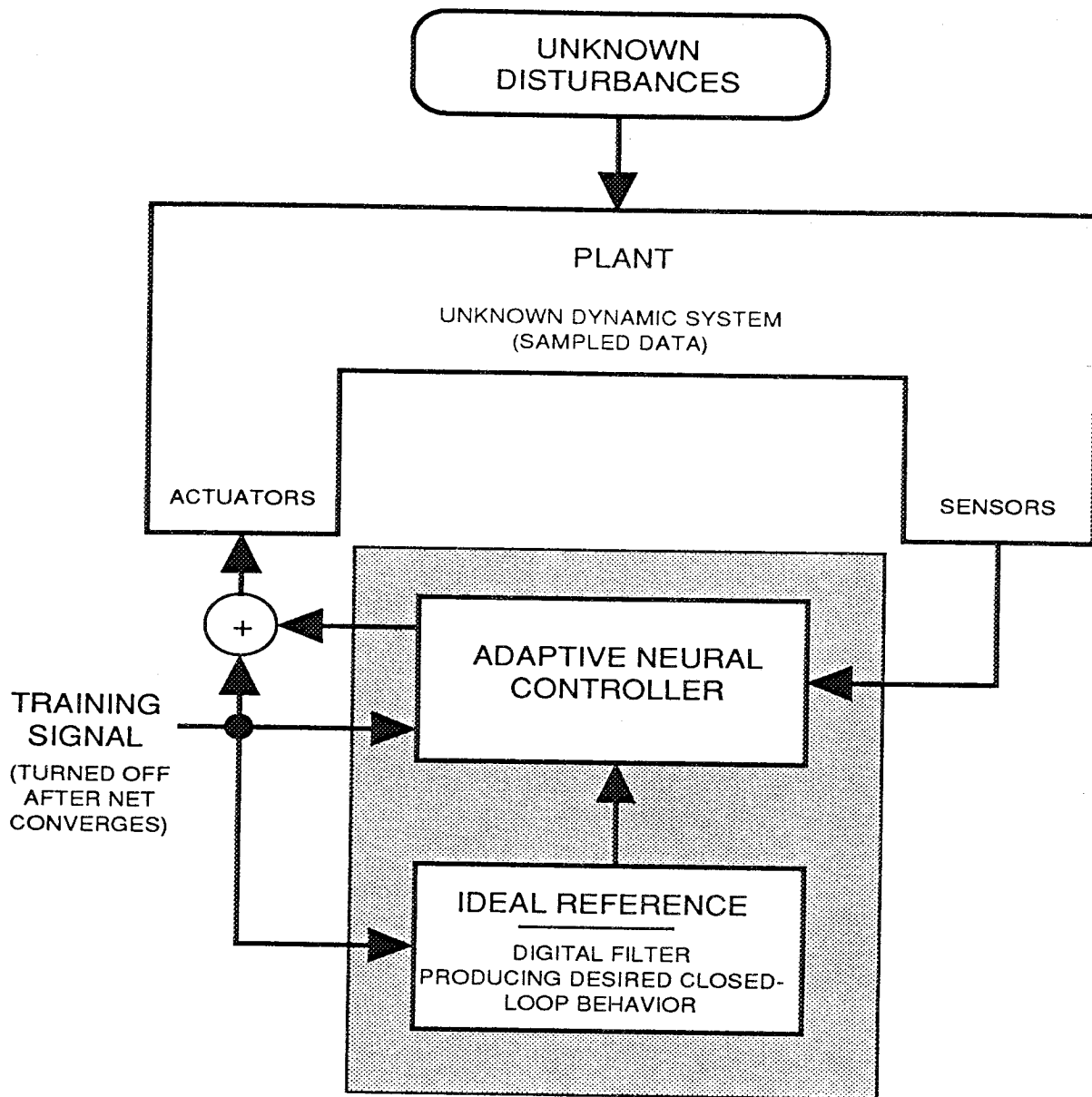


Figure 5.2-1 ANC Executes Simultaneous System Identification and Adaptively Optimized Control

There are several key features of this architecture that have made it particularly attractive. First, although the architecture can be visualized as a neural network, the control scheme is fundamentally a massively parallel, decentralized adaptive control algorithm that need not be *implemented* literally as a collection of artificial neurons. Secondly, these "neural" algorithms feature learning capability that is distributed down to the smallest computational unit. Decentralization (distributed learning) imparts the ability to autonomously recover from hardware failures – including damage to the neural processor itself. A third key feature is that the basic neural building blocks are hierarchically organized into a set of standardized modules. Analogous to a "Lego set," modules can be combined to build an enormous variety of systems and permits complex systems to be built up from simpler components in a transparent way. Finally, modularity and parallelism yield implementation flexibility. Specialized hardware is *not* required for implementation of the Harris ANC architecture. The entire identification or control algorithm can be distributed among several parallel processors, and hardware suitable for this purpose is currently available and is being used for engineering development. This means that we can progress in orderly fashion from the use of existing Integrated Circuits (IC's) to (ultimately) dedicated neural IC's, thereby building our capabilities gradually and systematically.

While details of the ANC architecture are given in recent papers and reports [42-44], we briefly review the basic features here. The hierarchy of modular structures is shown in Figure 5.2-2. This hierarchy starts, at the lowest level, with tapped delay lines and neurons with intrinsic back propagation. These are the same "static" neurons that would be utilized for such applications as pattern classification and nonlinear mapping. The key to applying such neurons to dynamic system identification is to organize them into larger building blocks, the *dynamic ganglia*. A ganglion is an array of neurons designed to establish temporal ordering within the network so as to process time histories of network signals. Ganglia are interconnected by bundles of synapses, called Toeplitz synapses, because the weights form Toeplitz matrices.

The next level in the hierarchy combines ganglia and Toeplitz synapses to form replicator units. The basic job of a replicator unit is to duplicate the output of a previously unknown sampled – data dynamic system when both replicator and system are stimulated by the same training input. Thus the replicator is the basic module for system identification. Several types of replicator have been developed, each corresponding to a particular model form. The work of NASA/LARC personnel in identification methods using systems observer Markov parameters [45, 46], led to discovery of a new model form for dynamic systems – the ARMarkov model, so-called because it combines features of impulse response (Markov parameters) with ARMA (Auto Regressive Moving Average) models. Figure 5.2-3 summarizes the various characteristics of

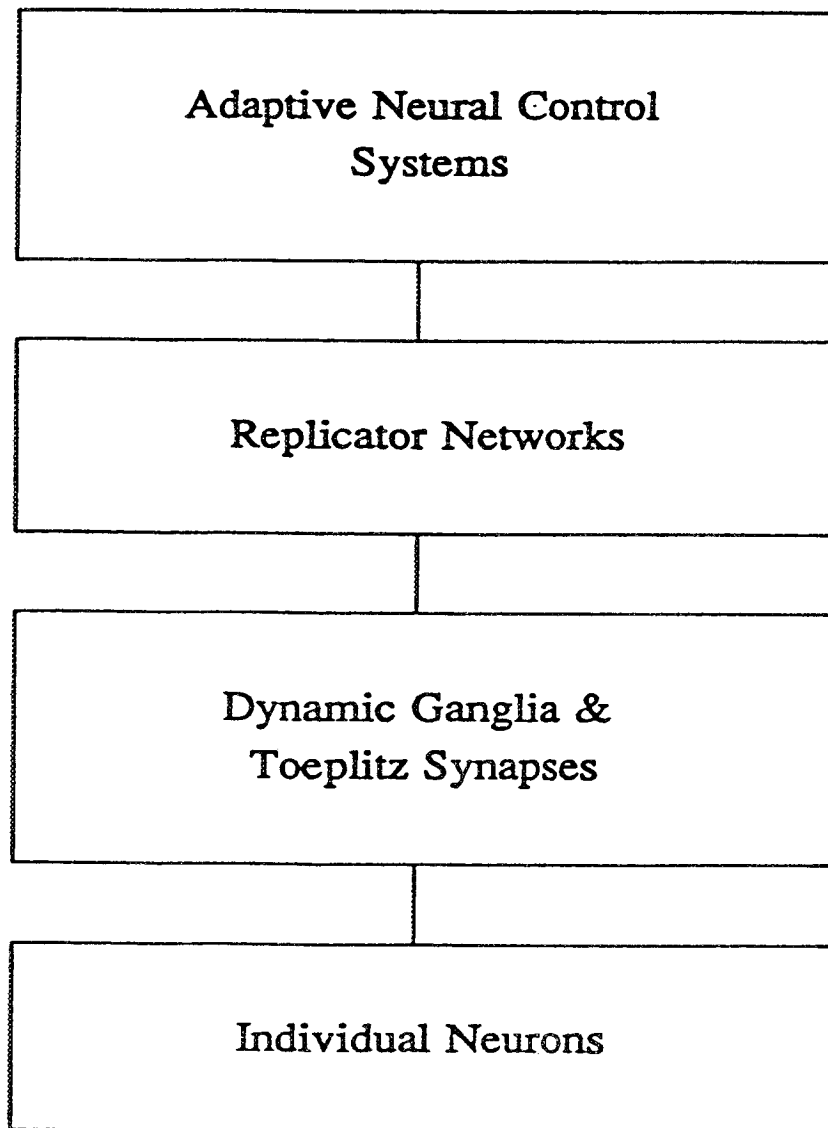


Figure 5.2-2 Hierarchy of Modular Neural Structures Progressing from Basic Constituents to Higher-Level Modules

Linear Replicators of Various Forms Correspond to Different model Forms

$$(x(\kappa + 1) = Ax(\kappa) + Bu(\kappa) + Dw(\kappa) \quad x \in \mathbb{R}^N; \quad y = Cx + v)$$

Impulse Response

$$y(\kappa) = v(\kappa) + \sum_{m=1}^{\infty} h_{u_m} u(\kappa - m) + \sum_{m=1}^{\infty} h_{w_m} w(\kappa - m)$$

(h_{u_m} and h_{w_m} are the “Markov Parameters”)

ARMA (Auto Regressive Moving Average)

$$y(\kappa) = \tilde{N}(\kappa) + \sum_{m=1}^M \alpha_m y(\kappa - m) + \sum_{m=1}^M \beta_{u_m} u(\kappa - m)$$

(\tilde{N} contains all contributions from v and w and $M \text{ rank } C \geq N$)

ARMarkov

$$y(\kappa) = N(\kappa) + \sum_{m=1}^M \mathcal{P}_m y(\kappa - L - m) + \sum_{m=1}^{M+L} \mathcal{L}_m u(\kappa - m); \quad L = 0, 1 \dots$$

- the first L \mathcal{L}_m 's are the Markov parameters.
- $L = 0$ gives the ARMA model.
- $\lim_{L \rightarrow \infty} \sum_m \mathcal{P}_m y(\kappa - L - m) = 0$ for a stable system. Therefore ARMarkov \rightarrow impulse response.

Batch ARMarkov

$$\bar{y}(\kappa) = \bar{N}(\kappa) + \text{Toep}[\mathcal{P}]\bar{y}(\kappa - 1) + \text{Toep}[\mathcal{L}]\bar{u}(\kappa - 1)$$

($\bar{y}(\kappa) = (y(\kappa), \dots, y(\kappa - R + 1))^T$, etc.; $\text{Toep}[\cdot]$ denotes a Toeplitz matrix formed from the vector (\cdot))

Figure 5.2-3 Linear Replicators of Various Forms Correspond to Different Model Forms

impulse response, ARMA and ARMarkov model forms. ARMarkov – based neural replicators have been found to offer superior stability and noise tolerance properties in handling IIR systems.

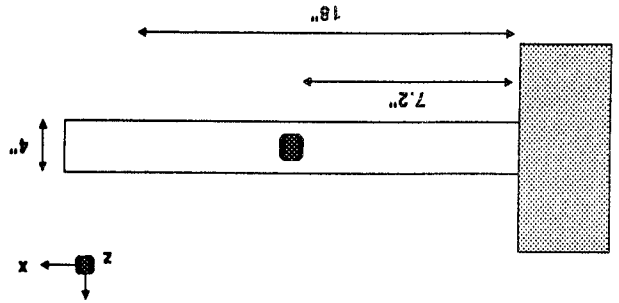
Numerous analytical examples have been produced to demonstrate structural identification using ARMarkov–based neural replicators. Some of these involve the use of simulated input/output data and others use actual test data. Also, a number of laboratory experiments have been performed. In some cases a MATLAB simulation was used to implement the neural algorithm, while in other cases the algorithm was implemented in real time using a DSP card. For example:

1. Figure 5.2-4 shows a simple beam experiment that produced excellent convergence of the adaptive model to the actual structural plant in 100 seconds.
2. The neural network system identification capability was also demonstrated on the Harris Multi-Hex Prototype Experiment (MHPE), which is a four meter Cassagrain test structure. Figure 5.2-5 show the network converged to the MHPE plant in 125 seconds.
3. Using a Digital Signal Processor (DSP), an Internal Research and Development (IR&D) experiment in active acoustical noise cancellation was completed in which over 20 dB broadband attenuation was achieved.

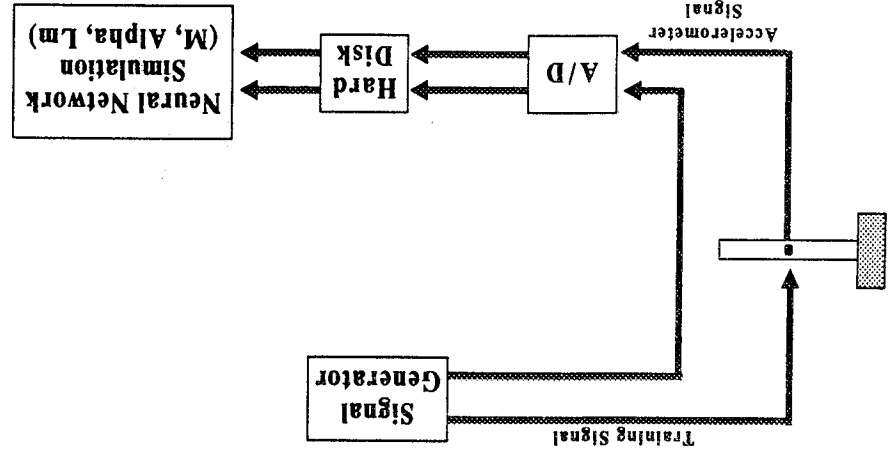
Many of these examples involve multiple inputs and outputs and nearly all involve fairly complex structures with many modes in the frequency band of interest. Also the laboratory experiments tested the algorithm under such real-world complications as sensor noise and ambient steady-state disturbances. Summarizing this experience, we can say that reasonably complex multi-mode systems can be identified with excellent accuracy with convergence times ranging from a few minutes to fractions of a second (depending on numerous factors, such as system sample rate, frequency band of interest, etc.).

Returning now to the hierarchy shown in Figure 5.2-2, several replicator units are combined in order to form the Adaptive Neural Control (ANC) system. An ANC performs on-line, simultaneous system identification and adaptively optimized control. The most basic ANC architecture for simultaneously replicating an unknown plant and adapting the controller so as to match the closed-loop input/output characteristics with a prescribed reference system has two parts: (1) the closed-loop modeller and (2) the control adaptor. The closed-loop modeller uses training signals and the plant sensor output to adapt the weights so that the closed-loop is replicated. After convergence, the modeller output matches the closed-loop system – in effect the modeller identifies the plant within the closed loop.

Neural Network Experimental Setup

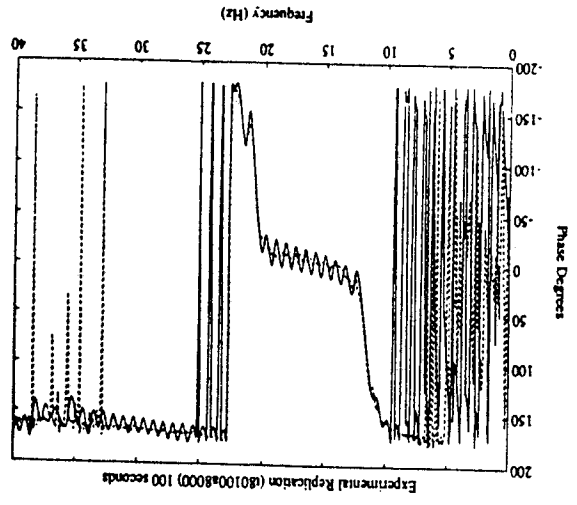
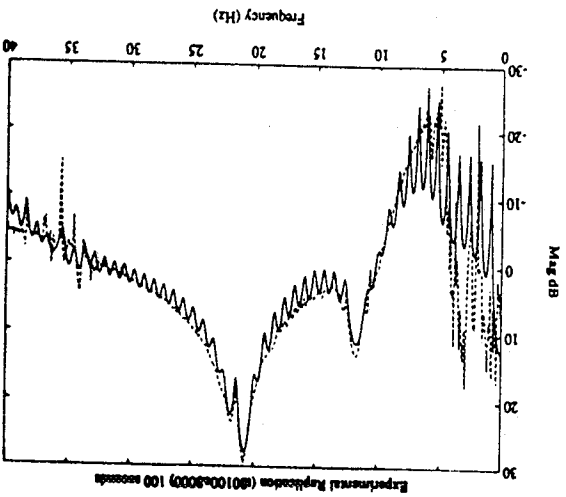


- Beam is cut from .125 inch thick aluminum sheet
- Beam is cantilevered horizontally
- LPACT acts in Z-axis (normal to paper)



- Training signal is logarithmic sine sweep from 5-40 Hz.
- 180 seconds of data stored
- A/D's clocked at 80 Hz sample rate

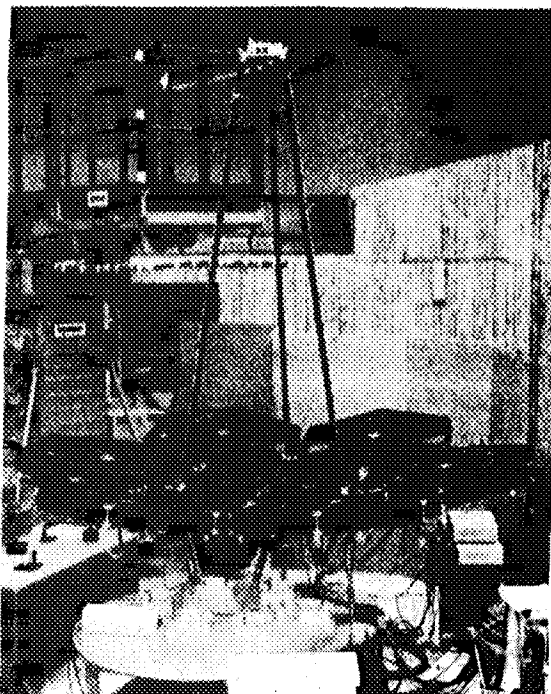
System ID Results



- Frequency Response Measurement
- Neural Replicator Frequency Response

Figure 5.2-4 Beam Experiment Shows Excellent Convergence Results After 100 Seconds

Multi-Hex Prototype Experiment (MHPE) Addresses Vibration In Large Optics



- 4M Diameter Cassagrain Configuration
- Vibration Control System Uses Nine LPACT Sensor/Actuator Units

MHPE System ID Results

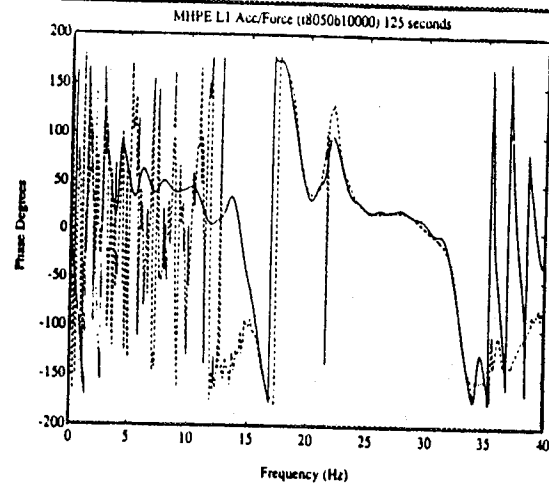
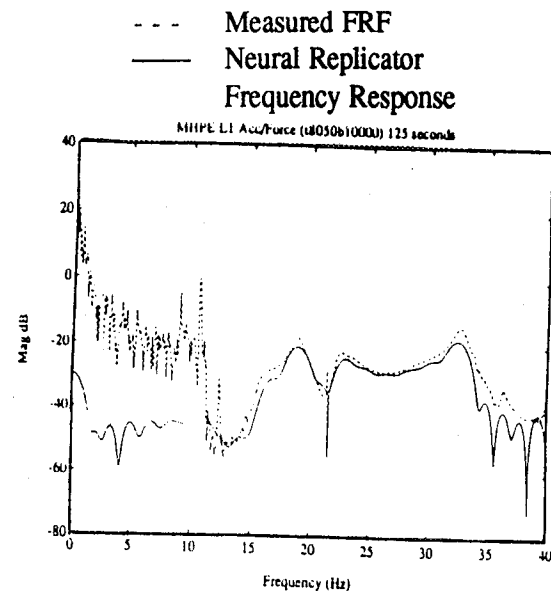


Figure 5.2-5 Neural Network Closed-Loop System Identification Experiment was Performed on the Dynamically Complex Multi-Hex Prototype Experiment (MHPE) Testbed

In the control adaptor, there is an internal model of the plant, copied from the plant modeller. Thus the control adaptor can, in effect, back-propagate error through the plant to the controller output location. With its internal model of the plant, the adaptor uses the training signal, its own output and that of the reference system to adjust its weights so that the reference system is replicated.

Figure 5.2-6 shows an early example of ANC operation. Using a simulation model of the Mini-MAST facility, an ANC simultaneously performed system identification and control optimization. In this example, the ANC was required to achieve more than an order of magnitude closed-loop attenuation of the first bending mode pair of Mini-MAST leaving higher frequency modes unaltered. This basic control objective was obtained within 7.5 sec. of adaptation and exact agreement with desired closed-loop response was attained after four minutes of adaptation.

In its detailed operation, the ANC carries out a sequence of steps analogous to the modelling ID and design refinement steps carried out by human designers within a streamlined design and test methodology. However, the ANC carries out these steps tremendously faster and without direct human supervision.

The above example helps to illustrate the potentially enormous savings in time and effort for development of initial space structure control design. Note that by typical performance standards set by the human G.I.s on the Mini-MAST testbed during the CSI GI Program Phase 1, the control design obtained by ANC (Figure 5.2-6) is quite respectable. However, rather than requiring an elaborate design model together with a man year of effort with several hours of on-site testing, ANC obtains its results without prior information on the testbed and within less than five minutes of unsupervised operation!

The above gives the motivation for demonstrating ANC in the laboratory using the CEM Phase 2 testbed. The CEM and subsequent results, described below, strongly reinforce our belief in the effectiveness of the ANC architecture for autonomous spacecraft control.

5.3 Adaptive Neural Control Testing on the Phase 2 CEM Facility

Originally, it was planned to test an ANC controller on-site at the Phase 2 CEM facility in July 1993. However, the fixed-gain control test scheduling difficulties described in Section 3 precluded an ANC test by the Harris team. Fortunately, because of long term technical collaboration and frequent informal interchanges in the ANC area, NASA/LaRC personnel were able to implement and test a basic version of ANC on the Phase 2 CEM in August 1993. Details of this work are described by Phan in [47] but for completeness, the approach taken and the experimental results obtained are reviewed here.

ANC Performance Goals: Reduce first bending mode response by > 20 dB

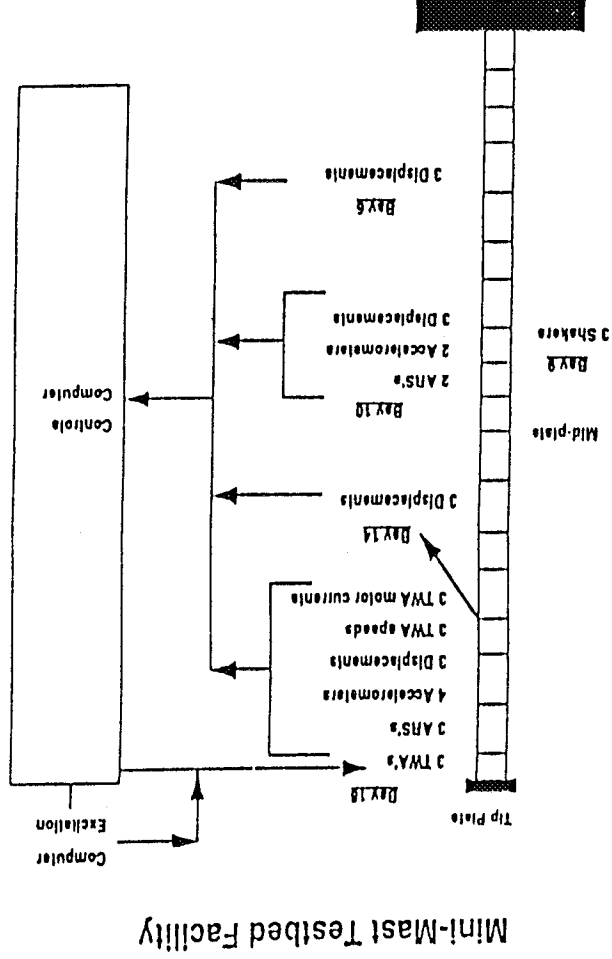
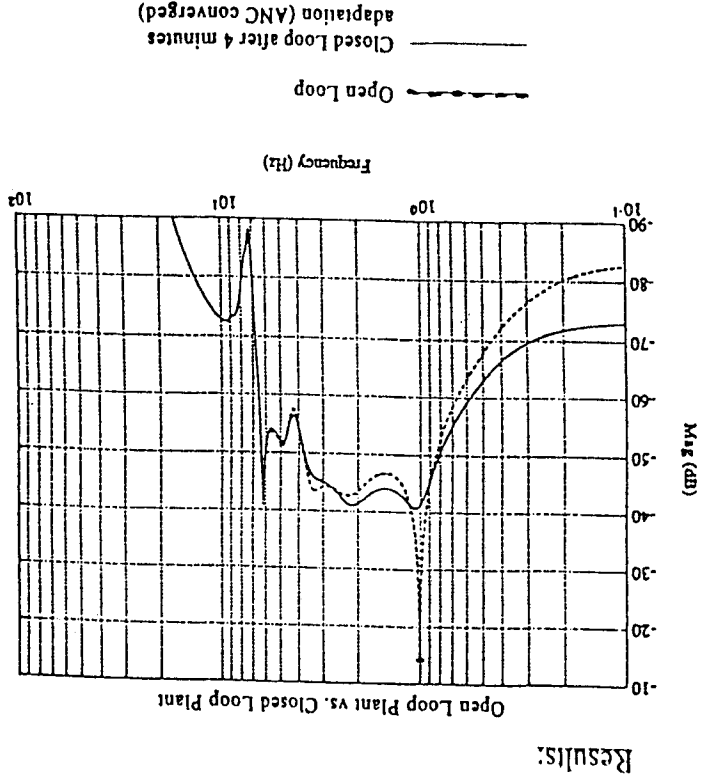


Figure 5.2-6 Simulation Results for the LaRC Mini-MAST Testbed Demonstrate Simultaneous System Identification and Control Optimization

First, a simplified version of the most general ANC model reference adaptive control scheme was used. Figure 5.3-1 sketches the overall controller architecture. The on-line controller is an IIR system that is constrained to be the optimal one-step ahead or deadbeat controller for the identified plant. In other words, the ARMA model coefficients of the controller are pre-specified as linear functions of the ID model coefficients (and reference model coefficients) such that when the ID model matches the plant, the controller will drive the plant to track the reference system within two time steps (allowing for the inherent delays in the system). This is a simplification of the most general ANC scheme which addresses the adaptive determination of the optimal L-step-ahead ($L \geq 1$) controller. With $L=1$, the adaptive control problem devolves into the plant identification problem. As indicated in Figure 5.3-1, only the ID model is adaptively updated and the controller is essentially copied from the plant model.

A basic aspect of the ANC approach is that the plant is identified using a series parallel model not a parallel model. The distinctions between these two basic identification schemes is illustrated in Figure 5.3-2. In the parallel model approach, the ID model retains its recursive character during training — i.e. delayed values of the model output, \hat{y} , are fed back. This scheme has serious difficulties connected with convergence of the adaptive process and sensitivity to initial neural weights. In contrast, during training of the series-parallel model, delayed values of the actual system output, y , and not the model output, are fed back to the model. Basically, the series-parallel model can be viewed as a *predictor* (or estimator): Given the past history of the system output, the goal of the ID model is to predict the next value of y . With the series-parallel approach, it is relatively straightforward, under broad conditions, to prove global convergence of the adaptive process. Moreover, after training is complete, one can then run the ID model in the parallel mode, with \hat{y} matching y . Not only does the series-parallel approach have better convergence properties but, the predictor/estimator character of the model permits the overall adaptive scheme to tolerate significant nonlinearities in the plant even when linear identification models are used.

As shown in Figure 5.3-1, the controller parameters are also dependent upon the reference model parameters. The ANC architecture allows wide latitude for the selection of the reference model and in the present implementation, the reference model is constructed using the OKID (Observer/Kalman Filter Identification) algorithm. Basically, the ID model generates an (A, B, C) realization of the plant. Using this data, OKID finds M such that $A+MC$ is deadbeat of order p . Finally, from A, B, C and M the ARMA coefficients of a reference model that is deadbeat of order p are computed. This process gives a reference model that represents a maximally damped version of the current plant model.

Figure 5.3-3 illustrates the manner in which the Phase 2 CEM facility was used for ANC testing. Gimbal #1 was used as the disturbance source by performing periodic scanning motion.

- Model reference adaptive control for both linear and non-linear systems with neural network ID model used as predictor

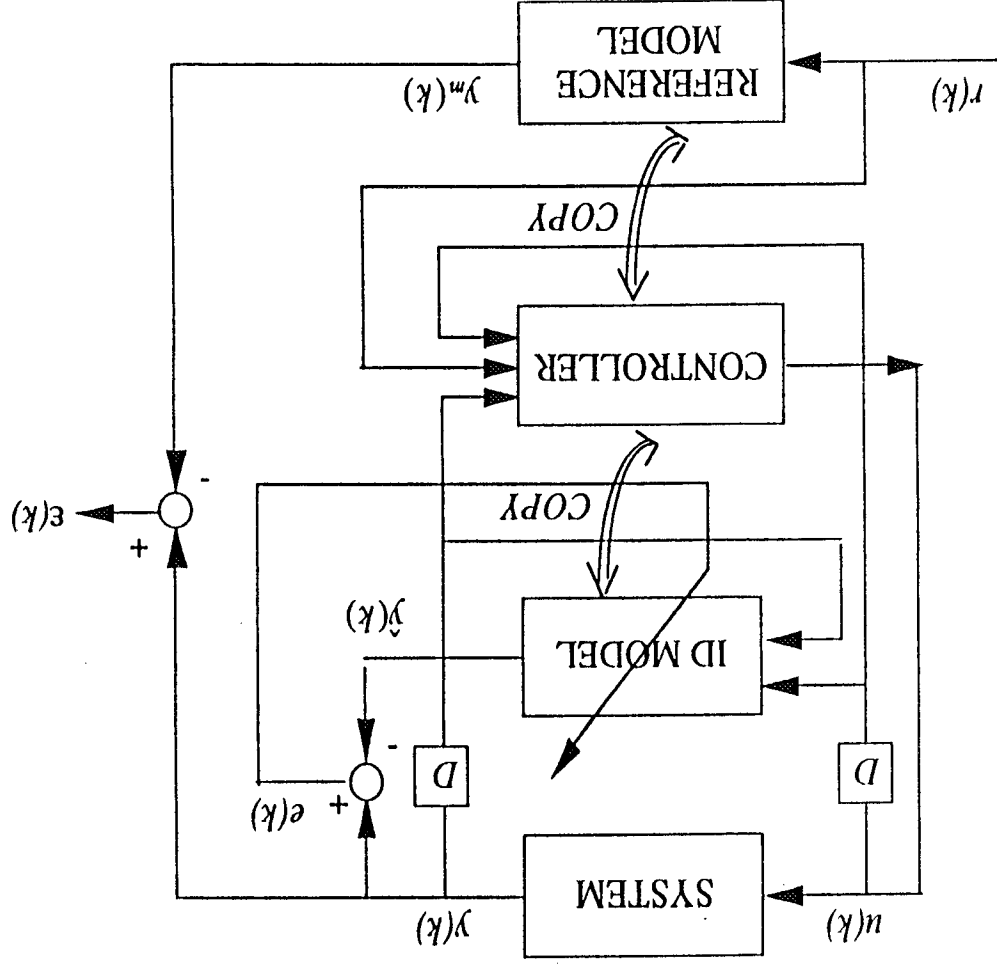
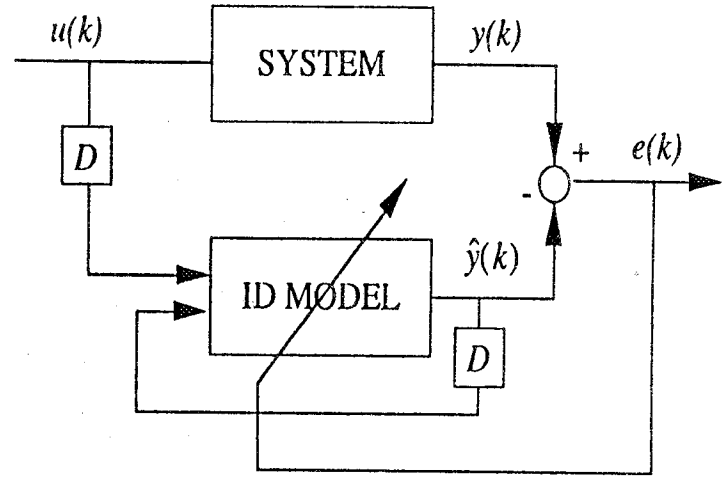


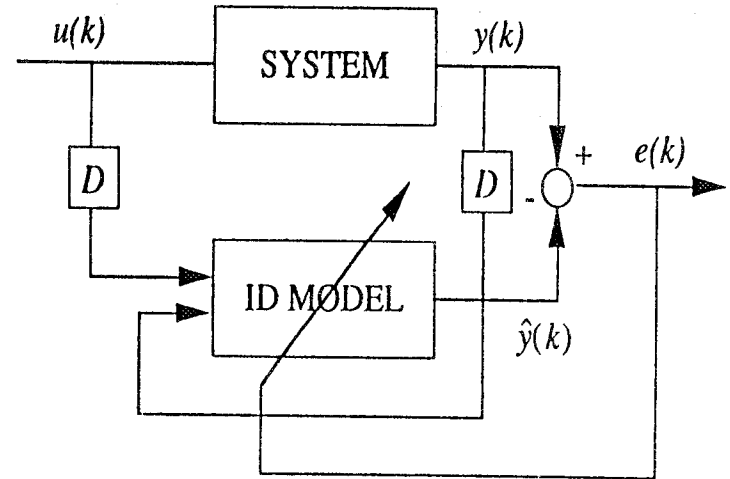
Figure 5.3-1 Control Using Neural Networks - Simplified Version of ANC Using a Constrained - Deadbeat Controller Form

Figure 5.3-2 Two Basic Identification Schemes

- Identification using parallel model



- Identification using series-parallel model



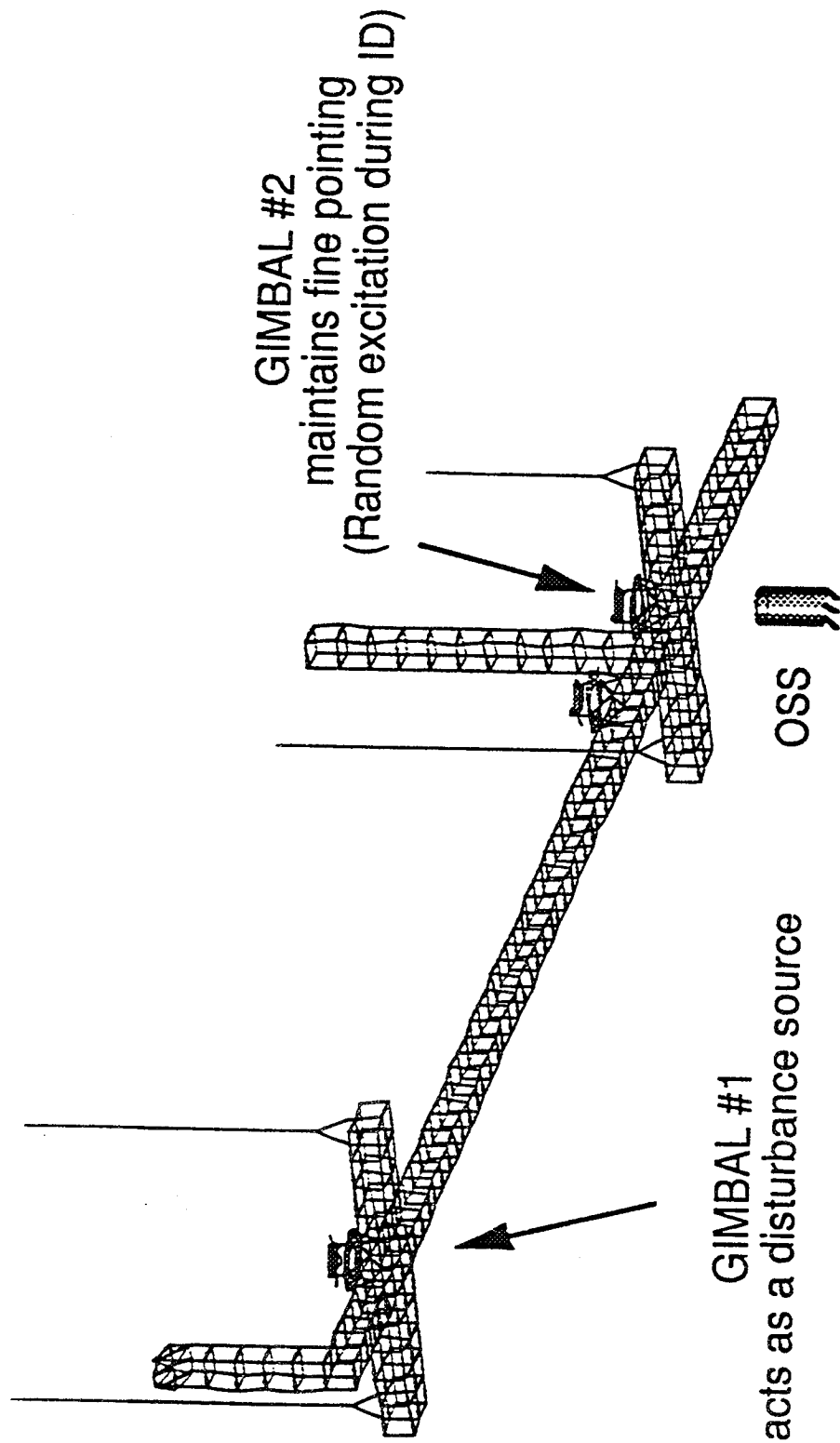


Figure 5.3-3 CEM Testbed Configuration used for Adaptive Neural Control Testing

The objective was to maintain fine pointing in Gimbal #2, using the OSS for line-of-sight performance measurements. The basic ANC algorithm, described above and in Figure 5.3-1 was implemented on-line in the CEM facility IBM RISC/6000 processor at 60 Hz sampling rate. The experimental results are due to C. Sandridge and M. Phan of the CSI Ground Test Method team.

Figure 5.3-4 and 5.3-5 show experimental results for Gimbal #1 commands (the disturbance) and corresponding OSS-measured line-of-sight errors for Gimbal #2 along two orthogonal gimbal axes. In a typical test sequence a broadband excitation is first commanded through Gimbal #1 for 10 seconds. This disturbance serves as the training stimulus for the identification process. Once the identification is completed a periodic scanning disturbance is injected into the system through Gimbal #1 for the remaining ten seconds (from time = 25 seconds to time = 35 seconds). During this ten second scanning disturbance period, the controller is first turned on for 5 seconds and is then turned off for 5 seconds. The pointing accuracies of Gimbal #2 along both axes during these events are shown in the lower plots of Figures 5.3-4 and 5.3-5. It is evident that, in the presence of the scanning disturbance, the controller achieves more than an order of magnitude improvement in the total rms pointing accuracy relative to the open-loop performance.

The performance of the identification process is illustrated in Figures 5.3-6 and 5.3-7. Figure 5.3-6 shows the convergence of the ID model parameters. Evidently, these parameters have attained their steady-state values during the ten second identification period.

This parameter convergence translates into ever decreasing model prediction error as illustrated by the prediction error time histories in Figure 5.3-7. With the small parameter errors and output prediction errors obtained at the end of the identification phase, the controller is then equipped to drive the actual plant to track the reference model.

In summary, thanks to close technical interchange and technology transfer the original goal for testing ANC was met. The above results demonstrate the effectiveness of a basic ANC implementation involving a deadbeat constrained controller coupled with a neural identifier.

5.4 Additional ANC Results and Further Directions

Since the CEM testing described above, more experimental results have been obtained and additional applications areas have been opened up for the ANC architecture. Here, we briefly sketch these more recent developments and indicate future avenues of progress.

The ANC algorithm tested on the CEM was limited in various respects. In particular, the scheme used sequential identification and control, employing an externally injected training signal for adaptation. Also, control was essentially demonstrated for only a relatively narrow frequency band (centered around the periodic scanning frequency). Various continuing efforts have

CEM EXPERIMENTAL RESULTS (Disturbance Rejection - First Input-Output Pair)

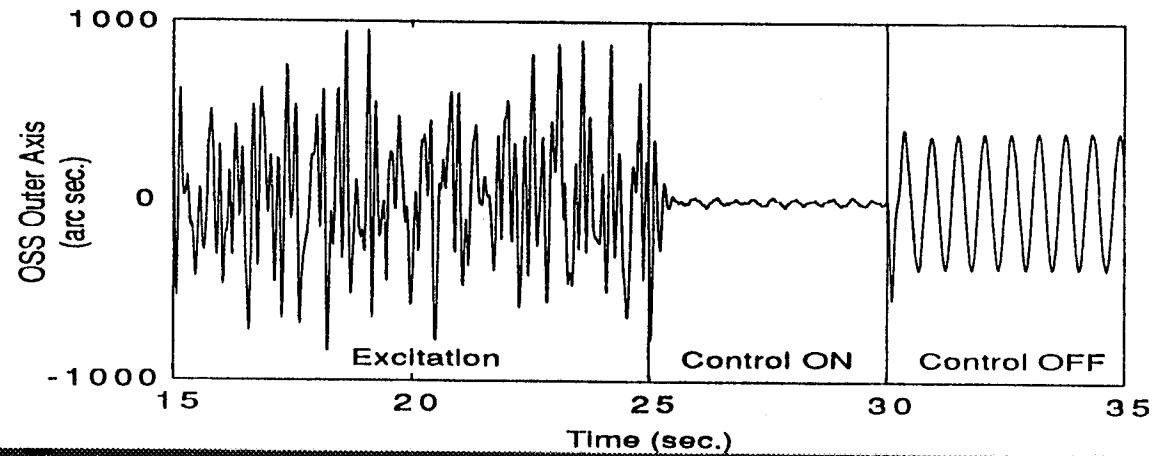
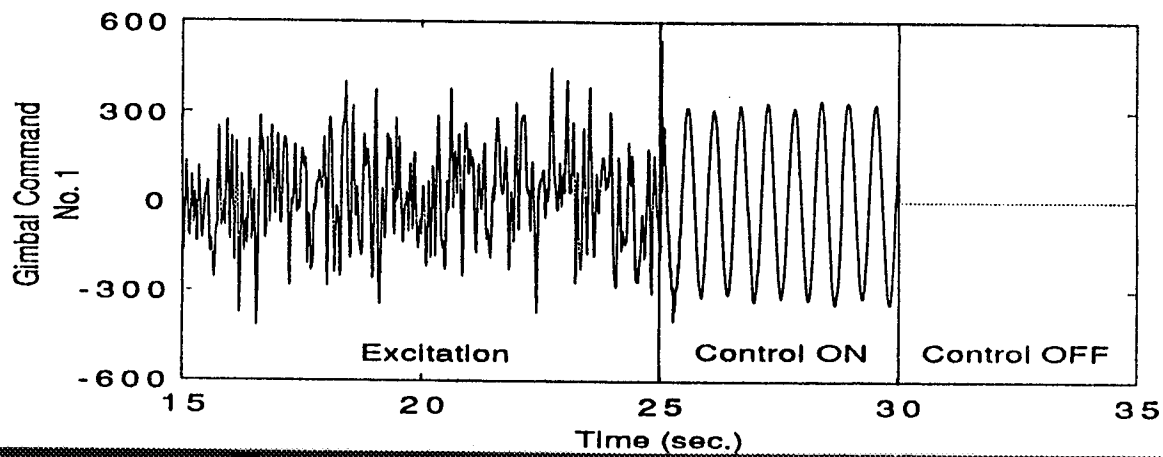


Figure 5.3-4 CEM Experimental Results
(Disturbance Rejection - First Input-Output Pair)

CEM EXPERIMENTAL RESULTS (Disturbance Rejection - Second Input-Output Pair)

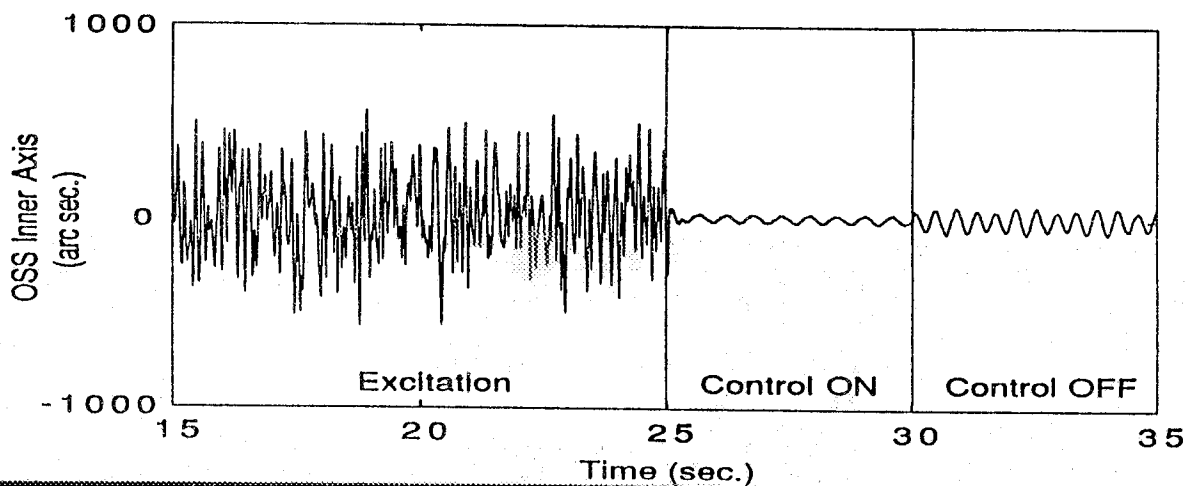
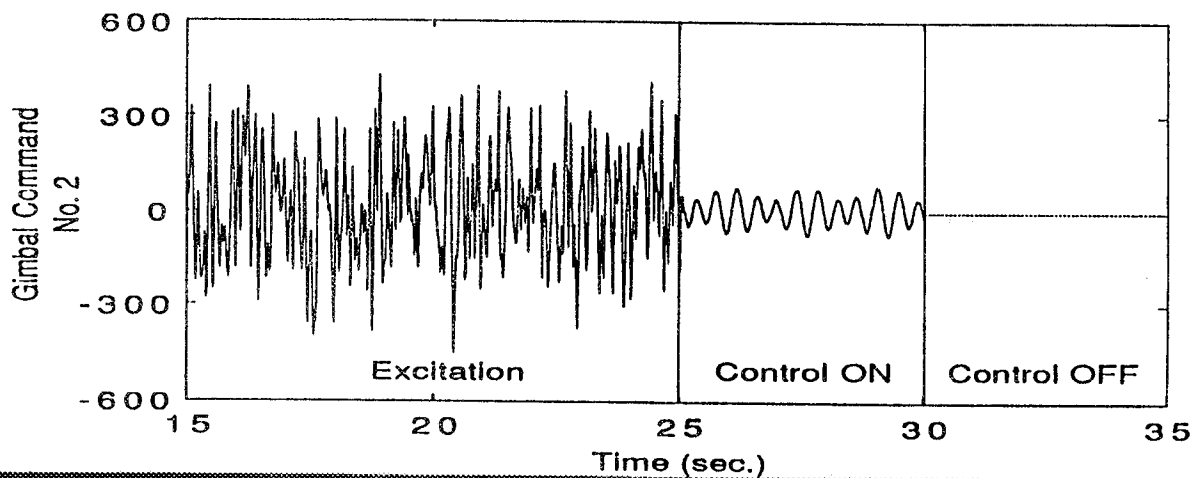


Figure 5.3-5 CEM Experimental Results
(Disturbance Rejection - Second Input-Output Pair)

**CEM EXPERIMENTAL RESULTS
(On-line Adaptive Parameter Identification)**

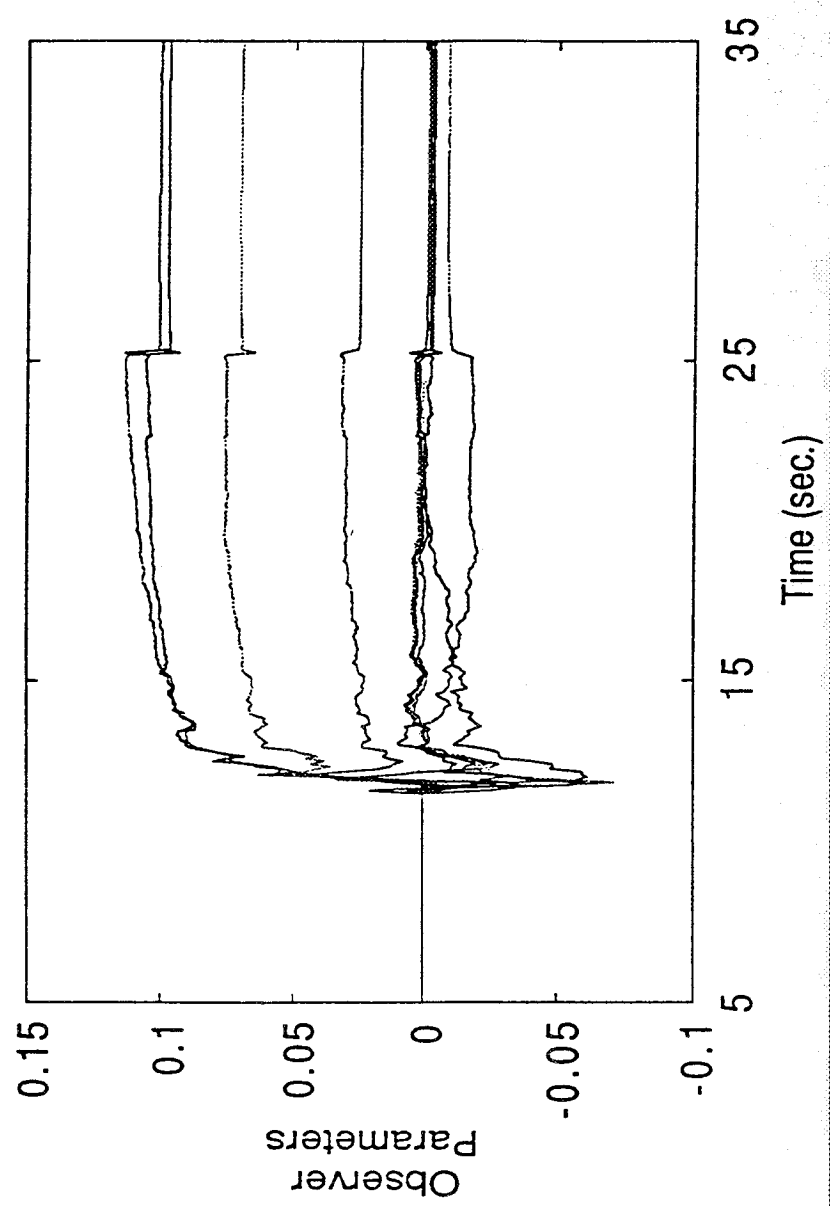


Figure 5.3-6 CEM Experimental Results
(On-Line Adaptive Parameter Identification)

CEM EXPERIMENTAL RESULTS (OSS On-line Prediction Error)

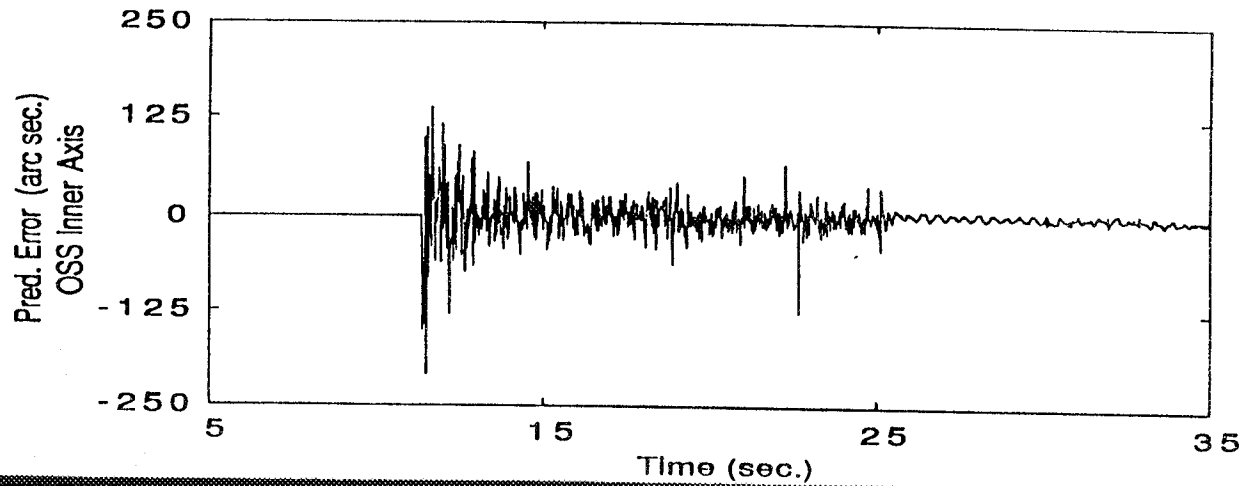
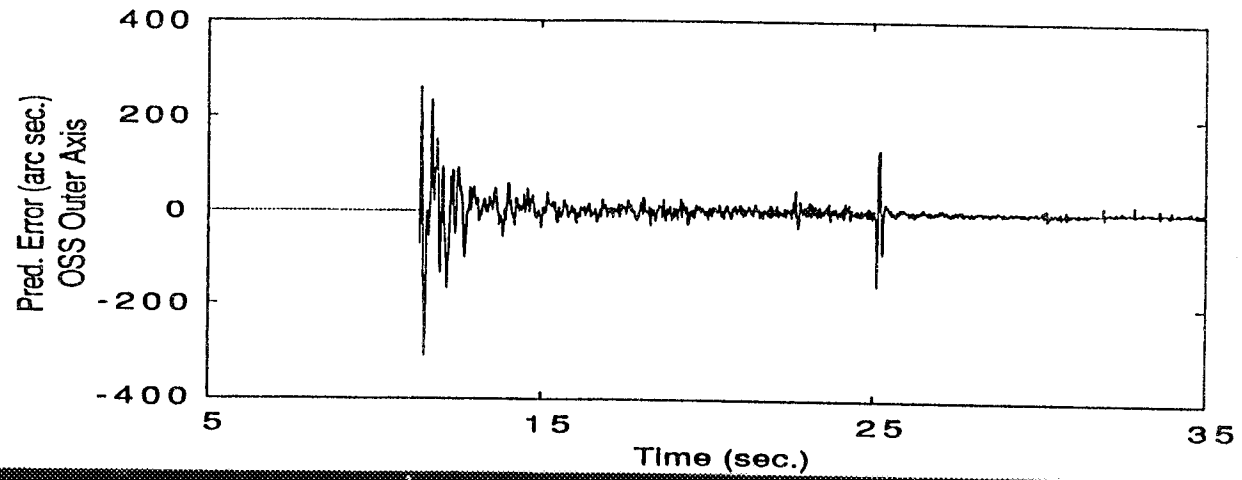


Figure 5.3-7 CEM Experimental Results
(OSS On-Line Prediction Error)

removed these restrictions to provide demonstration of a more complete realization of the ANC architecture.

In particular, Harris is finishing (at the time of writing) Phase 1 of the Adaptive Neural Control program for the Air Force Phillips Laboratory. The goals of this two year program are to design an advanced ANC system, fabricate the ANC hardware in the form of a multi-processor system and demonstrate the hardware on the Phillips Lab ASTREX testbed. The intermediate goal of Phase 1 is to demonstrate a basic ANC prototype on the Harris Multi-Hex Experiment (MHPE) test facility. The MHPE is in the form of a 4-meter diameter Cassagrain telescope with segmented primary and is instrumented with accelerometers and Linear Precision Actuators (LPACTs) to execute vibration control. The extended ANC algorithm that has been recently demonstrated on the MHPE using a PC-interfaced DSP uses no externally supplied broadband training signal and executes system identification and control adaptation simultaneously. The extended algorithm makes use of several accelerometers near the MHPE base as well as secondary mirror tower accelerometers (used to reconstruct LOS error) in order to secure the sensory redundancy needed to train the network on the ambient disturbances alone. Moreover, the experiment was designed to test LOS error suppression over a fairly broad frequency band in the presence of broadband disturbances. Figure 5.4-1 illustrates the results by showing open-loop versus closed-loop magnitude plots for the frequency response at one error sensor. Clumps of resonances near 10 and 15 Hz are reduced to the instrumentation noise floor. The convergence time of approximately 3 minutes is longer than for the CEM results and the harmonic and multi-harmonic disturbance results (discussed below) because, in this case, the system must identify the plant dynamics over the entire frequency band of interest not just near discrete frequencies.

The foregoing experimental activities deal with adaptive control for DoD space applications, emphasizing broadband disturbances. However, the vast majority of commercial vibration control applications (and a good many DoD applications as well) involve disturbance sources (motors, engines, rotors, etc.) that are not broadband but primarily periodic or a sum of harmonics.

The ANC architecture has been adapted to this simpler set of disturbances, in a manner that streamlines the algorithm and speeds up convergence. The adaptive neural controller for discrete spectrum disturbances is able to simultaneously identify all needed transfer functions *and* adapt the actuator inputs without interrupting normal operation or injecting an extraneous broadband test signal (dither). Moreover, the adaptive algorithm is fast: with no previous identification, completed vibration suppression is achieved in three iterations; once transfer coefficients are identified, control adjustment can be accomplished in one step. Thus the neural controller is able to autonomously react to rapid changes in the disturbances or in the system dynamic characteristics.

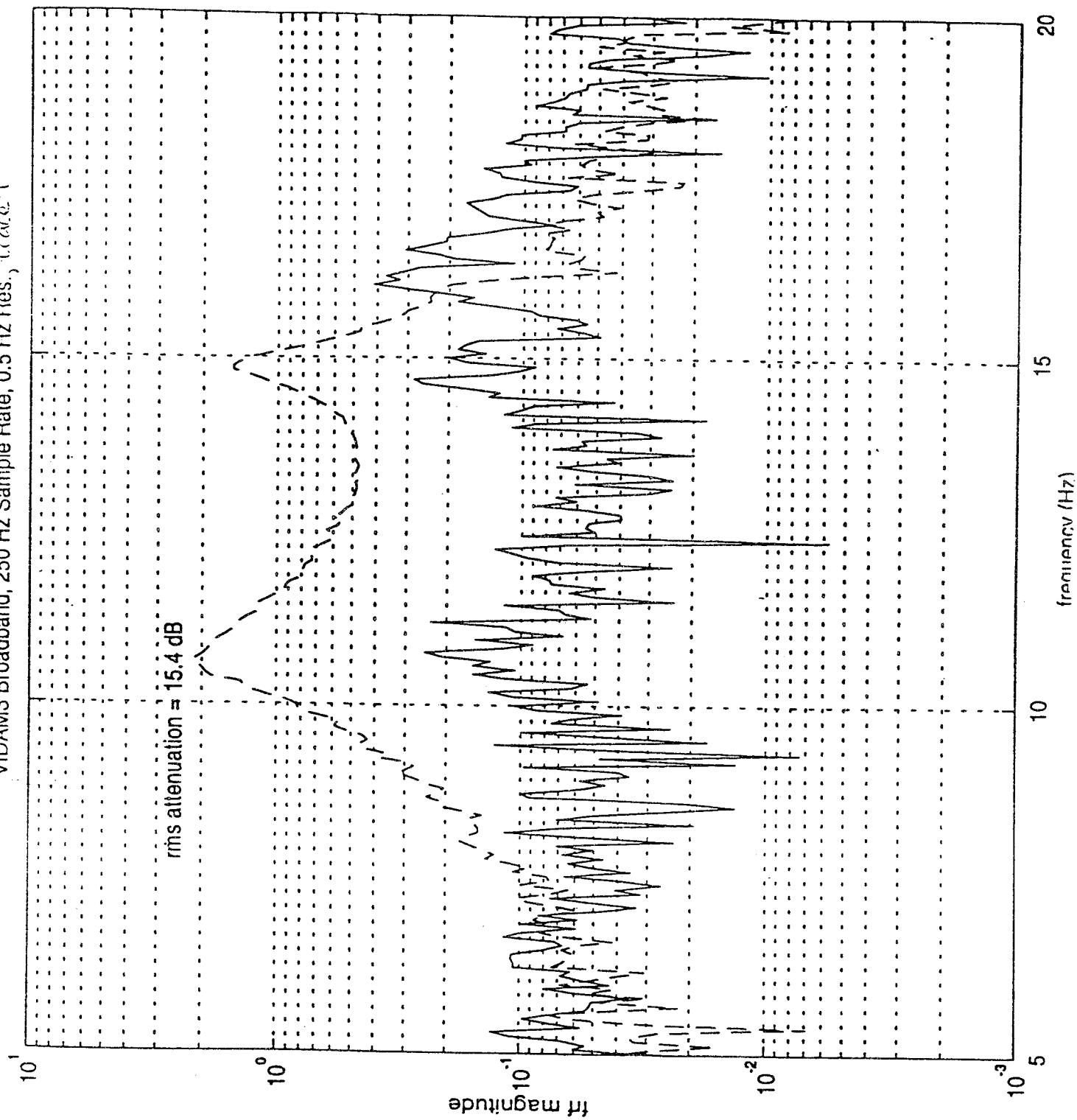


Figure 5.4-1 Adaptive Neural Control was Demonstrated using the MHPE Testbed

Recent Harris IR&D projects proceeded in two stages, with the following results.

1. **Single-Tone (Harmonic) Disturbances:** Disturbance sources for the majority of commercial applications (e.g. fan noise, automobile engine noise, aircraft cabin noise, etc.) are dominated by a fundamental harmonic component. The ANC algorithm for harmonic noise suppression was implemented with a PC interfaced DSP and demonstrated on three entirely different laboratory testbeds: An acoustic duct, a test rig for a vibration isolation proof mass actuator and the MHPE testbed, a precision optical structure. Live demos are documented in the Harris Corporation video "Adaptive Noise and Vibration Cancellation Demo". Starting from a clean slate (no prior identification data) the system converges in a fraction of a second. The video shows how ANC can track smooth changes in system dynamics, and can quickly recover after dramatic, sudden system changes. Moreover, the same algorithm, without modification, is shown to work on many different types of systems. Over 20 dB noise or vibration reduction is achieved in all cases.
2. **Multi-Tone (Several Harmonics) Disturbances:** This is a significant feature in most applications – e.g., nonlinearities in engines and motor mounts produce higher harmonics and sub harmonics in addition to the fundamental tone. The ANC system for this case combines a fast neural demodulator unit with an array of single tone cancellors. Multi-tone cancellation is routinely demonstrated in the laboratory. For example, Figure 5.4-2 shows results for two relatively closely spaced harmonics. Over 30 dB and approximately 40 dB attenuation is achieved on the two tones. Starting with no prior transfer coefficient information, simultaneous identification and control are achieved in approximately one second.

Judging from the work to-date, demonstrated ANC capabilities offer great promise in achieving the kind of autonomy, adaptability and fault tolerance features that are desired for intelligent commercial and space systems. Much remains to be done to implement practical ANC systems but the NASA/LARC and Harris collaboration, facilitated by the GI program has been an invaluable stimulus to the emergence of this new technology.

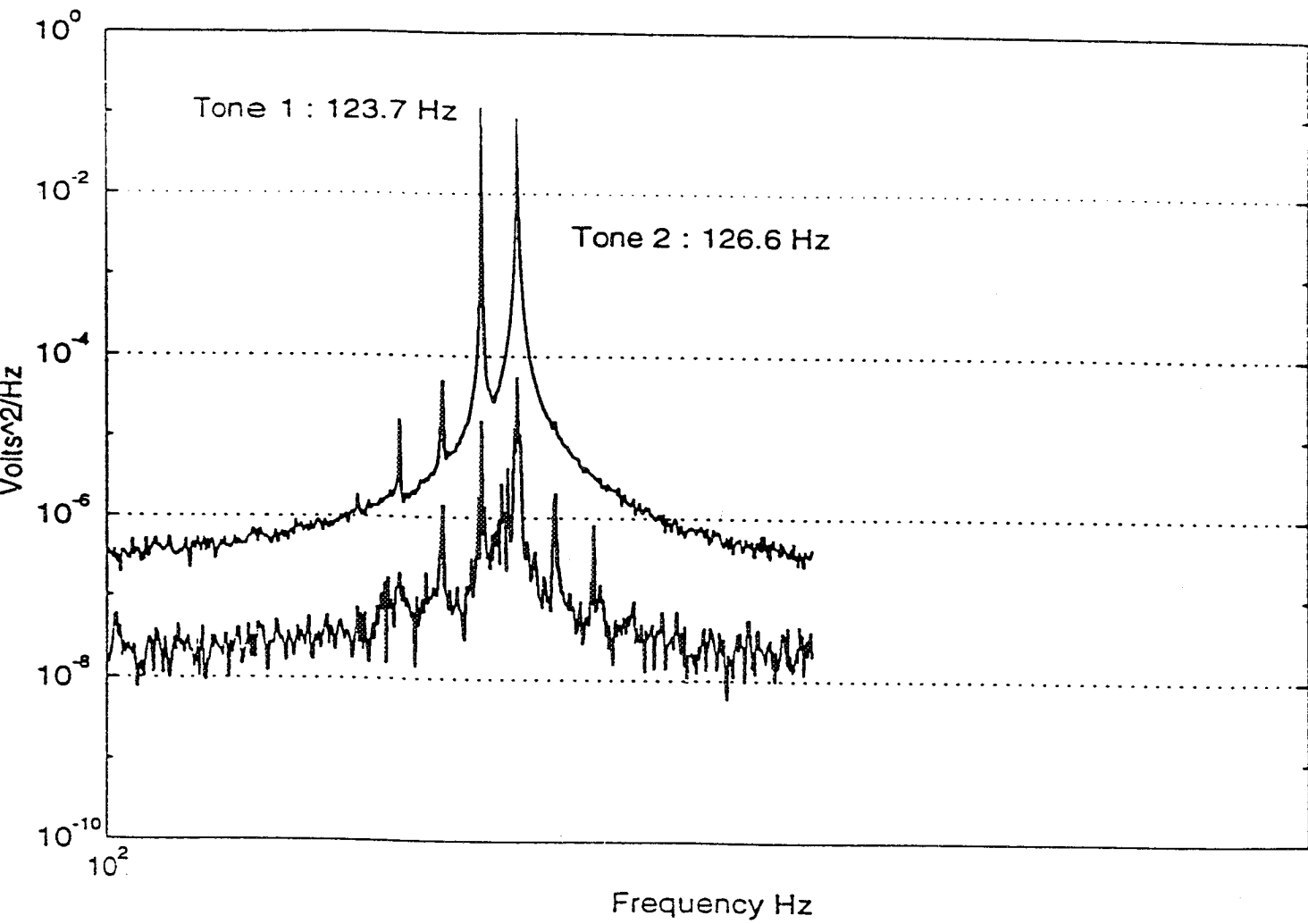


Figure 5.4-2 Multi-Tone Neural Algorithm Results



6. PHASE II: VIBRATION ATTENUATION MODULE TEST ON THE CEM

6.1 Introduction

Besides the development of streamlined and automated control design capabilities, one of the most pressing needs in vibration control is the refinement of self-contained, modular vibration suppression hardware. A key component in any overall vibration suppression strategy is the technology to either isolate sensitive equipment from vibrating structure or to isolate structure from a source of disturbances. Moreover, the vibration isolation strategy lends itself well to self-contained, modular hardware solutions. This was the inspiration for the invention of the Harris Active Isolation Fitting (AIF) and the related Vibration Attenuation Module (VAM).

The AIF is a high stiffness, active device for vibration isolation that replaces passive struts and end fittings in truss structures. The VAM is a six-degree-of-freedom vibration mount built up from six AIF's and capable of more than 20 dB isolation over a broad frequency band. These two devices are described in more detail in the next section.

By November 1993 a VAM unit was fabricated and bench-tested within a Harris IR&D program. The VAM hardware was installed and tested on the new Phase 3 CEM configuration (reassembled from the Phase 2 configuration in September 1993) in February 1994. Additional tests of a refined design were carried out under a Cooperative Technology Development Agreement between Harris and NASA/LaRC with Harris IR&D support. These results are reported separately. The approach was to replace a SIS support truss (connecting the gimbal package with the main CEM structure) with the VAM and, by measuring the SIS line-of-sight error, demonstrate active vibration isolation of the SIS from disturbances injected elsewhere on the CEM structure. AIF's and VAM's are discussed in Section 6.2. For completeness, Section 6.3 gives a description of the Phase 3 CEM configuration. The VAM test procedures and results are presented in Section 6.4.

6.2 AIF and VAM Overview

As part of Harris' vibration suppression hardware research efforts, the Active Isolation Fitting (AIF) has been under development for the past several years on IR&D. The AIF is an active device for vibration transmission cancellation that would replace ordinary mechanical end fittings and joints in truss structures for space systems.

To describe the basic capabilities of the AIF, it is important to distinguish between intrastructural damping approaches to isolation and *active* isolation. Figure 6.2-1 illustrates this distinction. We concentrate on the simplest case in which it is desired to modify a uniaxial member connecting a *base body* (wherein vibration disturbances originate) to an *isolated body* so as to reduce the isolated body's vibration. The intrastructural approach (left hand side of Figure

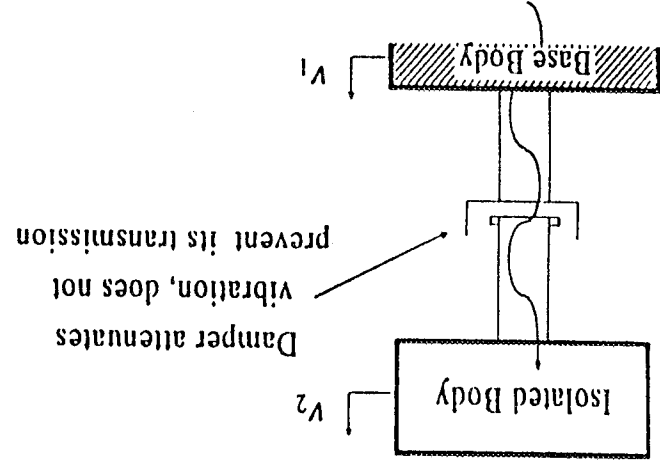
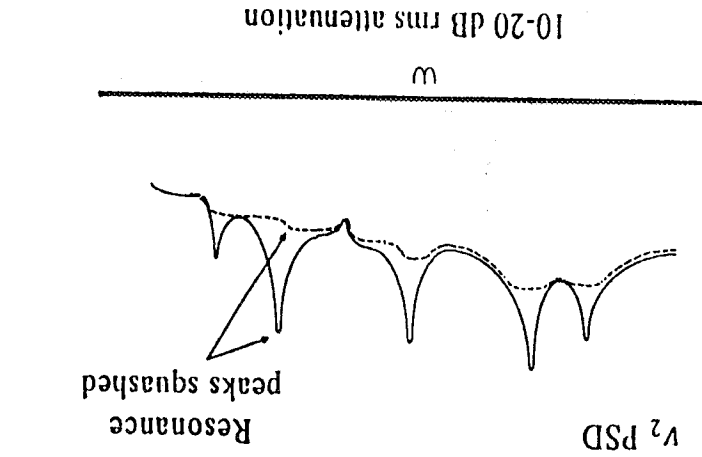
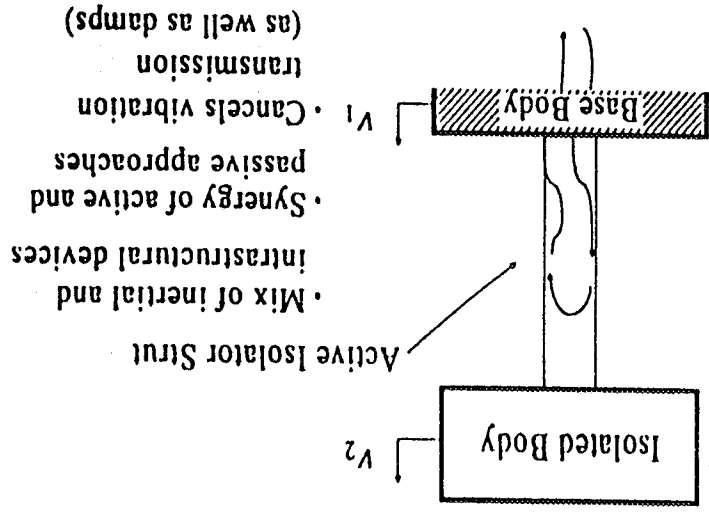
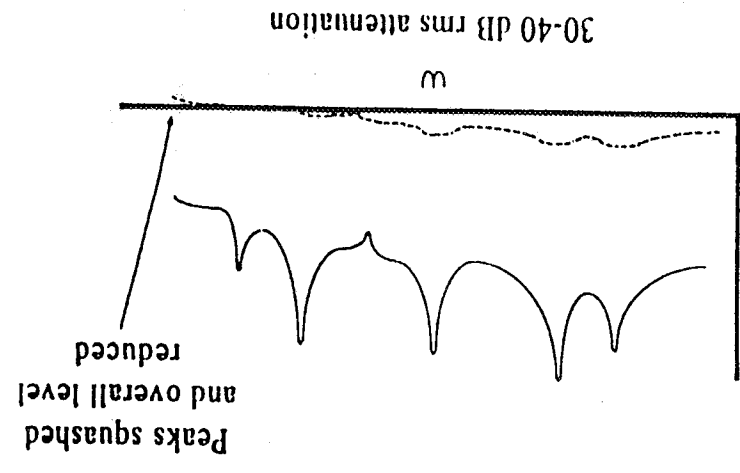


Figure 6.2-1 Both Resonant and Nonresonant Response is Suppressed Using Active Isolation

6.2-1), essentially inserts a damper between the two bodies so as to dissipate energy. This can be implemented passively (e.g., viscoelastic material treatment, fluid dampers, etc.) or actively (e.g., a piezoelectric actuator with collocated strain sensor closing a strain rate feedback loop). In any case, because the isolator member not only damps but also *transmits* vibrational energy, it is possible to reduce the resonance peaks of the isolated body response but not appreciably reduce the broadband, nonresonant response (see PSD sketch on lower left of Figure 6.2-1). This results in significant performance limitations.

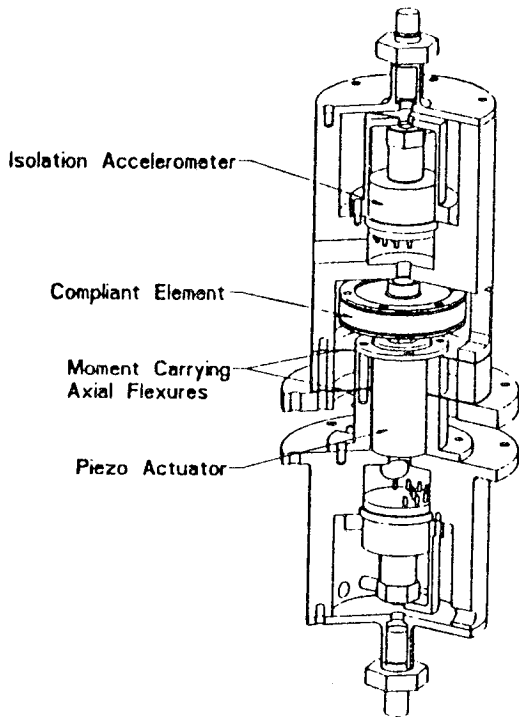
In contrast (see right side of Figure 6.2-1), the Harris AIF uses a mix of inertial and intrastructural devices and both active and passive control techniques to prevent vibration *transmission* into the isolated body. The AIF also implements active intrastructural damping to dissipate residual vibration energy. As indicated in the lower right of Figure 6.2-1, the effect on the isolated body is equivalent to reducing the overall disturbance input. Because of this principle, 20-30 dB of broadband isolation is achieved without exotic hardware. Both resonant and nonresonant response of the isolated body are suppressed over a broad frequency band. Moreover, the AIF device does not require detailed design knowledge of the isolated or base body dynamics nor of the disturbances, as is the case for feedforward cancellation of narrow band or harmonic disturbances, for example.

Unlike other active isolation approaches (e.g., magnetic suspension/isolation technology), the AIF is low power, consists of inexpensive off-the-shelf components (as illustrated in Figure 6.2-2) and (in contrast to voice coil concepts for intrastructural isolators) fails gracefully by reverting to a stiff mechanical member upon sensor or actuator failure.

The principal challenge in realizing the performance potential of active isolation, while achieving the high stiffness and robustness properties noted above for the AIF, was to discover the correct sensor and actuator types and the right feedback/feedforward control architecture. There are a multitude of conceptually plausible approaches but most of them fail in practice.

Over four years, Harris' Internal Research and Development (IR&D) efforts performed an exhaustive search for the most appropriate combination of sensors, actuators and control architecture. Figure 6.2-2 shows the essential mechanical and control aspects of the AIF design that finally resulted from this search. The design is a uniaxial connector device having an intrastructural actuator (a piezoelectric stack is the preferred embodiment but other types of prime-movers can be utilized, depending on stroke and bandwidth requirements) and two high bandwidth accelerometers, one near each end. The control strategy involves the interplay of two single, nonadaptive control loops. The "bottom" or "inboard" loop involves the base-body end accelerometer and the piezo stack and provides feedforward cancellation of the incoming disturbance.

Mechanical Configuration



- Off-The-Shelf Components:
 - Piezo stack actuator and integrated strain sensor
 - Two hybrid-accelerometers
 - Compliant interface element with passive damping treatment
- Can be packaged within a small envelope.

Control Architecture

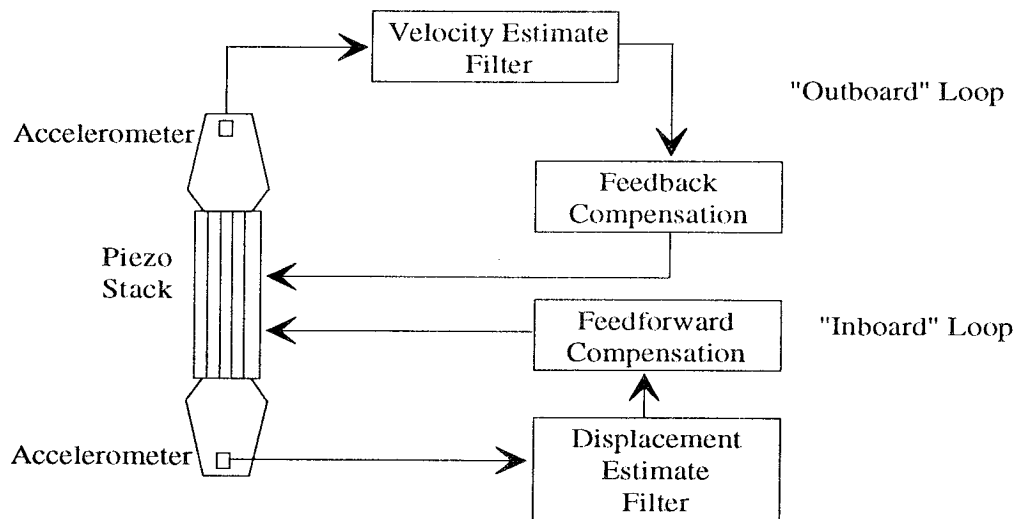


Figure 6.2-2 AIF Combines Off-The-Shelf Components to Provide Inexpensive, Highly Effective Isolation

The "top" or "outboard" loop involves the isolated-body-end accelerometer and the piezo stack to inertially stabilize the isolated body (or payload) end of the fitting. These two loops work synergistically to achieve high performance isolation. The inherently stable design depends only on the AIF dynamic characteristics and needs very little "tuning" to adjust to the detailed dynamic characteristics of the base body or the isolated body. Moreover, stability and performance are not sensitive to other AIF's in the system so that more complex isolators can be built up from independent AIF units.

Furthermore, both control loop compensator gains roll-down below a lower cutoff frequency. Below this frequency, the AIF behaves as a stiff, passive structural connector.

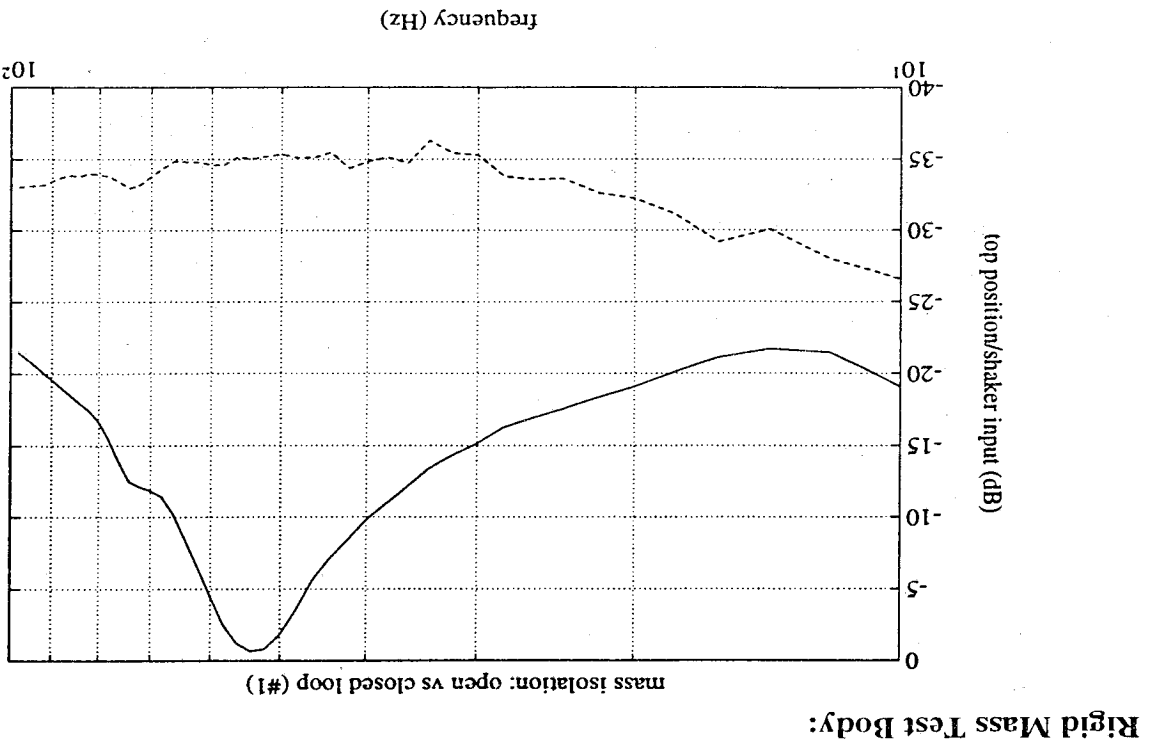
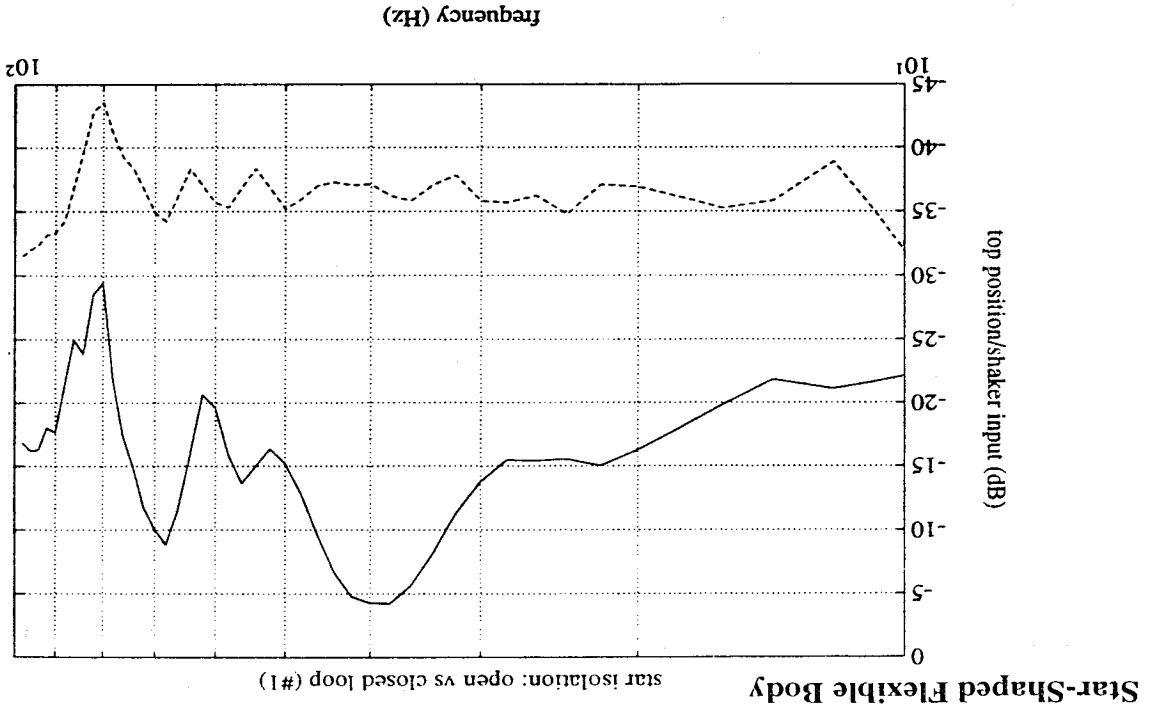
The AIF has been extensively demonstrated in the laboratory. Figure 6.2-3 shows test results for two kinds of isolated body (a rigid mass and star-shaped flexible body with complex modal dynamics in the frequency band of interest). For both cases, we show the magnitude of the shaker disturbance input to isolated body position transfer functions for open- and closed-loop operation. 10 to 35 dB attenuation is obtained over 10 to 100 Hz. These results also illustrate that performance is not sensitive to the dynamic characteristics of the isolated body.

Furthermore, the AIF design can be adapted to a variety of applications. For example Figure 6.2-4 shows uniaxial test results for a higher bandwidth design. This design achieves 30 dB root mean square (rms) vibration reduction over the 10 to 200 Hz frequency band. Finally, even more impressive isolation results can be achieved by stacking AIF's into multi-stage isolators. Test results for a two-stage configuration are shown in Figure 6.2-5. This configuration attains 42 dB rms attenuation over the 10 to 200 Hz band. We should note that all of the above isolation results are obtained without reducing the static mechanical stiffness of the AIF. In other words the AIF does not achieve isolation by virtue of low mechanical stiffness but, instead, through the use of strictly active control strategies utilizing the piezoelectric actuator and two accelerometers.

The AIF can be packaged to serve as an end fitting or joint in truss structures. Several basic AIF modules (each, as in Figure 6.2-2, being uniaxial) are combined to carry out more complex isolation tasks. For example, multi-degree-of-freedom isolators are built of several AIF's and passive strut members. The simplest such assembly is a six-member (hexapod) mount, called the Vibration Attenuation Module (VAM) which provides six degrees of freedom isolation for sensitive equipment mounted outboard.

The VAM originated as a potential solution to vibration problems studied for the Air Force Phillips Lab under the Defense Meteorological Satellite Program (DMSP) Vibration Damping Study conducted in 1992. In a possible system upgrade, it was proposed to add a vector magnetometer attached via a 45 ft. Astromast boom to the DMSP spacecraft. Various options for the stabilization of the magnetometer package in the presence of Astromast vibrations

Figure 6.2-3 Broadband Isolation Using the Harris AIF is Demonstrated by Experimentally Measured Results



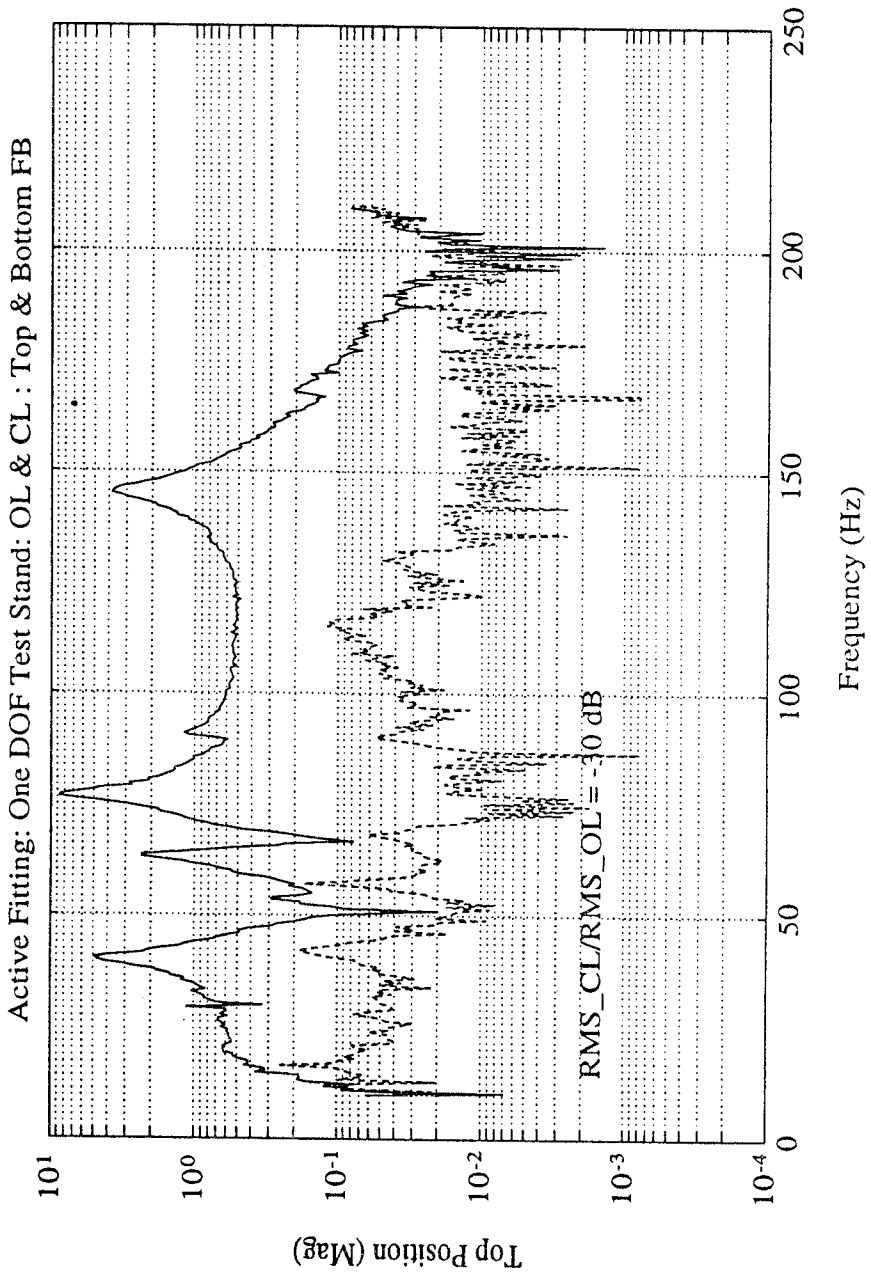
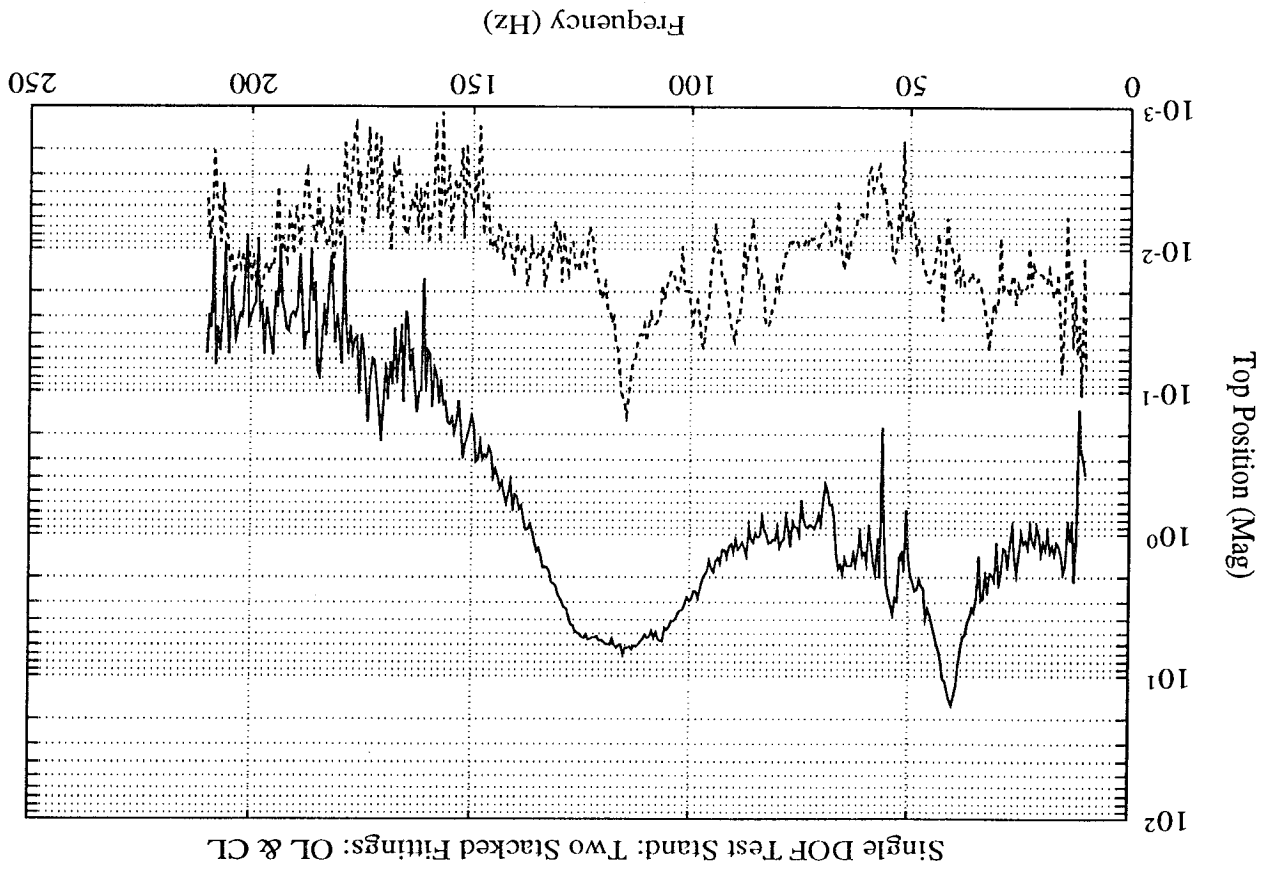


Figure 6.2-4 Active Fitting Test Data for a Higher Bandwidth Design and Flexible Isolated Body

Figure 6.2-5 Active Fitting Test Results for a Two-Stage System (Two AIF's in Series)



excited by spacecraft disturbances were studied. It was desired to devise a self-contained module requiring no modifications to the Astromast or deployment cannister and, more generally, arrive at a product that provides vibration protection to a wide variety of flexible appendages or gimbaled sensor packages. Furthermore, the device should protect against both spacecraft generated and appendage generated (e.g. thermal snap) disturbances. The resulting VAM design, shown in Figure 6.2-6, has an inboard interface plate and a smaller outboard interface ring connected together with six nominally identical AIF units each operating independently with its local sensors and actuator. VAM electronics is housed at the center of the inboard plate. As shown in Figure 6.2-7 for the DMSP application, the VAM is inserted between the DMSP bus and the Astromast deployment cannister. Figure 6.2-8 shows various open- and closed-loop results for the frequency response from a major spacecraft disturbance to the root-sum-square (rss) magnetometer attitude error. Note that if the VAM were used merely as an active augmented damper device (see the curve labeled "strain rate feedback only") only the vibration mode near 3 Hz and 19 Hz would be significantly attenuated. The attitude excursions below 2 Hz are unaffected in this case. However, with the full inertial isolation capabilities of the VAM (the solid curve in Figure 6.2-8), all response below approximately 4 Hz is significantly attenuated.

VAM's were found to have numerous space and ground-based applications involving noise abatement, vibration control and precision positioning, as Figure 6.2-9 illustrates. In the area of spacecraft applications, VAM's are particularly useful if one has a sensor payload that must be tightly coupled to the spacecraft bus (for precision pointing of the instrument via pointing of the bus) yet sensor precision requires significant isolation of the payload from bus generated vibration.

Although hexapods composed of AIFs have been successfully tested on other Government - supplied facilities, the first testing of a VAM as a integrated isolation mount occurred on the Phase 3 CEM. After a properly sized VAM unit was fabricated on IR&D in November 1993, it was installed and tested on the Phase 3 CEM in 1994 as part of the CSI GI program. In the next section we briefly review the Phase 3 CEM configuration then return to consideration of the VAM design and test results in Section 6.4.

6.3 Phase 3 CEM Testbed Description

In the fall of 1993, the Phase 2 CEM was reconfigured into a new configuration that exhibits dynamics representative of the EOS AM-1 spacecraft. This new EOS configuration is referred to as the Phase 3 CEM testbed.

The Phase 3 CEM model consists of a spacecraft bus structure, flexible appendages, gimbaled instrument simulators, and dummy masses to simulate both science payloads and spacecraft subsystems. In order to simulate the free-free behavior of the EOS AM-1 spacecraft in

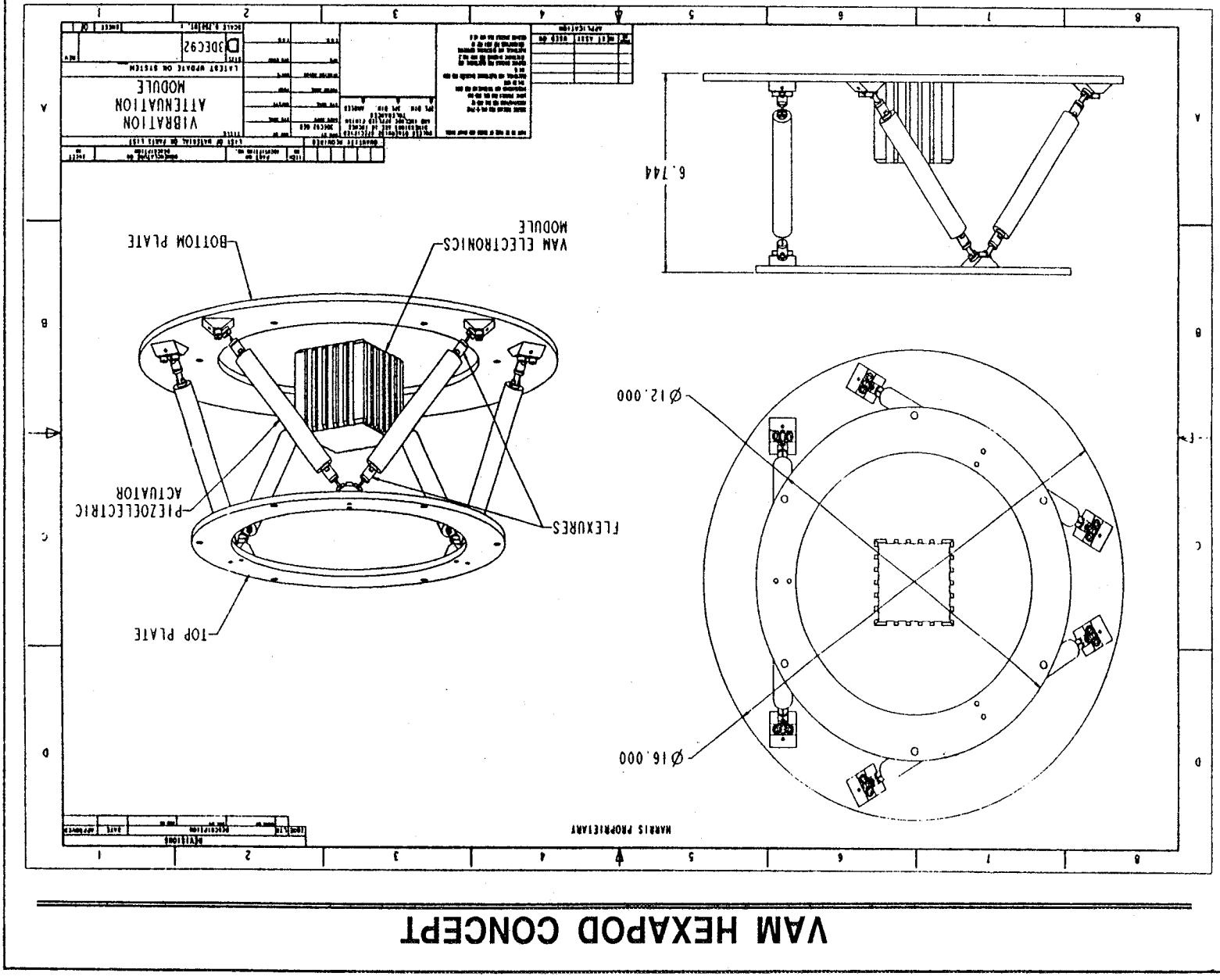


Figure 6.2-6 VAM Hexapod Concept



VAM HEXAPOD CONCEPT (CONTINUED)

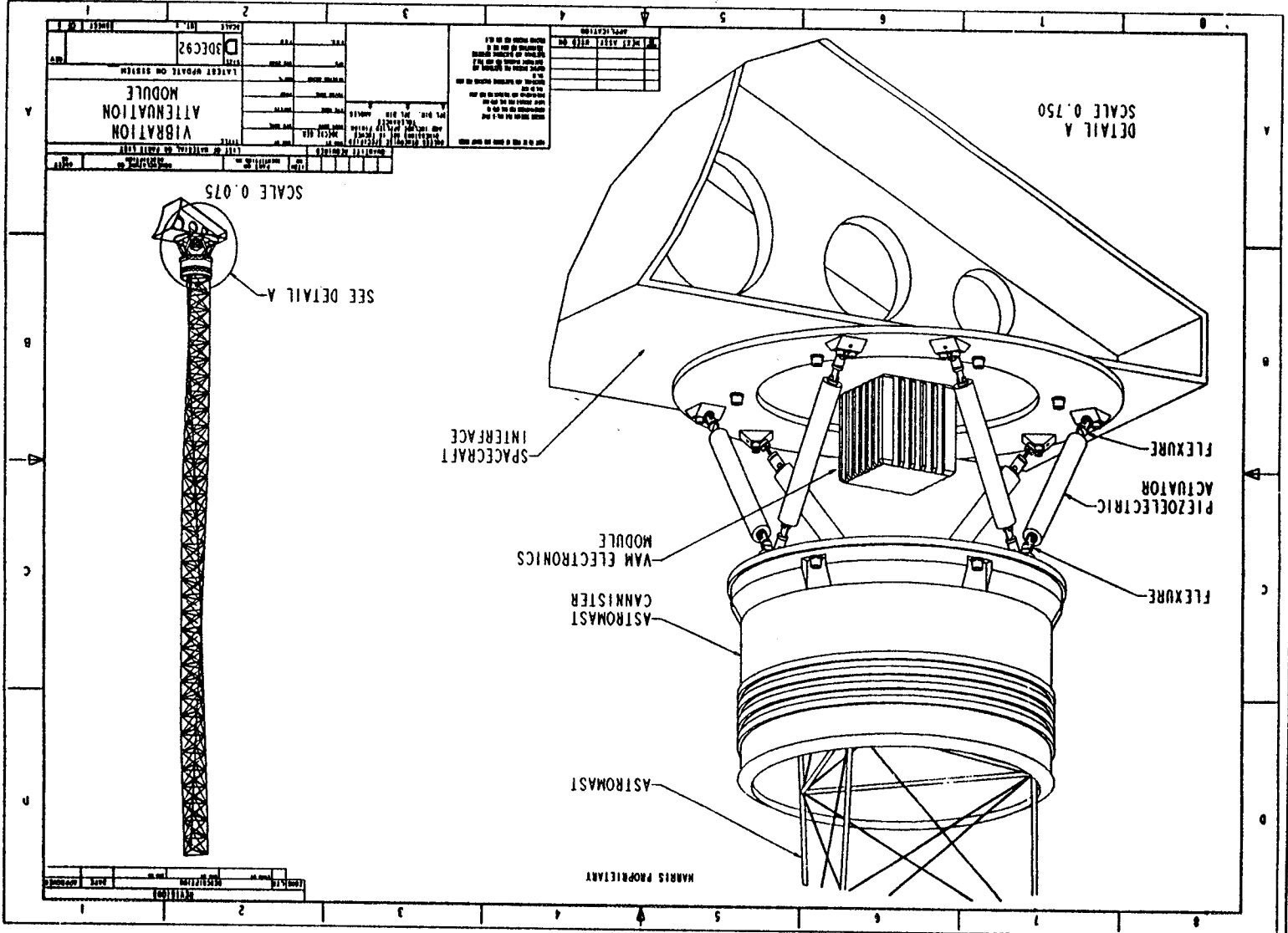


Figure 6.2-7 For the DMSP Applications, the VAM is Inserted Between the Astronaut Deployment Canister and the Spacecraft Bus



ISOLATOR GREATLY ATTENUATES SSMI DISTURBANCE IMPACT ON MAGNETOMETER ATTITUDE

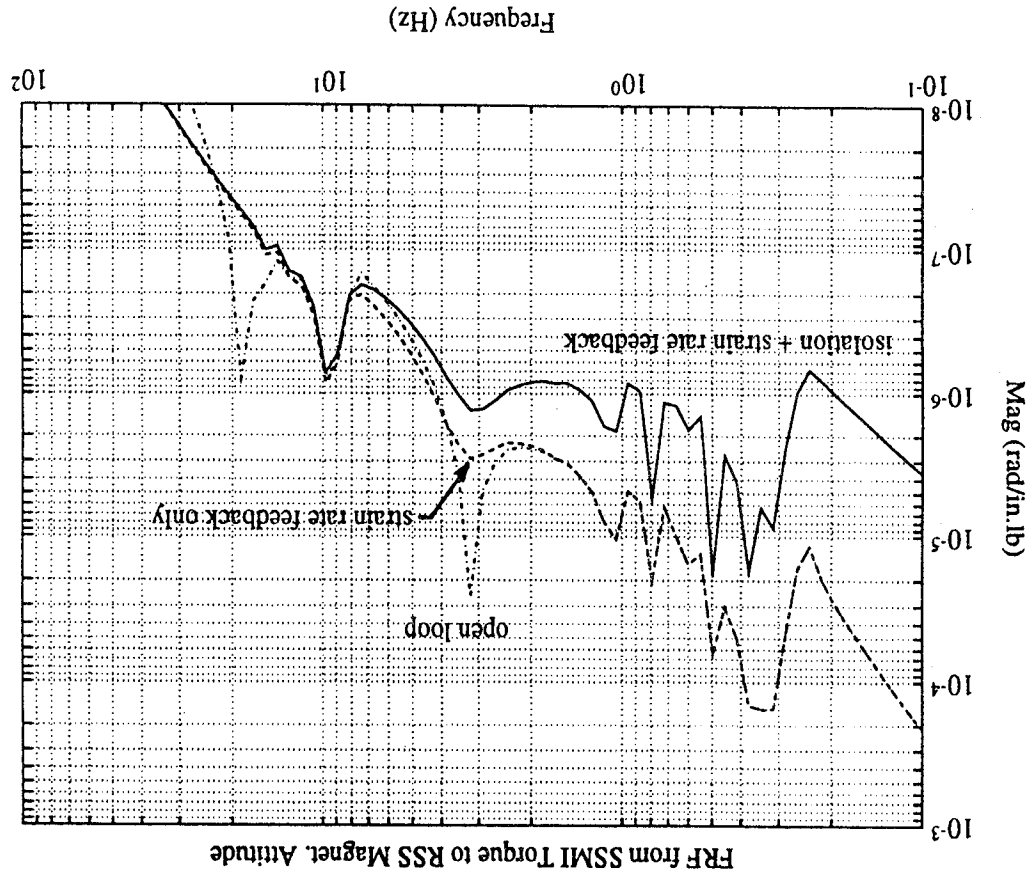
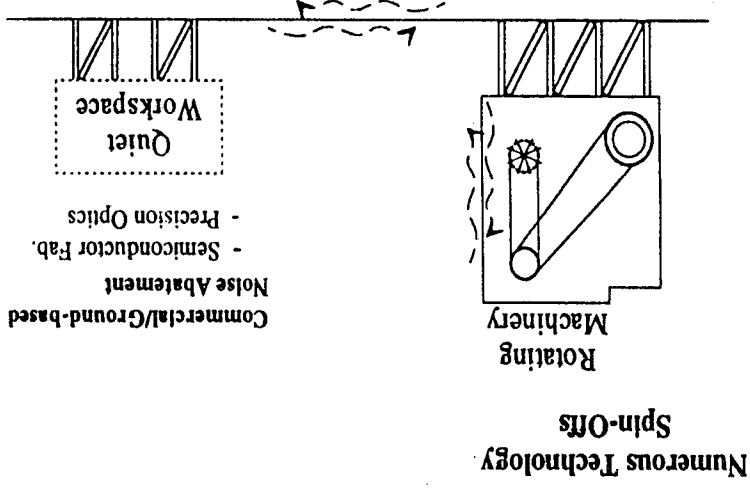


Figure 6.2-8 The VAM Isolator Greatly Attenuates the Impact of the Major Spacecraft Disturbances on the Magnetometer Attitude Errors

- AIFs = an augmentation to passive structure
- 6 AIFs form a self-contained 6 d.o.f. isolation platform (VAM).

Key:
 = Truss structure
 N = constructed of active isolator fittings (VAMs)

On the Ground



In Space

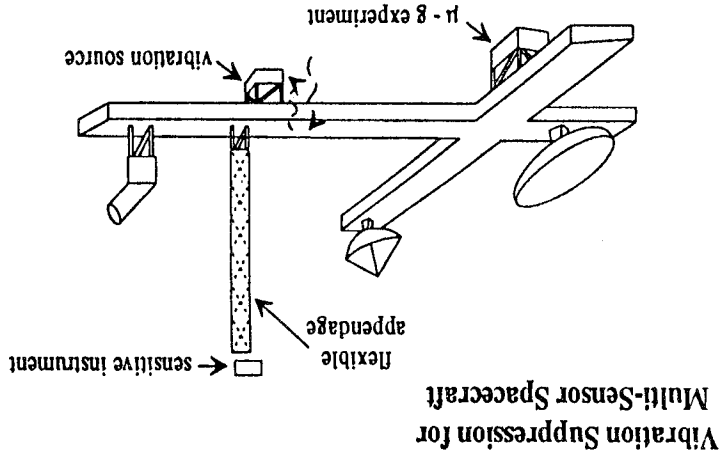


Figure 6.2-9 AIFs and VAMs Offer a Modular, Highly Adaptable Technology for Isolation and Precision Alignment

a 1-g environment, the Phase 3 CEM testbed is suspended using zero-g suspension devices which approximate free-free boundary conditions. The design requirement was to have all suspension modes less than or equal to 0.20 Hz to preclude interaction with the flexible-body modes of the testbed.

The goals of the Phase 3 CEM testbed design were to approximate the overall size, shape, inertia properties, first structural mode frequency, appendage bending mode dynamic interactions and weight of a scaled EOS AM-1 spacecraft using existing Phase 2 CEM hardware. New 1/10:1 multiple scaling parameters were developed to define the scaled properties for the Phase 3 CEM testbed. Using 1/10:1 multiple scaling, design parameters such as mass and stiffness properties scale as 1/10 of full-scale while geometry (length, area, and volume) and frequency scale as 1.0. This results in a testbed having the same overall size and structural frequencies as predicted for the full-scale EOS AM-1 spacecraft but at only 1/10 of the weight, allowing the testbed to be suspended from the existing Phase 2 CEM suspension system at NASA/LaRC.

The overall Phase 3 CEM testbed design, comprised of truss primary structure, flexible appendages, payload mass simulators 2-axis pointing gimbals, gas jet thrusters, and associated electronics boxes is shown in Figures 6.3-1 and 6.3-2. The testbed, shown with its suspension cables, has three 2-axis gimbals mounted on the underside of the structure which simulate the VNIR, MISR, and SWIR science payloads located on the nadir (+Z axis) side of the EOS AM-1 spacecraft. In this orientation, the gimbals are easier to access and have unobstructed fields of view. Lasers mounted on the 2-axis gimbals in conjunction with advanced optical scoring systems located on the lab floor are used to conduct pointing experiments. All of the remaining science payloads are modeled as mass simulators. Some of the mass simulators are mounted on payload towers (one of two bays of truss) in order to more accurately match the payload center-of-gravity (CG) locations in the EOS AM-1 model.

Two flexible appendages are required for the Phase 3 CEM testbed. The deployable articulated mast designed for the CEM Phase 2 testbed is used to simulate the low-frequency dynamics of the single EOS AM-1 solar array while a new Phase 3 CEM High Gain Antenna (HGA) simulator was developed to simulate the low-frequency dynamics of the EOS AM-1 high gain antenna. The HGA was designed, fabricated, and tested as part of the Phase 3 CEM design study. The horizontal orientation of the cantilevered CEM mast requires the use of zero-g suspension device to off-load its tip weight while the vertically mounted HGA is sufficiently robust and requires no off-loading.

The Phase 3 CEM testbed primary structure design is based on four truss system longerons, six truss bulkheads, system diagonals struts, and payload towers. The length of the Phase 3 CEM primary structure is slightly shorter than the EOS AM-1 bus structure (220" vs.

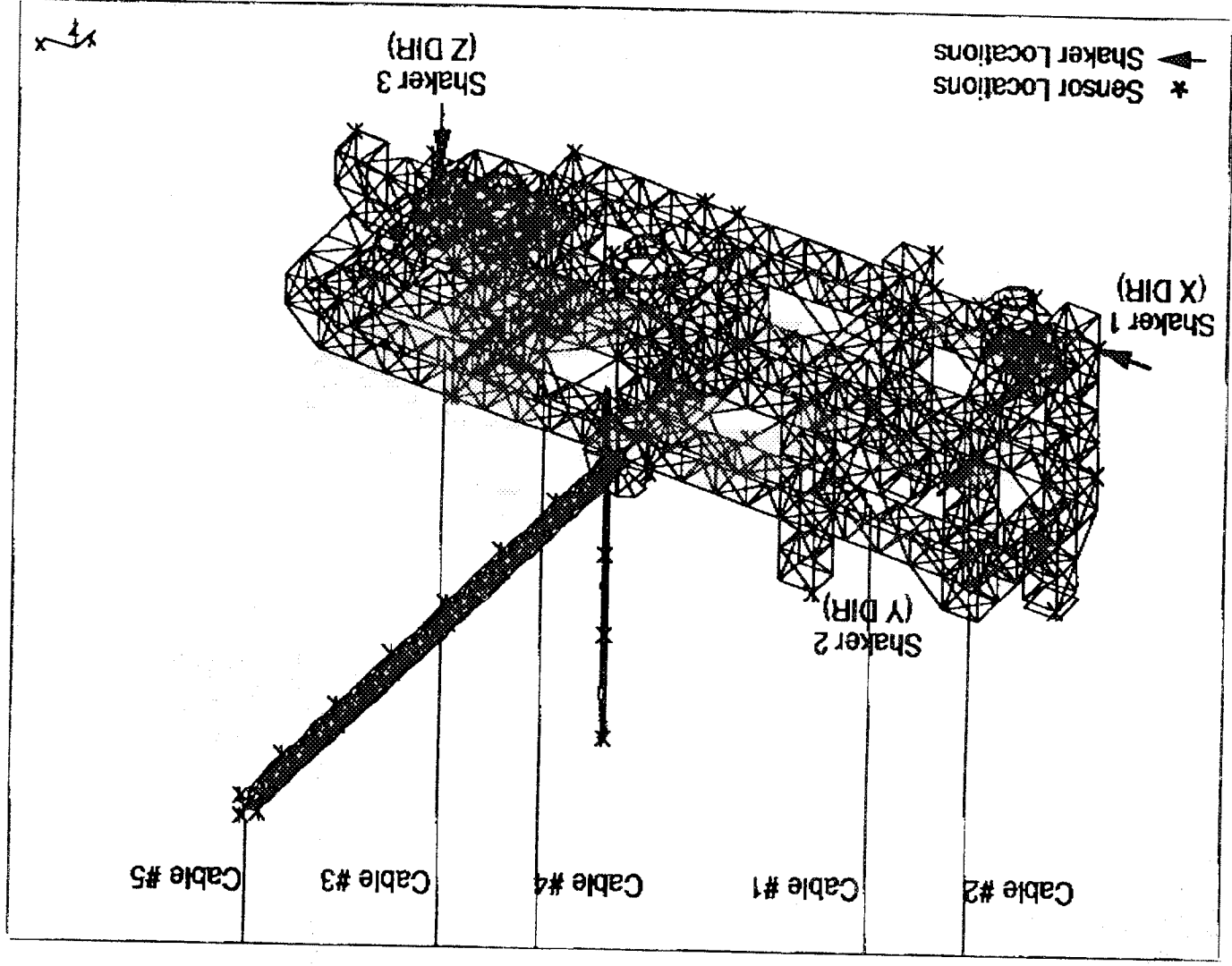


Figure 6.3-1 Phase 3 CEM Evolutionary Model

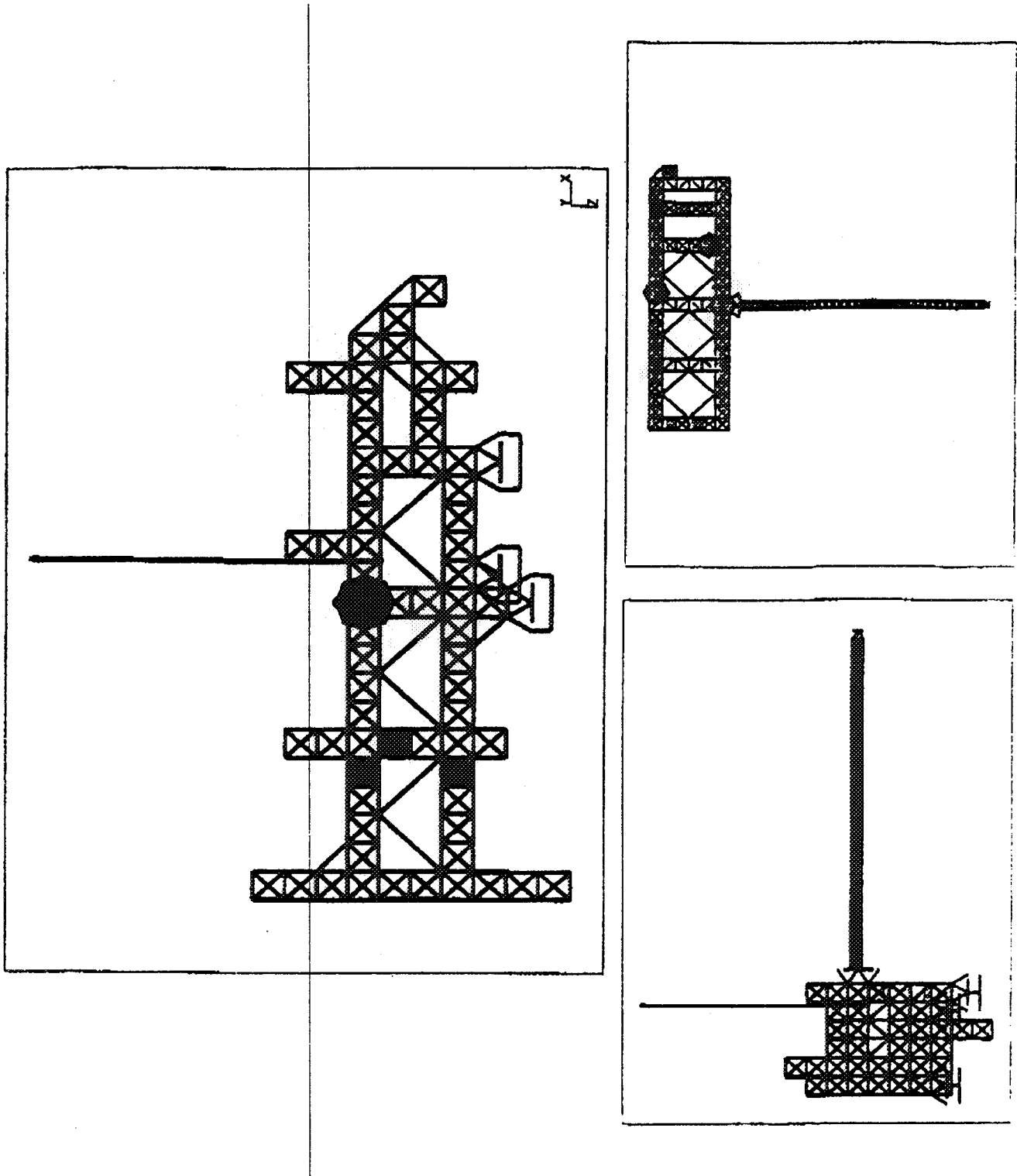


Figure 6.3-2 Phase 3 CEM Baseline Configuration (Orthogonal Views)

256") while the width (60" vs. 68") and height (80" vs. 78") dimensions of the two structures are fairly close.

All of the important science payloads and subsystems on the EOS AM-1 spacecraft were modeled on the Phase 3 CEM testbed using either a discrete rigid mass or a 2-axis gimbal with a mass payload. A total of 11 out of the 19 payloads simulated in the EOS AM-1 model were identified as important for the Phase 3 CEM model and therefore were included on the testbed. The remaining 8 payloads were deleted. The MISR, SWIR and VNIR payloads, each identified as key pointing payloads, were simulated using 2-axis gimbals in place of rigid masses. Table 6.3-1 contains a list of the 11 payloads included in the Phase 3 CEM model. The mass of the deleted payloads is offset by the weight increase resulting from using the 2-axis gimbals which are heavier than the EOS payloads they simulate.

The two flexible appendages used on the Phase 3 CEM testbed to simulate the EOS AM-1 solar array and high gain antenna are the deployable articulated mast originally designed for the Phase 2 CEM testbed and a newly developed HGA simulator. These two Phase 3 appendages approximate the low-frequency dynamics of the EOS appendages and simulate the modal interaction between the appendage and bus structure. The mast is cantilevered horizontally from a 2-axis gimbal stand mounted on the Y-side of the testbed while the HGA mounts directly to strut node balls and is cantilevered vertically upward along the Z-axis.

Table 6.3-1 Simulated EOS AM-1 Payloads

PAYLOAD DESCRIPTION	SIMULATOR TYPE	SCALED EOS WEIGHT (LBS)
VNIR	Gimbal	40.98
SWIR	Gimbal	29.11
MISR	Gimbal	29.77
CERES2	Rigid Mass	28.47
COMM	Rigid Mass	26.26
GNC Bench & Shell	Rigid Mass	32.18
MODIS	Rigid Mass	51.87
MOPITT	Rigid Mass	45.52
PMAD	Rigid Mass	69.16
TIR	Rigid Mass	35.94
TR	Rigid Mass	72.30
Total:		461.56

A free-free modal analysis of the Phase 3 CEM structure was performed to verify that the frequency of the first Phase 3 CEM primary structure mode matches the design goal of 23 Hz, which corresponds to the first primary structure mode of the EOS AM-1 on-orbit spacecraft. A description of the first 26 modes resulting from the analysis are shown in Table 6.3-2. The frequencies of the low-frequency appendage modes are not listed since the free-free analysis is not intended to quantify the low-frequency appendage dynamics.

Based on the modal analysis, the first system mode of the testbed occurs at the 23.97 Hz (mode No. 25) and is a torsion mode of the truss primary structure. The modes which occur prior to the first primary structure system mode are mainly rigid body modes, appendage modes, and local gimbal payload modes. It should be noted that closed-loop control of the 2-axis gimbals should eliminate the rotational payload mode at 14 Hz; therefore, this is not considered a true local payload mode. The first Phase 3 CEM payload modes are the gimbal plunge modes at 22 Hz.

Table 6.3-2 Phase 3 CEM Free-Free Modal Analysis

MODE NO.	FREQ (HZ)	DESCRIPTION
1-6	0.00	Rigid Body Modes
7-10	< 2.00	HGA & MAST First Bending
11	2.87	HGA First Torsion
12	5.74	Mast First Torsion
13	9.95	Mast Second Bending, Z-axis
14	10.05	Mast Second Bending, X-axis
15-17	13.8-14.1	Gimbal Payload X-axis rotation
18	21.48	Gimbal Payload Plunge
19	22.00	Gimbal Payload Plunge
20	22.12	HGA Second Bending, X-axis
21	22.48	Gimbal Payload Plunge
22	23.14	PMAD/HGA Bending
23	23.41	Second Bending, Y-axis
24	23.50	Towers/PMAD Bending
25	23.97	System 1st Torsion
26	24.88	System Bending/Torsion

6.4 First VAM Test Session on the Phase 3 CEM

As described above, the Phase 3 CEM features three science instrument simulators consisting of two-axis gimbal assemblies and arc-second resolution laser optical scoring systems (OSS) in order to implement precision pointing and jitter experiments. The VAM was installed underneath the center gimbal as indicated in Figure 6.4-1. The VAM system performance is based on the LOS error measured by the OSS. To demonstrate the benefits of Harris's VAM the two remaining gimbals are commanded with uncorelated white noise disturbance commands. These disturbances demonstrate the interaction between the different instruments. The LOS error of the open-loop (the VAM is off) is compared to the closed-loop (the VAM is turned on). The VAM controller tested on the CEM was a generic design that did not use any detailed models of the Phase 3 CEM. Thus the VAM testing reported here employed only on-site modifications to adapt the system to the dynamic characteristics of the CEM..

The goals of this initial test session were to integrate the VAM on the experimental facility and obtain some preliminary test data. Upon VAM installation the loop stability was evaluated. Each active fitting's stability was evaluated individually and with all of the other active fitting loops closed. Note that the VAM controller design consists of six independent local loops designed individually. The controller for each fitting consists of two loops, the outboard loop and the inboard loop, as described in Section 6.2. The outputs from both of these loops are summed together to form the control input to the piezo stack. The outboard loop's stability is evaluated by taking a loop transfer function from piezo command input to the outboard loop controller output. Similarly the inboard loop stability evaluated from the piezo command input to the output of the inboard loop controller (this is usually evaluated with the outboard loop closed). After the loops were modified to obtain the proper stability margins the performance of the VAM system can be evaluated.

In the above initial check-out testing, it was found that the inboard loops tended to become saturated by the low frequency, quasi-rigid body modes of the CEM. In consequence, we elected to carry out the remaining tests using alternative control configurations involving the operation of subsets of the inboard loops. Control configuration 1 uses only the outboard loops for every alternate fitting and the inboard loop for the remaining fittings. Configuration 2 uses the outboard loops only. Finally, configuration 3 is the same as configuration 2 except that a lower frequency (corner frequency at 10 Hz) high pass filter is used for the velocity estimators.

The performance of the VAM is determined from the amount of LOS error reduction obtained when the VAM control loops are turned on. The following plots show the performance improvement for the different control configurations. Figure 6.4-2 shows the LOS X error vs. LOS Y error for both the open-loop and closed-loop for configuration #1. Figure 6.4-3 shows similar results for configuration 2. Notice that the configuration 1 response shows a higher

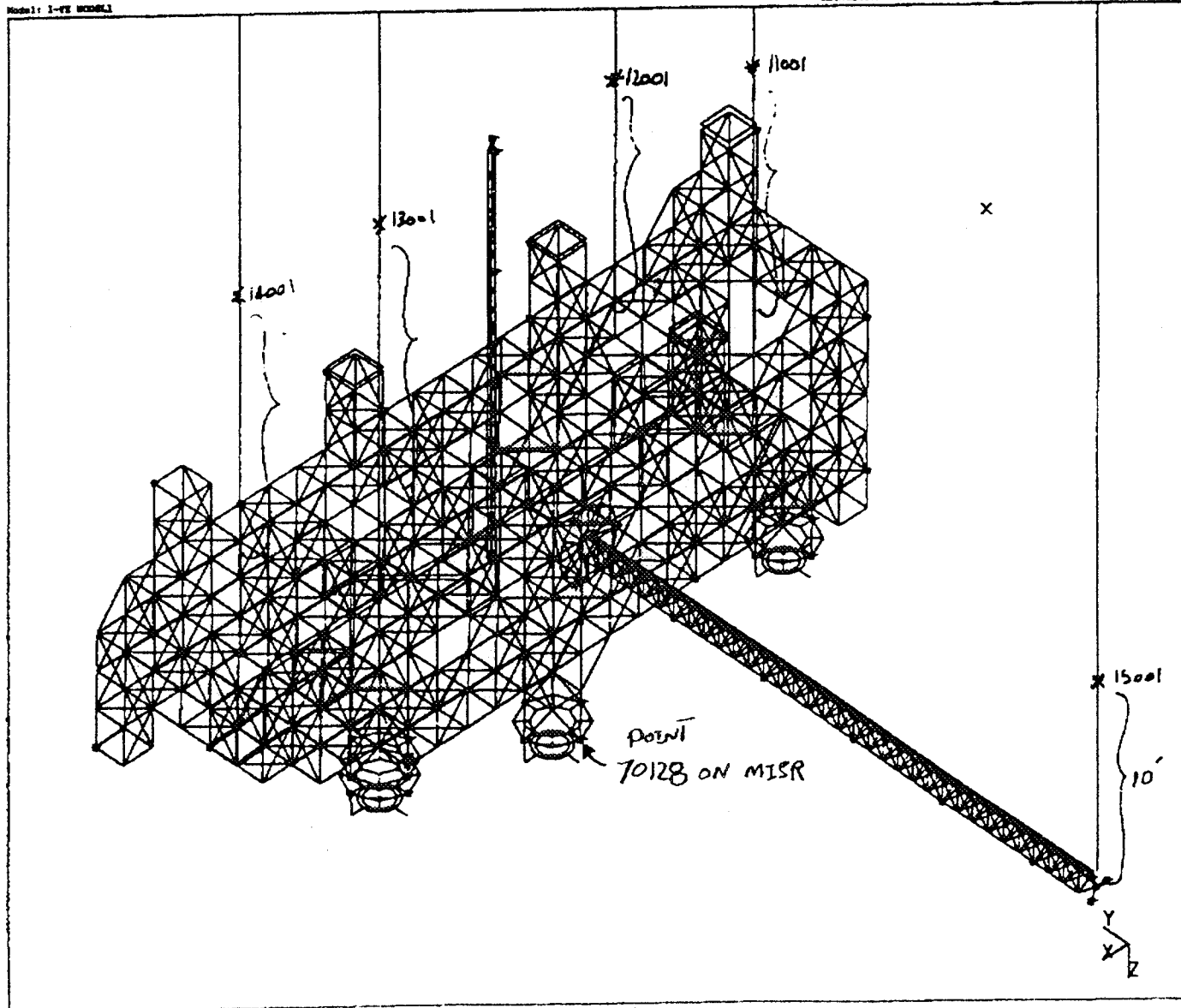
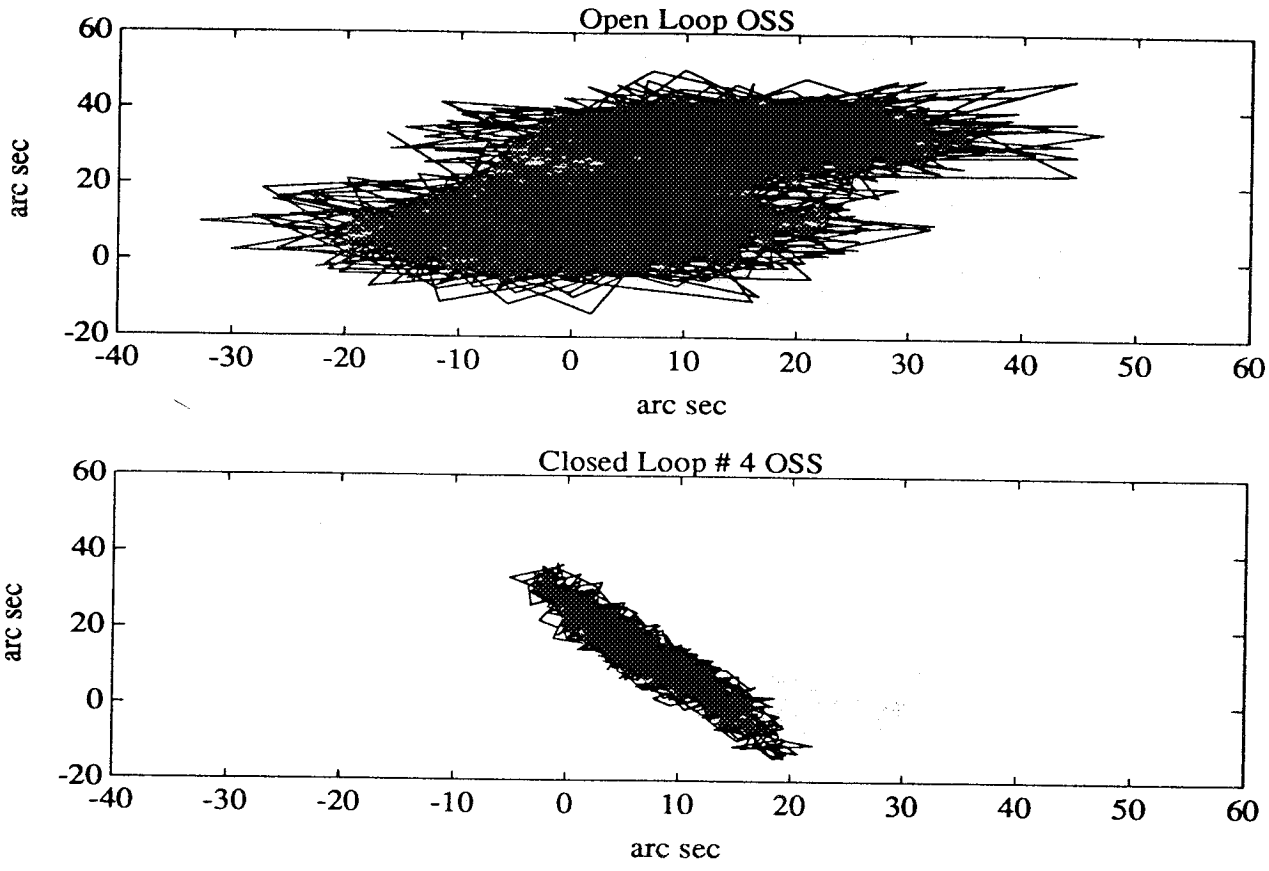


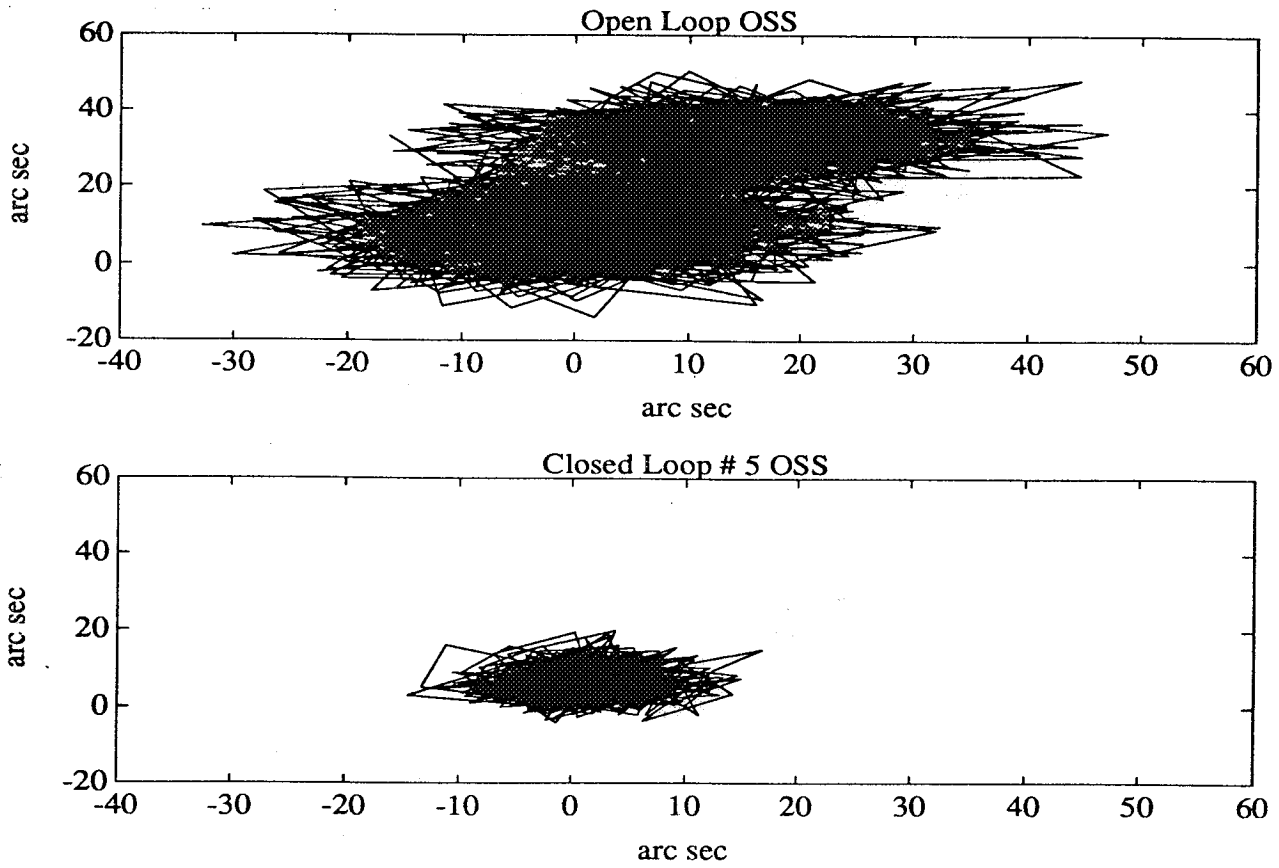
Figure 6.4-1 The VAM Replaced the Structural Mount of the MISR Simulator



a.

b.

Figure 6.4-2 LOS Error in the OSS Target Plane for (a) Open-Loop, (b) Closed-Loop, Control Configuration #1



a.

b.

Figure 6.4-3 LOS Error in the OSS Target Plane for (a) Open-Loop and (b) Closed-Loop, Control Configuration #2

susceptibility to the low frequency rigid body modes of the CEM. Figure 6.4-4 shows the corresponding z-axis accelerometer response for configuration 1. The LOS error results for configuration 3 shown in Figure 6.4-5 indicate only a marginal improvement over configuration 2. Notice the OSS LOS error is dominated by frequencies less than 10 Hz so approximately a factor of 4 reduction is obtained with the VAM. This is to be expected because the original design was intended to attenuate modes from 10 Hz to 100 Hz. Figure 6.4-6 shows the LOS error frequency response from the disturbance over this frequency band

Figure 6.4-6 indicates substantial isolation performance for the dominant structural modes. These results were obtained for a generic VAM design that was not refined in any way to account for the Phase 3 CEM dynamics. The test results do indicate ways to further improve the low frequency dynamic performance for the CEM. In this instance, the inboard loops were susceptible to the very low frequency CEM modes because of inadequate low frequency roll-off. This could not be remedied on-site because of the lack of sufficient states in the analog electronics. Subsequent activities address these issues through a variety of design refinements, including the use of a DSP chip to adaptively refine the inboard loop controller in order to optimize its performance for the structural system being isolated. The refined design testing is being carried out with financial support through Harris IR&D and in collaboration with NASA/LaRC under a Memorandum of Agreement (MOA) for a Cooperative Technology Development Program. The refined test program results obtained under this MOA will be reported separately. This NASA/Industry collaboration will serve as the vehicle for rapid, cost-effective maturation of a vibration isolation technology having wide space-borne and ground-based commercial applications.

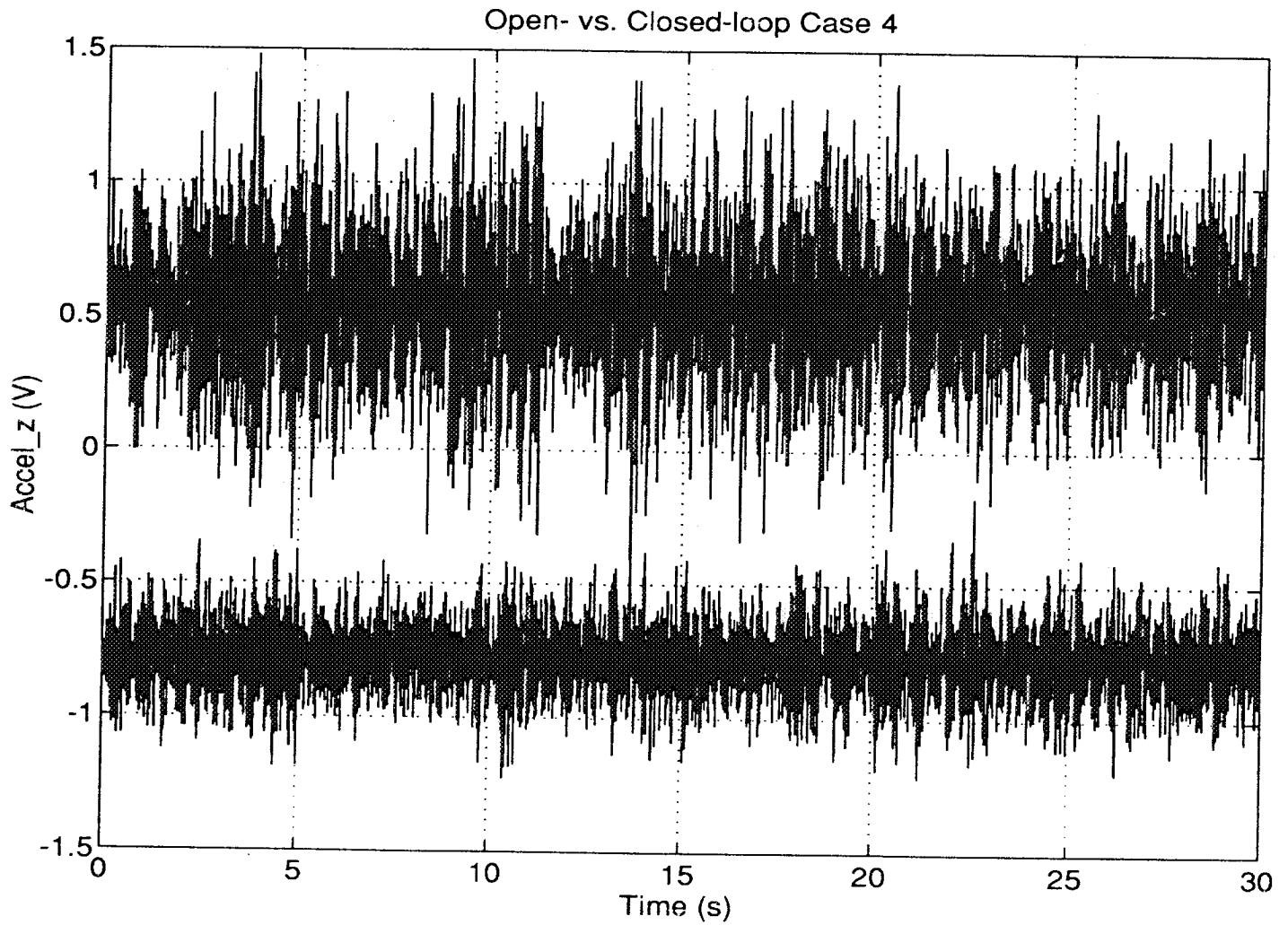


Figure 6.4-4 Z-axis Accelerometer Output Time Histories - Upper Plot Shows Open-Loop Response. Lower Plot Shows Closed-Loop Response for Control Configuration #1

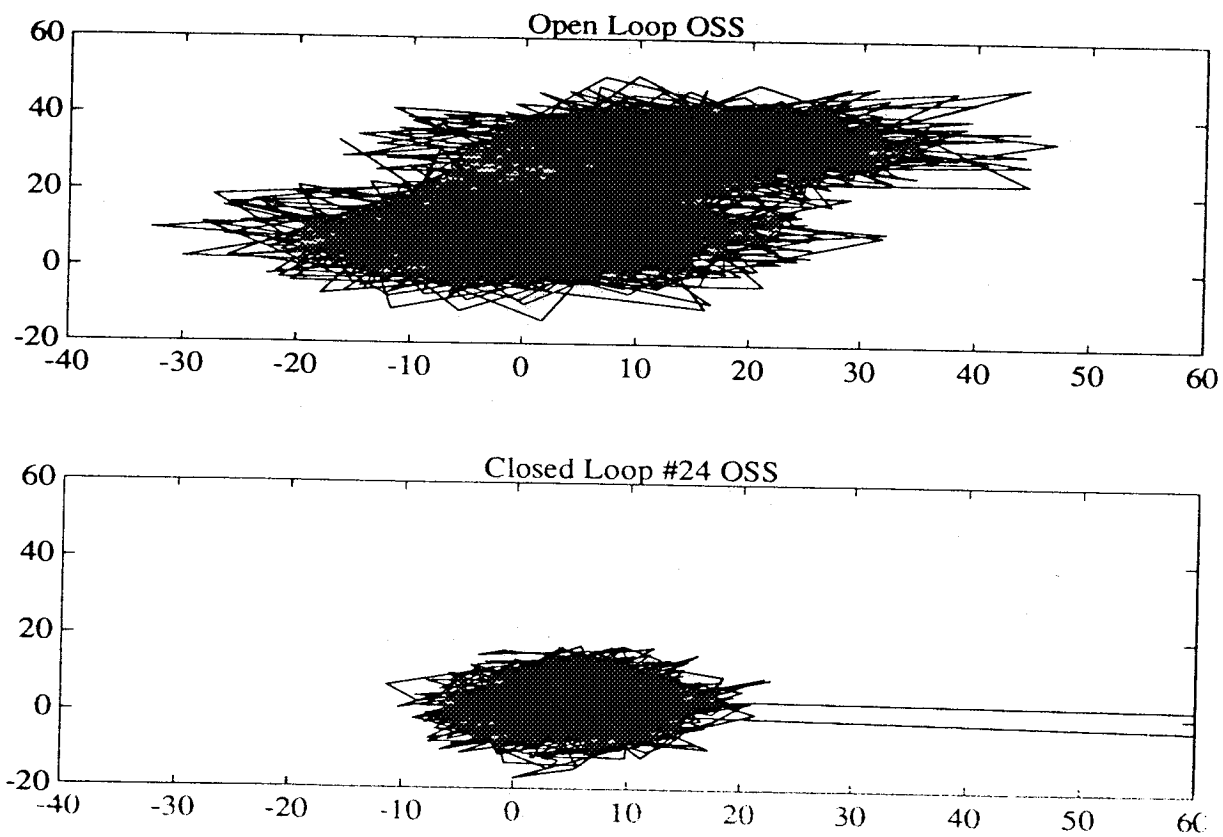


Figure 6.4-5 Open Versus Closed-Loop Responses for Control Configuration #3. The Top Pair of Plots Show LOS Error in the Target Plane. The Bottom Plots show the Two LOS Component Time Histories

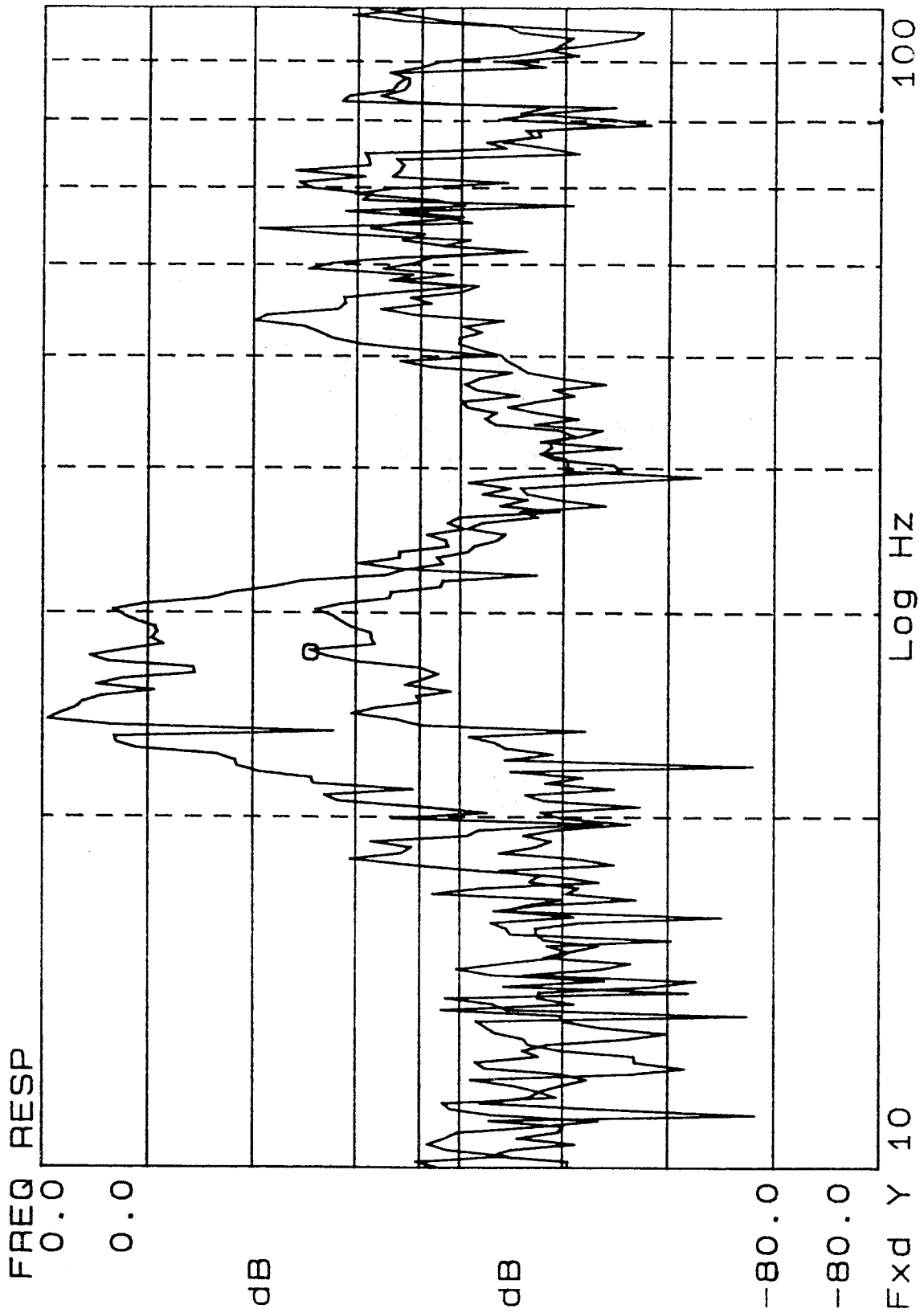


Figure 6.4-6 Open Versus Closed-Loop Frequency Responses from Disturbance to LOS Error

7. CONCLUDING REMARKS

To conclude this report, we wish to offer our heart-felt thanks to the NASA CSI office, supporting personnel at LaRC and MSFC as well as engineering personnel of Control Dynamics Corporation and all others concerned for making the experimental activities reviewed here a technically rewarding experience.

The variety and challenge of the testbeds and the rigor of this *independently refereed* test program helped us develop a *broad-based, well-balanced* technology. Even the "glitches" that inevitably occurred in such a complex undertaking were valuable in that they simulated the non-idealities of realistic spacecraft control design tasks. The challenges offered by this experimental program encouraged the Harris Guest Investigator team to achieve greater resourcefulness and efficiency as evidenced by:

1. The pioneering application of automated system ID and the integration of this capability with control design.
2. The development of streamlined, accelerated controls implementation and test processes.
3. The inauguration of initial development leading to autonomous spacecraft control with revolutionary implications for future control theory and practice.
4. Test, demonstration of new, modular, high impact controls *products* such as the Vibration Attenuation Module.

When Phase 1 of the Guest Investigator Program began Precision Space Structures control was still a "theoretical sand-box". Now, thanks to the GI Program we are much closer to making this a field of *professional competence* backed by *reliable, effective* tools. Finally, by drastically reducing the cost of applying these tools we have helped make the field *economically viable*. This, together with the recent modular/autonomous hardware developments bring us to the threshold of wide-ranging markets for this technology.



References

1. R. Smith-Taylor and S.E. Tanner, *Controls Structures Interaction Guest Investigator Program: Overview and Phase I Experimental Results and Future Plans*, NASA TM-4412, February 1993.
2. D.S. Bernstein and D.C. Hyland, "Optimal Projection for Uncertain System (OPUS): A Unified Theory of Reduced-Order, Robust Control Design," in *Large Space Structures: Dynamics and Control*, S.N. Atluri and A.K. Amos, eds., Springer-Verlag, New York, 1988.
3. D.C. Hyland, "Minimum Information Stochastic Modelling of Linear Systems with a Class of Parameter Uncertainties," *Proc. Amer. Contr. Conf.*, 620–627, Arlington, VA, June 1982.
4. D.C. Hyland, "Maximum Entropy Stochastic Approach to Controller Design for Uncertain Structural Systems," *Proc. Amer. Contr. Conf.*, 680–688, Arlington, VA, June 1982.
5. D.S. Bernstein and S.W. Greeley, "Robust Controller Synthesis Using the Maximum Entropy Design Equations," *IEEE Trans. Autom. Contr.* 31, 362–364, 1986.
6. D.C. Hyland and D.S. Bernstein, "The Optimal Projection Equations for Fixed-Order Dynamic Compensation," *IEEE Trans. Autom. Contr.* 29, 1034–1037, 1984.
7. D. S. Bernstein and D.C. Hyland, "The Optimal Projection/Maximum Entropy Approach to Designing Low-Order, Robust Controllers for Flexible Structures," *Proc. IEEE Conf. Dec. Contr.*, 745–752, Fort Lauderdale, FL December 1985.
8. D.S. Bernstein, L.D. Davis, and S.W. Greeley, "The Optimal Projection Equations for Fixed-Order, Sampled-Data Dynamic Compensation with Computation Delay," *IEEE Trans. Autom. Contr.* 31, 859–862, 1986.
9. D.S. Bernstein, L.D. Davis and D.C. Hyland, "The Optimal Projection Equations for Reduced-Order, Discrete-Time Modelling, Estimation and Control," *AIAA J. Guid. Contr. Dyn* 9, 288–293, 1986.

10. D.S. Bernstein and D.C. Hyland, "The Optimal Projection Approach to Robust, Fixed-Structure Control Design," in *Mechanics and Control of Space Structures*, 237–293, J.L. Junkins, Ed., AIAA, 1990.
11. S.W. Greeley and D.C. Hyland, "Reduced-Order Compensation: Linear-Quadratic Reduction Versus Optimal Projection," *AIAA J. Guid. Contr. Dyn.*, Vol. 11, pp. 328–335, 1988.
12. D.C. Hyland and S. Richter, "On Direct Versus Indirect Methods for Reduced-Order Controller Design," *IEEE Trans. Autom. Contr.*, Vol. 35, pp. 377–379, 1990.
13. D.C. Hyland and D.S. Bernstein, "The Majorant Lyapunov Equation: A Nonnegative Matrix Equation for Guaranteed Robust Stability and Performance of Large Scale Systems," *IEEE Trans. Autom. Contr.*, Vol. AC–32, pp. 1005–1013, 1987.
14. D.C. Hyland and E.G. Collins, Jr., "An M-Matrix and Majorant Approach to Robust Stability and Performance Analysis for Systems with Structured Uncertainty," *IEEE Trans. Autom. Contr.*, Vol. 34, pp. 691–710, 1989.
15. E.G. Collins, Jr. and D.C. Hyland, "Improved Robust Performance Bounds in Covariance Majorant Analysis," *Int. J. Contr.*, Vol. 50, pp. 495–509, 1989.
16. D.C. Hyland and E.G. Collins, Jr., "Some Majorant Robustness Results for Discrete-Time Systems," *Automatica*, Vol. 27, pp. 167–172, 1991.
17. D.S. Bernstein, "LQG Control with an H_∞ Performance Bound: A Riccati Equation Approach," *IEEE Trans. Autom. Contr.* 34, 293–305, 1989.
18. J.C. Doyle, K. Glover, P.P. Khargonekar and B.A. Francis, "State-Space Solutions to Standard H_2 and H_∞ Control Problems," *IEEE Trans. Autom. Contr.* 34, 1989.
19. W.M. Haddad and D.S. Bernstein, "Robust Stability and Performance Analysis for State Space Systems Via Parameter-Dependent Lyapunov Functions: The Popov Criterion Revisited," *Proc. IEEE Conf. Dec. Contr.*, Brighton, U.K., December 1991.

20. W.M. Haddad and D.S. Bernstein, "Parameter-Dependent Lyapunov Functions, Constant Real Parameter Uncertainty and the Popov Criterion in Robust Analysis and Synthesis," *IEEE Trans. Autom. Constr.*, to appear.
21. D.S. Bernstein, W.M. Haddad, D.C. Hyland and F. Tyan, "A Parameter Dependent Lyapunov Function for Maximum Entropy Design Approach," *Syst. Contr. Letters*, to appear.
22. S. Richter and E.G. Collins, Jr., "A Homotopy Algorithm for Reduced Order Compensator Design Using the Optimal Projection Equations", *Proc. 28th IEEE Conf. Decis. Contr.*, 506–511, Tampa, FL, December 1989.
23. E.G. Collins, Jr., and S. Richter, "A Homotopy Algorithm for Synthesizing Robust Controllers for Flexible Structures Via the Maximum Entropy Design Equations," *Third Air Force/NASA Symposium on Recent Advances in Multidisciplinary Analysis and Optimization*, 324–333, San Francisco, CA, September 1990.
24. H.B. Waites, R.D. Irwin, V.L. Jones, S.C. Rice, D.J. Tollison and S.M. Seltzer, *Active Control Technique Evaluation for Spacecraft (ACES)*, Final Report to Flight Dynamics Lab of AF Wright Aeronautical Labs, Report No. AFWAL-TR-88-3038, June 1988.
25. E.G. Collins, Jr., D.J. Phillips and D.C. Hyland, "Design and Implementation of Robust Decentralized Control Laws for the ACES Structure at Marshall Space Flight Center," NASA Contractor Report 4310, Langley Research Center, July 1990.
26. E.G. Collins, Jr., D.J. Phillips and D.C. Hyland, "Robust Decentralized Control Laws for the ACES Structure," *Contr. Sys. Mag.*, 62–70, April 1991.
27. J.-N. Juang and R.S. Pappa, "An Eigensystem Realization Algorithm for Modal Parameter Identification and Model Reduction," *J. Guid. Contr. Dyn.* 8, 620–627, 1985.
28. J.-N. Juang and R.S. Pappa, "Effects of Noise on Modal Parameters Identified by the Eigensystem Realization Algorithm," *J. Guid. Contr. Dyn.* 8, 620–627, 1985.

29. S.E. Tanner, R.S. Pappa, J.L. Sulla, K.B. Elliott, R. Miserentino, J.P. Bailey, P.A. Cooper, B.L. Williams, Jr. and A.M. Bruner, *Mini-MAST CSI Testbed User's Guide*, NASA TM-102630, 1992.
30. E.G. Collins, Jr., J.A. King, D.J. Phillips and D.C. Hyland, "High Performance, Accelerometer-Based Control of the Mini-MAST Structure at Langley Research Center," NASA Contractor Report 4377, May 1991.
31. E.G. Collins, Jr., J.A. King and D.J. Phillips, "High Performance, Accelerometer-Based Control of the Mini-MAST Structure," *AIAA J. Guid. Contr. Dyn.*, to appear.
32. V.L. Jones, A.P. Bukley and A.F. Patterson, "NASA/MSFC Large Space Structures Ground Test Facility". *A Collection of Technical Papers, Volume 2 — AIAA Guidance, Navigation and Control Conference*, pp. 792-806, August 1991. (Available as AIAA 91-2694).
33. J.-N. Juang, M. Plan and L.G. Horta, "User's Guide for System/Observer/Controller Identification Toolbox," *NASA Technical Memorandum 107566*, 1992.
34. L.D. Davis and J.A. King, "Fast MIMO System Identification of the Multi-Hex Prototype Experiment," *AIAA Journal of Guidance, Control and Dynamics*, to appear.
35. D.J. Phillips, D.C. Hyland, E.G. Collins, Jr. and J.A. King, "The Multi-Hex Prototype Experiment," *Proc IEEE Conf. Dec. Contr.*, Brighton, U.K., December 1991.
36. E.G. Collins, Jr., S. Richter and L.D. Davis, "Reliable Design of H_2 Optimal Reduced-Order Controllers Via a Homotopy Algorithm," *SPIE Aerospace Sensing Conf.*, Orlando, FL, April 1992.
37. Y. Ge, L.T. Watson and E.G. Collins, Jr., "A New Homotopy Method for Solving the H_2 Optimal Model Reduction Problem," *Fourth SIAM Conference on Optimization*, Chicago, IL, May 1992.
38. E.G. Collins, Jr., W.M. Haddad and D.S. Bernstein, "Small Gain, Circle, Positivity and Popov Analysis of a Maximum Entropy Controller for a Benchmark Problem," *Proc. Amer. Contr. Conf., Chicago, IL*, June 1992.

39. D.C. Hyland, E.G. Collins, Jr. and J.A. King, "Frequency Domain Performance Bounding for Uncertain Strictly Positive Real Plants Controlled by Positive Real Compensators," *Proc. Amer. Contr. Conf.*, San Francisco, CA, June 2-4, 1993.
40. K.W. Belvin, K.B. Kenny, L.G. Horta, J. Bailey, A. Bruner, J. Sulla, J. Won and R. Ugoletti, *Langley's CSI Evolutionary Model: Phase 0*. NASA TM-104165, 1991.
41. K.S. Narendra, E.G. Kraft and L.H. Ungar, "Neural Networks in Control Systems," *ACC Workshop Notes, 1991 American Control Conference*, Boston Massachusetts, 1991.
42. D.C. Hyland, "Neural Network Architecture for On-Line System Identification and Adaptively Optimized Control," *Proc. IEEE Conf. Dec. Contr.*, Brighton, U.K., December 1991.
43. D.C. Hyland and J.A. King, "Neural Network Architectures for Stable Adaptive Control, Rapid Fault Detection and Control System Recovery," *15th Annual AAS Guid. Contr. Conf.*, Keystone CO, February 1992.
44. D.C. Hyland, "Adaptive Neural Control (ANC) Architectures: a Tutorial," *Proceedings of the Industry, Government and University Forum on Adaptive Neural Control for Aerospace Structural Systems*, August 19-20, 1993 Melbourne, FL.
45. M. Phan, J.-N Juang and D.C. Hyland, "On Neural Networks in Identification and Control of Dynamic Systems," *NASA TM 107702*, NASA Langley Research Center, June 1993.
46. J.-N. Juang, M. Phan, L.G. Horta, and R.W. Longman, "Identification of Observer/Kalman Filter Markov Parameters: Theory and Experiments," *Proceedings of the AIAA Guidance, Navigation and Control Conference*, New Orleans, Louisiana, August 1991.
47. M. Phan, "New Concepts of Adaptive Neural Control," *Proceedings of the Industry/Government Forum on Adaptive Neural Control for Aerospace Structural Systems*, August 19-20, 1993, Melbourne, Florida.

REPORT DOCUMENTATION PAGE			Form Approved OMB No. 0704-0188	
Public reporting burden for this collection of information is estimated to average 1 hour per response, including the time for reviewing instructions, searching existing data sources, gathering and maintaining the data needed, and completing and reviewing the collection of information. Send comments regarding this burden estimate or any other aspect of this collection of information, including suggestions for reducing this burden, to Washington Headquarters Services, Directorate for Information Operations and Reports, 1215 Jefferson Davis Highway, Suite 1204, Arlington, VA 22202-4302, and to the Office of Management and Budget, Paperwork Reduction Project (0704-0188), Washington, DC 20503.				
1. AGENCY USE ONLY (Leave blank)	2. REPORT DATE December 1994	3. REPORT TYPE AND DATES COVERED Contractor Report 1-30-89 to 8-31-94		
4. TITLE AND SUBTITLE Streamlined Design and Self Reliant Hardware for Active Control of Precision Space Structures			5. FUNDING NUMBERS C NAS1-19372 WU 233-01-01-06	
6. AUTHOR(S) David C. Hyland, James A. King, and Douglas J. Phillips				
7. PERFORMING ORGANIZATION NAME(S) AND ADDRESS(ES) Harris Corporation Government Aerospace Systems Division P. O. Box 94000 Melbourne, FL 32902-9400			8. PERFORMING ORGANIZATION REPORT NUMBER	
9. SPONSORING/MONITORING AGENCY NAME(S) AND ADDRESS(ES) National Aeronautics and Space Administration Langley Research Center Hampton, VA 23681-0001			10. SPONSORING/MONITORING AGENCY REPORT NUMBER NASA CR-4637	
11. SUPPLEMENTARY NOTES Langley Technical Monitor: Rudeen Smith-Taylor				
12a. DISTRIBUTION/AVAILABILITY STATEMENT Unclassified - Unlimited Subject Category 18			12b. DISTRIBUTION CODE	
13. ABSTRACT (Maximum 200 words) Precision space structures may require active vibration control to satisfy critical performance requirements relating to line-of-sight pointing accuracy and the maintenance of precise, internal alignments. In order for vibration control concepts to become operational, it is necessary that their benefits be practically demonstrated in large scale ground-based experiments. A unique opportunity to carry out such demonstrations on a wide variety of experimental testbeds was provided by the NASA Control-Structure Integration (CSI) Guest Investigator (GI) Program. This report surveys the experimental results achieved by the Harris Corporation GI team on both Phases I and II of the program and provides a detailed description of Phase II activities. The Phase I results illustrated the effectiveness of active vibration control for space structures and demonstrated a systematic methodology for control design, implementation and test. In Phase II, this methodology was significantly streamlined to yield an on-site, single session design/test capability. Moreover, the Phase II research on adaptive neural control techniques made significant progress toward fully automated, self-reliant space structure control systems. As a further thrust toward productized, self-contained vibration control systems, the Harris Phase II activity concluded with experimental demonstration of new vibration isolation hardware suitable for a wide range of space-flight and ground-based commercial applications. The CSI GI Program Phase I activity was conducted under contract NAS1-18872, and the Phase II activity was conducted under NAS1-19372.				
14. SUBJECT TERMS Flexible Structures, Control, Experiment, Robustness, Adaptive Control, Neural Networks, Vibration Isolation			15. NUMBER OF PAGES 164	
			16. PRICE CODE A08	
17. SECURITY CLASSIFICATION OF REPORT Unclassified	18. SECURITY CLASSIFICATION OF THIS PAGE Unclassified	19. SECURITY CLASSIFICATION OF ABSTRACT	20. LIMITATION OF ABSTRACT	